



HAL
open science

Spreading of complex fluids : deposition laws and analysis of spreading defects

Marion Krapez

► **To cite this version:**

Marion Krapez. Spreading of complex fluids : deposition laws and analysis of spreading defects. Fluid mechanics [physics.class-ph]. Université Paris sciences et lettres, 2022. English. NNT : 2022UP-SLS076 . tel-04288610

HAL Id: tel-04288610

<https://pastel.hal.science/tel-04288610v1>

Submitted on 16 Nov 2023

HAL is a multi-disciplinary open access archive for the deposit and dissemination of scientific research documents, whether they are published or not. The documents may come from teaching and research institutions in France or abroad, or from public or private research centers.

L'archive ouverte pluridisciplinaire **HAL**, est destinée au dépôt et à la diffusion de documents scientifiques de niveau recherche, publiés ou non, émanant des établissements d'enseignement et de recherche français ou étrangers, des laboratoires publics ou privés.

THÈSE DE DOCTORAT
DE L'UNIVERSITÉ PSL

Préparée à l'ESPCI Paris PSL

Étalement de fluides complexes : lois de dépôt et étude de défauts d'étalement.

Spreading of complex fluids: deposition laws and analysis of spreading defects.

Soutenue par

Marion KRAPEZ

Le 4 octobre 2022

École doctorale n°397

Physique et Chimie des matériaux

Spécialité

Physico-chimie

Composition du jury :

Jean-François JOANNY
Professeur, Collège de France *Président du jury*

Marie-Caroline JULLIEN
Directrice de recherche, Université de Rennes - CNRS *Rapporteuse*

Ludovic PAUCHARD
Directeur de recherche, Université Paris-Saclay - CNRS *Rapporteur*

Guillaume OVARLEZ
Directeur de recherche, Université de Bordeaux - CNRS *Examineur*

David QUÉRÉ
Directeur de recherche, ESPCI Paris - CNRS *Examineur*

Annie COLIN
Professeur, ESPCI Paris *Directrice de thèse*

To my dad.

Remerciements

Tout d'abord, j'aimerais remercier ma directrice de thèse, Annie Colin, qui m'a donné l'opportunité de faire ce travail de thèse. Toujours disponible pour une réunion quand j'en avais besoin, elle m'a aiguillé vers les pistes à creuser et apporté le recul nécessaire pour réaliser ce travail. Elle m'a fait confiance en me laissant beaucoup d'autonomie et m'a permis de présenter mon travail à de nombreuses conférences internationales. J'aimerais également remercier Anaïs Gauthier pour son soutien au début de la thèse et Jean-François Joanny pour les discussions intéressantes que nous avons pu avoir.

Je voudrais également remercier l'équipe de l'Oréal qui est à l'origine de cette thèse et m'a suivi tout au long de sa réalisation, en particulier Odile Aubrun, Jean-Baptiste Boitte, Angelina Roudot, Danielle Le Verge et Christophe Kusina pour les nombreuses discussions que nous avons eu, ainsi que l'organisation de ma venue sur site à plusieurs reprises.

Je remercie également Marie-Caroline Jullien et Ludovic Pauchard pour avoir accepté d'être les rapporteurs de ma thèse, ainsi que David Quéré, Guillaume Ovarlez et Jean-François Joanny pour avoir accepté d'être membres de mon jury de thèse. Je vous remercie pour les échanges et les discussions scientifiques ainsi que pour votre retour bienveillant sur l'ensemble de mon travail.

Je remercie également les membres de l'atelier de mécanique de l'ESPCI, Ludovic Olanier, Alexandre Lantheaume, et Jean-Claude Mancier qui m'ont aidé à réaliser mes montages expérimentaux. Merci également à Hélène Dodier et Isabelle Borsenberger pour les commandes et l'aide administrative. Je souhaite aussi remercier l'IPGG et la plateforme technologique, ainsi que Bruno Bresson pour son soutien sans faille au MEB.

Je tiens à remercier tous mes collègues du MIE et en particulier Mickaël, Anh, Soufiane, Massi, Youcef, Anaïs, Nan, Edwige, Adrien, Corentin, que j'ai eu la chance de rencontrer et avec qui j'ai partagé des moments sympathiques. Je remercie également les doctorants du SIMM pour les weekends en Normandie, et les doctorants du PMMH pour le road trip post-conférence.

Merci à Maika pour avoir été une super bibi à l'ESPCI et m'avoir écouté pendant 3 ans parler de ma thèse au cours de nos repas hebdomadaires. Je remercie mes amis, les vieux et les plus récents, d'être là et de garder le contact.

Pour finir, je remercie mes parents, mon frère et mon compagnon pour leur soutien inconditionnel.

Table of contents

Symbols	xi
Résumé en français	xiii
General Introduction	xix
I Elastohydrodynamics	1
1 Introduction - Part I	3
1.1 Cosmetic context	3
1.2 Rheology	4
1.2.1 What is rheology?	4
1.2.2 Main fluid classes	5
1.2.3 Material solicitations and characterizations	9
1.2.4 Rheological measurements in practice	11
1.3 Spreading a fluid on a rigid plane	14
1.3.1 Wetting and spreading	14
1.3.2 Classic coating processes	16
1.3.3 Study of deposited thickness with soft blade coating	17
1.3.4 Coating of non-Newtonian fluids	21
1.4 Goals of this thesis - Part I	24
1.5 Conclusion	25
2 Soft blade coating of Newtonian fluid with finite reservoir of fluid	27
2.1 Motivations	28
2.1.1 Industrial motivations: cosmetics spreading	28
2.1.2 Academic motivations: elasto-hydrodynamic coupling	28
2.2 Spreading experiment	29
2.2.1 Experimental set-up	29
2.2.2 Silicone oil as a Newtonian fluid model	33

2.3	Spreading dynamics	34
2.3.1	Two regimes	34
2.3.2	Importance of the wetting length	35
2.4	Estimation of the deposited thickness with a scaling law	35
2.4.1	Elasto-hydrodynamic competition	36
2.4.2	Limits of the scaling law	37
2.4.3	Comparison with experiments	39
2.5	Numerical model of deposited thickness	40
2.5.1	Model presentation	40
2.5.2	Prefactor validation	49
2.5.3	Capillary effect	50
2.5.4	Shape of deposit	51
2.6	Flexible blade coating with finite size reservoir is not analogous to dip coating	53
2.7	Conclusion	54
3	Extension to shear-thinning fluids	55
3.1	Experiment	56
3.1.1	Fluid model: Xanthan gel	56
3.1.2	Spreading dynamics	59
3.2	A generalized scaling law to predict the film thickness	60
3.2.1	Elasto-hydrodynamic competition for shear-thinning fluids	60
3.2.2	Comparison with experimental data	62
3.3	Numerical solution of the elasto-hydrodynamic equations adapted to the shear-thinning fluids	63
3.3.1	Under-blade-area equations	64
3.3.2	Torque balance	68
3.3.3	Free surface equations	68
3.3.4	Numerical method	69
3.3.5	Results of the calculation for the shear rate	70
3.3.6	Comparison with experiments and scale law	71
3.4	Comparison of shear-thinning and Newtonian fluids	71
3.4.1	Choice of the equivalent Newtonian fluid	72
3.4.2	Mechanical work	75
3.4.3	Shape of the fluid deposit	77
3.4.4	Disentangle the effect of the rheological parameters n and k	78
3.5	Conclusion	79

4	Normal stress and Yield stress shear-thinning fluids	81
4.1	Normal stress fluid coating	82
4.1.1	HPAM solutions	82
4.1.2	Spreading experiment	84
4.1.3	Comparison with xanthan	85
4.1.4	Comparison with other coating geometry described in the literature	89
4.2	Yield stress fluid coating	90
4.2.1	Carbopol gels	90
4.2.2	Expectations for spreading dynamics by dimensional analysis	92
4.2.3	Huge variation of $e = f(l_w)$ relationship	92
4.2.4	Impact of Carbopol elasticity	93
4.2.5	Fluid partially stuck under the blade	95
4.3	Conclusion	98
4.4	Perspectives	99
II	Suspensions	101
5	Introduction - Part II	103
5.1	Suspension of particles	104
5.1.1	Phase diagram	104
5.1.2	Rheology of dense suspensions	107
5.1.3	Suspensions of particles in a yield stress fluid	111
5.2	Drying	112
5.2.1	Drying of a sessile droplet	112
5.2.2	Drying of complex fluids	112
5.3	Adhesion and cohesion	114
5.3.1	Differentiation between tackiness, stickiness, adhesion, and cohesion	114
5.3.2	Main categories of material adhesives	115
5.3.3	Adhesion tests	116
5.3.4	Results of a tack test	117
5.3.5	Link with rheological properties	119
5.4	Soft substrate: the skin	121
5.4.1	Skin structure	121
5.4.2	Mechanical characteristics	123
5.4.3	Surface properties	126
5.4.4	Skin Models in the literature	126
5.4.5	Focus on PDMS	128
5.5	Goals of this thesis - Part II	128

5.6	Conclusion	129
6	Impact of fillers in the formation of aggregates in cosmetic deposit	131
6.1	Context and evaluation	132
6.1.1	Industrial context	132
6.1.2	Industrial evaluation of defects	133
6.1.3	Problem definition and scope	134
6.2	Mimic the spreading of cosmetics	135
6.2.1	Proposition of a new skin model	135
6.2.2	New applicator	137
6.2.3	Protocol	138
6.2.4	Water-based formulations	139
6.3	Factors that influence the formation of aggregates	140
6.3.1	Discontinuity in the dry deposit	140
6.3.2	Solid particle concentration in the non-volatile phase	142
6.3.3	Normal force and velocity dependency	144
6.3.4	Carbopol role	146
6.4	Rheology of the dried formulations	147
6.4.1	Flow properties in the non-linear region	147
6.4.2	Viscoelastic properties in the linear region	149
6.4.3	Impact of Carbopol on rheology	150
6.5	Formation mechanism	151
6.5.1	Nucleation of the cylindrical shape	152
6.5.2	Proposal for a microscopic mechanism	153
6.5.3	Validation of the model with experimental results	155
6.5.4	Comparison of the different tests	164
6.5.5	How to favor spreading ?	165
6.6	Link with ϕ_M	166
6.6.1	Formulation tested	167
6.6.2	Evaluation of ϕ_M and calculation of volume fractions	168
6.6.3	Results on the industrial skin model	170
6.6.4	Origin of defects formation when $\phi < \phi_M$	172
6.6.5	Reducing aggregates formation by increasing ϕ_M	172
6.7	Conclusion	173
6.8	Perspectives	175
	Conclusion and perspectives	177
	References	181

Appendix	195
A. Impact of the Wetting Length on Flexible Blade Spreading	195
B. Measurement of the thickness of a transparent liquid film with an optical profilometer .	201
C. Schematic representation of the numerical resolution for Newtonian fluids	206
D. Spreading of complex fluids with a soft blade	207
E. Expression of the velocity for soft blade coating of shear-thinning fluid	226
F. Determination of the position of the solid region under the blade for yield stress fluids coating	228

Symbols

B	Blade rigidity
Ca	Capillary number
E, E^*	Young modulus, Young modulus including the Poisson ratio
F, F_c	Force, Capillary force
F_N, F_x	Normal force applied by the cylindrical applicator, Tangential force along the x direction
G, G', G''	Rigidity modulus, Storage or elastic modulus, Loss modulus
H	Heaviside function
I	Second moment of inertia of the blade $I = bu^3/12$
L	Blade length
N_1, N_2	First and second normal stress differences
R	Radius (of the rheometer geometry, of the meniscus curvature ...)
Re	Reynold number
V	Velocity of the substrate or applicator
V_{pb}	Pull-back velocity of the tack test
W_{deb}	Work of debonding (volumic except when stated otherwise)
Wi	Weissenberg number
λ_i, λ_o	Positions, in a yield stress fluid, separating the fluid and solid regions: $\tau(\lambda_i) = -\tau_y$ and $\tau(\lambda_o) = \tau_y$
l_w, l_{wi}	Wetting length (length of liquid in contact with the blade), Initial wetting length (numerical)
\mathcal{E}	Dimensionless number comparing the normal force pressure with the lubricating pressure
\mathcal{G}_0	Threshold fracture energy for vanishing rate of crack growth
$\mathcal{G}_c,$	Strain energy release rate
b	Blade width
c_v	Volume fraction of particles in the non-volatile phase
d	Gap for the parallel plate geometry
dy_c	Half width around y_0 delimiting the Newtonian and shear-thinning region such that $ \dot{\gamma}(y_0 \pm dy_c) = \dot{\gamma}_c$
e	Deposited thickness by a coating process
f_v	Viscous stress
g	Gravitational acceleration
h, h_l	Blade and free surface height
h_0	Initial thickness of the sample during the retracting phase of the tack test
k	Consistency index of the power law fluid
l	Dynamic meniscus length
l_c	Capillary length

l_d	Deposited length
l_x	Seiwert's deformation length
n	Shear-thinning index
n_r	Refractive index
p, p_L, p_{sw}	Fluid pressure relative to the atmosphere $p = P - P_{atm}$, Fluid pressure at the blade end, Fluid pressure at the back of the reservoir
q, q_l	Flow rate under the blade and the free surface
s, s_w, s_L	Curvilinear abscissae, at the back of the reservoir $s_w = L - l_w$, at the blade end $s_L = L$
t_d	Deposition time
t_v	Virtual time used in the numerical computation
u	Blade thickness
v	Fluid velocity
y_0	Position in the liquid under the blade where $\tau(y_0) = 0$
y_c	Position delimiting Newtonian and shear-thinning region in the deposited film where $\dot{\gamma}(y_c) = \dot{\gamma}_c$
$\tan \delta$	Dissipation factor $\tan \delta = G''/G'$
$\Gamma, \Gamma_{wet}, \Gamma_{dry}$	Torque, Torque induced by the fluid, Resisting torque of the blade
Ω_0, Ω_d	Initial volume of fluid under the blade, deposited volume of fluid
Φ	Dissipation function
$\delta, \delta_b, \delta_s$	Contact angle of a fluid at a triple contact line, at the back of the reservoir on the blade, or the substrate
ε	Nominal strain
η, η_f, η_0	Fluid viscosity, viscosity of the suspending liquid, viscosity of the Newtonian plateau at low shear rates
γ	Surface tension
$\Delta\gamma$	Thermodynamic work of adhesion
$\dot{\gamma}, \dot{\gamma}_c$	Shear rate, Critical shear rate delimiting the Newtonian and shear-thinning behavior
$\hat{\gamma}, \hat{\gamma}_0$	Strain, Strain amplitude
μ	Coefficient of friction
ν	Poisson's ratio
ω	Angular velocity
ω_f	Angular frequency
ϕ	Volume fraction of particles in a liquid
ϕ_M	Maximum volume fraction of particles in a liquid
ρ, ρ_s	Fluid density, Surface density (solid)
σ, σ_y	Shear stress, Yield stress
$\boldsymbol{\sigma}, \sigma_{ij}$	Stress tensor, Stress component (i surface orientation, j direction of vector)
σ_N	Nominal stress
$\boldsymbol{\tau}, \tau$	Deviator of the stress tensor, Shear stress in fluids (equivalent to σ_{xy} also sometimes simplified in σ)
τ_y	Yield stress
θ, θ_l	Angles describing the shape of the blade and free surface (between the vertical and the tangent)
$\theta_{msw}, \theta_{mL}$	Angles between the vertical and the tangent of the meniscus at the back of the reservoir s_w and the blade tip L

Résumé en français

Cette thèse est l'aboutissement des recherches que j'ai effectuées au laboratoire Chimie Biologie Innovation dans le groupe Matériaux Innovants pour l'Énergie sous la direction d'Annie Colin. Ces travaux ont été réalisés en collaboration avec L'Oréal. Ils ont mené à la publication de deux articles [1, 2].

Contexte général

Les crèmes hydratantes, les crèmes solaires et les fonds de teint sont largement utilisés pour protéger ou embellir la peau. De nombreux soins pharmaceutiques se présentent également sous forme de crèmes à application externe. L'étalement de ces produits est une étape clé car elle conditionne les performances réelles du produit lors de son utilisation par le consommateur et elle est liée aux perceptions sensorielles. L'idéal est d'obtenir un dépôt fin et homogène en épaisseur afin d'assurer des performances optimales. En pratique, l'étalement au doigt génère des défauts, par exemple un dépôt irrégulier en épaisseur ou la formation d'agrégats, ces derniers affectant également les perceptions sensorielles. La modélisation de l'application d'une crème est complexe puisqu'elle nécessite de faire intervenir de nombreuses physiques, qui sont parfois interdépendantes, ce qui explique pourquoi ce processus reste encore assez largement incompris et fait l'objet de nombreuses recherches. De plus, la transition actuelle vers des matières premières biosourcées a remis au premier plan des problématiques telles que la formation d'agrégats, ce qui représente un challenge pour l'industrie cosmétique. Dans notre étude, l'objectif était de réduire la complexité de ce processus à travers des systèmes modèles qui permettent de mettre en évidence les principes fondamentaux liés aux phénomènes étudiés. Nous avons cherché à répondre aux questions suivantes : Quels sont les paramètres qui contrôlent l'épaisseur déposée lors de l'étalement d'un fluide ? Quels sont les éléments responsables de l'apparition d'agrégats, quel est leur mécanisme de formation, et comment les éviter ? L'objectif final étant de mieux comprendre le dépôt formé sur la peau pour donner des conseils aux formulateurs afin d'optimiser les performances des produits cosmétiques.

Résumé du manuscrit

Ce manuscrit s'articule en deux parties quasi-indépendantes: seules les bases de la rhéologie présentées dans le Chapitre 1 (section 1.2) peuvent être utiles à la compréhension de la partie II.

Partie I : Élastohydrodynamique

La partie I est composée de quatre chapitres traitant de l'étalement de fluides complexes par lamelle flexible. Le premier chapitre introduit le sujet et les trois autres décrivent les résultats obtenus en étalant des fluides aux propriétés de plus en plus complexes. Dans tous les cas, il s'agit de fluides modèles (polymères purs ou en suspensions) qui ne contiennent pas de particules solides.

Chapitre 1 : Introduction - Partie I

L'étalement de fluides complexes fait intervenir des connaissances portant à la fois sur les fluides et leurs comportements sous cisaillement, ainsi que sur les processus d'étalement. Ce chapitre introductif se présente donc en deux parties. Dans la première partie sont abordés les principes fondamentaux de la rhéologie. Les principales catégories de fluides sont décrites, ainsi que les outils expérimentaux d'évaluation des propriétés et leurs limites. Dans une seconde partie, les différentes géométries d'étalement sont présentées. Nous montrons que l'enduction par trempage et l'étalement par lame rigide ont été largement étudiés avec des fluides newtoniens et non-newtoniens. A contrario, un nombre très limité de travaux portent sur l'étalement par lamelle flexible, en particulier en ce qui concerne les fluides non-newtoniens. La revue bibliographique montre également que l'étalement d'une quantité de fluide fini, c'est à dire avec un réservoir de fluide qui se vide au cours de l'étalement, a été très peu considéré. Cette situation est cependant primordiale pour modéliser l'étalement de crèmes, de peinture ou de confiture par exemple. Si l'on s'intéresse à l'étalement par lamelle flexible, choisie pour modéliser un doigt capable de se déformer sous contrainte, une seule étude à notre connaissance, menée par Kusina [3], fait intervenir un réservoir de fluide fini. Son travail a porté sur le cas particulier des fluides à seuil. L'étalement d'une quantité finie de fluide par une lamelle flexible est donc un problème académique largement ouvert à de nouvelles investigations et qui trouve également une forte résonance dans le milieu industriel.

Dans les Chapitres 2, 3 et 4 nous avons cherché à comprendre l'impact d'un réservoir de taille finie sur la loi de dépôt et comment les propriétés rhéologiques influencent l'épaisseur du dépôt et la dynamique d'étalement.

Chapitre 2 : Étalement par lamelle flexible d'un réservoir fini de fluide newtonien

Dans ce deuxième chapitre, nous modélisons le premier mouvement de l'application d'une crème en étalant par une lamelle flexible une petite quantité de fluide newtonien. Pour des questions de simplification, nous avons utilisé un substrat rigide et réalisé un mouvement d'étalement linéaire. L'épaisseur déposée lors du vidage du réservoir est mesurée par un profilomètre optique. Le paramètre choisi pour suivre et quantifier le niveau de remplissage du réservoir est la longueur de mouillage du fluide sur la lamelle. Nous avons montré qu'à vitesse constante le film déposé a une épaisseur qui décroît au fur et à mesure que le réservoir se vide. L'épaisseur déposée augmente avec la vitesse et la viscosité du fluide et diminue lorsque la rigidité de la lame augmente. Nous avons proposé, en équilibrant les forces élastiques et visqueuses, une loi d'échelle donnant l'épaisseur déposée en fonction notamment de la longueur de mouillage, et permettant ainsi de prédire les données expérimentales. Nous avons validé le préfacteur employé par un modèle numérique plus détaillé qui a donné des résultats en bon accord

avec les données expérimentales sans avoir à utiliser de paramètre ajustable. Cette approche numérique a également permis de montrer que les effets capillaires sont du second ordre et ont un impact significatif sur l'épaisseur déposée uniquement pour des surfaces (lamelles et substrats) très hydrophobes. Dans ce cas, l'épaisseur déposée augmente. L'impact de la vitesse d'étalement et de la viscosité du fluide sur le profil du film déposé a également été étudié. Ainsi, l'épaisseur du dépôt gagne en homogénéité en diminuant la viscosité du fluide. Enfin, nous avons montré que l'analogie entre capillarité et élasticité [4–6] n'est pas valide lorsque le niveau de liquide sous la lamelle est variable.

Chapitre 3 : Extension au cas des fluides rhéofluidifiants

Ce chapitre suit une méthode très similaire à celle présentée dans le Chapitre 2 : les expériences, lois d'échelle et calculs numériques ont été adaptés au cas de fluides rhéofluidifiants. Nous avons utilisé des suspensions de polymères dont la viscosité diminue lorsque le taux de cisaillement augmente. En modélisant le fluide avec l'équation de Ostwald et de Waele, nous avons obtenu une loi d'échelle permettant de prédire l'épaisseur déposée en fonction des paramètres rhéologiques du fluide. L'approche numérique a été utilisée pour comparer l'étalement de fluides rhéofluidifiants et de fluides newtoniens. En définissant le "newtonien équivalent" comme le fluide qui permet de déposer un même volume de fluide en un même temps que le fluide rhéofluidifiant d'intérêt (à vitesse et longueur de mouillage initiale identiques) nous avons montré qu'étaler un fluide rhéofluidifiant nécessite plus d'énergie qu'étaler un fluide newtonien. Le profil du film de fluide déposé est également différent. Nous avons ainsi relevé une différence de courbure qui se traduit par un dépôt moins homogène en épaisseur mais plus long dans le cas d'un fluide rhéofluidifiant. Avec ces résultats, il est donc possible pour le formateur de déterminer si l'ajout d'un polymère dans le but d'obtenir un comportement rhéofluidifiant est nécessaire ou non selon les effets souhaités.

Chapitre 4 : Cas des fluides rhéofluidifiants générant des forces normales ou présentant un seuil

Les fluides utilisés en industrie présentent souvent une combinaison de plusieurs propriétés. Dans une première partie, nous avons traité le cas de fluides rhéofluidifiants qui additionnellement génèrent des forces normales sous cisaillement. Nous nous attendions à obtenir des épaisseurs déposées plus importantes du fait de la pression exercée par les forces normales sur la lamelle. Cependant, la génération de forces normales n'a pas montré expérimentalement d'effets sur la loi de déposition. Les fluides à forces normales ont pu être décrit de manière satisfaisante en considérant uniquement leurs propriétés rhéofluidifiantes, ce qui s'explique par la géométrie employée. Pour prédire si les forces normales ont un effet, il ne faut pas se baser sur le nombre de Weissenberg qui compare les contraintes visqueuses et normales, mais sur un nombre sans dimension comparant les pressions associées. Cela fait apparaître un facteur géométrique qui dépend de l'épaisseur déposée et de la longueur de mouillage. Dans notre situation, ce terme est petit, ce qui explique l'absence d'effet des forces normales, contrairement à ce qui a pu être rapporté dans la littérature lors d'expériences d'enduction par trempage pour lesquelles les forces normales entraînent un gonflement du film déposé. Dans ce dernier cas, la longueur caractéristique correspond à la déformation du ménisque ce qui conduit à un nombre sans dimension supérieur à un.

Dans une seconde partie, nous avons traité le cas de fluides rhéofluidifiants dits "à seuil". Au repos, ils se comportent comme un solide et s'écoulent uniquement lorsque la contrainte appliquée dépasse la contrainte seuil. L'étalement de fluides à seuil par une lamelle flexible donne lieu à des résultats expérimentaux très dispersés. Nous avons identifié deux phénomènes pouvant expliquer cette dispersion. Premièrement, du fait du seuil, des forces élastiques provenant du liquide interviennent dans l'équilibre des forces définissant la forme de la lamelle. Ces forces élastiques pourraient expliquer pourquoi on observe parfois un vidage du réservoir de bas en haut au lieu de s'effectuer latéralement, ce qui se traduit par une longueur de mouillage constante au cours de l'étalement. Cette situation n'est pas prévue dans notre modèle. Deuxièmement, une partie du fluide présent dans le réservoir peut rester bloquée sous la lamelle et amener à des cycles de redéposition successifs. Cela se traduit concrètement par un dépôt du fluide en îlots. Ces deux phénomènes ont limité la possibilité de modéliser simplement l'étalement de fluides à seuil par lamelle flexible, la longueur de mouillage ne décrivant plus le vidage du réservoir. Dans la plupart des expériences, les deux situations sont combinées, ce qui résulte au final en une importante dispersion des données. Nous pensons qu'avec une lamelle rigide (dont l'écart avec le support et la position sont fixés), il serait possible d'étudier et de prédire l'épaisseur déposée dans le cas de fluides à seuil en adaptant le modèle proposé par Kusina [3], mais cela ne modéliserait plus vraiment l'étalement de crème par un doigt.

Ce modèle d'étalement en mouvement linéaire par une lamelle flexible sur un substrat rigide est assez éloigné des cas réels d'applications de cosmétiques, il représente au mieux le tout premier mouvement réalisé lors de l'étalement d'une crème, processus qui donne lieu généralement à des mouvements complexes circulaires, en aller-retour... Cette étude a permis cependant de donner des pistes de formulation en montrant que le fluide qui s'étale de la manière la plus homogène et avec le moins d'énergie est un fluide newtonien, de faible viscosité, et étalé lentement. Une piste intéressante à poursuivre serait d'étudier l'effet de l'élasticité du substrat en utilisant un matériau mou en guise de substrat, par exemple du polydiméthylsiloxane réticulé. Corvalan prévoit dans le cas d'un réservoir infini que l'épaisseur déposée sera plus faible toutes autres conditions égales par ailleurs [7]. La mesure expérimentale n'est pas évidente avec notre système car il repose sur une lecture de l'épaisseur déposée par profilomètre optique et se pose alors la question de la mesure de la référence (substrat sans liquide) dont la position peut varier du fait de la présence de liquide.

Partie II : Suspensions

Dès l'application d'une crème cosmétique, ou plus tard en frottant un dépôt cosmétique "sec", on peut voir apparaître des agrégats qui ressemblent à des petits cylindres et qui finissent par tomber de la peau sous l'action de la gravité. Un exemple est montré en Figure 5.18. Ces agrégats sont très pénalisants car ils induisent des sensations déplaisantes et empêchent une couverture homogène et uniforme du produit cosmétique. Les retours consommateurs sont variables et surprenamment dépendants des régions du monde ce qui laisse présager un problème complexe ne dépendant pas uniquement de la formulation du

produit. L'utilisation de certaines nouvelles matières biosourcées a engendré une apparition accrue de ces défauts. Il est donc primordial de se pencher sur ces problèmes, qui, bien qu'ils aient toujours existé, reviennent au premier plan du fait de la transition vers les particules biosourcées.

La deuxième partie du manuscrit comporte deux chapitres. Le premier, introductif, présente le cadre de l'étude et l'état de l'art pertinent à la compréhension et à l'interprétation des résultats. Le second présente l'étude expérimentale de l'apparition d'agrégats de particules lors de l'étalement d'une formulation de type crème cosmétique et le mécanisme proposé pour expliquer leur formation. Un critère formulatoire simple pour limiter l'apparition des agrégats est enfin présenté.

Chapitre 5 : Introduction - Partie II

Dès son application et tout au long de sa vie sur la peau, une crème cosmétique passe par de nombreux états et est soumise à de nombreux mécanismes différents. Nous avons donc présenté dans ce chapitre une revue de littérature assez large concernant les aspects suivants. Initialement, une crème cosmétique peut être assimilée à une suspension semi-diluée de particules dont les propriétés dépendent principalement de la phase liquide. Lors du séchage, la fraction volumique en particules solides augmente et nous avons montré que cela s'accompagne souvent de comportements non-newtoniens liés aux contacts et aux interactions entre les particules. Lors du séchage au repos d'une suspension, des études ont également signalé la formation d'une croûte de particules conduisant à une distribution non-uniforme des particules dans le dépôt. Enfin, lors du cisaillement d'un dépôt cosmétique sec, on s'attend à ce que l'adhésion et la cohésion jouent un rôle. Ce point a été principalement étudié dans le contexte des adhésifs sensibles à la pression, mais pas dans le contexte de l'étalement de couches minces de fluides complexes. Nous avons également effectué une revue bibliographique sur la peau et ses modèles synthétiques dans le but de construire une expérience nous permettant d'étudier la formation d'agrégats en reproduisant en partie les propriétés mécaniques de la peau. Sous l'angle de cet état de l'art, nous avons cherché à comprendre : comment expliquer la formation d'agrégats ? Quels sont les paramètres et mécanismes impliqués dans leur apparition ? L'objectif final du point de vue industriel était de proposer des pistes permettant d'éviter en pratique la formation d'agrégats. C'est principalement sur les aspects formulatoires que nous avons cherché ces pistes, car c'est le levier sur lequel l'industriel peut facilement avoir un impact, contrairement à la gestuelle et la technique d'application du produit.

Chapitre 6 : Impact des particules solides sur la formation d'agrégats dans les dépôts cosmétiques

Dans cette seconde partie, nous avons complexifié les systèmes étudiés en ajoutant des particules solides et un liquide non-volatile dans la formulation pour se rapprocher de la composition des cosmétiques. Le montage expérimental d'étalement a lui aussi été rendu plus réaliste par l'utilisation de surfaces molles et/ou rugueuses pour le substrat et l'applicateur. Des mouvements en aller-retour, également plus proches d'une gestuelle classique, ont été réalisés par un robot à des valeurs de vitesses et de pressions réalistes. Ces modifications permettent d'étudier la formation d'agrégats de particules qui apparaissent lorsque le dépôt de cosmétique est cisailé après séchage. Nous avons identifié les principaux paramètres impliqués dans l'émergence de ces défauts. Ces observations ont été complétées par des tests de caractérisation (notamment via des mesures rhéologiques et de pégoité), nous permettant de proposer un modèle de

mécanisme de formation des agrégats qui explique pourquoi au lieu de s'étaler de façon régulière le dépôt de fluide génère ces défauts. Enfin, nous avons proposé un critère basé sur la fraction volumique en particules solides pour réduire le risque de formation d'agrégats.

Normalement, la présence d'une phase non-volatile doit assurer le maintien d'un milieu continu capable de s'étaler. Lorsque la concentration de particules est plus grande que la concentration maximale d'empilement, la formation d'agrégats est attendue et s'apparente à de la granulation. Prendre en compte le gonflement et la porosité des particules est essentiel pour évaluer correctement cette limite à ne pas dépasser par les formulateurs. Cependant, nous avons observé des agrégats en dessous de ce seuil. Nous considérons que les agrégats se forment lorsque la cohésion de la formulation séchée l'emporte sur l'adhésion aux parois de l'applicateur et du substrat. Dans le cas inverse, le dépôt sec est étalé ou fracturé. Il est possible de passer de l'une à l'autre de ces situations en jouant sur : la concentration en particules solides, la présence ou non de polymère, la vitesse d'étalement, la force appliquée, et les propriétés adhésives aux parois. Alors que les mesures rhéologiques se sont révélées très limitées sur les formulations séchées à haute concentration en particules, les tests d'adhésion/cohésion (de type tests de pégoité) ont permis d'évaluer cet équilibre adhésion/cohésion en fonction du mode de rupture observé. De notre point de vue, le test de pégoité représente une voie à poursuivre dans l'étude de la formation de ces agrégats, notamment pour permettre une validation quantitative du modèle que nous proposons. Il serait intéressant d'utiliser les mêmes surfaces que celles du test d'étalement pour améliorer la comparaison entre ces expériences. Le test de pégoité peut être facilement utilisé en industrie, car il est facile à mettre en place et pourrait permettre une évaluation rapide du risque de formation d'agrégats pour une formulation donnée, qui ne soit pas dépendant du testeur, comme c'est le cas actuellement.

Les annexes apportent des informations complémentaires aux différents chapitres et reproduisent les deux articles publiés à *Physical Review Letters* et *Physical Review Fluids*.

General Introduction

The skin is the largest and heaviest organ of the human body, covering about 2 m² of surface on average for a mass ranging from 3 to 5 kg [8]. It maintains the inside of the body almost perfectly isolated from the outside, ensures the protection against external aggression (physical, chemical and radiative) and is the organ of the touch. It also has strong social implications (particularly for the skin on the face), as it corresponds to what others see of us.

To protect, maintain and improve the skin, it is common to use cosmetics or pharmaceutical products for external use, in the form of liquids, creams or gels. Many manufacturers work on the elaboration of these products, whose complex formulations are designed to ensure very diverse properties (UV protection, anti-aging, moisturizing ...). The spreading of these products on the skin is a key step because it impacts the performance of the products and acts on sensory perceptions. The objective is to obtain a thin deposit, as homogeneous as possible in thickness, to ensure equivalent properties throughout the product's application area. In reality, everyone knows that when you start spreading a small amount of sunscreen linearly, for example from the shoulder to the elbow, the deposit is thicker at the starting point than at the end of the movement. This means that you have to complexify your movements in order to better homogenize the product thickness. In addition, spreading defects, such as aggregates, can appear and strongly affect not only the properties but also the sensory perceptions. When trying to model the application step, one is confronted to the complexity of the problem which involves numerous and sometimes interdependent physics (e.g. rheology, tribology, drying, wetting, fluid and solid mechanics). This explains why it remains a large field of research at the present time. In addition, the transition to bio-based products in cosmetic formulations leads to new behaviors and challenges, especially during the spreading process, shaking the cosmetics industry. The stakes are high when we see that L'Oréal's objective is to reach 95% of bio-based raw materials in its products by 2030!

It is therefore essential to understand the following: what are the parameters that govern the spreading and control the deposited fluid thickness? What are the elements responsible for the observed defects? What are the processes of creation of these defects?

In order to answer these questions, the manuscript is articulated in two parts. The first part focuses on understanding the deposited thickness at the beginning of the spreading process using a "simple fluid" - with no solid particles. We mimic a one-way linear spreading with a soft blade coating system and study experimentally, theoretically, and numerically the impact of the fluid rheology on the spreading

process and the fluid film profile. The second part focuses on the spreading defects arising at the end of the spreading process using fluid with solid particles.

Each part begins with an introductory chapter explaining the framework of the study and presenting the state-of-the-art relevant to the discussion of the results.

Part I

Elastohydrodynamics

Chapter 1

Introduction - Part I

In this chapter, the bibliographical study concerning the spreading of complex fluids is presented. It serves as a basis for understanding Chapters 2, 3 and 4. We first present the fundamental principles of rheology and the different categories of fluids studied thereafter. Then, we describe the wetting and the spreading of a fluid. After a brief presentation of the main spreading geometries, we focus on the specific case of soft blade coating.

Contents

1.1	Cosmetic context	3
1.2	Rheology	4
1.2.1	What is rheology?	4
1.2.2	Main fluid classes	5
1.2.3	Material solicitations and characterizations	9
1.2.4	Rheological measurements in practice	11
1.3	Spreading a fluid on a rigid plane	14
1.3.1	Wetting and spreading	14
1.3.2	Classic coating processes	16
1.3.3	Study of deposited thickness with soft blade coating	17
1.3.4	Coating of non-Newtonian fluids	21
1.4	Goals of this thesis - Part I	24
1.5	Conclusion	25

1.1 Cosmetic context

Most personal care and cosmetic products, such as creams, lipsticks, mascaras, need to be spread by the consumer in order to obtain their desired function. This application step is crucial. If the spreading is difficult and leads to non-uniform deposit in thickness, or heterogeneities in composition, then the

product used in real condition does not meet its desired properties, even if they were obtained during laboratory tests (e.g. the level of sun protection for a sunscreen). Furthermore, spreading plays an important role in the user experience of products: if the sensory perceptions are not pleasant for the consumer, this is detrimental. Therefore, there is a current need to understand and improve the spreading properties of cosmetics products [9].

Most cosmetic products are composed of several ingredients, which gives them a non-trivial behavior when spread. Focusing on liquid formulations, the presence of solid particles and polymers is often responsible for non-Newtonian behavior. Rheological measurements allow the fluid to be classified into different categories based on its behavior (see section 1.2.2). A topic of interest in the literature has been to try to predict sensory perceptions (ease of spreading or spreadability) by physical and in particular rheological measurements [10–12] but this sometimes lacks reproducibility [10]. Others have investigated the impact of composition on the spreadability by measuring the area covered by a product spread under gravity and capillarity effect [9] or by pressing the product between two plates to evaluate the deposited thickness [13]. In these cases, spreadability does not refer to sensory perceptions but to the ability of a product to cover the largest area with the thinnest film. It is not well understood how the rheological properties affect the physical characteristics of a spread film such as the thickness. In particular, knowing whether (and why) different classes of fluids give rise to different spreading results, such as the shape of the deposited film, which may be more or less homogeneous, or the energy required to spread the product, is of interest in providing formulation advice that are not tied to a certain composition but are intended to be generalized to an entire fluid category.

In the following we describe the fundamentals of rheology that are used to distinguish the main types of fluid behavior encountered in cosmetics. Then the coating techniques are presented, focusing on the one that we believe is most relevant to mimic finger spreading: flexible (or soft) blade coating.

1.2 Rheology

1.2.1 What is rheology?

Rheology, literally the science of flow, is the study of fluids under solicitation (flow, deformation...). It has been developing from the beginning of 20th century, to fill a gap left between the theories of solid mechanics and fluid mechanics, which were unable to describe and explain the behavior of complex fluids. Complex fluids, also called non-Newtonian fluids, are defined in opposition to simpler fluids, namely Newtonian fluids (for which stress and strain rate are proportional). They correspond, but not exclusively, to polymers melts or solutions, suspensions, emulsions, gels, foams... Most non-Newtonian fluids have an intermediate behavior between a perfectly elastic solid (for which stress and strain are proportional) and a Newtonian fluid. Rheology allows us to categorize the different types of fluids according to their properties (shear-thinning, shear-thickening ...). Fluid properties have a direct impact on product processability and performances, making rheology a powerful tool for formulators to evaluate

and control them. Results of macroscopic rheological measurements are also a direct consequence of the material's microstructure, which provides insight into it. For instance, Koumakis and Petekidis [14] linked the two yields measured with an attractive colloid gel at high volume fraction to the breaking of bonds within particle cages, and the breaking of the cages into smaller constituents. Nguyen Le *et al.* showed that microscopic characteristics, such as inter-particle friction, could be directly linked to the bulk rheology [15].

1.2.2 Main fluid classes

The simplest solicitation is to shear a fluid cell between two parallel plates (Fig. 1.1). The upper plate is in motion, transmitting the force to the material as there is no slip. The stress is defined by the force applied over the surface $\sigma_{yx} = \frac{F}{S}$, in Pa.

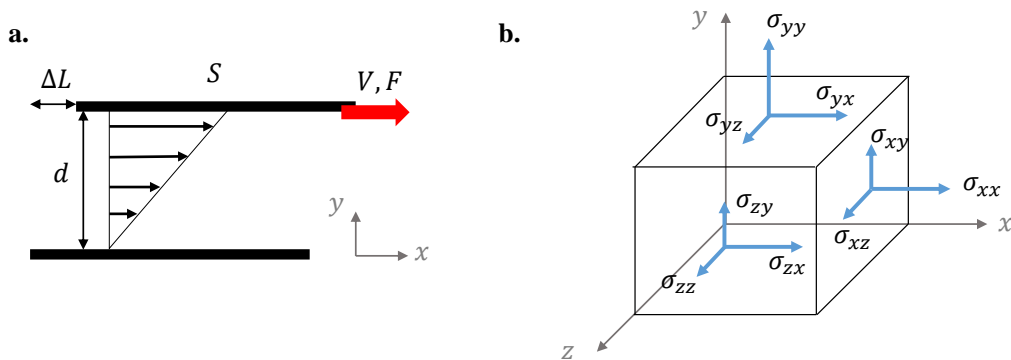


Fig. 1.1 – **a** Simple shear flow between two plates of surface S , the upper plate being moved at velocity, V . The velocity profile is linear. **b** The stress components for a small volume of fluid.

Newtonian fluids

In 1687, Newton hypothesised that "the resistance which arise from the lack of slipperiness of the part of the liquid [...] is proportional to the velocity with which the parts of the liquids are separated from one another" for a simple shear flow [16]. This can be expressed by $\sigma_{yx} = \eta \frac{V}{d}$ with $\frac{V}{d}$ the velocity gradient, in s^{-1} , also known as the shear rate, and η the fluid viscosity, in Pa.s, which is a measure of the resistance to flow. This equation describes the behavior of Newtonian fluids for which the viscosity is independent of the shear rate. In the current definition of Newtonian fluid, there are additional requirements:

- The two normal stress differences ($\sigma_{xx} - \sigma_{yy}$ and $\sigma_{yy} - \sigma_{zz}$) are zero.
- There is no time-dependence of viscosity, and stress or shear rate when the other one is maintained constant.
- The viscosities measured for different types of deformation (shear vs extension) are in direct proportion.

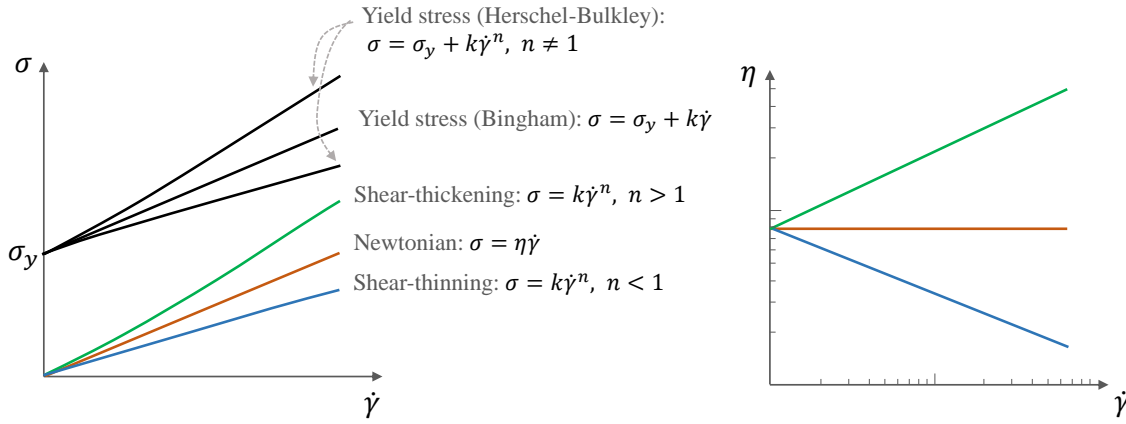


Fig. 1.2 – Schematic representation of the rheological curves for the main categories of fluid: $\sigma = f(\dot{\gamma})$ and $\eta = f(\dot{\gamma})$ in linear and logarithmic scales respectively.

Let σ_{ij} being the stress component, with i denoting the surface orientation and j referring to the direction of the stress vector. The relevant stress distribution for Newtonian fluids is:

$$\left. \begin{aligned} \sigma_{xy} = \sigma_{yx} = \sigma = \eta \dot{\gamma}, \quad \sigma_{xz} = \sigma_{yz} = 0 \\ \sigma_{xx} - \sigma_{yy} = 0, \quad \sigma_{yy} - \sigma_{zz} = 0 \end{aligned} \right\} \quad (1.1)$$

The use of the stress differences is made to avoid considering the isotropic pressure p_i ($\sigma_{xx} = \sigma_{yy} = \sigma_{zz} = -p_i$).

For non-Newtonian fluids, more complex behavior can be observed. The viscosity defined in the general case $\eta = \sigma/\dot{\gamma}$ is not necessarily constant anymore (Fig. 1.2). The following types of fluids describe particular properties and, in practice, complex fluids often exhibit a combination of these properties. Several examples are given to illustrate the physical origin of such behavior, others, specific to suspensions, are given in section 5.1.2.

Shear-thinning fluids

For *shear-thinning* fluids, the viscosity decreases with increasing shear rate (Fig 1.2). Several models describing the viscosity are used such as the Cross (1965) and Carreau models (1972) [16]. One popular model for its simplicity is the power-law model (Ostwald and de Waele) :

$$\eta = k\dot{\gamma}^{n-1} \quad (1.2)$$

with k the consistency (in Pa.s ^{n}), and n the shear-thinning index. It describes a pure shear-thinning fluid (no Newtonian plateau at low or high shear rate), which is in many cases sufficient to describe the behavior of the fluid.

Shear-thinning reflects a reduction of the resistance to flow. It can have various physical origins. For instance it can result at the microscopic level from the alignment of the solid particles or polymer chains in the flow direction [16]. For particle suspensions, the fluid slip on the particles [17] and the breaking of aggregates under shear [18] have also been presented as origins to explain shear-thinning.

Shear-thickening fluids

Shear-thickening fluids exhibit a viscosity that increases with the shear rate (Fig 1.2). A well-known example of a shear-thickening fluid is a suspension of cornstarch that behaves like a solid under shear and resumes flowing at rest. This behavior is typically encountered for highly concentrated suspensions of solid particles. The contact interactions between the particles transition from lubricated to frictional, leading to force chains that oppose the shear [19, 20]. This phenomenon is accentuated for rough and irregular particles that combine high sliding and rolling friction [21].

Yield stress fluids

Yield stress fluids present a stress, σ_y , called the *yield stress*: it has to be overcome for the system to start flowing. When the fluid behaves like a Newtonian fluid when flowing, it can be described by the *Bingham* model [16]:

$$\sigma = \sigma_y + \eta \dot{\gamma} \quad (1.3)$$

Most of the time, the system does not only exhibit a yield stress but is also shear-thinning. The *Herschel-Bulkley* model [22] is used to describe both phenomena:

$$\sigma = \sigma_y + k \dot{\gamma}^n \quad (1.4)$$

Yield stress fluids have a solid-like behavior at rest and fluid-like behavior under sufficient shear. On a small scale, the yield stress results from a stress bearing network that exists for *soft glassy materials*. This material category is vast. These networks can originate, for instance, from attraction interactions in suspensions [23], sometimes combined with high friction and rolling constraints amplifying jamming [24]. System jamming can also be obtained with soft beads when pressed against each others (e.g. microgel [25–27] and emulsions [28]).

Normal stress fluids

The relevant stress distribution for elastic liquids is :

$$\left. \begin{aligned} \sigma_{xy} = \sigma = \dot{\gamma} \eta(\dot{\gamma}), \quad \sigma_{xz} = \sigma_{yz} = 0 \\ \sigma_{xx} - \sigma_{yy} = N_1(\dot{\gamma}), \quad \sigma_{yy} - \sigma_{zz} = N_2(\dot{\gamma}) \end{aligned} \right\} \quad (1.5)$$

with N_1 and N_2 the first and second normal stress difference respectively, in Pa. Sometimes the normal stress coefficient notation, Ψ_1 and Ψ_2 is preferred with: $N_1 = \dot{\gamma}^2 \Psi_1$ and $N_2 = \dot{\gamma}^2 \Psi_2$. The normal stress

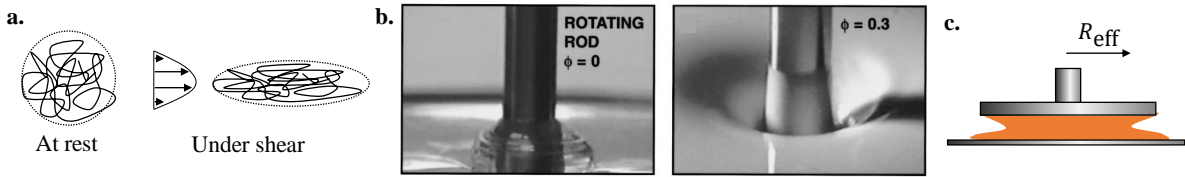


Fig. 1.3 – **a.** Deformation of polymer chain in a capillary tube the arrows represent the velocity profile. **b.** Weissenberg rod climbing effect for pure PDMS polymer (left) and a suspension of glass sphere at 0.3 v% (right) from Aral and Kaylon [33] **c.** Edge fracture in a parallel plate geometry.

differences are observed for non-linear solicitations of the sample (for large-amplitude oscillatory shear or for steady flow at high shear rate). N_1 can generally be fitted by: $N_1 = \alpha \dot{\gamma}^m$ with α and m two constants [16].

The emergence of unbalanced normal stress, and thus non-zero normal stress differences, arises from the anisotropy generated by the flow in the microstructure. For example, for polymer systems, the chains at rest have a spherical shape whose characteristic size is the radius of gyration of the polymer chain. When subjected to a flow field, the chains are elongated in the flow direction, giving to the enveloping volume an ellipsoidal shape [16], as shown in Figure 1.3a. Deformations related to the normal stress differences are also observed on the droplets of an emulsion [29]. These anisotropically deformed microstructures generate restoring forces that are consequently anisotropic. These forces give rise to the normal stress components of the normal stress difference. In most situations, the restoring force is greater in the flow direction, resulting in $N_1 \geq 0$ (i.e. $\sigma_{xx} \geq \sigma_{yy}$). Negative values of N_1 can be observed in strongly-orientated systems. For instance negative N_1 has been linked to the formation of flocculated rod-like structures aligned along the vorticity [30, 31] or the change in orientation of deformed emulsion droplets [29]. The second normal stress difference N_2 is generally considered as small compared to N_1 for dilute polymers but begins to be non-negligible for particle suspensions for which N_2 is often on the order of N_1 [32].

An example of normal stress fluid behavior is called the Weissenberg effect or "rod climbing" effect: the fluid rises along the stirring rod instead of being pushed towards the beaker rims (Fig. 1.3b). Another classic example is the swelling of a polymer jet outside a capillary tube [16]. An example of this effect is shown in Chapter 4, Figure 4.5.

Viscoelastic fluids

Up to now we have presented general laws of behavior that are time independent. In reality, the response to a sollicitation of a fluid often depends on the time. Thus, for some fluids, the behavior lies between an elastic response and a viscous behavior, depending on the time scale of the experiment relative to some characteristic time scale of the material. For slow solicitations, the material will appear more viscous than elastic, whereas for relatively fast solicitations, the opposite is true. In practice, almost all the real materials can be assumed to be viscoelastic to some extent. To take into account the viscoelastic properties, partial derivatives needs to be added.

A simple model for a viscoelastic fluid is the Maxwell model. It corresponds to a spring ($\sigma = G\hat{\gamma}$) and a viscous damper ($\sigma = \eta\dot{\gamma}$) connected in series giving: $\dot{\gamma} = \frac{\dot{\sigma}}{G} + \frac{\sigma}{\eta}$. The first term represents the equation of Hookean elasticity (with G the rigidity modulus and $\hat{\gamma} = \Delta L/d$ the strain - see Fig. 1.1) and the second one the Newtonian viscous flow. This differential equation expresses a short term elastic behavior and a long term viscous behavior. This linear equation is only valid for small deformations, other models, such as Oldroyd B model, involves more complex time derivatives of the stress tensor and extend its applicative range to large deformations [34].

1.2.3 Material solicitations and characterizations

There are two main categories of rheological measurements: in *flow* or in *oscillation*. They are used to access different information: in the first case, it is the non-linear regime that is evaluated (large to infinite deformation), while in the second case, the measurement is often made in the linear regime (small deformations). The choice depends on the conditions of use of the material to be reproduced.

Principle of measurement in flow

In this case, the strain is infinite, the material flows continuously under an imposed stress or shear rate. The structure of the fluid is usually lost after a few seconds of continuous shear. The flow properties are assessed and particularly η , σ and N_1 as a function of $\dot{\gamma}$, allowing to identify the type of the fluid (Newtonian, shear-thinning ...). Viscoelasticity can be observed by performing creep or relaxation experiments (focusing on the transient regime of flow at constant stress or strain). However, this property of the fluid is investigated more thoroughly by performing oscillation measurements.

Principle of measurement in oscillation

In this case, the material is deformed around its equilibrium state by small amplitude oscillatory shear. The experiment are performed either at constant angular frequency ω_f or at constant strain amplitude $\hat{\gamma}_0$. The oscillating strain $\hat{\gamma}(t)$ can be written:

$$\hat{\gamma}(t) = \hat{\gamma}_0 \cos(\omega_f t) \quad (1.6)$$

For small amplitude solicitations, the stress in the material is proportional to the deformation, it oscillates at the same frequency but with a phase shift δ :

$$\sigma(t) = \sigma_0 \cos(\omega_f t + \delta(\omega_f)) \quad (1.7)$$

Using the formalism of complex numbers (identified by a star $*$) the strain and stress can be rewritten: $\hat{\gamma}^* = \hat{\gamma}_0 e^{i\omega_f t}$ and $\sigma^* = \sigma_0 e^{i(\omega_f t + \delta(\omega_f))}$.

The Hooke law formalism can be used $\sigma^* = G^* \hat{\gamma}^*$, with G^* the complex modulus expressed as a combination of the storage modulus G' which represents the in-phase part measuring the elastic response,

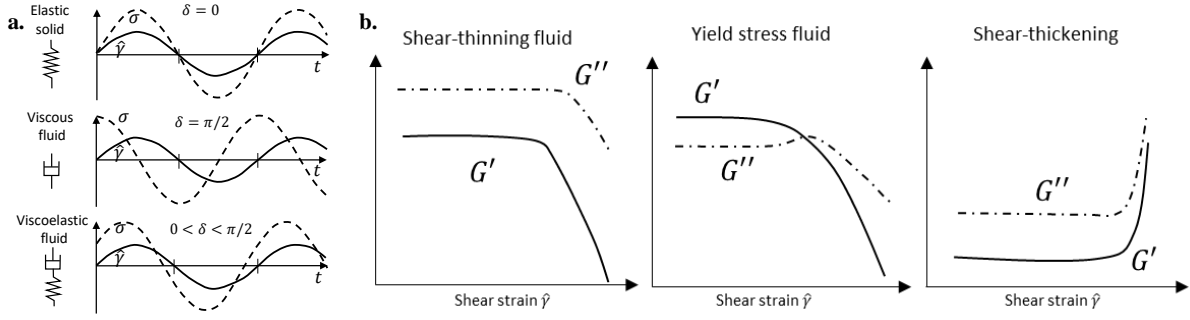


Fig. 1.4 – **a.** σ and $\hat{\gamma}$ in the linear region for a pure elastic solid, a pure viscous fluid and a viscoelastic fluid. **b.** Three types of behavior for G' and G'' during an amplitude sweep describing from left to right: shear-thinning, yield stress fluids, and shear-thickening fluids.

and the loss modulus G'' which represents the out-of-phase part measuring the dissipation, such that $G^* = G' + iG''$. Thus, by identifying the real and imaginary parts, $G' = \frac{\sigma_0}{\hat{\gamma}_0} \cos(\delta)$ and $G'' = \frac{\sigma_0}{\hat{\gamma}_0} \sin(\delta)$. The material response is written:

$$\sigma(t) = \hat{\gamma}_0 [G'(\omega_f) \cos \omega_f t + G''(\omega_f) \sin \omega_f t] \quad (1.8)$$

For a purely viscous fluid, $\sigma = \eta \dot{\gamma}$, the stress is in phase quadrature resulting in $G'(\omega_f) = 0$ and $G''(\omega_f) = \eta \omega$. For a purely elastic solid, $\sigma = G \hat{\gamma}$, giving $G' = G$ and $G'' = 0$ (Fig. 1.4a).

In practice, viscoelastic materials have more complex behaviors where both $G''(\omega_f)$ and $G'(\omega_f)$ take non-zero values. For instance, the Maxwell model described before gives $G' = G \frac{\omega_f^2 t_R^2}{1 + \omega_f^2 t_R^2}$ and $G'' = G \frac{\omega_f t_R}{1 + \omega_f^2 t_R^2}$ with $t_R = \eta/G$ the relaxation time of the material. At low frequency, the viscous term is dominant while at high frequency the elastic term dominates. More sophisticated models relying on complex combination of multiple springs and dashpots exist to describe finer viscoelastic materials. For high deformations (or oscillation frequency), the shear stress is no longer a sinusoidal function of time and G' and G'' become dependant on $\hat{\gamma}$: the material is solicited in the non-linear viscoelastic range.

It is possible to use oscillatory measurements to identify the fluid type (Fig. 1.4). For instance, the relative positions of G' and G'' in the linear region (G' and G'' constant) indicate the presence of a yield stress, in that case $G' > G''$. It is sometimes easier to determine the yield stress σ_y with this type of experiment rather than in flow: it is materialized by a change of slope of the curve $\sigma = f(\hat{\gamma})$ represented with logarithmic scales. For a viscous fluid, G'' is greater than G' . If, in addition, the fluid is shear-thinning, then G' and G'' decrease in the non-linear regime. The opposite happens for shear-thickening fluid (with a possible crossover of the two curves).

1.2.4 Rheological measurements in practice

Main geometries

Rheological measurements in flow and in oscillation are carried out on rotational rheometer using different types of geometries. The main ones are parallel plate, cone and plate and Couette (Figure 1.5) [16].

The choice between these different geometries depends mainly on the viscosity of the fluid. Thus, a Couette cell should be chosen for low viscosity fluids, while small diameter parallel plate or cone and plate are preferred for highly viscous fluids. Reducing the contact area decreases the value of the torque, which helps maintaining its value within the measurement range. Other considerations justify the choice of one geometry over another. For instance, the gap d needs to be greater than 10 particles in size to consider the material homogeneous in its composition. This is often a limitation to the use of cone and plate geometry for solid suspensions of non-Brownian particles. However, with the cone and plate, the shear rate is theoretically the same in the entire sample, whereas with the parallel plate, the shear rate increases with the distance from the center (Table 1.1), resulting to potential particle migration. Moreover, using parallel plate or cone and plate geometries does not give access to the same data regarding the normal stress differences: with cone and plate N_1 is measured while with parallel plate it is $N_1 - N_2$.

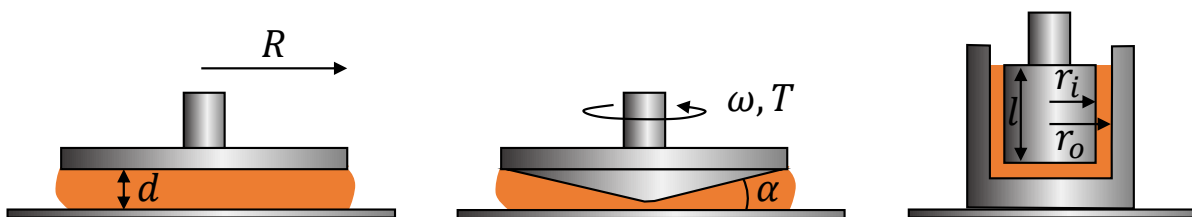


Fig. 1.5 – Three most commonly used geometries for rheological experiments: from left to right, parallel plate, cone-and-plate and Couette geometries. The geometries are rotated either by imposing the angular velocity ω or by imposing the torque T .

Measurement performed by the rheometer

Regardless the geometry chosen, the sample is positioned between the stator (bottom part of the geometry) and the rotor (top part). Two types of rotational rheometer exist: either the torque T is imposed, and both the angular velocity ω and the angular displacement Θ are measured, or the opposite. In practice, a computer control feedback loop allows to impose indistinctly the torque or the angular velocity/angular displacement. The rheometer also measures the vertical force F applied on the mobile. Geometric parameters are used to convert the raw measurements (T , ω and Θ) in term of shear rate $\dot{\gamma}$ and shear stress σ . To evaluate them the rheometer software makes the assumption that: the fluid is Newtonian (assuming a linear velocity profile), there is no wall slip, and the flow is homogeneous and

stationary. The expressions of the shear rate, shear stress and normal stress differences are given in Table 1.1 [16]. Note that the equation of the shear rate used for the cone and plate is valid only for a small opening angle α . In fact rigorously for a linear velocity profile: $\dot{\gamma} = \frac{\omega r}{d(r)}$ with $d(r)$ the local gap height. The Weissenberg-Rabinowitsch correction is applied on the apparent shear rate for non-Newtonian fluids. In fact the rheometer compute the shear rate making the assumption of a velocity profile corresponding to the Newtonian case. For non-Newtonian fluid the velocity profile is not known and the apparent wall shear rate $\dot{\gamma}_a$ needs to be corrected to access the real shear rate experienced by the fluid : $\dot{\gamma}_R(\sigma) = \dot{\gamma}_a \left[\frac{1}{4} \left(3 + \frac{d \ln \dot{\gamma}_a}{d \ln \sigma} \right) \right]$ [35].

Table 1.1 Expression of the apparent shear rate, shear stress, and normal stress corresponding to the different geometries.

	Couette	Parallel plate	Cone and plate
Shear rate $\dot{\gamma}_a$	$\frac{r_o \omega}{r_o - r_i}$	$\frac{R\omega}{d}$ (<i>maximum value</i>)	$\frac{\omega}{\alpha}$
Shear stress σ	$\frac{T}{2\pi r_o^2 l}$	$\frac{2T}{\pi R^3}$	$\frac{3T}{2\pi R^3}$
Normal stress difference	l	$N_1 - N_2 = \frac{2F}{\pi R^2} \left(1 + \frac{1}{2} \frac{d \ln F}{d \ln \dot{\gamma}} \right)$	$N_1 = \frac{2F}{\pi R^2}$

Note that in the case of the Couette geometry, the equations in Table 1.1 are written for a narrow gap cell (which is usually not the case with commercial rheometers such as the TA DHR2 used in this work leading thus to more complex equations not shown here).

Classic side effects

Slip at the wall

Rheological measurements assume a no-slip condition at the walls. However, in practice, slip can occur at the walls and is sometimes difficult to noticed it with the naked eye, especially at low shear rates. If slip does occur, the stress or shear rate values are underestimated, which amounts to underestimating the viscosity. Materials that are susceptible to wall slip include polymer melts, and dispersed systems such as colloidal suspensions, emulsions [36], and soft particles [37]. The particles do not adhere to the surface, and an interstitial fluid film is created at the wall by depletion of the particles [36], or by soft particle squeezing [37]. This film often has a lower viscosity than the bulk material. To avoid slippage, rough surfaces are used (using sandpaper for instance). However they can lead to fracture inside the material [38], this internal slip layer again leading to an inhomogeneous flow field.

Edges fractures

Edge fracture is most often observed for highly elastic materials at relatively high shear rates with the cone-plate or parallel plate geometry. The air/liquid interface deforms and becomes pinched like an hourglass. The sheared surface then decreases ($R_{\text{eff}} < R$, see Fig. 1.3c) resulting in a drop in stress, which limits the usable range of shear rates. This phenomenon occurs when the second normal stress difference

N_2 exceeds a certain critical value depending on the surface tension and the gap height [39, 40]. To reduce this effect, it is possible to reduce the gap or immerse the flow cell in a viscous liquid [41].

This edge fracture is not related to another limiting phenomena observed at high shear rates, and encountered also with Newtonian fluids, which is the sample ejection due to the effect of centrifugal forces.

Inhomogeneity in particle concentration

For suspensions, sedimentation [42], but also shear-induced particle migration [43, 44], lead to inhomogeneity in particle concentration and affect rheological measurements. Ovarlez demonstrated migration of non-colloidal particles in both Newtonian [43] and yield stress [44] fluids in a Couette geometry. The particles migrate to the region of lowest shear rate (radial outward flow) and this effect increases with the volume fraction of the particles.

Air bubbles

Most of the time, bubbles can easily be avoided. However, with yield stress fluids, it is more difficult to ensure a perfect contact with the mobile and the liquid because the surface shape is not controlled by surface tension forces but is held fixed by the action of the yield stress. Bubbles decrease the contact area between the solid surfaces and the sample leading to underestimated values of the viscosity.

Inertia

Inertia can come both from the fluid or from the rheometer :

- Fluid inertia can be at the origin of negative normal stress that can become significant for high geometry radius, fluid viscosity and angular velocity. The contribution to the N_1 value related to the inertia is $N_1^{\text{inertia}} = -\frac{3}{20}\rho\omega^2R^2$ with ρ the fluid density [45]. Subtracting it from the apparent value of N_1 gives access to its true value. Fluid inertia can also be the cause of increased stress at high shear rates, sometimes leading to an apparent increase in viscosity that should not be mistaken for shear-thickening.
- The rheometer's inertia means that the torque or angular velocity input are not applied instantaneously. The time needed to reach the set value has to be short to avoid detrimental effect on the measurement results. This affects the measurements performed in oscillations at high frequency or high amplitude, limiting the achievable range of measurements.

1.3 Spreading a fluid on a rigid plane

1.3.1 Wetting and spreading

Spontaneous spreading, and wetting at equilibrium

When a fluid droplet is deposited on a surface, it is initially out of equilibrium and can spread spontaneously if it is energetically favoured. To characterize the spreading capacity of a fluid on a surface, the spreading coefficient S_p is defined: $S_p = \gamma_{SO} - \gamma_{LV} - \gamma_{SL}$, with γ_{LV} (also named γ) and γ_{SL} , the surface tensions of liquid/vapor and solid/liquid interface respectively, in N.m^{-1} [46]. Physically, γ_{SO} is associated with a "dry" solid surface, it is used instead of γ_{SV} (the solid/vapor surface free energy) since initially the solid and the vapor are not in thermodynamic equilibrium. The spreading coefficient compares the work of adhesion between the substrate and the liquid, with the work of cohesion within the liquid [47]. Therefore, if $S_p > 0$, spontaneous spreading occurs until the droplet reaches its equilibrium angle δ_e (assuming no metastability). At equilibrium, the contact angle of the droplet on the substrate, is given by the Young's equation:

$$\gamma_{SV} = \gamma_{SL} + \gamma_{LV} \cos \delta_e \quad (1.9)$$

The wettability is quantified by the value of δ_e . Three main cases exist and are presented in Figure 1.6. When $\delta_e = 0^\circ$, this corresponds to a perfect wetting situation and $S_p^{eq} = 0$ [48], the drop forms a very thin film set by the drop volume and potentially van der Waals forces [49]. When $\delta_e = 180^\circ$, the liquid is perfectly dewetting, it keeps a spherical shape to minimize its surface tension. In between, the fluid is partially wetting ($S_p^{eq} < 0$). Another situation, called pseudo-partial wetting, can be observed: the droplet, while maintaining a finite contact angle, is surrounded by a molecular film. The latter originates from van der Waals forces whose interaction amplitude is given by the Hamaker constant [50].

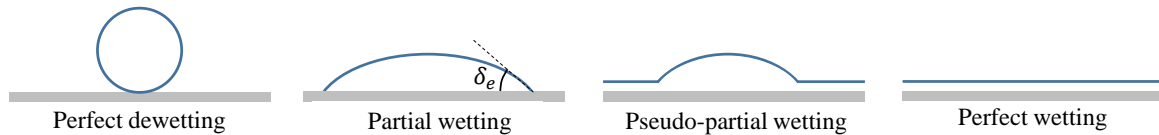


Fig. 1.6 – Different wetting situations according to Young's equation, and the particular case of pseudo-partial wetting.

Dynamic regime

Dynamic contact angles

When a droplet moves on a surface (for instance by tilting it), the shape changes: the droplet adopts an advancing angle δ_a and a receding angle δ_r such that $\delta_a > \delta_e > \delta_r$ (Fig. 1.7). The difference between these two angles increases with the tilt angle, but also with the number of defects present on the substrate [49]. If the surface is sufficiently rough (micrometer size), the triple contact line is anchored to the substrate [51] and can no longer move. It can only be depinned by applying an external force above a

certain threshold [49].

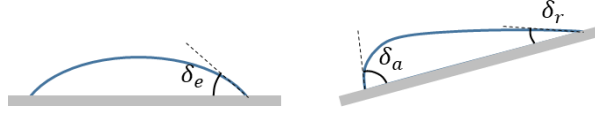


Fig. 1.7 – Schematic representation of advancing and receding angles adopted by a droplet on a slope.

Forced spreading and dynamic contact line

When a fluid does not spread spontaneously on a surface, it can be forced by an external force, for example with a blade, as done in the experiments described later. The capillary number, $Ca = \frac{V\eta}{\gamma}$ is a dimensionless number comparing the effect of the viscous forces to the surface tension. V is the characteristic velocity of the system. This number is key to understand the dynamics of the contact line.

Here we describe the example of a dip coating experiment, which is one of the simplest method to spread a liquid on a surface. An object is dipped into a bath of fluid and withdrawn at a controlled velocity. At rest, the liquid adopts a contact angle δ_e at the triple contact line. Different behaviors are observed depending on the wetting properties of the fluid (Fig. 1.8). For a perfectly wetting fluid, a film of fluid of thickness $e \sim l_c Ca^{2/3}$ is deposited on a plate with $l_c = \sqrt{\gamma/(\rho g)}$ the capillary length and g the gravity constant (see section 1.3.3 for the detailed calculation) [52]. For partial wetting, the situation is more complex: a critical capillary number must be exceeded for the liquid to spread on the object. If the capillary effects are dominant over the viscous effects ($Ca < Ca_c$), the liquid tends to minimize its surface energy and resists the extension of its surface: the contact line remains at an equilibrium height. If the viscous forces are greater than the capillary forces ($Ca > Ca_c$), a liquid film is formed during the object's withdrawal. The resulting deposited film no longer simply follow the Landau-Levich rule, e.g. an overhanging ridge may form near the contact line, leading to more complex fluid profiles than represented in Fig. 1.7 [53]. This critical capillary number reflects the fact that there is a maximum speed at which the contact line can move relative to the plate [54]. If this velocity is exceeded, there is no longer a stationary solution for the contact line, which is dragged along by the object, and a macroscopic film is formed.

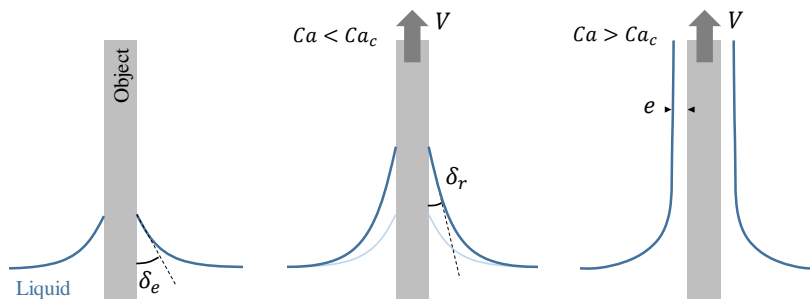


Fig. 1.8 – Dynamics of wetting, with, from left to right, the meniscus at rest, the static meniscus at low velocity and the formation of the liquid film at high velocity.

The lower the surface tension and the higher the viscosity and spreading speed, the easier it is to form a liquid film. However, the withdrawal velocity cannot be increased indefinitely since destabilization of the contact line occurs at high speeds [55], and it is also sometimes limited by the set-up. Another method to achieve spreading is to use a rough substrate that pins the contact line even if $Ca < Ca_c$. This solution is adopted in Chapter 3 and 4 since the fluids studied are insufficiently wetting on a smooth substrate while it was non-necessary in Chapter 2 because silicon oil is a highly wetting fluid.

1.3.2 Classic coating processes

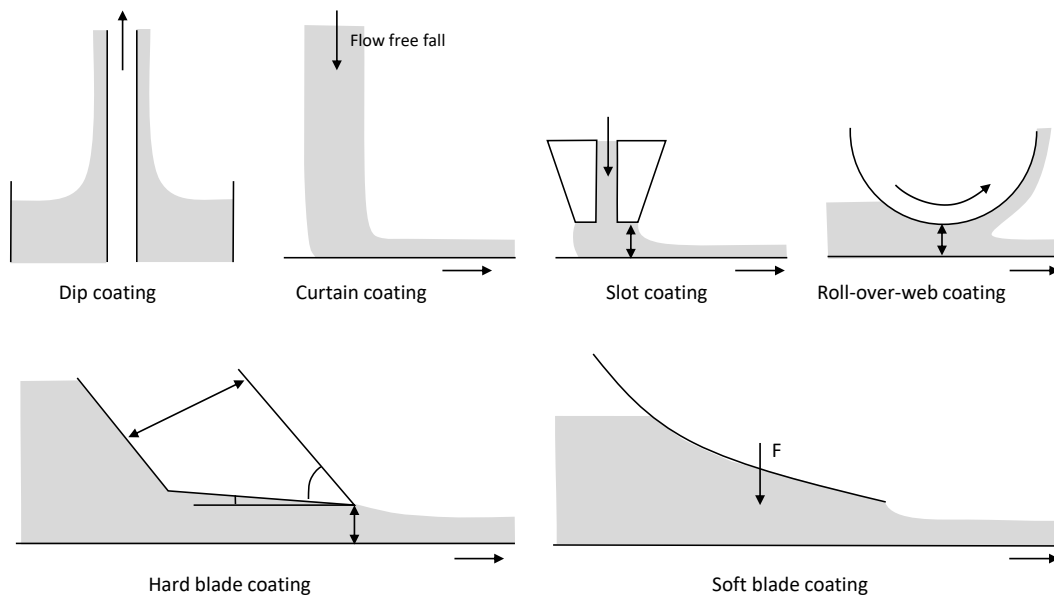


Fig. 1.9 – Schematic representation of coating geometries.

Different spreading techniques, more or less widespread, are used in industry (Fig. 1.9). These include the previously discussed *dip coating*, but also *slot coating*, where the fluid is fed vertically through a die, *curtain coating*, which, as its name implies, consists of passing the object through a curtain of liquid, and *roll coating*, where a roller is used to deposit the fluid. The family of blade coatings includes many subcategories. In the rigid blade category there is the case where the support is a moving plane, often referred to just as a *blade coating* (or *doctor blade coating*), and the case where the support is a cylinder, called *blade-over-roll coating*. When the blade is flexible, it is referred to as *soft blade* or *flexible blade coating*. This situation is very different from the hard blade coatings because the gap is not fixed but results from the balance between elastic forces exerted by the blade on the liquid underneath, and the viscous forces applied by the liquid on the blade.

In industry, flexible blade coating is primarily used to apply mineral pigmented, latex, or functional coatings to paper at very high speeds [56]. Spreading icing on a cake with a flexible spatula or painting with a brush are more or less direct examples of flexible blade coating. We chose this coating technique to model the spreading of a cosmetic product by a finger on a skin. The detailed motivations can be

found in section 2.1. Thus, we focus our literature review on flexible blade coating with occasional references to other blade coating techniques and dip coating.

1.3.3 Study of deposited thickness with soft blade coating

Few studies exist on soft blade coating geometries, and they all consider an infinite reservoir of fluid with the exception of Kusina [3]. An infinite reservoir of fluid does not necessarily cover entirely the blade but extends indefinitely over the substrate behind it, an example is shown later in Figure 1.12. Most studies are numerical [4, 7, 57–61] although some experimental work can be found [3, 4, 62]. Additionally to a numerical and experimental approach, Seiwert also proposed a scaling law to predict the deposited thickness [4]. Corvalan focused on the special case of a soft substrate [7]. Deblais and Kusina were the only ones to include non-Newtonian fluids in their study: Deblais performed experiments on viscoelastic polymer solutions and Kusina on yield stress fluids [3].

Dynamic effects in soft blade coating

Similar to dip coating, a critical capillary number has to be overcome to spread a partial wetting liquid with a flexible blade. This was demonstrated by Deblais on Newtonian fluids and viscoelastic polymers solutions [62]. Kusina also showed that a critical velocity must be exceeded for yield stress fluids to be spread on a smooth substrate. He also showed that increasing the velocity leads at some point to discontinuities such as bumps and holes in the fluid film (Fig. 1.10) [3].

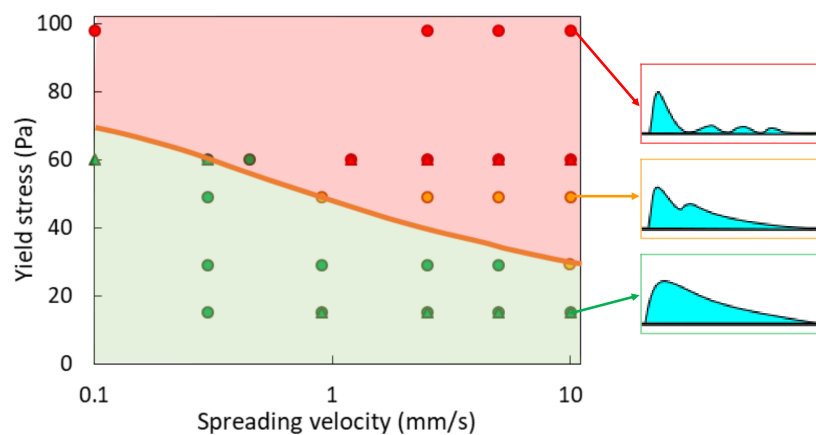


Fig. 1.10 – Map showing the emergence of instabilities in the fluid film as a function of velocity and yield stress (from [3]).

Scaling law for an infinite reservoir of Newtonian fluid

To propose a scaling law for the deposited thickness, Seiwert drew an analogy between soft blade coating and dip coating of a plate. To understand this analogy, we first briefly present a dimensional approach

based on Landau and Levich's theoretical derivation [52] to predict the film thickness in a dip coating experiment.

The deposition law of dip-coating:

At rest, we have seen that a partially wetting fluid ($0^\circ < \delta_e < 90^\circ$) adopts a meniscus shape at the contact with the object to minimise its surface energy. Its spatial extension is limited by gravity and is of the order of the capillary length l_c . When withdrawing the object out of the fluid bath to coat it with a liquid film, the static meniscus is locally deformed to transition towards a film of constant thickness e (Fig. 1.11). Landau and Levich made the assumption that this deformation affects only a small region of the static meniscus of size l , called the dynamic meniscus.

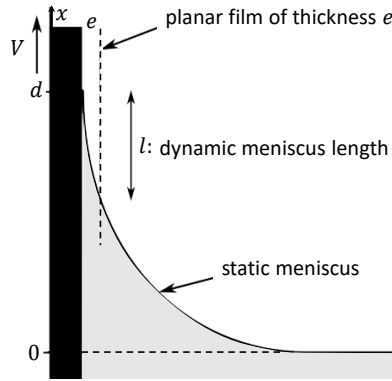


Fig. 1.11 – Schematic representation of the dip coating experiment and the dynamic meniscus region. The figure is adapted from [4].

At low Reynolds number, the fluid inertia can be neglected. From the viscous shear stress $\tau = \eta \dot{\gamma} \sim \eta V/e$ one can write the viscous stress gradient $\tau/e \sim \eta V/e^2$. The Laplace pressure in the static meniscus is $\Delta P = \gamma/R$ with the radius of curvature $R \sim l_c$. Since ΔP is zero in the fluid film, a pressure gradient can be defined in the dynamic meniscus: $\Delta P/l \sim \gamma/(l_c l)$. Gravity has been neglected in front of capillary effects implying that $\gamma/(l_c l) \gg \rho g$, and therefore that $l \ll l_c$ since $l_c = \sqrt{\gamma/(\rho g)}$. The expression of l can be determined by writing the continuity of the curvatures of the static and dynamic menisci. The curvature of the static meniscus scales as $1/l_c$, and the curvature of the dynamic meniscus as e/l^2 . Thus:

$$l \sim \sqrt{e l_c}$$

Finally, balancing the viscous and capillary gradients allows expressing the deposited thickness as:

$$e \sim l_c \left(\frac{\eta V}{\gamma} \right)^{2/3} \sim l_c Ca^{2/3} \quad (1.10)$$

With this equation, Landau and Levich made explicit the dependency of the deposited thickness on velocity, first observed by Ward and Goucher in 1922. Derjaguin showed that when gravity is no longer

negligible ($Ca \ll 1$), the thickness can be described by a slightly different equation: $e \sim l_c Ca^{1/2}$ [63].

Back to the flexible blade coating:

In the case of dip coating, the deposited thickness results from a balance between viscous forces and capillary forces resulting from meniscus deformation. Seiwert considered flexible blade scraping, when the tip is tangent to the surface, to be analogous to dip coating by considering that "the liquid meniscus has been replaced by an elastic one" [64]. This analogy has also been used by Warburton and Dixit to study plate withdrawal situations where an elastic film is present at the fluid/air interface [5, 6] and more generally can be useful in a wide range of elastocapillary phenomena [65].

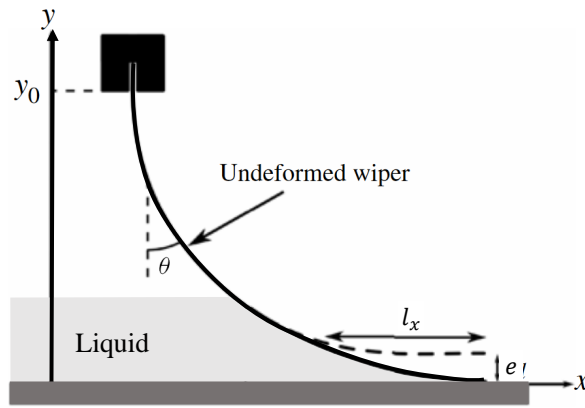


Fig. 1.12 – Schematic representation of the Seiwert's soft blade coating experiment. The figure is adapted from [4], the liquid region has been added to the drawing.

In Seiwert's study, the capillary number is large, and the Reynolds number is small, which allows both surface tension and fluid inertia to be neglected. Therefore, a balance between the elastic and viscous force determines the deposited thickness. He makes the assumption that the blade is deformed only over a small part of length l_x and that $l_x \ll L$ where L is the blade length (Fig. 1.12). For a static blade just tangent to the surface the curvature $\frac{d\theta}{ds}$ is zero at the blade tip so its shape goes as $y \sim \frac{-x^3}{L^2}$ near the contact, and considering the gap at the tip of the order of the deposited thickness e , the deformation region l_x can finally be expressed as:

$$l_x \sim (eL^2)^{1/3} \quad (1.11)$$

The viscous forces scale as $\eta V/e^2$. The force exerted by the blade per unit length is of order B/L^2 since the curvature of the blade can be approximated by $1/L$ and with B the blade rigidity. The related elastic pressure gradient along the deformed length l_x is $\frac{B}{l_x^2 L^2}$. Balancing the viscous and elastic forces, and using the Eq. 1.11 gives:

$$e \sim L^{5/2} \left(\frac{\eta V}{B} \right)^{3/4} \sim LCe^{3/4} \quad (1.12)$$

By defining $Ce = \eta VL^2/B$ a dimensionless number comparing the viscous and elastic forces, Seiwert highlighted the parallel with the equations of Landau, Levich and Derjaguin (Eq. 1.10), with the

elasticity of the blade replacing the capillary forces of the meniscus. This approach relies on the fact that the blade is only deformed on a small region $l_x \ll L$.

The scaling law points out the increase of the deposited thickness with velocity and viscosity. This is in agreement with the work of Pranckh and Scriven, that previously showed numerically that the downstream film thickness increases with the velocity, viscosity and blade length but reduces with the bending stiffness. The effect of the blade length was also pointed out by Giacomini [61]. When an external loading is additionally applied on the blade, pressing it onto the fluid, additional parameters impact the deposited thickness [57]. Corvalan showed that with a compressible substrate the deposited thickness is thinner than with a rigid substrate, without having to increase the blade loading [7].

Difference between hard and soft blade coating of Newtonian fluids

The scaling law proposed by Seiwert highlights that hard blade and soft blade coating are not similar and give strongly different results. In fact, the hard blade coating of a Newtonian fluid gives a deposited thickness around a half of the geometric gap separating the blade from the coated surface. Hwang showed mainly theoretically that e decreased slightly with blade velocity and fluid viscosity, which is the opposite of what was seen by Seiwert with soft blade coating [66]. The impact can be reversed but only at large velocities where inertia begins to play a role which is not the scope of our study [56]. Sullivan even observed that the velocity does not have an impact with blade-over-roll coating [67] and that the coated thickness is only dependant on the geometric characteristics of the blade (gap, blade angle, blade length ...). This difference of behavior between hard and soft blade coating, in the simple case of a Newtonian fluid, makes it clear that studies done on non-Newtonian fluids with a hard blade cannot be extrapolated to soft blade coating.

Numerical approach

Soft blade coating is a coupled problem of fluid dynamics (fluid under the blade and fluid in the air) and elastic deformation (blade). The coupling exists in the sense that the shape acquired by the blade constitutes the geometrical limit of the channelled fluid while the viscous forces and the fluid pressure constitute the distributed load applied to the blade. Capillarity must be taken into account to express the formation of a meniscus in the deposit at the exit of the blade. Besides, for the problem we are interested in here, we must also take into account the surface tension at the free surface of the reservoir, which is considered as finite.

Most of the time, the lubrication approximation is introduced when the fluid is confined, which allows to simplify the flow considered [4, 7, 58–60]. The flexible blade equations can be written in different forms, depending on the particular geometries (and sometimes additional external load [7, 57, 60]), but they often amount to non-linear differential equations, up to the fifth order if the blade height is chosen as the blade descriptor [4, 58, 59, 61]. It belongs to the boundary value problems for which boundary conditions are specified at more than one point (e.g. at both ends of the blade). Several methods of resolution are employed: the finite element method is the most commonly used [57, 58],

sometimes combined with the Galerkin method of weighted residuals [7, 60], or the collocation method [59], otherwise numerical integration can be performed [4, 61].

The study conducted by Trinh is interesting because it proposes to solve the fifth order equation describing the blade shape in combination with a third order equation for the shape of the thin film deposited behind the blade [59]. This second equation allows him to use the atmospheric pressure condition in the liquid film far from the blade tip as one of the boundary conditions of the problem. The goal is to account for the formation of a liquid meniscus at the blade tip that impacts the thickness of the flat film (Fig. 1.13). In this case, the pressure in the liquid film reaches a maximum under the blade and is lower than the atmospheric pressure at the blade tip due to the meniscus [68].

The flexible blade coating configuration we are interested in is the one with a vertically hanging blade that was considered by Seiwert as well (Fig. 1.12). In Seiwert's study, the external forces applied to the blade were calculated in the approximation of small deformation, which is valid in the nearly tangent part of the blade only. The full blade form actually corresponds to a large deflection problem. Since the load applied by the fluid under the blade is a distributed load, it is thus possible to draw inspiration from theoretical studies of beams undergoing large deflection with distributed loading [69, 70] for the derivation of the flexible blade coating, using the Navier Stokes equations to express the load applied by the fluid.

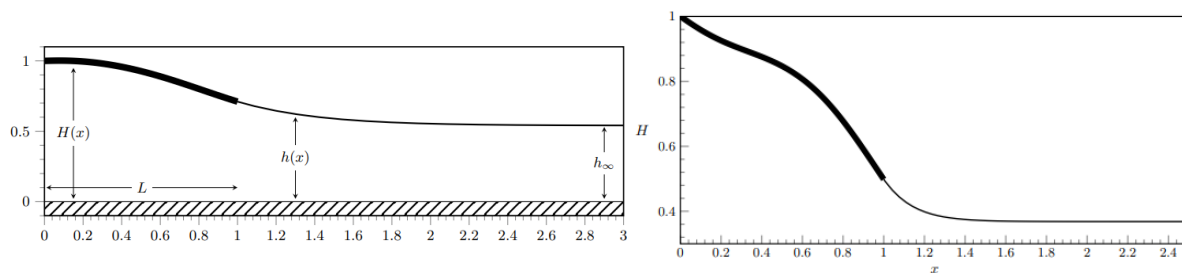


Fig. 1.13 – Numerical solutions obtained for the blade (thick line) and liquid film (thin line) shapes. From left to right the capillary number increases and the reservoir pressure decreases (from [59]).

1.3.4 Coating of non-Newtonian fluids

With soft blade coating

Few studies deal with the spreading on non-Newtonian fluids with a flexible blade. Deblais focused on the regime of instabilities observed below the critical capillary number and showed that shear-thinning properties give instabilities (filaments) over a wider velocity range, while viscoelastic properties stabilize the resulting patterns [62]. Kusina studied the thickness deposited during the spreading of yield stress fluids [3]. He revealed the presence of instabilities in the film (see Fig. 1.10) and extended Seiwert's scaling law (Eq. 1.12) to yield stress fluids, modeled by Herschel Buckley's equation (Eq. 1.4), following the same reasoning but making another choice for the curvature [3].

Based on Seiwert's scaling law (Eq. 1.12), it appears that flexible blade coating is more comparable to dip coating than hard blade coating. With this in mind, we have chosen to present the results for dip coating of complex fluids in more detail than for hard blade coating.

With dip-coating

Numerous works have been conducted on dip-coating of complex fluids, often theoretically, sometimes with discrepancies with the few experimental data [71, 72] showing that the effect of the shear-thinning behavior, in particular, is difficult to predict quantitatively. Most studies agree that a Newtonian fluid gives a thicker coating than a shear-thinning fluid [71–73]. This is predicted by the scaling law derived by Quéré for the dip coating of a fiber (radius r), balancing capillary pressure and shear stress gradients: $e \approx \left(\frac{r^3 k^2}{\gamma^2}\right)^{1/(2n+1)} V^{2n/(2n+1)}$. One of the factors explaining the divergence of results is the effect of gravity and inertia which might or might not be taken into account and lead to different results. Spiers also stressed that most fluids studied in the studies are in fact viscoelastic (in the sense that they generate normal stress) and not purely shear-thinning. Additionally, the fluids used for the experiments are often Carbopol solutions at low concentrations [71, 72] whose yield stress has been neglected but might have an impact.

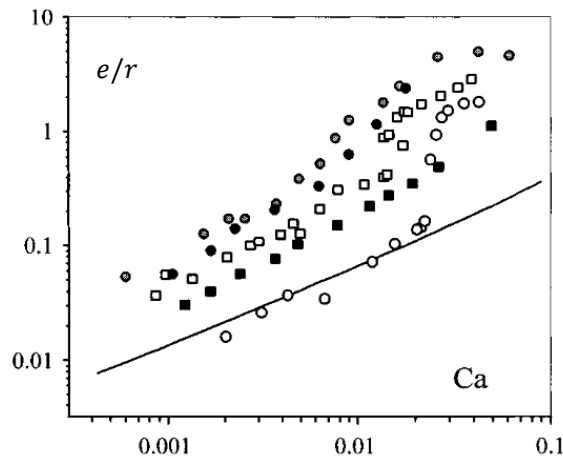


Fig. 1.14 – Dimensionless thickness e/r as a function of the capillary number for solutions of different concentrations (empty circles, $c = 0.001\%$; empty squares, $c = 0.01\%$; gray circle, $c = 0.1\%$; full circle, $c = 0.5\%$; full squares, $c = 1\%$). The solid line correspond to the Landau Levich equation $e = 1.34 r Ca^{2/3}$ for Newtonian fluid (from [73]).

The effect of fluid elasticity (related to normal stress) on dip coating of fibers, has been investigated by de Ryck and Quéré [73]. The fluids were also shear-thinning. They observed experimentally, and confirmed theoretically, an increase in deposited thickness compared to the Newtonian case and attributed it to normal stresses. Thus, in Figure 1.14 we can see that the deposited thickness is greater for a given capillary number compared to the Landau Levich situation. The capillary number was carefully evaluated for shear-thinning fluids by estimating the typical shear rate as V/e and deducing

the corresponding viscosity. Quéré proposed a scaling law for the deposited thickness, when normal stresses are dominant, by balancing the capillary pressure and normal stress gradients: $e \approx \left(\frac{\Psi_1 r}{\gamma}\right)^{1/2n} V$, with Ψ_1 the first normal stress coefficient.

Ashmore *et al.* extended this study to other coating geometries and particularly to roller coating [74]. Two regimes could be identified. In the weakly elastic limit, the viscous stress is dominant over the elastic stress which can be neglected and the deposited thickness is less than that of the Newtonian fluid. In the strongly elastic limit, the elastic stress dominates and results in thicker film.

For a yield stress fluid, Smit *et al.* showed that the deposited thickness is strongly influenced by the size of the fluid reservoir and the withdrawal velocity and decreases as the yield stress increases relatively to the shear stress [75]. He proposed flow diagrams predicting e in different domains that depend on the ratio of yield stress versus viscous stress or versus gravitational stress, capillary number, and fluid confinement. This article highlights the difficulty to compare different works and to draw conclusions on the effect of the fluid rheology due to the multiplicity of domain of definition for different behavior laws. This could explain why Spiers reported that the yield stress leads to an increase in film thickness [72].

With hard blade coating

For a pure shear-thinning fluid, Sullivan numerically predicted that the deposited thickness is increased compared to a Newtonian fluid with blade-over-roll geometry [67, 76]. For a purely elastic fluid (Boger fluid), Mitsoulis reported a reduced thickness [77]. As both effects are usually coupled in viscoelastic fluids the deposited thickness can be either increased or decreased compared to the Newtonian case depending on the relative contribution of the viscous and elastic properties. Greener made this observation for the blade geometry and Sullivan for the blade-over-roll geometry [67, 76, 78]. We can notice that the thickness variations are reversed with respect to dip-coating.

Maillard focused on yield stress fluids and showed that the thickness is about 10% greater than the gap, and consequently the thickness of a Newtonian film (e around half the gap) [79].

There is a wide variety of spreading behavior of non-Newtonian fluids, which leads to many deposition models and laws that are not easy to sort out to be adapted to new geometries. Thus, the deposited thickness depends on various parameters: capillary, elastic (related to the fluid and also to the geometry in the case of a flexible blade), and viscous, which play a different role depending on the geometry. The use of complex fluids allows to finely probe the different mechanisms at play. By judiciously choosing complex fluids with various properties and behaviors, it is possible to identify and disentangle the effects of the different parameters.

1.4 Goals of this thesis - Part I

The literature review presented above shows that the spreading of a finite amount of fluid, i.e. with a reservoir of fluid that empties during spreading, has been very little investigated. Yet, this situation is essential to study the spreading of cosmetic and pharmaceutical products, for example, when the user spreads a patch of cream whose volume reduces as spreading proceeds. Concerning the soft blade coating, whose geometry is relevant to model the spreading by a finger capable of deforming under stress, only one study, conducted by Kusina [3], deals, to our knowledge, with a finite fluid reservoir. He was interested in the special case of yield stress fluids. No work has been reported on flexible blade coating of a finite volume of Newtonian, shear-thinning fluid, or fluid generating normal stresses (Fig. 1.15). Because the blade geometry is not fixed (e.g. the gap), but results from balance with the fluid forces, emptying the reservoir of fluid implies an evolution of the whole system (fluid reservoir and blade) during spreading. This problem is not trivial and we expect the results to differ from studies dealing with infinite reservoir of fluid. The spreading of a finite amount of fluid by a blade is therefore an academic problem that is wide open to new investigations, which also finds a strong resonance in industry.

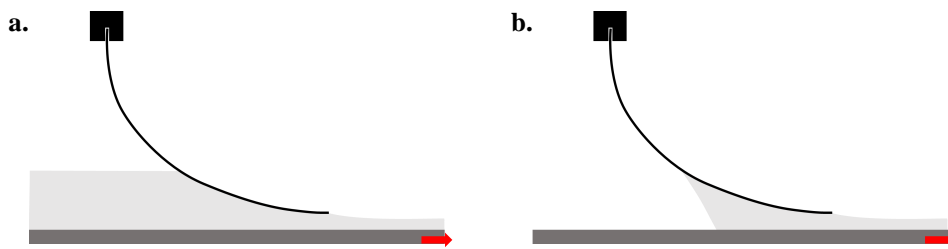


Fig. 1.15 – Soft blade coating of **a.** an infinite fluid reservoir such as the one studied by Seiwert [4], or **b.** a finite reservoir of fluid.

Following this introductory chapter, in Chapter 2 we focus on answering the question: how does finite size reservoir influence the spreading dynamics in soft blade coating? To answer this question, we concentrate on the simple case of a Newtonian fluid and investigate experimentally, numerically, and propose a theoretical prediction of the deposited thickness as a function of the liquid filling level under the blade.

Subsequently, Chapters 3 and 4 aim at determining: what are the impacts of the rheological behavior of the fluid on the deposition law? In Chapter 3, we extend the study describing the case of Newtonian fluids to shear-thinning fluids. In Chapter 4, we analyze the case of shear-thinning fluids that also exhibit normal forces or yield stress.

From an industrial point of view, it is important to know which formulation tracks are to be encouraged. For instance, one can wonder if adding polymer in formulation, to obtain products that generate normal stresses, has an advantage over the spreading or not. Such a question is answered by evaluating the effect of rheological properties on criteria such as the magnitude of the film height, the

homogeneity of the deposit in thickness, or the ease of spreading (concretely linked to a lower energy needed to spread the fluid).

Conclusion – Chapter 1

Fluid spreading is a broad and complex subject due to the wide variety of fluid behaviors under shear, and the diversity of spreading processes. Many combinations of fluid type and spreading geometry are possible. We showed that dip coating and hard blade coating have been widely studied with Newtonian fluids, but also with non-Newtonian fluids (shear-thinning, normal stress and yield stress). In contrast, studies concerning flexible blade coating have been less numerous, especially when dealing with non-Newtonian fluids, which leaves room for future investigations.

One case, that to our knowledge has not yet been addressed, is the spreading by a flexible blade of a finite reservoir of fluid that empties during spreading. This case is not intended to analyze classical industrial processes used on production lines, but it is interesting to model the spreading of small quantities of material such as cosmetic cream, paint or jam. ***What is the impact of a finite size reservoir on the deposition law? How do fluid rheological properties influence the deposit thickness and spreading dynamics?***

To answer these questions, we first focus on Newtonian fluids since they exhibit a simpler behavior than complex fluids (Chapter 2), then we extend the study to non-Newtonian fluids (Chapter 3 and 4).

Chapter 2

Soft blade coating of Newtonian fluid with finite reservoir of fluid

In this chapter, we discuss the soft blade coating of a small quantity of Newtonian fluids. We study the variation of the deposited thickness during the emptying of the fluid reservoir. We analyze the forces at stake and propose to model the coating process by a scaling law and numerical calculations. Finally, we compare our model to the case of an infinite reservoir of fluid.

The results presented in this chapter have been published in Physical Review Letters [1]. The article can be found in Appendix A.

Contents

2.1	Motivations	28
2.1.1	Industrial motivations: cosmetics spreading	28
2.1.2	Academic motivations: elasto-hydrodynamic coupling	28
2.2	Spreading experiment	29
2.2.1	Experimental set-up	29
2.2.2	Silicone oil as a Newtonian fluid model	33
2.3	Spreading dynamics	34
2.3.1	Two regimes	34
2.3.2	Importance of the wetting length	35
2.4	Estimation of the deposited thickness with a scaling law	35
2.4.1	Elasto-hydrodynamic competition	36
2.4.2	Limits of the scaling law	37
2.4.3	Comparison with experiments	39
2.5	Numerical model of deposited thickness	40
2.5.1	Model presentation	40
2.5.2	Prefactor validation	49

2.5.3	Capillary effect	50
2.5.4	Shape of deposit	51
2.6	Flexible blade coating with finite size reservoir is not analogous to dip coating	53
2.7	Conclusion	54

2.1 Motivations

2.1.1 Industrial motivations: cosmetics spreading

The classic way of spreading a cream, such as a moisturizing cream, a foundation or a sunscreen, consists in depositing a small quantity of formulation on the skin. This deposit is then usually spread with the tip of the fingers. Everyone has already experienced that a linear movement leads to an inhomogeneous deposit in thickness. The cream layer becomes thinner and thinner until it reaches zero thickness when there is no more cream driven by the fingers. This is equivalent to consider that the fluid reservoir, corresponding to fluid under the fingers, has emptied. This inhomogeneity pushes the user to perform more complex movements, such as combining linear and circular movements, and going back and forth, in order to even out the thickness deposited on the surface to be coated. Finding what are the different parameters controlling the decreasing thickness profile of the deposit is key to be able to propose application tips, or formulation advice, to reduce inhomogeneity. The more homogeneous the deposit is in thickness from the first movement, the less the user will need to spread the deposit further. Studying a linear spreading motion, although it corresponds to a very simplified situation, seems therefore a good approach to capture the essence of the inhomogeneity problem.

The choice of a flexible blade was made to mimic the spreading done by the fingers. From a geometrical point of view, its curved shape reminds that of a finger. We also consider that the spreading of cosmetic products is not done with a fixed gap, as the user cannot maintain a fixed distance between his finger and the skin surface. Consequently, a hard blade geometry, for which the gap is fixed, does not seem appropriate. The fingers impose a pressure on the fluid to be spread, which corresponds to the characteristics of a soft blade geometry for which the elasticity of the blade imposes a force on the fluid.

While the vast majority of cosmetic products are complex fluids with non-trivial behavior, we decided to start by focusing on Newtonian fluids. Their constant viscosity makes them much easier to model and understand. Moreover, no literature was found on the soft blade coating of a finite reservoir of Newtonian fluid. It seemed relevant to lay the foundations before increasing the complexity with non-Newtonian fluids.

2.1.2 Academic motivations: elasto-hydrodynamic coupling

Soft blade coating is an example of fluid-structure problems, involving the coupling of a flexible sheet with a fluid flow, which presents a rich non-linear behavior [58, 59, 68]. On these small scales, the fluid is confined by the elastic plate and the forces responsible for the deformation of the solid are

viscous instead of inertial: for instance paper sheets gliding on thin air just above the floor after falling from a table [58]. The use of a flexible blade in the industrial process of paper coating has motivated earlier studies [7, 57, 60, 61, 80]. More recently, this problem has been studied in the light of an elasticity-capillarity analogy [4] and compared with another well-known system, dip coating [52, 63]. Following this analogy, soft blade coating is viewed as an "elastic" dip-coating problem [4–6], where elastic forces due to the bending of the blade replace the capillary forces and resist the viscous forces of the fluid. This approach was used to predict the film thickness as a function of the blade properties [4, 6] and was shown to successfully model the experiments [4]. However they studied the case of a blade scraping a continuous deposit of fluid initially present on the substrate, which is the same as considering an infinite fluid reservoir (Fig. 1.12). Moreover they assumed that the blade, while in motion, is only deformed over a length l_x from the tip. This internal length is analogous to the dynamical meniscus length in dip-coating. However, in a large majority of everyday situations, such as the spreading of a paint on a wall, or cream on the skin, the liquid reservoir is finite and the wetting of the blade varies during spreading. This introduces a new length scale, the wetting length l_w (as shown in Fig. 2.1), and its existence challenges the Landau-Levich approach [4–6]. For these reasons, we decided to study the spreading of a finite reservoir of fluid by a soft blade.

2.2 Spreading experiment

2.2.1 Experimental set-up

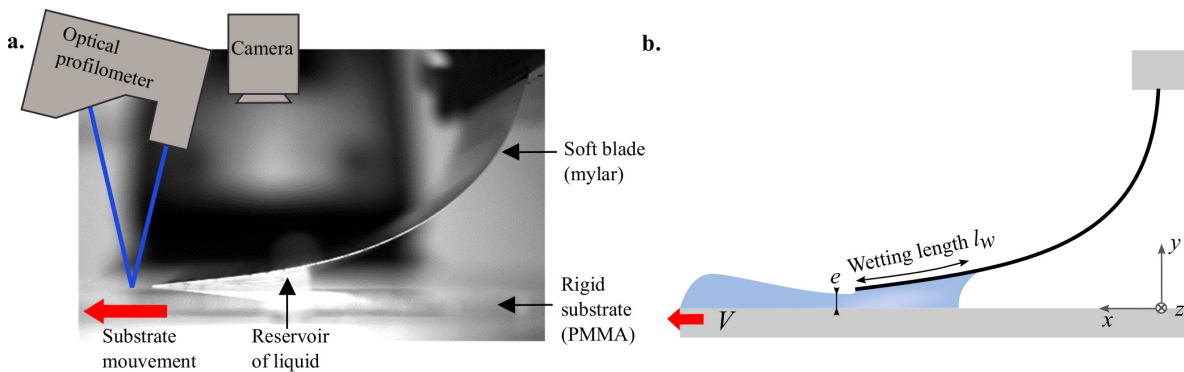


Fig. 2.1 – **a.** Picture of the experimental setup and **b.** schematic representation

Principle

To perform a soft blade coating, a small amount of liquid is deposited on a rigid plate and then spread with a flexible scraper [3, 4]. In this experiment the flexible scraper remains immobile while the substrate moves to perform the spreading (Fig. 2.1). The substrate is a smooth poly(methyl methacrylate) (PMMA) plate of 5 mm thickness. The upper surface is smooth while the lower one is sandblasted with roughness

of approximately $20 \mu\text{m}$, to ensure a good scattering of the laser beam emitted by the profilometer (see next paragraph).

Blade characteristics

The flexible blade is made of smooth poly(ethylene terephthalate) (PET) also called mylar. It is laser cut in a rectangular shape, with a constant width $b = 4 \text{ cm}$, a length L of typically 5.7 cm and thickness $u = 125$ or $250 \mu\text{m}$. The upper part of the blade is clamped perpendicularly to the surface, at the height $H = 0.46L$. This clamping height ensures that the free edge of the blade is exactly tangent to the surface in absence of liquid. Seiwert *et al.* showed that the deposited thickness is strongly dependent on the configuration of the blade : the thickness is the largest in the tangent configuration (Fig. 2.2).

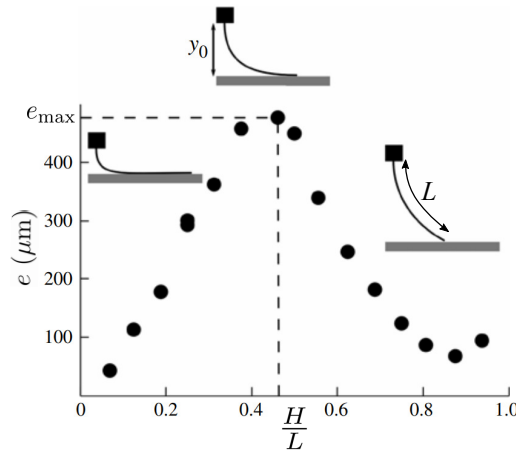


Fig. 2.2 – Deposited thickness e as function of the ratio between the height of the clamping point and the length of the blade. The dashed line corresponds to $H = 0.46L$. The experimental conditions are $V = 8.2 \text{ mm/s}$, $B = 4.210^{-3} \text{ N.m}$, $L = 4 \text{ cm}$ and $\eta = 17.4 \text{ Pa.s}$. Figure from Seiwert *et al.*, 2013 [4]

The rigidity of the blade B is determined by measuring its deflection under its own weight [64, 81, 82]. Two methods were used depending on the stiffness of the blade. The first method consists in vertically clamping the blade and measuring the length of the blade L so that the clamping point and the free end are at same height when it deforms under its own weight (Fig. 2.3a). At this particular point $z_f = 0$ the adimensioned number, $\Delta = \frac{\rho_s g L^3}{B}$, comparing the effect of gravity to stiffness, is equal to 13.634 [64], with ρ_s the surface density, g the gravity constant, L the blade length and B the blade rigidity by unit width. The surface density is measured experimentally, giving $173 \pm 1 \text{ g.m}^{-2}$ and $347 \pm 2 \text{ g.m}^{-2}$ for 125 and 250 μm thick mylar respectively which implies a density of 1.38, in good agreement with the density of mylar reported by suppliers (1.38 – 1.4). The rigidity is determined using the equation: $B = \frac{\rho_s g L^3}{13.634}$. This method is efficient for flexible enough mylar. However, as the maximum length is limited by the sheet dimensions, in the case of rigid mylar it is not possible to reach a sufficient deformation. Another method is used: it consists in measuring the deformation of a blade clamped horizontally (Fig. 2.3b). The re-

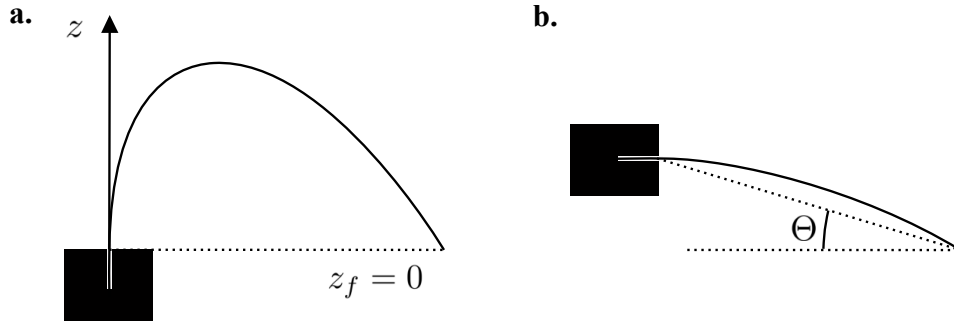


Fig. 2.3 – **a** Schematic representation of the method used to measure stiffness of highly flexible blade and **b** more rigid ones.

lation between the angle Θ , defined between the blade tip and the clamping point, and Δ is tabulated [64].

B is typically varied by a factor 7 when changing the blade thickness, with $B = 1.0 \pm 0.1$ mN m for $u = 125$ μm and $B = 7.1 \pm 0.5$ mN m for $u = 250$ μm . The force applied by the blade on the substrate is thus higher for a thicker blade, i.e. for a more rigid blade [3]. Using $B = \frac{E^*u^3}{12}$, we obtain a modified Young Modulus E^* of the material, that already includes the Poisson ratio correction, such that $E^* = \frac{E}{1-\nu^2}$. Experimentally, $E^* \simeq 6.2 \pm 0.5$ GPa, a value in good agreement with what is expected for type A mylar [83].

Protocol

To perform a spreading experiment, a small volume of liquid ($0.05 < \Omega_0 < 2$ mL) is deposited under the blade so that it completely fills the corner formed between the blade and the plate. The substrate performs a single linear motion at a constant velocity ($2.5 < V < 10$ mm/s) over a distance of 10 cm. If not stated otherwise the blade rigidity is $B = 1.0$ mN m and the blade length is $L = 5.7$ cm. The liquid reservoir empties progressively and two variables are measured simultaneously :

- The deposited thickness e : An optical profilometer (Keyence LJ-V7060K) positioned above the film, analyses the surface 2 millimeters from the edge of the blade (Fig. 2.1a). A laser sheet of length 16 mm (in the z direction) is projected onto the film, from which the film thickness $e(z, t)$ is measured as a function of position z and time t .
- The wetting length l_w : It is defined as the length of the blade in contact with the liquid (as visible in Fig.2.1b). During an experiment, $l_w(t)$ varies with time and typically diminishes by 2 cm as the reservoir empties. It is measured from the side and from the top using two optical cameras (Basler acA1920-150um with 50 mm and 16 mm focal length lenses), at 10 frames per second.

The camera and the profilometer are synchronized using an in-house Labview software, so that e and l_w are recorded simultaneously during the spreading. The initial time, $t = 0$, corresponds to the setting in motion of the horizontal stage. The camera positioned on the side is also used to measure the dynamic contact angle at the back of the reservoir.

Measurement of the deposited thickness with an optical profilometer

Optical profilometers are designed to measure the topography of an object based on the optical reflections of a laser. To measure the thickness of the deposited film of fluid in its central part a two step protocol is required: *i*) the position of the substrate is first measured as a reference and *ii*) a second measurement is made while spreading the liquid. The difference between these two measurements gives access to the deposited thickness. However, measuring transparent liquid such as silicone oil, can be quite challenging with an optical profilometer. Contrary to metal for instance, most of the beam is not reflected on the surface but instead penetrates the liquid, and even, in our case, the transparent PMMA plate underneath, before being reflected by a scattering surface. This gives rise to multiple rays that can be partially reflected or refracted at each change of medium, an example is given in Figure 2.4). The recorded rays have an optical path more complex than considered by the manufacturer, which implies the use of corrective factors to access the true topography. In addition, the profilometer is tilted, away from the vertical, to measure the scattered rays and avoid spurious specular reflections, which adds a new layer of complexity (see Appendix B). Typically, the tilt, ϕ_t , is on the order of 20° .

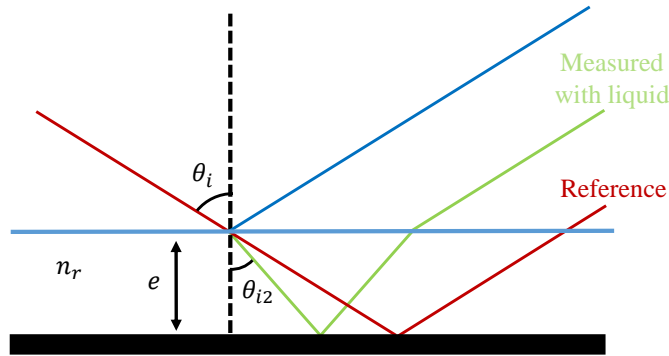


Fig. 2.4 – Illustration of the optical path of the rays emitted by the profilometer in a telecentric configuration. The incident ray can either be directly reflected on the film (blue ray) or refracted in the liquid before being reflected on the substrate (green ray). This last one is compared to the red ray (measured in the absence of liquid) to calculate the coating thickness e (figure adapted from [3]).

Several hypotheses have to be taken in order to propose a simple corrective factor. The details of the hypothesis and the different steps to obtain the corrective factor are presented in Appendix B. The corrective factor applied to the thickness measured by the profilometer is :

$$\text{Corrective factor} = \frac{\tan \alpha \cos \phi_t}{\tan \alpha - \tan \left(\sin^{-1} \left(\frac{\sin \alpha}{n_r} \right) \right)} \quad (2.1)$$

where $\tan \alpha = \sqrt{\tan^2 \theta_i + \tan^2 \phi_t}$ with θ_i the incident angle without tilt (fixed at 17.5°) and ϕ_t the tilt angle. In the case of silicone this factor is 3.1735 (without tilt). This factor has been verified experimentally with different materials of known thicknesses and various tilt angles (error $< 5\%$ for $1^\circ \leq \phi_t \leq 30^\circ$).

2.2.2 Silicone oil as a Newtonian fluid model

The fluid spread is silicone oil from Sigma Aldrich. It is made of polydimethylsiloxane. By using polymers of various chain length a wide range of viscosity is accessible. We used silicone oils of different viscosity ($275 \text{ mPa}\cdot\text{s} < \eta < 1 \text{ Pa}\cdot\text{s}$). Silicone oil shows a Newtonian behavior over a wide range of shear rates as seen on the rheological curves in Figure 2.5. The rheology is measured using a cone and plate geometry (40 mm diameter, 2° angle) on a TA instrument DHR2 controlled-stress rheometer at 25°C . A computer-controlled feedback loop on the torque is used to keep a constant angular velocity (hence a constant mean shear rate) without any fluctuations ($\frac{\delta\dot{\gamma}}{\dot{\gamma}} < 0.001$). Technical data given by some supplier indicate that shear-thinning behavior can be observed for shear rates above 10^3 s^{-1} and high molecular weight (in terms of viscosity: $\eta \geq 1000 \text{ mPa}\cdot\text{s}$). In most of our experiments, we used silicone oil $480 \text{ mPa}\cdot\text{s}$ and the shear rate remained below 200 s^{-1} . The viscosity slightly depends on the temperature: 10% variation is expected for changes of 5°C around 25°C [84].

Other advantages of silicone oil are its low volatility at room temperature and its highly wetting capabilities which facilitate reservoir filling. Glycerol, although a more common cosmetic product, was not chosen as a Newtonian fluid model because it is hygroscopic and its viscosity strongly depends on the water content, making it difficult to use in a reproducible way.

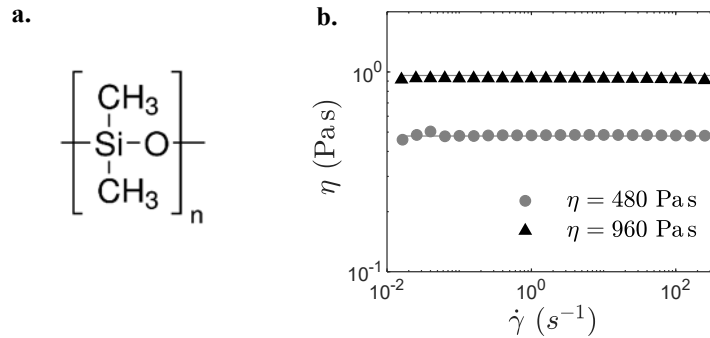


Fig. 2.5 – **a** Silicone oil chemical formula. **b** Flow behavior of silicone oil is constant with the shear rate. Silicon $480 \text{ mPa}\cdot\text{s}$ and $960 \text{ mPa}\cdot\text{s}$

For the purpose of the simulation (see section 2.5.1, Eq. 2.11), the dynamic contact angles between the fluid and the blade, δ_b , and the fluid and the substrate, δ_s , were measured with a camera during spreading experiments. In a typical experiment, $\delta_s \simeq 100 \pm 10^\circ$, and $\delta_b \simeq 15 \pm 10^\circ$ (Fig. 2.11). δ_s varies a little with the velocity from 90 to 120° for velocity increasing from 2.5 to $10 \text{ mm}\cdot\text{s}^{-1}$.

The density of silicone oils varies little in the range studied ($\rho = 0.96 - 0.97 \text{ g/ml}$). The surface tension was measured by the drop weighing technique using Tate's law, giving $\gamma = 26 \pm 2 \text{ mN}\cdot\text{m}^{-1}$. This value is higher than those classically reported in the literature, around $20 \text{ mN}\cdot\text{m}^{-1}$, but it has already been measured for 1000 cSt silicone [85].

2.3 Spreading dynamics

2.3.1 Two regimes

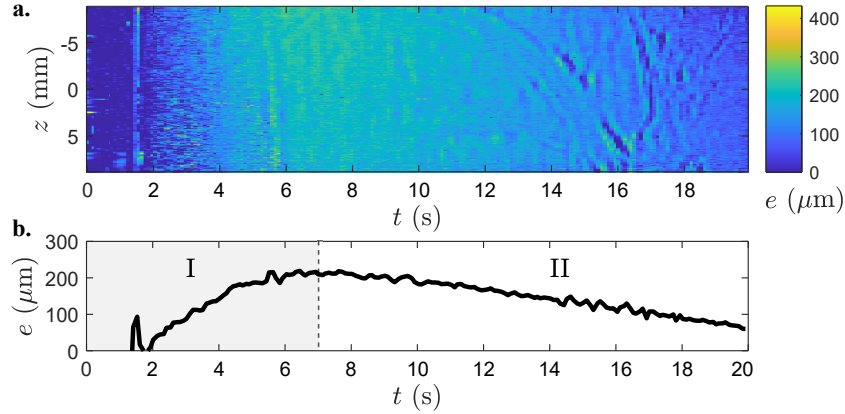


Fig. 2.6 – **a.** Map of the central part of the film (with viscosity $\eta = 960$ mPa s) during the spreading at $V = 5$ mm/s, as a function of the lateral position z and time t . The color code varies from dark blue for $e \simeq 0$ up to bright yellow for $e = 400$ μm . **b.** The line shows the corresponding mean thickness $e(t)$ over the film width, as a function of time. The coated film can be divided in two phases I and II, separated by a vertical dashed line (see text).

A typical thickness profile from a soft blade coating experiment is shown in Figure 2.6a. The colour maps represents the thickness e of a silicone oil film (with viscosity $\eta = 960$ mPa s) as a function of time t and position z ($z = 0$ corresponding to the center of the film, and the center of the laser beam). Despite a small residual noise due to multiple light reflections, the film thickness is relatively uniform in the z -direction along the width of the blade: edge effects are only visible 2 mm from the edges, as shown in Figure 2.7. The edge effects represent only 10% of the blade width and are not in the measurement range of the laser beam for standard experiments (centered positioning). Therefore the signal can be averaged and filtered along the z -direction, the resulting mean thickness is plotted in Figure 2.6b.

However, the film exhibits very large variations with time. The coating profile can be divided into two parts. First the film profile exhibits a sharp increase in the first 6 seconds, where the thickness grows from 0 to 230 μm . This corresponds to a transient state (phase I), associated with the setting in motion of the liquid below the blade, which was previously observed in similar systems [4]. The second part of the plot corresponds to the steady state (phase II). Unlike experiments carried out with a liquid level maintained constant under the blade, the deposited thickness varies during the spreading process. We observe here a continuous reduction of the film thickness e with time t - from 230 to 80 μm between 7 s and 20 s. In our work, we focus on the steady part (phase II) and all data displayed afterward corresponds to this phase.

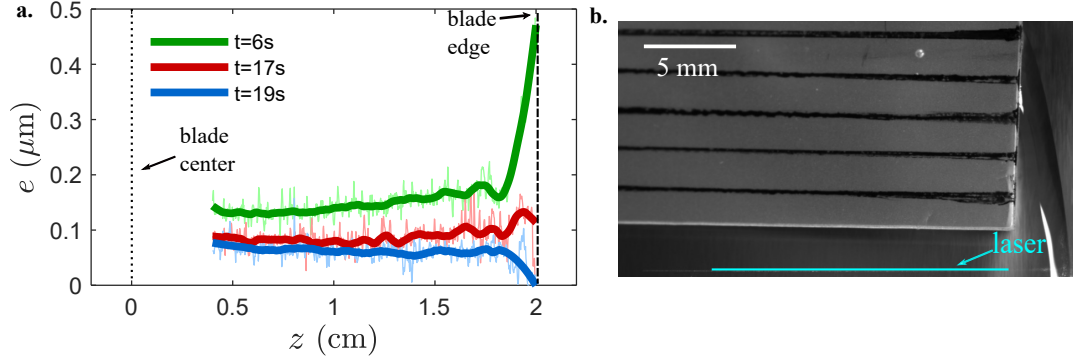


Fig. 2.7 – **a.** Film thickness e measured near the edge of the blade at three different times t of the experiment. e is measured between the center of the blade ($z = 0$) and the side edge ($z = 2$ cm). The presence of liquid in excess (respectively missing liquid) at the edges causes an increase (resp. decrease) of the film thickness over 2 mm to the edge. **b.** Top view picture of the side of the blade showing the position of the laser used in **a.** In this experiment, $L = 5.7$ cm, $\eta = 480$ mPa.s, $B = 1.0 \pm 0.1$ mN and $V = 5$ mm/s. Some liquid in excess can be seen on the right of the blade.

2.3.2 Importance of the wetting length

We interpret this reduction in film thickness as a consequence of the finite size of the reservoir. Indeed, the decrease in thickness of the deposit is accompanied by the emptying of the reservoir which can be monitored by the decrease in the length $l_w(t)$ of the blade actually wet by the liquid. This relationship between $e(t)$ and $l_w(t)$ is highlighted in Figure 2.8a, where $e(l_w)$ is measured for two silicone oils of viscosity $\eta = 480$ mPa.s (gray circles) and $\eta = 960$ mPa.s (black triangles). e is measured sufficiently close to the tip of the blade (2 mm away) so that at a time t it can be associated with the value l_w related to the volume remaining under the blade: these two variables are treated quasi-statically. The initial volume of liquid, Ω_0 was varied by a factor 3 for each fluid. For a given viscosity, the data for all initial volumes of liquid overlap, which indicates that the film thickness does not depend on the initial state of filling, but only on the actual volume of the reservoir at a time t . As shown in Figure 2.8a, the relation between e and l_w is non-linear: e increases more slowly for larger l_w . In addition, a strong dependency of e with the fluid viscosity η is observed: e increases by roughly 50% from $\eta = 480$ mPa.s to $\eta = 960$ mPa.s for the same filling l_w . The spreading velocity is also found to have an impact on the deposited thickness: e increases from 120 to 200 μm when V goes from 5 to 10 mm/s at $l_w = 10$ mm (Fig. 2.8b). A higher spreading velocity means a thicker fluid film.

2.4 Estimation of the deposited thickness with a scaling law

Experimentally, a strong dependency between the deposited thickness and the wetting length is observed. Two main hypotheses can be proposed to explain this dependency. Either it results from an elasto-capillary competition due to the presence of the meniscus at the back of the liquid reservoir at $s = s_w$ (Fig. 2.11). Or it results from an elasto-hydrodynamic competition between the elasticity of the blade

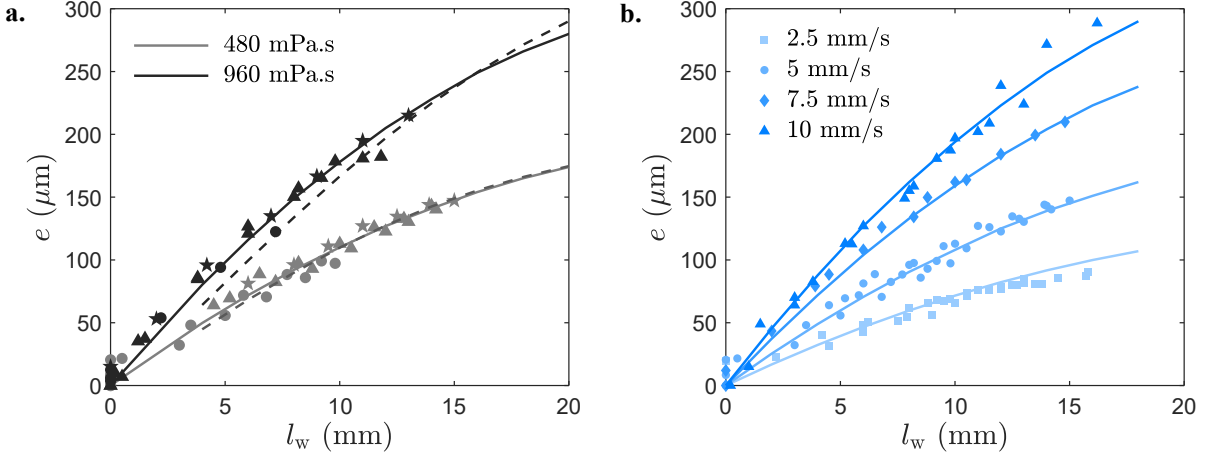


Fig. 2.8 – **a.** Film thickness $e(t)$ as a function of the wetting length l_w at the same time t , for two different oils with viscosity $\eta = 480$ mPa s (gray) and $\eta = 960$ mPa s (black). The markers correspond to different initial fluid volumes Ω_0 : \bullet : $\Omega_0 = 0.21 \pm 0.01$ cm³, \blacktriangle : $\Omega_0 = 0.50 \pm 0.03$ cm³ and \star : $\Omega_0 = 0.60 \pm 0.02$ cm³. The continuous lines show the scaling law (Eq. 2.4) with prefactors 0.15 (for $\eta = 480$ mPa s) and 0.17 (for $\eta = 960$ mPa s) corresponding to the best fits. The dashed lines are the numerical solutions. In both experiments, $V = 5$ mm/s, $B = 1.0$ mN m and $L = 5.7$ cm. **b.** $e = f(l_w)$ for four different velocities $V = 2.5, 5, 7.5$ and 10 mm/s. The continuous line shows the scaling law adjusted with prefactors 0.14, 0.15, 0.18 and 0.19 respectively.

and the pressure exerted by the fluid underneath. Concerning the first hypothesis, we show in section 2.4.2 that the capillary pressure is negligible as compared to viscous pressure. The numerical results presented in section 2.5.3 also show that capillary is a second order phenomenon that slightly affects the deposited thickness, but does not explain the interplay between e and l_w . The second hypothesis is developed below.

2.4.1 Elasto-hydrodynamic competition

Under the hypothesis of elasto-hydrodynamic competition, the thickness is determined by a balance between viscous torque on the one hand, and elastic torque on the other hand: those are the two components we try to evaluate here by scaling laws. Navier Stokes equation is used to estimate the viscous torque:

$$\rho \left(\frac{\partial \vec{v}}{\partial t} + (\vec{v} \cdot \nabla) \vec{v} \right) = -\vec{\nabla} P + \eta \Delta \vec{v} + \rho \vec{g} \quad (2.2)$$

To simplify this equation the following assumptions are made:

- The regime is considered stationary (e and l_w are quasi-static).
- The Reynold number is sufficiently low to neglect inertia and also to place ourselves in the framework of the approximation of lubrication because we are in a case where the liquid is strongly confined between two surfaces. The Reynolds number $Re = \frac{\rho V e}{\eta}$ is five orders of magnitude smaller than $\frac{l_w}{e} \simeq 100$ for typical value of $\eta \sim 1$ Pa s, $l_w \sim 10^{-2}$ m, $e \sim 10^{-4}$ m and $V \sim 10^{-2}$ m.s⁻¹. Moreover, the tip of the blade is almost parallel to the substrate (the mean angle

in the wet part of the blade is typically 3°). The lubrication approximation implies neglecting the velocity component perpendicular to the walls, neglecting the velocity variations along the flow and considering that the pressure is constant along the y -axis.

- The problem is considered invariant according to z , which is equivalent to consider a blade of infinite width (section 2.3.1).
- Gravity is neglected.

The Navier-Stokes equation (Eq. 2.2) can be rewritten under these assumptions:

$$\eta \frac{\partial^2 v}{\partial y^2} = \frac{\partial P}{\partial x} \quad (2.3)$$

The viscous term writes in scaling law: $\eta \frac{V}{e^2}$. It is balanced by a pressure gradient established over the length of liquid under the blade l_w :

$$\eta \frac{V}{e^2} \sim \frac{p}{l_w}$$

with p the fluid pressure defined as the pressure relative to the atmosphere $p = P - P_{atm}$. The region of the blade wet by the liquid is submitted to a lubricating pressure $p \sim \eta \frac{V}{e^2} l_w$. It induces a torque Γ_{wet} , pushing up the wet part of the blade (of area bl_w). The lever arm is $\sim L - l_w$, so that Γ_{wet} writes $\Gamma_{wet} \sim \eta \frac{V}{e^2} bl_w^2 (L - l_w)$. At equilibrium, this torque is compensated by the rigidity of the dry part of the blade, leading to a resisting torque written from Euler's Elastica: $\Gamma_{dry} \sim E^* I \frac{d\theta}{ds} \sim \frac{E^* I}{(L - l_w)}$. With s the curvilinear abscissa, $\theta(s)$ the angle describing the shape of the blade (defined between the vertical and the blade tangent vector – see Fig. 2.11), and I the second moment of inertia of the blade, $I = \frac{bu^3}{12}$. The torque balance sets the deposition law:

$$e \sim l_w \sqrt{\frac{\eta V L^2 b}{E^* I} \left(1 - \frac{l_w}{L}\right)} \quad (2.4)$$

The scaling law evidences the fundamental impact of the wetting length l_w . We recall that this model implies that $l_w \ll L$ from the lubrication approximation, and the Γ_{dry} approximation (see below for more details), so it cannot be used to predict the deposited thickness when $l_w \rightarrow L$. This scaling law also gives the dependency of the deposited thickness on other parameters: e increases as $\eta^{\frac{1}{2}}$ and $V^{\frac{1}{2}}$ which is in agreement with the experiments (Fig. 2.8). Conversely, the stiffer the blade ($\frac{EI}{b}$ increases), the thinner the deposited thickness.

2.4.2 Limits of the scaling law

When establishing the scaling law, all capillary effects have been neglected. The capillary pressure arising from the presence of the meniscus at the back of the reservoir can be expressed with Laplace pressure equation $p_{capi} = \frac{\gamma}{R}$, with R the meniscus radius, and thus be compared to the viscous pressure p :

$$\frac{p_{capi}}{p} \sim \frac{\gamma e^2}{\eta V l_w R} \sim 10^{-3}$$

with $R \simeq 10^{-3}$ m, $e \simeq 10^{-4}$ m, $l_w \simeq 10^{-2}$ m and $\gamma \simeq 10^{-2}$ N.m $^{-1}$.

Capillary can also have an effect by directly applying a force to the blade at the triple point corresponding to the menisci on the back of the reservoir and the blade tip. The associated torque $\Gamma_{\text{capi}} \sim \gamma b(L - l_w)$ is compared to the viscous torque and is found to be negligible as well:

$$\frac{\Gamma_{\text{capi}}}{\Gamma_{\text{wet}}} \sim \frac{\gamma e^2}{\eta V l_w^2} \sim 10^{-4}$$

Neglecting capillary effects in the scaling law is thus justified. However, the numerical computations reveal they nevertheless have an impact on the deposited thickness, which we considered is second order (see section 2.5.3) and is included in the numerical prefactor of the scaling law.

The matching point of the torque balance can be challenged. In fact the equation mathematically describe a parabola. Consequently, for $l_w \geq L/2$, the deposited thickness is expected from Equation 2.4 to be decreasing with l_w , which is not expected physically. In the extreme case of a blade fully wet ($l_w = L$), considering the lever arm to still be $L - l_w$ makes no sense. However, for smaller value of l_w , the wet region remains quite straight making this expression of the lever arm plausible. In Figure 2.9, the blade shape $h(x)$ is shown for two different wetting lengths $l_w = 6$ mm and $l_w = 14$ mm and in the absence of fluid. The blade which is curved over its whole length in the absence of liquid present a straight part corresponding to the wetting length in contact with the liquid. We believe this definition of the matching point is the main source of discrepancy between the scaling law and the experiments for large volume of reservoir ($l_w \geq 15$ mm). This discrepancy was not observed with silicone oil, because filling the reservoir to this level is made difficult by the high wettability of the oil, but is quite strong for

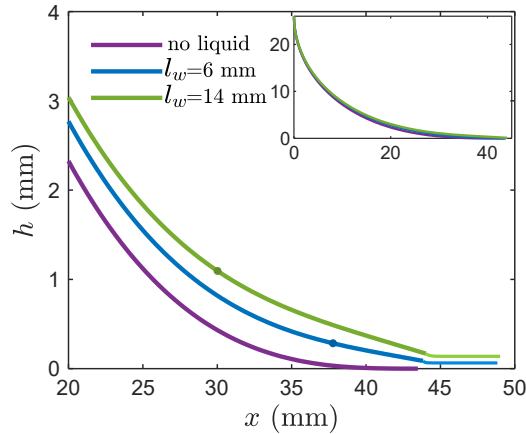


Fig. 2.9 – Effect of the wetting length on the blade shape and deposited film thickness, as calculated numerically with parameters $L = 5.7$ cm, $\eta = 480$ mPa.s, $B = 1.0 \pm 0.1$ mN and $V = 5$ mm/s . Three configurations are shown: the dry blade (in purple), $l_w = 6$ mm (blue) and $l_w = 20$ mm (green). The inset shows the full blade, while the main figure focuses on the free end of the blade (thick line). The thin line represents the deposited fluid film.

shear-thinning and normal stress fluids (see Chapter 3 and 4).

The lubrication approximation remains largely verified even for l_w up to 22 mm as the thickness of the fluid sheared and the angle between the blade and the substrate stays small. This was verified by numerical calculation. The blade approaches the surface with a small angle α in presence of liquid which increases with l_w : we measure $\alpha = 1.7^\circ$ for $l_w = 6$ mm and $\alpha = 2.9^\circ$ for $l_w = 14$ mm (Fig. 2.9).

2.4.3 Comparison with experiments

The scaling law (Eq. 2.4) is plotted in Figure 2.8a (with a continuous line). It reproduces very convincingly the dependency of the film thickness e with both l_w and η . The best fits are obtained with similar prefactors: 0.15 for $\eta = 480$ mPa.s and 0.17 for $\eta = 960$ mPa.s.

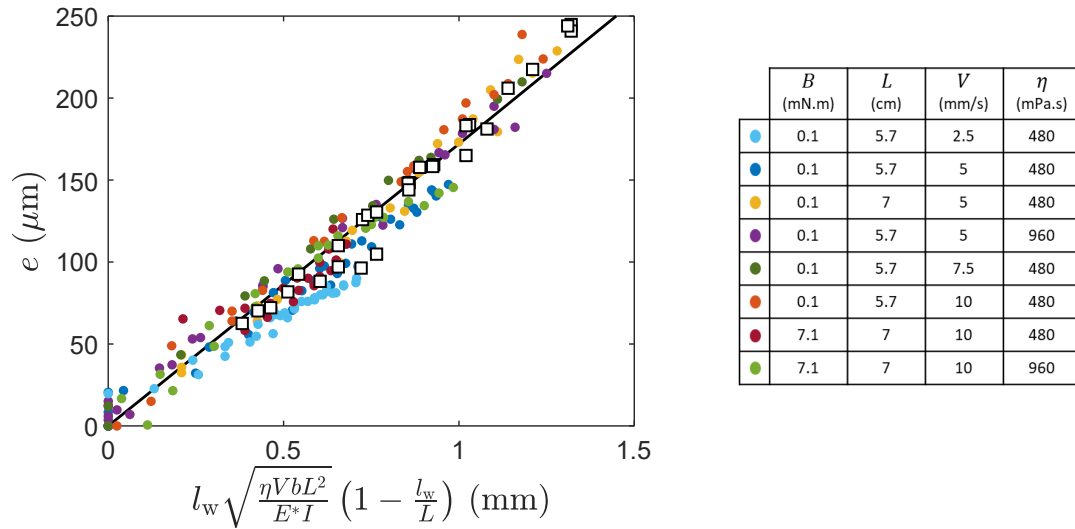


Fig. 2.10 – Experimental (color dots) and numerical (white squares) film thickness, plotted as a function of the theoretical thickness (Eq. 2.4). The black line is a linear fit whose slope indicates that the optimal prefactor is 0.17. Data correspond to varying velocities $V = 2.5$ mm/s (light blue), 5 mm/s (blue, yellow, purple), 7.5 mm/s (dark green) and 10 mm/s (red, fuchsia pink, light green), viscosities $\eta = 960$ Pa.s (purple, light green) and 480 Pa.s (all other colors), blade rigidities $B = 7.1 \pm 0.5$ mN m (light green and fuchsia pink) and 1.0 ± 0.1 mN m (all other colors) and lengths $L = 7$ cm (yellow, fuchsia pink, light green) and 5.7 cm (all other colors). The different combinations are summarized in the table.

The validity of the scaling law is checked by varying the different parameters at stake (Fig. 2.10). Thus the film thickness is measured for different blade rigidities B , blade lengths L , liquid viscosities η , spreading velocities V (respectively varied by a factor 8, 0.3, 2 and 4). Each color corresponds to a different set of parameters (refer to the legend). When plotted as a function of the theoretical film thickness, all data collapse on a single line with slope 0.17. The residual scattering of the data, observed particularly with V , might be explained by the influence of capillarity, which was neglected in Equation 2.4. The dynamic contact angles are observed to vary with the velocity [86, 87] meaning capillary effects

are velocity dependent. They could be the cause of the prefactor variation: 0.14 to 0.19 for velocity ranging from $V = 2.5$ mm/s to $V = 10$ mm/s (Fig. 2.8b).

2.5 Numerical model of deposited thickness

To take into account capillary effects, and validate the prefactor used for the scaling law, a full numerical study of this experiment was performed. It also gives access to the spreading dynamics which allows to study the shape of the deposited fluid film.

2.5.1 Model presentation

In the following, we describe the calculation done to determine the fluid thickness deposited on a plate by a flexible elastic blade. Since e and l_w evolve quasi-statically with time, we solve the elasto-hydrodynamic equations statically, with a constant l_w as an input variable and the corresponding e as the output variable. Furthermore, the geometry is split in two zones:

- the blade itself, which interacts with the fluid below over a length l_w ($< L$).
- the free liquid film, spread by the blade.

On one hand, we start by deriving the expressions of each of the external forces acting on the blade using the hydrodynamic equations and then we express the torque balance on the blade. On the other hand, we state the equations describing the free surface after the end of the blade. Finally, the coupling by boundary conditions at the tip of the blade of this two set of equations, along with the numerical resolution method are presented.

Blade equations

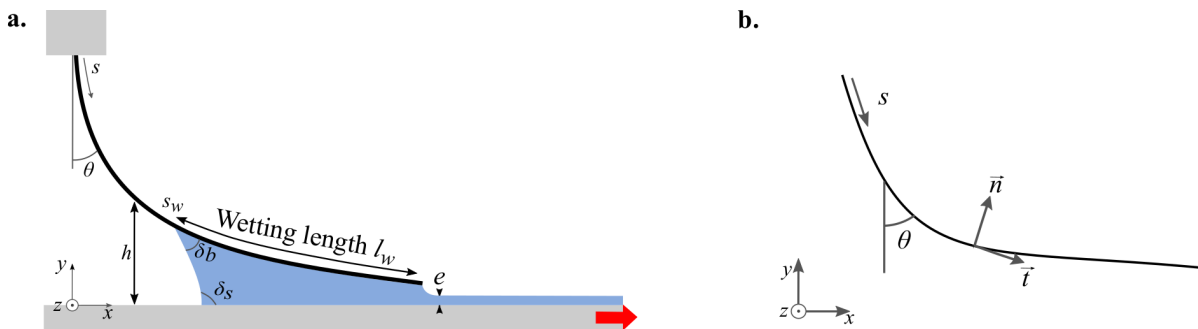


Fig. 2.11 – **a.** Soft blade coating notations **b.** Axes convention.

We consider an elastic blade submitted to non uniformly distributed forces, due to the presence of a Newtonian liquid under the blade, as shown in Figure 2.11a. The liquid is tightly confined between the blade and the substrate and, as shown previously, the Reynolds number in the fluid is low; thus the lubrication approximation holds, and we use it to determine the flow within the reservoir.

The fluid motion below the blade generates two forces distributed along the wet part of the blade: a lift force, due to the lubrication pressure p , which is exerted normally to the blade, and viscous force f_v coming from the no-slip boundary condition, which is exerted locally along the tangent to the surface. In addition, we consider the capillary forces, F_c^{sw} and F_c^L , applied along the tangent to the meniscus at $s = s_w$ and L (due to the local surface tension). These local forces are expected to be of small influence, as discussed before with scaling laws. This is confirmed with numerical computation and they can therefore be neglected (see Figure 2.13). However, the contribution of the Laplace pressure arising from the curvature of the interfaces at $s = s_w$ and $s = L$ (which acts as a boundary condition on the lubrication pressure p) has a significant impact on the film thickness e .

The full shape of the blade is modeled from the clamping point $s = 0$ to the free edge $s = L$. In this large deflection problem, the normal \vec{n} and tangent \vec{t} vectors (as defined in Fig. 2.11b) depend on the curvilinear abscissa s . The local equilibrium equations of curvilinear media mechanics gives [88]:

- the local equilibrium for forces:

$$\frac{d\vec{F}}{ds} + \vec{f}_{ext} = 0$$

With $F(s)$ the internal force exerted on point s by the portion of the blade located on the interval $]s; L]$, and f_{ext} the linear density of the forces.

- the local equilibrium for torques:

$$\frac{d\Gamma}{ds} + (\vec{t} \times \vec{F}) \cdot \vec{u}_z + m(s) \cdot \vec{u}_z = 0 \quad (2.5)$$

With $\Gamma(s)$ the torque exerted on point s by the portion of the blade located on the interval $]s; L]$, and m the linear density of moments, here $m = 0$.

By taking into account the forces that we listed above, the total internal force $F(s)$ acting to the right of s on the blade writes:

$$\vec{F}(s) = \int_s^L \vec{f}_{ext} ds = \int_s^L (p(s')\vec{n}(s') + f_v(s')\vec{t}(s')) b ds' + H(s_w - s)\vec{F}_c^{sw} + \vec{F}_c^L \quad (2.6)$$

with $H(s_w - s)$ the Heaviside step function which expresses the fact that the meniscus capillary force at s_w only plays a role for $s < s_w$.

Calculation of the forces

Fluid pressure

We consider a stationary flow in the lubrication approximation as presented previously in section 2.4.1. For ease of reading, the lubrication equation (Eq. 2.3) is recalled here :

$$\eta \frac{\partial^2 v}{\partial y^2} = \frac{\partial p}{\partial x}$$

To calculate the excess pressure p in the reservoir, the velocity is integrated over y with no-slip boundary conditions at the moving plate ($v(0) = V$) and the blade ($v(h) = 0$) so that:

$$v(y) = \frac{1}{2\eta} \frac{\partial p}{\partial x} (y^2 - hy) + V \left(1 - \frac{y}{h}\right) \quad (2.7)$$

The flow rate q is calculated by integrating v over y :

$$q = \int_0^h v b dy = -\frac{b}{12\eta} \frac{\partial p}{\partial x} h^3 + \frac{Vbh}{2} \quad (2.8)$$

Rewriting Equation 2.8:

$$\frac{\partial p}{\partial x} = 6\eta \frac{Vh - 2q/b}{h^3} \quad (2.9)$$

The derivative along the curvilinear abscissa, obtained using the relation $\frac{\partial p}{\partial s} = \frac{\partial p}{\partial x} \sin \theta$, is integrated between s_w and s which gives the fluid pressure p :

$$p(s) = \int_{s_w}^s 6\eta \left(\frac{Vh(s') - 2q/b}{h(s')^3} \right) \sin \theta(s') ds' + p_{sw}, \quad (2.10)$$

with p_{sw} the Laplace pressure arising from the deformation of the meniscus at $s = s_w$. We model the meniscus by an arc to obtain an expression of p_{sw} and the local radius of curvature R as a function of the wetting angles δ_s and δ_b (Fig. 2.12). An example is given for a wetting situation, using the relations $(h+x)/R = \cos(\delta_b)$ and $x/R = \sin(\delta_s - \pi/2)$, we get:

$$p_{sw} = \frac{\gamma}{R} = -\frac{\cos(\delta_b + \pi/2 - \theta(s_w)) + \cos \delta_s}{h} \gamma \quad (2.11)$$

Writing the equations in the dewetting case (δ_b and $\delta_s > \pi/2$) give the same relation for p_{sw} .

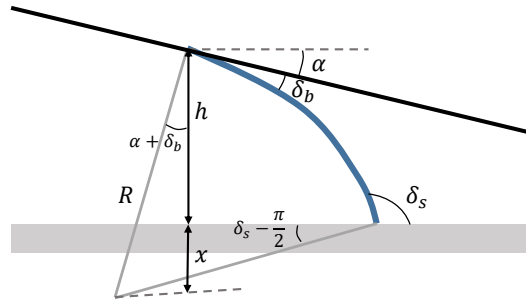


Fig. 2.12 – Meniscus at the back of the fluid reservoir

The flow rate is expressed using Equation 2.10 at the position $s = L$:

$$q = \frac{b \int_{s_w}^L \frac{V \sin \theta}{h^2} ds' + \frac{p_{sw} - p_L}{6\eta}}{\int_{s_w}^L \frac{\sin \theta}{h^3} ds'} \quad (2.12)$$

This expression is later used in the calculation of the fluid pressure p . Finally, from the pressure at $s = L$, an initial guess is used to start the numerical computation before it is determined iteratively by coupling the blade and the free surface calculation (see sections *Free surface equation* and *Numerical method*).

Viscous stress

The viscous stress f_v , exerted by the fluid on the blade, is defined as :

$$f_v = -\eta \left. \frac{\partial v_x}{\partial y} \right|_{y=h} \quad \text{where} \quad \left. \frac{\partial v_x}{\partial y} \right|_{y=h} \quad \text{is derived from Equation 2.7 so that:} \quad f_v = -\frac{h}{2} \frac{\partial p}{\partial x} + \frac{\eta V}{h} \quad (2.13)$$

Using Equation 2.9, f_v writes:

$$f_v = \frac{2\eta}{h^2} \left(\frac{3q}{b} - Vh \right) \quad (2.14)$$

Capillary forces

The capillary forces are expressed as:

$$\vec{F}_c^L = \gamma b \vec{e}_\gamma^L, \quad \text{and} \quad \vec{F}_c^{sw} = \gamma b \vec{e}_\gamma^{sw} \quad (2.15)$$

with \vec{e}_γ the vector tangent to the liquid surface at the triple line position. For the meniscus at $s = s_w$, the projection of \vec{e}_γ^{sw} on the x and y -axis is written: $e_\gamma^{sw} = \sin \theta_{msw} \vec{x} - \cos \theta_{msw} \vec{y}$, with $\theta_{msw} = \theta(s) - \delta_b$. For the meniscus at $s = s_L$, the expression is similar, instead of θ_{msw} the angle is $\theta_{mL} = \theta(L)$.

Torque balance

In the large deflection problem, the calculation of the total torque $\Gamma(s)$ (corresponding to the sum of the torques applied by the fluid on the blade between s and L) involves the projection angle θ on the x and y axis. Combining Equation 2.5 and 2.6 gives:

$$\begin{aligned} \frac{d\Gamma}{ds} &= -\vec{t} \wedge \left[\int_s^L b (p(s') \vec{n} + f_v(s') \vec{t}) ds' + H(s_w - s) \vec{F}_c^{sw} + \vec{F}_c^L \right] \cdot \vec{u}_z \quad (2.16) \\ &= - \begin{vmatrix} \sin \theta(s) \\ -\cos \theta(s) \\ 0 \end{vmatrix} \wedge \left[\int_s^L b \begin{pmatrix} \cos \theta(s') \\ \sin \theta(s') + f_v(s') \\ 0 \end{pmatrix} ds' + \gamma b \begin{pmatrix} H(s_w - s) \sin \theta_{msw} \\ -\cos \theta_{msw} \\ 0 \end{pmatrix} + \begin{pmatrix} \sin \theta_{mL} \\ -\cos \theta_{mL} \\ 0 \end{pmatrix} \right] \cdot \vec{u}_z \\ &= -b \left[\int_s^L [p \cos(\theta(s) - \theta(s')) - f_v \sin(\theta(s) - \theta(s'))] ds' - \gamma b [H(s_w - s) \sin(\theta(s) - \theta_{msw}) + \sin(\theta(s) - \theta_{mL})] \right] \quad (2.17) \end{aligned}$$

Following the classical way of solving the beam equation [70, 89], and according to the Euler-Bernoulli beam equation, under the assumption the material of beam remains linearly elastic, the relationship of bending moment and beam deformation is:

$$\Gamma = E^* I \frac{d\theta}{ds} \quad (2.18)$$

The differentiation of Equation 2.18, using Equation 2.17 results in:

$$\frac{d^2\theta}{ds^2} = \frac{b}{E^*I} \int_s^L [-p \cos(\theta(s) - \theta(s')) + f_v \sin(\theta(s) - \theta(s'))] ds' + F_c \left[\sin(\theta(s) - \theta_{mL}) + \sin(\theta(s) - \theta_{msw}) \right] \quad (2.19)$$

By replacing p , f_v and F_c by their expressions (Eq. 2.10, 2.14 and 2.15 respectively), an equation describing the shape of the blade $\theta(s)$ is obtained. Note that in the dry zone the terms p and f_v are zero.

Influence of the local capillary forces

The second term of Equation 2.19, $F_c \left[\sin(\theta(s) - \theta_{mL}) + \sin(\theta(s) - \theta_{msw}) \right]$ can be neglected when compared to the torque derivative arising from the pressure in the lubricated film. This point was previously discussed using scaling laws (see section 2.4.2). Here, we confirm it by comparing the numerical solutions of Equation 2.19 in the presence and in the absence of this capillary term. The blade shapes calculated in both cases perfectly match, showing that local capillary forces can indeed be safely neglected. Both results are shown in Figure 2.13, with the full solution in gray, and the simplified one (where the contribution of F_c is neglected) in black. However, and as discussed in section 2.4.2, the contribution of the Laplace pressure (due to the local deformation of the liquid interface) on the lubricating film itself is small but not fully negligible, as it imposes the fluid pressure in $s = s_w$ and $s = L$.

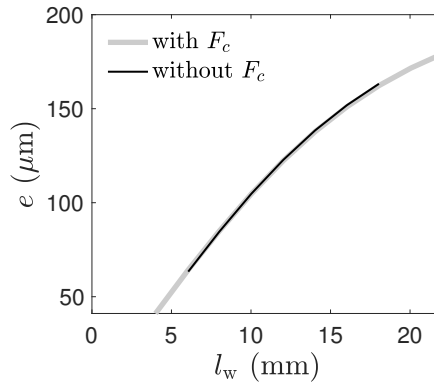


Fig. 2.13 – Influence of the local capillary forces on the film thickness e , as calculated from the numerical integration of Equation 2.19. Two situations are compared, in presence of capillary forces $\vec{F}_c = \gamma b \vec{e}_\gamma$ (in gray) or in the absence of this term (corresponding to $F_c = 0$, in black). The two plots almost perfectly overlap, indicating that the influence of capillary forces on the torque balance is almost completely negligible.

Free-surface equations

Following Trinh *et al.* [59], the pressure at $s = L$ is obtained by determining the shape of the free surface of the deposited liquid. The equations governing the free surface are presented below. To distinguish the variables of the free surface from those of the blade, we use an index l (for "liquid").

In this part we consider the liquid deposited behind the blade, typically over a length of 0.5 cm, an interval chosen sufficiently large to reach the atmospheric pressure in the liquid: $p(x = \infty) = 0$. The lubrication Equation 2.3 integrated with the no-slip boundary condition on the substrate ($v(0) = V$) and no tangential stress on the free surface, $\frac{\partial v}{\partial y}|_{h_l} = 0$, gives :

$$v(y) = \frac{1}{2\eta} \frac{\partial p}{\partial x} (y^2 - 2h_l y) + V \quad (2.20)$$

This expression of the velocity is integrated to give the flow rate, $q = -\frac{b}{3\eta} \frac{\partial p}{\partial x} h_l^3 + Vbh_l$, which can be rewritten to express the derivative of p :

$$\frac{\partial p}{\partial x} = 3\eta \frac{Vh_l - q/b}{h_l^3} \quad (2.21)$$

By writing the Laplace pressure equation in the meniscus at the end of the blade we obtain another expression for p :

$$p = -\gamma \frac{d\theta_l}{ds} \quad (2.22)$$

The differentiation of 2.22, using Equation 2.21, and the relation between the derivatives with respect to s and x finally gives:

$$\frac{d^2 \theta_l}{ds^2} = -\frac{3\eta}{\gamma} \left(\frac{Vh_l - q/b}{h_l^3} \right) \sin \theta_l(s) \quad (2.23)$$

This equation governs the shape of the free surface of the deposited layer of fluid behind the blade. The liquid flow rate involved in this equation should be equal at any point in the fluid because the it is incompressible. In the numerical resolution we use the value of the flow rate at $x = \infty$, $q = Vbh_l(\infty) = Vbe$.

Boundary conditions

The boundary conditions depend on the solved set of equations:

- for the blade: the fixed mounting imposes $\theta(0) = 0$, and there is not torque at the end of the blade leading to $\frac{\partial \theta}{\partial s} \Big|_L = 0$.
- for the free surface: as the deposited layer is horizontal at $x = \infty$, $\theta_l(\infty) = \pi/2$, and the Laplace pressure equation written at L gives the second condition: $\frac{\partial \theta_l}{\partial s} \Big|_L = -\frac{\rho L}{\gamma}$.
- Finally, the matching of the solutions of Equations 2.19 (for the blade) and 2.23 (for the free film) is done by imposing a continuity of the flow rate q at $x = L$, as well as of the liquid height: $h(x = L) = h_l(x = L)$.

Numerical method

The governing equations for the shape of the blade (Eq. 2.19) and of the free surface (Eq. 2.23) have the same structure and can be both rewritten as:

$$\frac{d^2\theta}{ds^2} = -S(s, \theta(s)) \quad (2.24)$$

where $-S$ is the right member of Equations 2.19 and 2.23 depending on s and θ . Note that the local height of the blade, present in the description of p and f_v , is directly linked to θ with $\frac{dh}{ds} = \cos \theta$; the same relation is used to compute h_l from θ_l for the free surface. Equation 2.24 is a piecewise 2nd order non linear boundary value problem. It is non linear in the sense that the function S depends itself on the angle distribution $\theta(s)$ we are looking for. There are different methods to solve this problem such as the shooting method, projection methods, and difference methods [90]. We chose to apply the false transient (or pseudo transient) method [91–93]. We solve the Equation 2.24 using an analogy with the heat equation. Equation 2.24 can be seen as a 1D steady-state non-linear heat equation where θ is equivalent to temperature at abscissa s , with a heat conductivity equal to 1 and a heat source distribution S . In order to solve it, we refer to the transient heat equation (2.25) where the derivative of θ versus a virtual time, $\frac{\partial\theta}{\partial t_v}$, is added (the volumetric heat capacity is also chosen equal to 1):

$$\frac{\partial\theta}{\partial t_v} = \frac{\partial^2\theta}{\partial s^2} + S(s, \theta) \quad (2.25)$$

We start with a guess for $\theta(s, t_v = 0)$. Solving numerically by finite difference (see next) the transient heat equation (Eq. 2.25) with proper boundary conditions, we obtain a time dependent distribution $\theta(s, t_v)$ sequentially. The stable asymptotic state obtained after a while corresponds to the steady state solution of Equation 2.24 we are looking for (since then $\frac{\partial\theta}{\partial t_v} = 0$). An implicit-explicit scheme [94, 95] has been chosen as a compromise between stability and computation time. The scheme is not strictly implicit because it is explicit for the source which is expressed at time step n instead of $n + 1$ in the case of the purely implicit scheme :

$$\frac{\theta_i^{n+1} - \theta_i^n}{\Delta t_v} = \frac{\theta_{i-1}^{n+1} - 2\theta_i^{n+1} + \theta_{i+1}^{n+1}}{\Delta s^2} + S(s, \theta^n) \quad (2.26)$$

where $\theta_i^n \approx \theta(i\Delta s, n\Delta t_v)$ with i the spacial indexes, i going from 1 to N (Fig. 2.14), and n the temporal index, $n = 1$ corresponding to the initial state of the system . To obtain the corresponding matrix the Equation 2.26 is rewritten :

$$-K\theta_{i-1}^{n+1} + (1 + 2K)\theta_i^{n+1} - K\theta_{i+1}^{n+1} = \theta_i^n - S_i^n \Delta t_v \quad \text{with} \quad K = \frac{\Delta t_v}{\Delta s^2} \quad (2.27)$$

And the transcription of the boundary conditions writes:

blade, p_L , as well as the meniscus angle at this position, θ_{mL} . The initial guess of $\theta(s)$ was obtained from the static blade without liquid, whose shape has been modified to show a small gap at the end, while the free surface was initially considered nearly flat $\theta_l(s) \approx \pi/2$. These guesses are used for the computation of the transient heat equations (Eq. 2.19 and Eq. 2.23) which give updated $\theta(s)$, $\theta_l(s)$, and $\theta_{mL} = \theta_l(L)$. The arbitrary value of p_L is adjusted through a corrective factor extracted from the difference between the two values of flow rates, q and q_l ($p_L(n+1) = p_L(n) - (\frac{q_l}{q} - 1)a$ with a a numerical factor). This process is iterated until the flow rates can be considered equal, usually $10^{-2}\%$, leading to the "correct" value of p_L . The fluid thickness e is finally extracted from the height of the deposited fluid for $x \rightarrow \infty$ (in practice 4 to 10 mm after the blade tip). A schematic representation of the numerical resolution is given in Appendix C .

Results for the calculation of shear rate, fluid velocity and pressure

In this section we show the numerical results of some of the physical variables defined before: the shear rate, the velocity and the pressure (Fig. 2.15). For this example, the spreading velocity is $V = 10$ mm/s, the viscosity is $\eta = 478$ mPa.s and the wetting length is $l_w = 14$ mm.

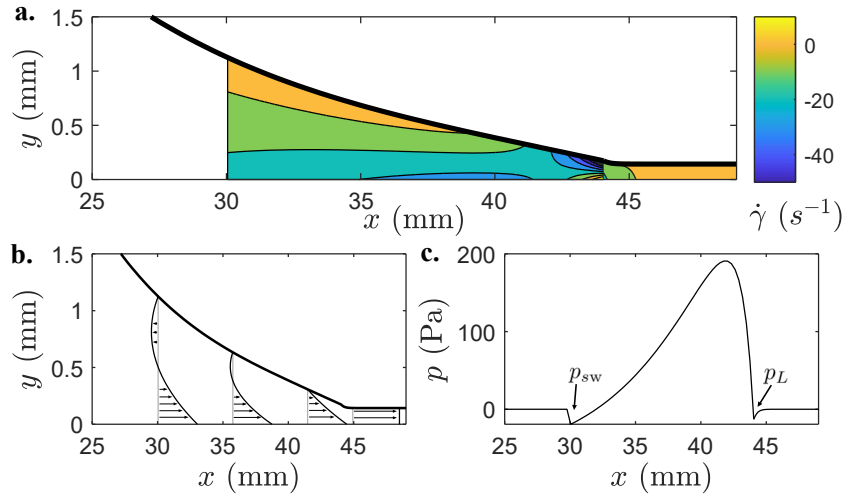


Fig. 2.15 – Calculated values of physical parameters in the liquid region under the blade ($30 \leq x \leq 44$) and in the deposited film ($44 < x$) for $\eta = 480$ mPa.s, $V = 5$ mm/s and $l_w = 14$ mm. The dark line in **a** and **b** represents the blade shape $h(x)$ and the free surface $h_l(x)$. **a.** Map of the shear rate $\dot{\gamma}$ within the film. The negative value comes from the axis convention. **b.** Velocity profile $v = f(x, y)$ plotted against the reference value $v = 0$ (vertical gray line) for different abscissas. **c.** The fluid pressure $p = f(x)$ presents a maximum at $x = 42$, the negative values of the pressure, p_w and p_L correspond to the menisci.

The shear rate is represented in Figure 2.15a. The blade shape $h(x)$ and the free surface $h_l(x)$ are shown with a thick black line. The colormap indicates the local shear rate $\dot{\gamma}$ within the film. Note that the shape of the meniscus at the back of the reservoir is not represented as it is not calculated in our simulation: the meniscus is only considered to provide a boundary value for p . Since the substrate is

moving (in the positive x direction), the shear rate is negative almost everywhere in the fluid under the blade. We observe an almost constant shear rate gradient as a function of y (at a given x position), in good agreement with what is expected of a Stokes flow, where $\frac{\partial \dot{\gamma}}{\partial y} = \frac{1}{\eta} \nabla p$, is a constant for a given x position.

The velocity of the fluid is represented in Figure 2.15b. Four types of velocity profile are observed:

- Near $x = 42$ mm, a nearly linear velocity profile is observed as in a Couette flow.
- At the back of the fluid reservoir, the velocity changes direction near the blade [61]. The fluid goes towards the left in a recirculation movement.
- At the blade tip, the fluid velocity pass through a maximum slightly higher than the velocity of the substrate. This can be explained by the strong pressure drop near the tip of the blade which generates an additional Poiseuille flow (Fig. 2.15c).
- Under the free surface, the velocity profile is quickly homogenized after the meniscus and $v \simeq V$ over the whole height.

The fluid pressure goes through a maximum $p(x = 44) = 190$ Pa.s (Fig. 2.15c). This maximum corresponds to linear velocity profile and constant shear rate. This naturally derives from the Stokes flow. The negative pressures arising from the menisci presence at x_{sw} and x_L are observed around -19 and -11 Pa respectively.

2.5.2 Prefactor validation

Comparison with experiment and scale law

In Figure 2.8a, the numerically calculated film thicknesses (black and grey dashed lines) are compared to the experiments for different values of the wetting length l_w . They match the experimental data for both $\eta = 480$ mPa.s and $\eta = 960$ mPa.s, without any adjustable parameter. The good agreement between the numerical calculation, the experiments and the scaling law is further highlighted in Figure 2.10. The numerical solutions of the elasto-hydrodynamic equations (Eq. 2.19 and Eq. 2.23) are shown with white squares. Here, the same parameters (η , V and B) as in the experiments are used. For this figure, capillary action is neglected (capillary forces and $p_{sw} = 0$) to compare scaling law and numerical calculation in the same scope. All data, including the numerical ones, were obtained without any adjustable parameter. They collapse on the same master curve with slope 0.17, thus confirming the prefactor used for the scaling law.

In addition, the numerical solution of the blade shape is compared to the experiment. The picture of a blade taken during an experiment while spreading liquid ($l_w = 16$ mm), or not, is shown in Figure 2.16a. From this picture we are able to determine the shape of the blade $h(s)$, except towards the end of the blade where the image is not sharp enough in the presence of liquid. The computed profile $h(s)$ (Eq. 2.19) nicely overlaps the experiment, as shown in Figure 2.16b.

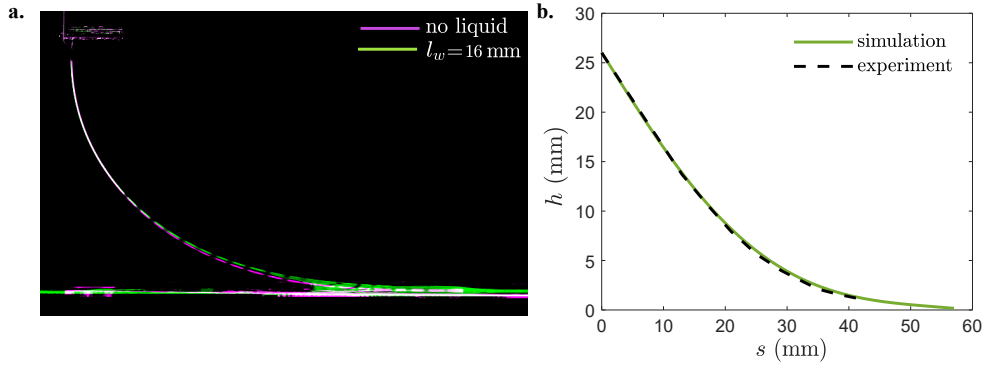


Fig. 2.16 – **a.** Picture of the moving blade during a typical spreading experiment ($L = 5.7$ cm, $\eta = 960$ mPa.s, $B = 1.0 \pm 0.1$ mN and $V = 5$ mm/s) for $l_w = 16$ mm (in green), and in absence of liquid (purple). **b.** Comparison of the experimental blade shape $h(s)$ (dashed line) and the numerical solution (calculated through the integration of the elasto-hydrodynamic equations), with parameters $L = 5.7$ cm, $\eta = 480$ Pa/s, $B = 1.0 \pm 0.1$ mN and $V = 5$ mm/s (green line). The simulation is seen to match the experimental shape.

Limits

Even if capillary is taken into account, the results obtained from the numerical calculations still show some discrepancy, particularly for $\eta = 960$ mPa.s (Fig. 2.8). These differences between the experiments and the numerical results can arise from experimental uncertainty over the measurement of the parameters involved in the calculation (the contact angles δ_b and δ_s , the surface tension γ , the viscosity η , the blade rigidity B), or directly from the measurement of l_w and e . A parametric study was conducted to test the sensitivity of the calculated thickness to these different input parameters. We observed that e is very little affected by variations in γ , δ_b and δ_s ($< 2\%$) but varies by about 6–7% with η , V and B for a $\pm 10\%$ variation in the value of these parameters. Consequently a poor evaluation of the viscosity or the blade rigidity can be at the origin of systematic error for the numerical results.

Moreover the lubrication approximation, the approximation of the p_{sw} equation, and the assumption of a zero transverse flow may cause the discrepancy between numerical and experimental data. Seiwert *et al.* showed an important impact of the deposited thickness with the blade width b , questioning the hypothesis of invariance in the transverse direction z [4]. However, in our situation the finite size of the reservoir limits this effect: no liquid was observed escaping from the side of the blade in most experiments. The potential exception concerns the beginning of the spreading due to the initial deposit shape (Fig. 2.7), however it mostly corresponds to the transient phase I (not taken into account in the data).

2.5.3 Capillary effect

The numerical approach easily allows testing the assumption made in section 2.4: it assumed that the dependency between e and l_w would result from an elasto-capillary competition due to the presence of

the meniscus at the back of the reservoir. We compare in Figure 2.17 numerical simulations of $e(l_w)$ in two different configurations: in absence of a pressure jump at $s = s_w$ (gray line), and for varying wetting conditions (dotted lines). This is achieved by modifying the contact angles δ_s and δ_b on the surface and on the blade (as in Fig. 2.17). They are directly linked to the pressure at p_{sw} (Eq. 2.11). A major observation from Figure 2.17 is that e varies with l_w even when capillary forces are absent. This confirms that the pressure jump at the meniscus does not cause the dependency of e with l_w .

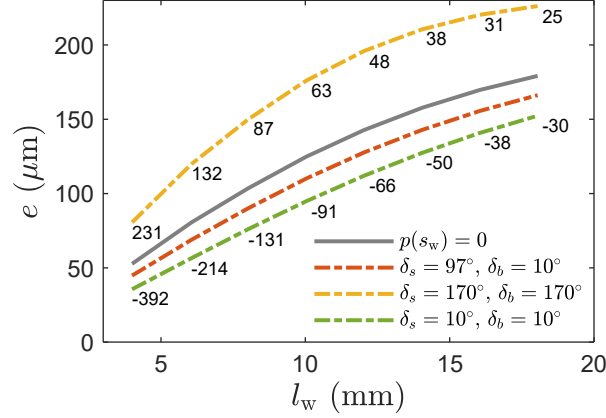


Fig. 2.17 – Effect of wetting on $e(l_w)$. The continuous gray line corresponds to the absence of a pressure jump $p(s_w) = 0$. A typical experiment ($\delta_b = 10^\circ$, $\delta_s = 97^\circ$) is plotted in red, and two extreme situations of almost perfect wetting ($\delta_s = \delta_b = 10^\circ$) and non-wetting ($\delta_s = \delta_b = 170^\circ$) are shown in green and yellow. The numbers indicate the pressure jump $p(s_w)$ due to the meniscus (in Pa).

However wetting conditions still have an influence on the film thickness: the $e(l_w)$ curves are shifted. Thus e is potentially increased by a factor two when comparing the almost perfect wetting ($\delta_s = \delta_b = 10^\circ$) to the non-wetting situation ($\delta_s = \delta_b = 170^\circ$). However the latter is highly unlikely as the film would be unstable and dewet the substrate. In classical wetting configurations (green and red plots), capillary forces cause a modest variation of e , close to 20%. Experimentally, the surface condition of the PMMA support and the mylar blade must be controlled to avoid variations in wetting and limit the discrepancy of the data.

2.5.4 Shape of deposit

The profile of the fluid film can be computed from the numerical data describing the blade shape $h(x)$. The conservation of the volume of fluid during the emptying the reservoir from l_{wj} to $l_{w(j+1)}$ gives: $\Delta\Omega_d = \bar{e}V\Delta t_d = \bar{e}\Delta l_d$. With $\bar{e} = (e_j + e_{j+1})/2$ the averaged deposited thickness, Δt_d the deposition time, Δl_d the deposited length and $\Delta\Omega_d$ the deposited volume which is also equal to the variation of volume under the blade, $\Delta\Omega_d = \int_{x_j}^L h_j dx - \int_{x_{j+1}}^L h_{j+1} dx$. The length interval Δl_d to transition from a deposited thickness e_j to $e_{j+1} (< e_j)$ can thus be expressed:

$$\Delta l_d|_{e_j \rightarrow e_{j+1}} = \frac{\int_{x_j}^L h_j dx - \int_{x_{j+1}}^L h_{j+1} dx}{\bar{e}} \quad (2.28)$$

The small quantity Δl_d is integrated to give access to the deposited length resulting from an emptying of the reservoir, starting from $l_w = 18$ mm. The thickness is plotted as a function of the deposited length l_d which gives access to the profiles of the fluid film. For the final part of the reservoir emptying ($l_w < 4$), the profile is approximated by considering a triangular shape for the deposited film and represented by dotted lines (Fig. 2.18a). Experimentally, the deposition length l_d^{exp} is measured (directly proportional to t in Fig. 2.6) but it cannot be considered as directly equivalent to the numerically calculated deposition length since: *i*) the "initial" l_w (measured at the beginning of phase II) must be the same for a comparison to be possible, *ii*) and the transient regime is taken into account in l_d^{exp} . For each experiment, an offset is applied to the first value of l_d^{exp} in phase II, in order to obtain the best fit between the experimental and numerical data. The comparison of the experimental data with the numerical data does not enable to validate the values of l_d obtained numerically but allows to check the slope of $e = f(l_d)$. Figure 2.18a shows a good agreement between the numerically calculated profile shape and the experimentally obtained one.

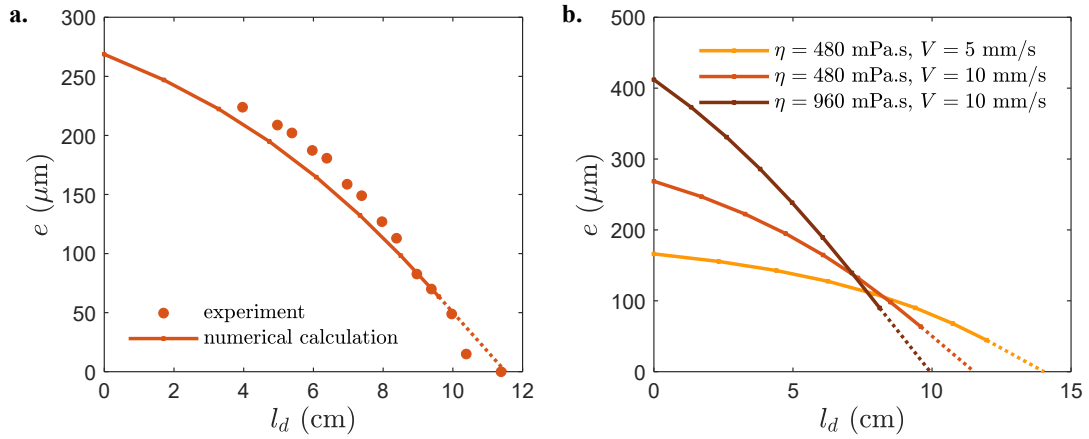


Fig. 2.18 – Profile of the deposited fluid film for an initial value $l_w = 18$ mm. **a.** Comparison of the experimental datas (markers) with the numerically calculated profile (plain line) for $\eta = 480$ mPa.s and $V = 10$ mm/s. The dashed lines correspond to approximated values. **b.** Effect of V and η on the shape of the deposited profile. The thicker deposits are spread on shorter distance with high local variation of the thickness.

The numerical calculation is useful to complement the results obtained from the scaling law. In particular it gives additional information about the dynamic of the spreading. Previously, we have shown that the scaling law predicts that e increases with the velocity V and the viscosity η , for a given l_w . However, it gives no information on the shape of the fluid deposit. The numerical computation allows access to this information: in Figure 2.18b the film profile is plotted for three combinations of η and V . At the beginning of the film ($l_d = 0$) we observe the results predicted by the scaling law, $e(V = 5$ mm/s, $\eta = 480$ mPa.s) $<$ $e(V = 10$ mm/s, $\eta = 480$ mPa.s) $<$ $e(V = 10$ mm/s, $\eta = 960$ mPa.s). Then this order is not maintained, the initially thicker deposit is also the shorter one. Since the initial volume of fluid under the blade is not the same in these different situations (e.g. $\Omega_0(V = 10$ mm/s, $\eta = 960$ mPa.s) $>$ $\Omega_0(V = 10$ mm/s, $\eta = 480$ mPa.s)), this results is not straightforward. Additionally, the

thickness decreases non-uniformly as it tends to fall slowly before plummeting. This slope variation is stronger for the low values of velocity and viscosity. Concretely, from a cosmetic point of view, reducing the spreading velocity or the viscosity of the fluid allows achieving a more homogeneous deposit.

2.6 Flexible blade coating with finite size reservoir is not analogous to dip coating

The scaling law, confirmed numerically, allows us to put a central point forward. In the case of a finite reservoir, the viscous forces of the lubricated film are exerted over an externally imposed distance l_w that varies over the course of the spreading. This is fundamentally different from the capillary-elasticity analogy approach, where the pressure is applied over an internal dynamical length $l_x \sim (eL^2)^{1/3}$ [4, 65] that varies with the parameters of the blade and the liquid. This length, in turn, impacts the scaling of the film thickness, which writes $e \sim L \left(\frac{\eta V b L^2}{E^* I} \right)^{3/4}$ in the blade-meniscus analogy [4–6].

Furthermore, the blade here is deformed by the film along its entire length, as highlighted in Figure 2.19, where the blade shapes, numerically calculated for different velocities, are shown. This is contrary to the meniscus in dip-coating experiments, which is only locally deformed. For this reason, the blade shape cannot be resolved using asymptotic matching, as usually done for a liquid interface. Consequently the analogy between soft blade coating and dip coating does not seem to be valid in the case of a finite reservoir of fluid.

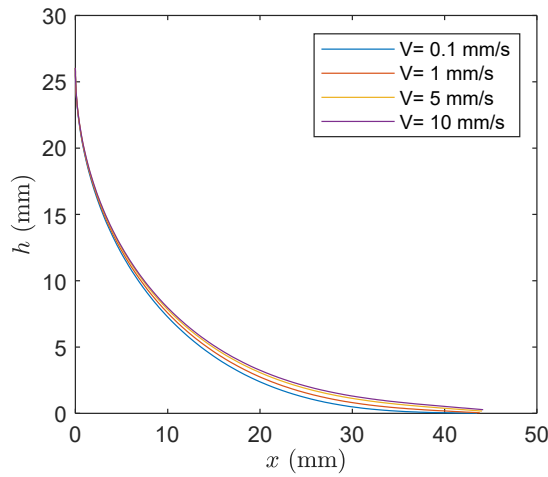


Fig. 2.19 – Comparison of the blade shape at varying velocities $V = 0.1, 1, 5$ and 10 mm/s. The fluid viscosity is $\eta = 460$ mPa s, the wetting length $l_w = 14$ mm, $B = 1.0$ mN m and $L = 5.7$ cm. With a finite reservoir and a finite blade length, the whole blade is deformed over its whole length.

Conclusion – Chapter 2

In this chapter we have studied the film thickness of a Newtonian fluid spread by a soft blade. We focused on a finite reservoir of fluid to mimic spreading situations such as cosmetic spreading or painting. This study has an important application scope:

1. We demonstrated that it is impossible to obtain a deposit of constant thickness with an elastic blade if the spreading is done at constant speed. By using the Stokes equation and elastic beam theory we proposed a scaling law able to predict the experimental data.
2. We proposed a more detailed model by numerical calculations. We obtained good agreement with the experimental data without any adjustable parameter, which allowed us to validate the prefactor used for the scaling law.
3. We evidenced the effect of capillarity: it is a second order phenomena and plays a significant role only for very hydrophobic substrates.
4. We showed how viscosity and spreading velocity influence the shape of the deposit.
5. We suggested that the analogy between elastic and capillary interfaces is not valid when the level of liquid under the blade varies (finite reservoir).

Now that the basis have been laid in the Newtonian case, we seek to extend this study to more complex fluids that are primarily used in industry. The addition of polymers is often responsible for changing the fluid properties. Chapter 3 presents the case of shear-thinning fluids. And Chapter 4 deals with the spreading of shear-thinning fluids which additionally generates normal forces or display a yield stress.

Chapter 3

Extension to shear-thinning fluids

In this chapter, we consider the spreading of complex fluids with a soft blade and focus on shear-thinning fluids. We combine experiments, the scaling law approach and numerical computations to compare the film deposition of shear-thinning and Newtonian fluids. We point out the differences in shape and mechanical work required to spread the fluid: more energy is required to spread at constant velocity a given volume in a given time of a shear-thinning fluid.

The results presented in this chapter have been published in Physical Review Fluids [2]. The article can be found in Appendix D.

Contents

3.1	Experiment	56
3.1.1	Fluid model: Xanthan gel	56
3.1.2	Spreading dynamics	59
3.2	A generalized scaling law to predict the film thickness	60
3.2.1	Elasto-hydrodynamic competition for shear-thinning fluids	60
3.2.2	Comparison with experimental data	62
3.3	Numerical solution of the elasto-hydrodynamic equations adapted to the shear-thinning fluids	63
3.3.1	Under-blade-area equations	64
3.3.2	Torque balance	68
3.3.3	Free surface equations	68
3.3.4	Numerical method	69
3.3.5	Results of the calculation for the shear rate	70
3.3.6	Comparison with experiments and scale law	71
3.4	Comparison of shear-thinning and Newtonian fluids	71
3.4.1	Choice of the equivalent Newtonian fluid	72
3.4.2	Mechanical work	75
3.4.3	Shape of the fluid deposit	77

3.4.4	Disentangle the effect of the rheological parameters n and k	78
3.5	Conclusion	79

3.1 Experiment

3.1.1 Fluid model: Xanthan gel

Xanthan gum is a natural polysaccharide, produced by the fermentation action of a bacterium, *Xanthomonas campestris*. Discovered in the 1950s at the United States Department of Agriculture, it has since been used in many industrial applications for its thickening, stabilizing or suspending properties. This biopolymer is used in the cosmetic and pharmaceutical industries, as well as in the formulation of paints and cements for the construction industry, and in the oil and gas industry. In the food industry, it is often used as a food additive under the European code E415, for its thickening properties.

Xanthan is a polymer consisting of a main chain of cellulose branched by side chains of trisaccharide. The presence of carboxyl groups gives it a good solubility in water. At room temperature and up to 40°C, xanthan is in an ordered native conformation [97]. This is a helical structure that is stabilized by intermolecular and intramolecular hydrogen bonds. A xanthan macromolecule can be modeled as a semi-rigid rod with a typical hydrodynamic length of 1.5 μm [98].

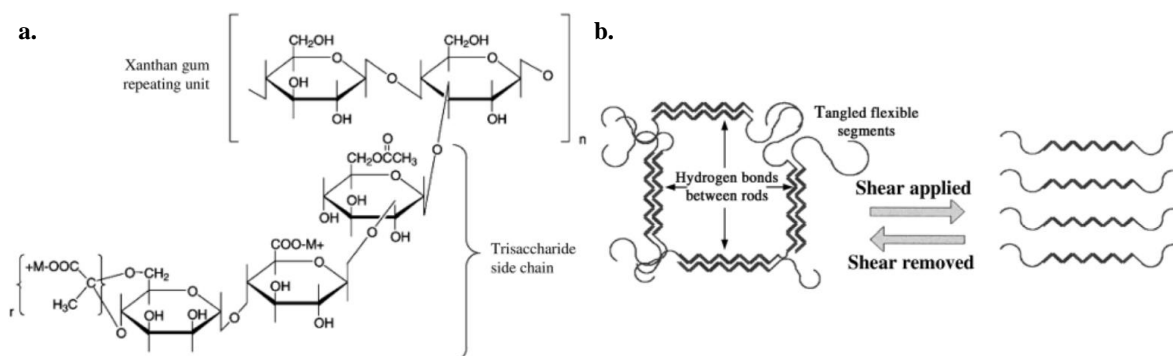


Fig. 3.1 **a.** Structure of xanthan gum. **b.** Schematic representation of the effect of shear on the polymer network. The rod-shaped polymer aligns along the shear (from Song et al. [99]).

This rod shape confers to xanthan in aqueous solution a specific rheological behavior. Xanthan is known to be a strong shear-thinning fluid exhibiting at low shear rates either a Newtonian plateau or a low yield stress (a few Pa) for dilute and concentrated suspensions respectively [98, 99]. The values reported in the literature to define the limits at rest of the dilute, semi-dilute and concentrated regime vary: formulated below 0.13-1 w% the xanthan is in the dilute regime, and above 1.1 – 7 w% it reaches the concentrated regime [100]. The pronounced shear-thinning behavior may be interpreted as a conformational change of the polymer molecules. Figure 3.1 gives the representation proposed by Song et al [99]. At low shear rates and at rest, the xanthan macromolecules can form a network structure through entanglement and hydrogen bonding between the rods. The resulting viscosity is

significant and some yield stress can even be observed at high concentration. When a stress is applied, these non-covalent bonds break and disentanglement happens, so that the macromolecules begin to align parallel to the shear direction [101]. Viscosity decreases as the alignment facilitates the flow. By removing the shear, the disordered lattice structure is instantly re-formed and the initial viscosity is recovered [102]. Several models have been used to describe the rheological shear-thinning behavior of xanthan gel [99, 102, 103], such as Oswald and de Waele power law, and, in the case of an initial yield stress is considered, the Casson model.

Preparation of polymer solutions

Solutions of xanthan gel (Rhodicare® XC, Solvay) in water have been obtained by dissolving the polymer under mechanical agitation at room temperature. First, a small amount of a biocide, the 2-phenoxyethanol, is added to the water (0.5 w%). The xanthan is well known to be quickly contaminated by bacteria, notably as some might not have been completely eliminated during the production process. Without biocide, the shelf life of the sample is only a few days while otherwise by keeping the sample in the refrigerator it can be increased at least to a month. The powder is then added little by little in the solution to avoid agglomerates. The samples are kept under continuous stirring from a few hours to 24 hours for the highest concentrations. We mainly studied the samples at 0.4 and 0.9 w% to focus on the shear-thinning behavior. At a higher concentration, a yield stress could appear. At a lower concentration, the fluid was not sufficiently viscous to obtain a fluid film thick enough to have a high signal-to-noise ratio from the profilometer, and avoid dewetting interfering with the measurement.

Prior to the first experiment, the solutions are kept at rest for a minimum of 24 hours so the samples can reach their equilibrium state.

Rheology of xanthan gel

The flow curves were obtained with cone and plate geometry, using a shear-imposed flow-sweep, with 5 points per decade. The shear rate $\dot{\gamma}$ was incremented between 10^{-3} and 400 s^{-1} . The stress value is given when three consecutive 10 s measurements have given the same results with a tolerance of 5%, or when the sample has undergone 60 s of constant shear rate. This maximum time is long enough for the measurements not to be sensitive to the rheometer inertia, or to the fluid inertia (for high viscosity fluids).

The rheological measurements are presented in Figure 3.2. Xanthan is strongly shear-thinning at any concentration. The viscosity decreases by three orders of magnitude for an applied shear rate increasing from 0.01^{-1} to 400 s^{-1} . At low shear rates, a Newtonian plateau is clearly visible at 0.4 w% while it is less obvious at 0.9 w%. The viscosity at the Newtonian plateau is denoted η_0 . A critical shear rate, $\dot{\gamma}_c$, can be defined as the limit between the Newtonian and shear-thinning regions. Above $\dot{\gamma}_c$, the viscosity follows the classical Ostwald and de Waele power law for polymer solutions. Finally, the viscosity is

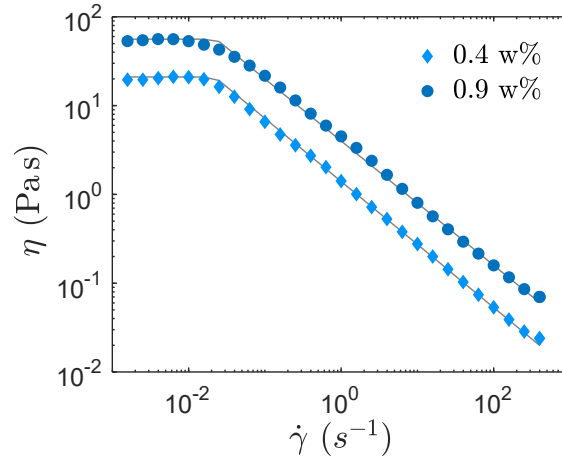


Fig. 3.2 – Viscosity as a function of the shear rate $\dot{\gamma}$ for xanthan gel at 0.4 w% and 0.9 w%.

written:

$$\eta = \begin{cases} \eta_0 & \text{for } \dot{\gamma} < \dot{\gamma}_c \\ k\dot{\gamma}^{n-1} & \text{for } \dot{\gamma} > \dot{\gamma}_c \end{cases} \quad (3.1)$$

with η_0 , k and n constants whose values were determined by least square fitting. They are given in Table 3.1.

Table 3.1 Rheological properties of xanthan gels.

	0.4%	0.9%
η_0 (Pa s)	21	56
k (Pa s ⁿ)	1.5	4.0
n	0.29	0.30

Surface tension

The surface tension of xanthan varies with polymer concentration. Various values are reported in the literature, ranging from 42 to 74 mN.m⁻¹ for concentrations between 0.1 and 1 wt% [104, 105]. Since the values have not been reported specifically for 0.9 and 0.4 w% we measured them by the drop weighing technique using Tate's law and obtained $\gamma = 54.5 \pm 4$ mN.m⁻¹ at 0.9 w% and $\gamma = 60 \pm 4$ mN.m⁻¹ at 0.4 w%. These values are in good agreement with those described in the literature: they show a decrease of surface tension with concentration and they fall within the range reported by Prud'Homme & Long who measured $\gamma = 42.3$ mN.m⁻¹ at 1 w% concentration and $\gamma = 70.7$ mN.m⁻¹ at 0.1 w% concentration [104].

Dynamic contact angles

The dynamic contact angles at the back of the fluid reservoir, between the fluid and the blade (δ_b), and between the fluid and the substrate (δ_s) were measured during the spreading experiments of the two xanthan solutions at $V = 5$ and 10 mm/s. Although they appear to vary slightly with the velocity and the concentration, these variations are comprised within the error of measurement and no distinction was made between these different situations: in practice, we considered $\delta_b = 16 \pm 10^\circ$ and $\delta_s = 115 \pm 10^\circ$ for xanthan solutions.

3.1.2 Spreading dynamics

The same type of spreading experiment, as described in Chapter 2, was performed, except that this time the fluid spread is a shear-thinning fluid instead of a Newtonian fluid. To avoid slippage and dewetting, the surfaces of the blade and substrate were sandblasted to achieve a roughness of approximately 5 to $10 \mu\text{m}$. A typical film thickness profile obtained for xanthan at 0.9 w% and $V = 10$ mm/s is shown in Figure 3.3. This profile appears at first glance to be similar to that of silicone: after an initial increase (until $t = 2$ s), the thickness decreases continuously with time as the reservoir empties. Again, only the data corresponding to the decreasing phase, here $t > 2$ s, are studied in the following.

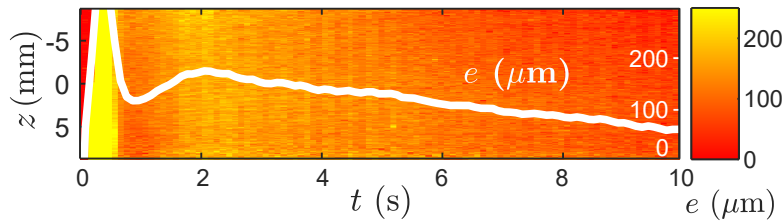


Fig. 3.3 – Map of thickness of the central part of the film for 0.9% xanthan during spreading at $V = 10$ mm/s, as a function of the lateral distance z and time t . The color code ranges from red for $e \simeq 0$ up to yellow for $e = 250 \mu\text{m}$. The first peak is an artifact and is not taken into consideration. The white line shows the thickness $e(t)$ averaged over the width of the film, as a function of time.

In Figure 3.4a, the mean thickness e is plotted as a function of time t , for three initial xanthan gel volumes $\Omega_0 = 0.30 \pm 0.03$ mL (triangles), 0.58 ± 0.02 mL (squares) and 1.01 ± 0.1 mL (stars). Two effects are evidenced: first, e increases with Ω_0 , typically by a factor 2 when Ω_0 is multiplied by 3. In addition, and more importantly, e also decreases during the course of an experiment: for $\Omega_0 = 0.30$ mL, e diminishes from $100 \mu\text{m}$ to $20 \mu\text{m}$ at the end of the 10 s long blade movement. Both effects are a consequence of the finite size of the reservoir, as discussed previously in Chapter 2. Indeed, and as shown in Figure 3.4b (blue points), all the curves for varying initial liquid volumes almost perfectly overlap when plotted as a function of the wetting length $l_w(t)$, measured at the same time. Figure 3.4b also evidences a strong correlation between the film thickness and the polymer concentration: for example, for $l_w = 15$ mm the film thickness varies by a factor 2.6 between the 0.4% xanthan solution and the 0.9% solution (with e increasing from $60 \pm 12 \mu\text{m}$ to $155 \pm 24 \mu\text{m}$). In the case of Newtonian fluids, these variations are directly related to the fluid viscosity η since $e \sim \sqrt{\eta}$. In the case of shear-thinning fluids,

the viscosity is no longer constant as a function of the shear rate. A new expression of the thickness, as a function of the different spreading and rheological parameters, is needed to describe the experimental results.

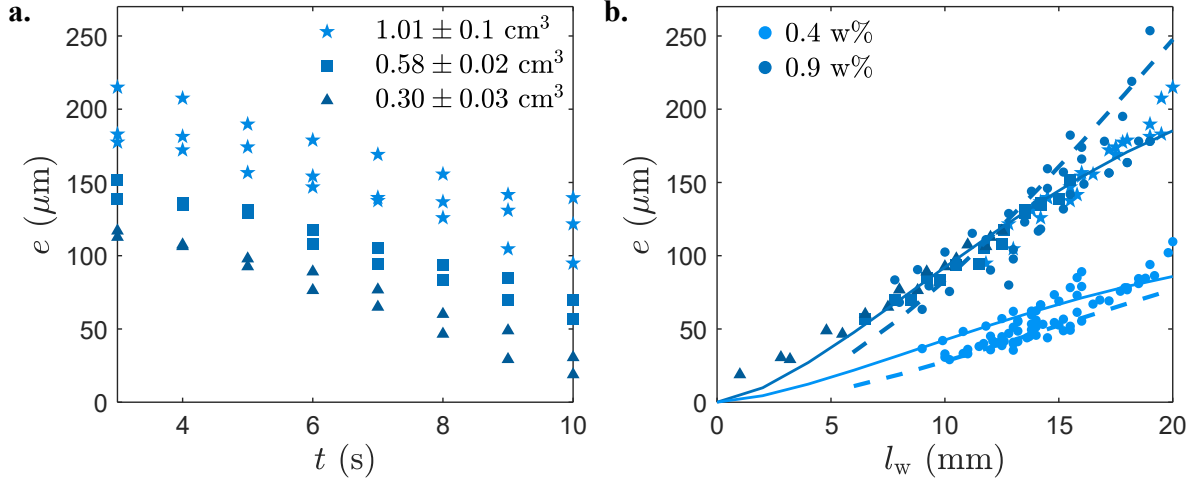


Fig. 3.4 – **a.** Profile of the fluid mean thickness e as a function of time t and initial volume Ω_0 for a 0.9 % xanthan gum solution ($V = 10 \text{ mm/s}$). The symbols correspond to different initial liquid volumes $\Omega_0 = 0.3 \pm 0.03 \text{ mL}$ (triangles), $\Omega_0 = 0.58 \pm 0.02 \text{ mL}$ (squares) and $\Omega_0 = 1.01 \pm 0.1 \text{ mL}$ (stars). **b.** Evolution of the fluid thickness e with the wetting length l_w for two concentrations: 0.9% in dark blue and 0.4% in light blue. The data used for xanthan 0.9 w% in **b.** combine those from **a** and those from experiments corresponding to other $\Omega_0 \in [0.27, 1.34]$ (circles). The solid lines show the scaling law (Eq. 3.7) with prefactor 0.06 for both concentrations. The dashed lines are obtained from numerical calculations. The parameters are $V = 10 \text{ mm/s}$, $B = 1.0 \text{ mN.m}$ and $L = 5.7 \text{ cm}$.

3.2 A generalized scaling law to predict the film thickness

3.2.1 Elasto-hydrodynamic competition for shear-thinning fluids

Our objective is to propose a scaling law to describe the spreading dynamics of a shear-thinning fluid. The principle is the same as in the case of a Newtonian fluid (balance between elastic and viscous torque) except that the model must take into account the variable viscosity of the shear-thinning fluid. As mentioned earlier, we consider the flow beneath the blade to be a simple shear flow. The Reynolds number $Re = \rho e V / \eta$ is smaller than 10^{-1} for xanthan (denoting $\rho \simeq 10^3 \text{ kg/m}^3$ the fluid density and $\eta > 10^{-2} \text{ Pa s}$ the fluid viscosity). As for the silicone oil, the liquid is highly confined under the blade: $l_w \gg e$ and the tip of the blade is almost parallel to the substrate, the conditions are fulfilled to make the lubrication approximation.

Tensorial approach

Since the viscosity is not constant, it is not possible to directly use the expression of the Navier Stokes equation used in Chapter 2 (directly written for a Newtonian fluid) to express the lubricating pressure. In this paragraph, we use a tensorial approach to obtain the general hydrodynamic equations of a fluid. The Cauchy momentum equation that describes the momentum transport in any continuum is:

$$\frac{D\mathbf{v}}{Dt} = \frac{1}{\rho} \nabla \cdot \boldsymbol{\sigma} + \mathbf{f} \quad (3.2)$$

with \mathbf{v} the flow velocity vector field, $\frac{D\mathbf{v}}{Dt}$ the material derivative of \mathbf{v} which is equal to $\frac{D\mathbf{v}}{Dt} = \frac{\partial \mathbf{v}}{\partial t} + \mathbf{v} \cdot \nabla \mathbf{v}$, $\boldsymbol{\sigma}$ the stress tensor and \mathbf{f} the body forces per unit mass. In our experiment, gravity is neglected (\mathbf{f} equals zero), the regime is considered stationary ($\frac{\partial \mathbf{v}}{\partial t} = 0$) and the lubrication approximation is made ($\mathbf{v} \cdot \nabla \mathbf{v} = 0$).

The Cauchy equation reduces to:

$$\nabla \cdot \boldsymbol{\sigma} = 0 \quad (3.3)$$

The stress tensor is $\boldsymbol{\sigma} = -p\mathbf{I} + \boldsymbol{\tau}$ denoting p the hydrodynamic pressure within the fluid, \mathbf{I} the identity matrix and $\boldsymbol{\tau}$ the deviator of the stress tensor. The normal stresses appear in the diagonal components of the deviator tensor: the first normal stress difference N_1 is defined as $N_1 = \tau_{xx} - \tau_{yy}$ and the second normal stress difference N_2 is equal to $\tau_{yy} - \tau_{zz}$. In addition, the trace of the deviator is equal to zero, $\tau_{xx} + \tau_{yy} + \tau_{zz} = 0$. By combining these elements, the stress tensor $\boldsymbol{\sigma}$ writes:

$$\boldsymbol{\sigma} = \begin{pmatrix} -p + \tau_{xx} & \tau_{xy} & \tau_{xz} \\ \tau_{yx} & -p + \tau_{yy} & \tau_{yz} \\ \tau_{zx} & \tau_{zy} & -p + \tau_{zz} \end{pmatrix} = \begin{pmatrix} -p + \frac{2N_1 + N_2}{3} & \tau_{xy} & \tau_{xz} \\ \tau_{yx} & -p + \frac{-N_1 + N_2}{3} & \tau_{yz} \\ \tau_{zx} & \tau_{zy} & -p + \frac{-N_1 - 2N_2}{3} \end{pmatrix} \quad (3.4)$$

Replacing this expression of $\boldsymbol{\sigma}$ (Eq. 3.4) in Cauchy equation (Eq. 3.3) gives for the projection on the x -axis:

$$-\frac{\partial p}{\partial x} + \frac{\partial}{\partial x} \left(\frac{2}{3}N_1 + \frac{N_2}{3} \right) + \frac{\partial \tau_{xy}}{\partial y} + \frac{\partial \tau_{xz}}{\partial z} = 0 \quad (3.5)$$

The first and second normal stress differences are negligible for a simple shear-thinning fluid. This approximation for the xanthan solutions is discussed and validated in Chapter 4. Moreover the problem is considered invariant along the z -axis, so $\frac{\partial \tau_{xz}}{\partial z} = 0$. The Navier-Stokes equation thus reduces to a simple steady-state Stokes equation, which is written:

$$\frac{\partial p}{\partial x} = \frac{\partial \tau_{xy}}{\partial y} \quad (3.6)$$

with τ_{xy} the shear stress under the blade. We place ourselves in the case of a pure shear-thinning fluid (no Newtonian plateau or yield stress at low $\dot{\gamma}$), thus $\tau_{xy} = \eta(\dot{\gamma})\dot{\gamma} = k\dot{\gamma}^n$.

Using the Equation 3.6, the pressure (responsible for the lifting of the blade) therefore scales as $p \sim \tau_{xy} \frac{l_w}{e} \sim k \left(\frac{V}{e}\right)^n \frac{l_w}{e}$. We recall the Newtonian case: $p \sim \frac{\eta_{\text{newt}} V l_w}{e^2}$ for ease of comparison. Following the same reasoning as in the previous chapter, the correspond viscous torque is: $\Gamma_{\text{wet}} \sim k \left(\frac{V}{e}\right)^n \frac{l_w^2 b}{e} (L - l_w)$. This torque is compensated by the rigidity of the blade. The expression of the elastic torque is unchanged: $\Gamma_{\text{dry}} \sim \frac{E^* I}{L - l_w}$. The equilibrium of the two torques sets the film thickness for the shear-thinning fluids:

$$e \sim \left(l_w \left(1 - \frac{l_w}{L} \right) \sqrt{\frac{k V^n L^2 b}{E^* I}} \right)^{2/(n+1)} \quad (3.7)$$

If $n = 1$, we obtain the Newtonian case: the viscosity is independent of the shear rate ($\eta = k$) and this equation becomes identical to the one derived in Chapter 2 (Eq. 2.4).

3.2.2 Comparison with experimental data

Figure 3.4b displays a comparison between Equation 3.7, in continuous line, and the experimental data using n and k values from Table 3.1. A prefactor of 0.06 was used for all concentrations. One can note that this prefactor is close to the prefactor used for silicone oils (0.17 in Fig. 2.10) at the power $2/(n+1)$. This could however be only a coincidence. The scaling law fits well with the data: it reproduces in particular the dependency of e with l_w and the relative variations of e with the rheology of the fluids.

Discrepancies at large volume of reservoir

A sharp increase in thickness for the experimental data is observed for large reservoir sizes, typically here for $l_w > 15$ mm. One can refer to section 2.4.2 which describes the potential sources of discrepancies between the experimental data and the scaling law. In the case of xanthan, the capillary pressure and the torque coming from the meniscus are still negligible compared to the viscous pressure and viscous torque :

$$\frac{p_{\text{capi}}}{p} \sim \frac{\gamma e^{n+1}}{k V^n l_w R} < 10^{-1} \quad \text{and} \quad \frac{\Gamma_{\text{capi}}}{\Gamma_{\text{wet}}} \sim \frac{\gamma e^{n+1}}{k V^n l_w^2} < 10^{-2}$$

However, the difference between the viscous and capillary terms is smaller than before, suggesting an increased effect of capillarity.

The choice of the matching point used in the torque equilibrium calculation may also be responsible for these discrepancies. With xanthan, larger volumes of liquid can be spread because it is more viscous and less wetting than the silicone oils used in the previous chapter. As discussed previously, taking $L - l_w$ as a lever arm no longer makes sense when $l_w \geq 28$ mm ($\geq L/2$) and can be questioned below

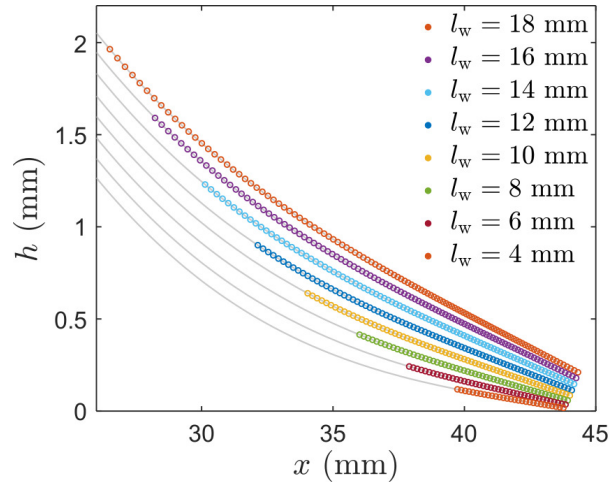


Fig. 3.5 – Shape of the blade $h = f(x)$ (gray line) obtained by numerical calculations for wetting length ranging for 4 to 18 mm. The liquid spread is xanthan at 0.9 w% at $V = 10$ mm/s. The wet portion of the blade is highlighted by the color markers. The angles between the blade tip and the horizontal range from 1.4 to 5.4° .

that. In Figure 3.5, the shape of the blade $h(x)$, obtained numerically, can be considered linear in the wetted region for small volumes of fluid only. As the volume increases, the blade becomes curved in the liquid part (e.g. $l_w = 16$ and 18 mm) which challenges the choice of the matching point for large volumes. The angle between the tip of the blade and the substrate also increases with l_w but remains quite small, for $l_w = 18$ mm the angle is only 5° , the small angle approximation still holds. The lubrication approximation also relies on the fact that $Re \ll \frac{l_w}{e}$. This condition is still valid.

3.3 Numerical solution of the elasto-hydrodynamic equations adapted to the shear-thinning fluids

To extend our numerical calculation to the case of shear-thinning fluids, the equations and the resolution method must be adapted from the Newtonian case, even if the general idea remains the same. We present in this section the modifications resulting from the adaptation of the calculation to the case of shear-thinning fluids.

As done previously for Newtonian fluids, we first present two sets of equations describing: *i*) the interaction of the blade with the hydrodynamic forces arising from the fluid sheared beneath it (Equations 2.15, 3.21, 3.23, 3.24 and 3.25), and *ii*) the free film after the tip of the blade (Equations 3.30 and 3.32). Then, we detail the numerical resolution method, and the peculiarities of the convergence criteria in the case of a shear-thinning fluid.

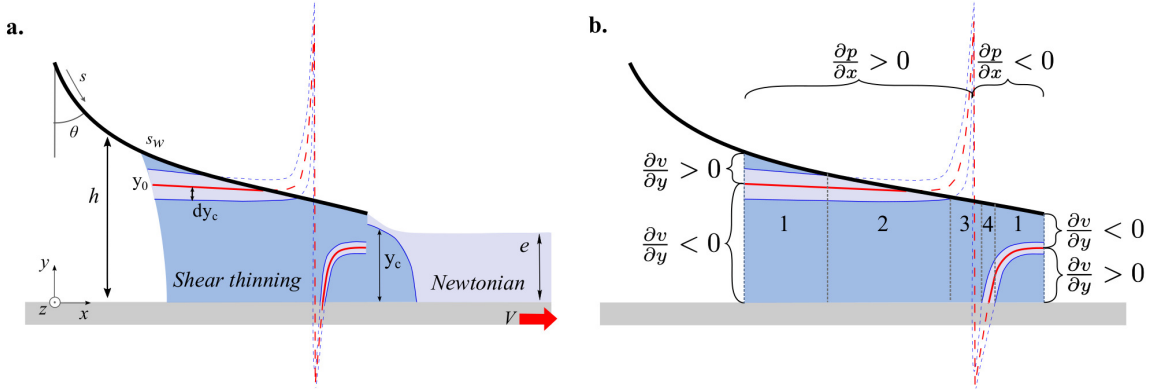


Fig. 3.6 **a.** Schematic representation of Newtonian and shear-thinning areas in the liquid. The notations and conventions used are the same than in Chapter 2 (Fig. 2.11). **b.** Representation of the different zones considered separately to write the equations of the shear rate and velocity. The order (and presence) of the Newtonian and shear-thinning areas differs between these zones. The signs of $\frac{\partial p}{\partial x}$ and $\frac{\partial v}{\partial y}$ also change depending on the position under the blade. More details can be found in Appendix E.

3.3.1 Under-blade-area equations

The dependency of viscosity on shear rate implies a different set of equations to describe the fluid contribution (the lubrication pressure and the viscous drag force). The capillary forces keep the same expression as in the Newtonian case (Eq. 2.15) and are not presented here.

Calculation of the pressure and stresses

Fluid pressure

The same approximations as described for the establishment of the scaling law in section 3.2.1 are made, leading to the simple Stokes equation:

$$\frac{\partial \tau}{\partial y} = \frac{\partial p}{\partial x} \quad (3.8)$$

we use here the notation $\tau = \tau_{xy}$ for simplicity.

The shear-thinning fluid is modeled as in the Equation 3.1. Depending on the local shear rate in the flow, the fluid behaves as a Newtonian fluid (when $|\dot{\gamma}| < \dot{\gamma}_c$) or as a power-law fluid (when $|\dot{\gamma}| > \dot{\gamma}_c$). Thus we can express the shear stress τ as:

$$\tau = \begin{cases} \eta_0 \dot{\gamma} & \text{for } |\dot{\gamma}| < \dot{\gamma}_c \\ k |\dot{\gamma}|^{n-1} \dot{\gamma} & \text{for } |\dot{\gamma}| > \dot{\gamma}_c \end{cases} \quad (3.9)$$

Note: τ can also be written more compactly in the shear-thinning zone, $\tau = k \langle \dot{\gamma} \rangle^n$ using the notation $\langle x \rangle^a = \text{sgn}(x) |x|^a$.

Contrary to the scaling law, the Newtonian plateau is taken into account. Concretely, we expect to have different areas under the blade corresponding to either a Newtonian fluid or a shear-thinning fluid. The Figure 3.6 gives a schematic representation of a classical situation encountered in our calculations. In addition, we must take into account that $\dot{\gamma}$ and the pressure gradient can be negative in some parts of the fluid, and that the power-law index n is inferior to 1. In order to avoid errors in numerical calculations, it is therefore mandatory to carefully control the power manipulations and identify the sign of the calculated quantities.

To determine the fluid equations, we define y_0 such that $\tau(y_0) = 0$, it marks the separation between the positive and negative shear rate. The vertical asymptote observed in the y_0 curve (red line) corresponds to the position of the maximum fluid pressure which, from Eq. 3.8, implies a constant shear stress along y . Integrating Equation 3.8 over y gives, since under the lubrication approximation $\frac{\partial p}{\partial x}$ does not depend on y :

$$\tau = \frac{\partial p}{\partial x}(y - y_0) \quad (3.10)$$

To calculate the pressure in the reservoir, we consider the continuity of the shear rates at the limit between the shear-thinning and Newtonian regions. The Newtonian region is symmetrical around y_0 as expected from the Stokes equation when $\frac{\partial p}{\partial x}$ does not depend on y . We can therefore define dy_c the half width of the area where the shear rate is less than $\dot{\gamma}_c$ and the shear stress is expressed as Newtonian (Fig. 3.6a). The shear rates are calculated in both regions by combining Equations 3.9 and 3.8, and the continuity of $\dot{\gamma}$ at $y = y_0 \pm dy_c$ writes:

$$\frac{\partial p}{\partial x} \frac{dy_c}{\eta_0} = \left\langle \frac{\partial p}{\partial x} \frac{dy_c}{k} \right\rangle^{1/n}. \quad (3.11)$$

Rewriting this equation gives an expression for the pressure gradient, but the sign still needs to be determined:

$$\left| \frac{\partial p}{\partial x} \right| = \frac{1}{dy_c} \frac{\eta_0^{\frac{n}{n-1}}}{k^{\frac{1}{n-1}}} \quad (3.12)$$

In this equation there are two unknowns: the value of dy_c and the sign of $\frac{\partial p}{\partial x}$. To access those, we use Eq. 3.9 and combine it with Eq. 3.10. The shear rate ($\dot{\gamma} = \frac{\partial v}{\partial y}$) is then integrated over y with no-slip boundary conditions at the moving plate ($v(0) = V$) and at the blade ($v(h) = 0$). At the position $y = y_0 \pm dy_c$ we use the continuity of the velocity. We distinguish four zones based on the presence and position of the Newtonian region (Fig. 3.6b). For each of them, a set of equations describing the velocity in the different parts of the fluid is written and the flow rate q is calculated by integrating v over y . The presentation of the different zones and some detailed equations of the velocity can be found in Appendix E. A general

equation for the flow rate is obtained:

$$q = Vy_0 - \frac{1}{3\eta_0} \frac{\partial p}{\partial x} \left(\operatorname{sgn}(y_0) \min(|y_0|, dy_c)^3 + \operatorname{sgn}(h - y_0) \min(|h - y_0|, dy_c)^3 \right) + \left\langle \frac{1}{k} \frac{\partial p}{\partial x} \right\rangle^{1/n} \left(\frac{-\langle y_0 \rangle^{1/n+2} - \langle h - y_0 \rangle^{1/n+2} + \operatorname{sgn}(y_0) \min(|y_0|, dy_c)^{1/n+2} + \operatorname{sgn}(h - y_0) \min(|h - y_0|, dy_c)^{1/n+2}}{1/n + 2} \right) \quad (3.13)$$

A close analysis of Eq. 3.13 shows that the sign of $\frac{\partial p}{\partial x}$ is the same as that of $Vy_0 - q$ which gives, from Eq. 3.12 :

$$\frac{\partial p}{\partial x} = \operatorname{sgn}(Vy_0 - q) \frac{1}{dy_c} \frac{\eta_0^{\frac{n}{n-1}}}{k^{\frac{1}{n-1}}} \quad (3.14)$$

By writing the condition of velocity continuity at y_0 we obtain another equation:

$$0 = V - \frac{1}{2\eta_0} \frac{\partial p}{\partial x} \left(\min(|y_0|, dy_c)^2 - \min(|h - y_0|, dy_c)^2 \right) - \left\langle \frac{1}{k} \frac{\partial p}{\partial x} \right\rangle^{1/n} \left(\frac{\max(|y_0|, dy_c)^{1/n+1} - \max(|h - y_0|, dy_c)^{1/n+1}}{1/n + 1} \right) \quad (3.15)$$

By injecting Eq. 3.14 into Eq. 3.13 and 3.15 we obtain two equations that are used to calculate y_0 and dy_c for a given flow rate, q , and blade local height, $h(x)$. Note that in some zones these values are not defined within the fluid but they can still be evaluated and they are represented by dashed lines in Figure 3.6. It is now possible to calculate the fluid pressure: the derivative along the curvilinear abscissa, obtained using the relation $\frac{\partial p}{\partial s} = \frac{\partial p}{\partial x} \sin \theta$, is integrated between s_w and s :

$$p(s) = \int_{s_w}^s \frac{\partial p}{\partial x} \sin \theta \, ds + p_{sw} = \int_{s_w}^s \operatorname{sgn}(Vy_0 - q) \frac{1}{dy_c} \frac{\eta_0^{\frac{n}{n-1}}}{k^{\frac{1}{n-1}}} \sin \theta(s') \, ds' + p_{sw}, \quad (3.16)$$

p_{sw} is evaluated in the same way as in the Newtonian case (using Eq. 2.11). In contrast, it is not possible to use the value of the pressure at the position $s = L$ to obtain an explicit equation of the flow rate $q = f(h, \theta, p_L, p_{sc}, V, b, s_w)$ as done with Newtonian fluids. Here, the problem is highly non linear, so we use solvers to find a value of q , y_0 and dy_c . Once injected in Eq. 3.16 for $s = L$, it gives a pressure at the blade tip which should, after convergence, be approximately equal to its guess value p_L (see below *Convergence criteria* in 3.3.4). This value of the guess is determined by considering the pressure at $x = +\infty$ fixed to P_{atm} so $p(x = +\infty) = 0$, and using this condition to solve the shape of the liquid surface after the blade (see section *Free surface equations* 3.3.3).

Viscous stress

The viscous stress f_v , exerted by the fluid on the blade, is defined as:

$$f_v = -\tau(h) = -\frac{\partial p}{\partial x}(h - y_0) \quad (3.17)$$

which writes, using equation 3.14, f_v :

$$f_v = -\text{sgn}(Vy_0 - q) \frac{1}{dy_c} \frac{\eta_0^{\frac{n}{n-1}}}{k^{\frac{1}{n-1}}}(h - y_0) \quad (3.18)$$

Simplification : pure shear-thinning fluid under the blade

We observed numerically that taking into account the Newtonian zone under the blade has a very limited impact on the results: the pressure profile only differs by less than $10^{-3}\%$ between a simple power-law fluid and the fluid described by Equation 3.1 (with a Newtonian viscosity plateau at low shear). We therefore used the assumption of pure shear-thinning behavior under the blade to speed up the computation. With this simplification, Equation 3.13 becomes:

$$q = Vy_0 - \left\langle \frac{1}{k} \frac{\partial P}{\partial x} \right\rangle^{1/n} \left[\frac{\langle y_0 \rangle^{1/n+2} + \langle h - y_0 \rangle^{1/n+2}}{1/n + 2} \right] \quad (3.19)$$

The velocity continuity at y_0 gives :

$$V(1/n + 1) = \left\langle \frac{1}{k} \frac{\partial P}{\partial x} \right\rangle^{1/n} \left(|y_0|^{1/n+1} - |h - y_0|^{1/n+1} \right) \quad (3.20)$$

By combining Eq. 3.20 and 3.19 we obtain a new equation of the flow rate that depends only on y_0 and h :

$$q = V \left[y_0 - \frac{1/n + 1}{1/n + 2} \left(\frac{\langle y_0 \rangle^{1/n+2} + \langle h - y_0 \rangle^{1/n+2}}{|y_0|^{1/n+1} - |h - y_0|^{1/n+1}} \right) \right] \quad (3.21)$$

We can express the pressure derivative from Eq. 3.19 :

$$\frac{\partial P}{\partial x} = k \left\langle \frac{(Vy_0 - q)(1/n + 2)}{\langle y_0 \rangle^{1/n+2} + \langle h - y_0 \rangle^{1/n+2}} \right\rangle^n \quad (3.22)$$

$$p(s) = \int_{s_w}^s k \left\langle \frac{(Vy_0 - q)(1/n + 2)}{\langle y_0 \rangle^{1/n+2} + \langle h - y_0 \rangle^{1/n+2}} \right\rangle^n \sin \theta ds + p_{sw} \quad (3.23)$$

The viscous stress f_v becomes:

$$f_v = -k \left\langle \frac{(Vy_0 - q)(1/n + 2)}{\langle y_0 \rangle^{1/n+2} + \langle h - y_0 \rangle^{1/n+2}} \right\rangle^n (h - y_0) \quad (3.24)$$

3.3.2 Torque balance

The equation describing the torque balance (Eq. 2.19) is recalled here:

$$\frac{d^2\theta}{ds^2} = \frac{b}{E^*I} \int_s^L [-p \cos(\theta(s) - \theta(s')) + f_v \sin(\theta(s) - \theta(s'))] ds' + F_c [\sin(\theta(s) - \theta_{mL}) + \sin(\theta(s) - \theta_{msw})] \quad (3.25)$$

It depends on the pressure and viscous stress exerted by the fluid beneath. Hence, p and f_v must be replaced by their new expressions describing the shear-thinning fluid influence (Eq. 3.23 and 3.24 respectively). One should refer to section 2.5.1 paragraph *Torque balance* for more details on this matter.

3.3.3 Free surface equations

In a second part, we define a second set of equations to calculate the thickness, shape and flow in the free liquid film downstream of the tip of the blade. The analyzed area, about 0.8 cm long, was a little longer than with Newtonian fluids.

The lubrication equation (Eq. 3.8) is integrated with the boundary condition $\tau(0) = 0$ on the free surface at local height h_l (no tangential stress), which gives:

$$\tau = \frac{\partial p}{\partial x} (y - h_l) \quad (3.26)$$

Again, we have to consider separately two regions, in which the fluid behaves either as a Newtonian fluid (at low shear rate), or as a power-law liquid (at high shear rate). We define the boundary height between these two regions y_c . Since most of the liquid in the free film is at rest ($\dot{\gamma}$ is rapidly vanishing), it is particularly important to take into account the Newtonian plateau in the rheological law, contrary to what is done under the blade.

The shear rate equality at y_c gives an expression for the derivative of p :

$$\frac{\partial p}{\partial x} = \text{sgn} \left(\frac{\partial p}{\partial x} \right) \frac{1}{h_l - y_c} \frac{\eta_0^{\frac{n}{n-1}}}{k^{\frac{1}{n-1}}} \quad (3.27)$$

To determine y_c , the no-slip boundary condition on the substrate ($v(y=0) = V$) and the velocity continuity at y_c are used to obtain the expressions of the velocity in both regions. The integration gives the flow rate:

$$q_l = Vh_l - \frac{1}{3\eta_0} \frac{\partial p}{\partial x} (h_l - y_c)^3 + \left\langle \frac{1}{k} \frac{\partial p}{\partial x} \right\rangle^{1/n} \frac{(h_l - y_c)^{1/n+2} - h_l^{1/n+2}}{1/n + 2} \quad (3.28)$$

From this equation it can be shown that the sign of $\frac{\partial p}{\partial x}$ is equivalent to the sign of $Vh_l - q_l$. This results leads to a new expression for the pressure derivative from Eq. 3.27:

$$\frac{\partial p}{\partial x} = \text{sgn}(Vh_l - q_l) \frac{1}{h_l - y_c} \frac{\eta_0^{\frac{n}{n-1}}}{k^{\frac{1}{n-1}}} \quad (3.29)$$

The equation describing the flow rate (Eq.3.28) can be rewritten as a function of only the variables h_l and y_c by using Eq. 3.29:

$$q_l = Vh_l - \text{sgn}(Vh_l - q_l) \left(\frac{\eta_0}{k} \right)^{\frac{1}{n-1}} \left(\frac{1}{3}(h_l - y_c)^2 + \frac{1}{(h_l - y_c)^{1/n}} \frac{(h_l - y_c)^{1/n+2} - h_l^{1/n+2}}{(1/n + 2)} \right) \quad (3.30)$$

Since the liquid is incompressible, the flow rate q_l is equal to the flow rate q below the blade. Thus, we use in the numerical resolution of the equations that at $x = \infty$, $q_l = Vh_l(\infty) = Ve$.

The pressure p in the liquid at the end of the blade is set by the Laplace pressure within the meniscus, which gives a second expression for p :

$$p = -\gamma \frac{d\theta}{ds} \quad (3.31)$$

By combining equations 3.31 and 3.29, and using the relation between the derivatives with respect to s and x , we finally obtain:

$$\frac{d^2\theta}{ds^2} + \text{sgn}(Vh_l - q_l) \frac{1}{h_l - y_c} \frac{\eta_0^{\frac{n}{n-1}}}{\gamma k^{\frac{1}{n-1}}} \sin(\theta) = 0 \quad (3.32)$$

This equation governs the shape of the free surface of the deposited layer of fluid behind the blade. To accelerate the convergence, Eq. 3.32 is used when $y_c \in [0, h_l]$ and the equation for pure Newtonian fluid (Eq. 2.23) when $y_c \leq 0$.

3.3.4 Numerical method

The numerical method used to solve the two sets of equations governing the blade shape (Eq. 3.25) and the shape of the fluid free surface (Eq. 3.32 and 2.23) is the same as in the previous Chapter. It is based on an analogy with the heat equation; details can be found in section 2.5.1.

The resolution method and the coupling of the blade and free surface equations are similar to those for Newtonian fluids. The differences include in particular the choice of the initial guess for $\theta(s, t_v = 0)$ and $\theta_l(s, t_v = 0)$. The initial shape of the blade is obtained by a rough calculation for a Newtonian fluid using the numerical calculation presented in the previous chapter but without taking into account the free surface (the value of p_L corresponds to the initial guess). The viscosity of this Newtonian fluid is $\eta = 480$ mPa s and, to facilitate the following calculations, it has the same wetting properties (surface tension and contact angles) as the shear-thinning fluid that is studied next. The shape of the free surface

is initially modeled with the help of a hyperbolic tangent (to reproduce the shape of the meniscus). The initial flow rate is obtained by making the assumption of a linear velocity profile at the output of the blade ($q_{\text{init}} = V * h(L, t_v = 0) / 2$). It is used to compute $y_0(s, t_v = 0)$ using Eq. 3.21. During the following iterations, q is computed by combining Eq. 3.21, and Eq. 3.23 expressed for $s = L$. For the free surface the general idea is the same, q_l is equal to $Vh_l(\infty, t_v = 0)$ and this value is used to compute $y_c(s, t_v = 0)$ (note that initially q_l is different from q). It is thus possible to calculate the source term and solve the transient heat equation (Eq. 2.25) for both regions.

The spatial discretization of the blade equations is $\Delta s \in [0.1, 0.5]$ mm. The spacing is non-uniform for the free surface calculation: the size of the cell is exponentially increased from the meniscus area to the "end" of the free film, with Δs going from 10^{-5} to 10^{-1} mm.

Convergence criteria

For shear-thinning fluids the equation of the flow rate under the blade (Eq. 3.21) requires an additional convergence criterion than what is needed for a Newtonian fluid. Thus, the convergence of the numerical simulation is achieved when three conditions are simultaneously met:

1. The steady state is reached for the transient heat equation (Eq. 2.25) which provides the solution for the governing equations of the blade shape (Eq. 3.25) and the free surface (Eq. 3.32).
2. The two flow rates, q , calculated from the blade equations (Eq. 3.21), and $q_l = Vh(\infty)$ in the free film, equalize (at 10^{-4}).
3. The pressure at L , calculated through Eq. 3.23, corresponds to the guess value of p_L . This guess value is iteratively adjusted during the computation by a corrective factor proportional to the difference between the two flow rates.

3.3.5 Results of the calculation for the shear rate

In this section, we examine the new shear rate map obtained numerically in the case of a shear-thinning fluid. The shear rate map is expected to strongly differ from what was previously shown in the section 2.5.1 because it is no longer $\frac{\partial \dot{\gamma}}{\partial y}$ which is constant at a given x (Newtonian case) but instead $\frac{\partial \dot{\gamma}^n}{\partial y}$. This result is derived by rewriting the Stokes equation with the definition of τ (Eq. 3.8 and 3.9). In Figure 3.7, the shear rate is represented below the blade, and in the free surface. The spreading velocity is $V = 1$ cm/s and the wetting length is $l_w = 14$ mm. Note that the negative value of the shear rate comes from the fact that it is the substrate and not the blade which is moving. To highlight the differences between these two situations, the case of a Newtonian fluid with viscosity $\eta = 300$ mPa.s (Fig. 3.7b) is presented next to the shear-thinning fluid, a 0.9 w% xanthan solution (Fig. 3.7a). Comparison of Figures 3.7a and b illustrates the effect of shear-thinning on fluid flow. For the shear-thinning fluid, the shear rate varies more rapidly close to the substrate (where the shear stress is maximal) than close to the blade. This observation, again, is consistent with what is expected of a shear-thinning fluid, which viscosity is the lowest where the stress is the highest. For the Newtonian fluid, the shear rate isolines are evenly distributed over y , as observed previously. These flow differences, which might seem incidental at first

glance, have a strong (and counter-intuitive) impact on the spreading which will be further discussed in 3.4.2.

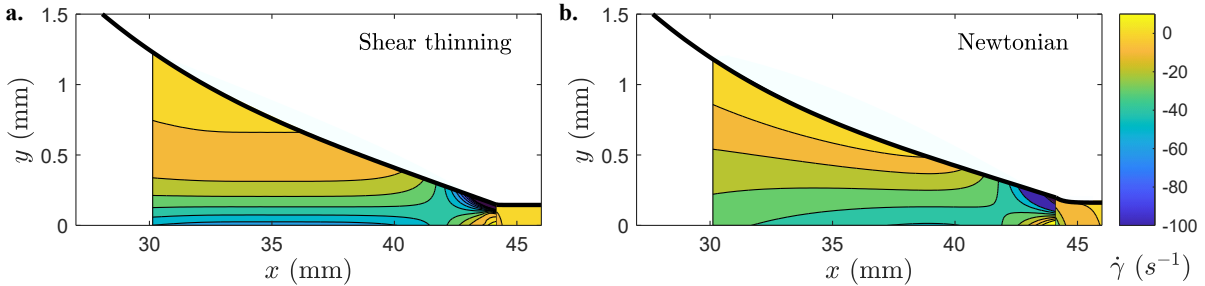


Fig. 3.7 Comparison of the shear rate below the blade **a.** For a shear-thinning fluid (with $\eta_0 = 56 \text{ Pa s}$, $k = 4 \text{ Pa s}^n$, $n = 0.30$), corresponding to a 0.9% xanthan gum solution and **b.** For a Newtonian fluid, with viscosity $\eta = 300 \text{ mPa s}$. The dark lines depict the shape of the blade (for $x < 44 \text{ mm}$) and the free surface. The parameters are $l_w = 1.4 \text{ cm}$ and $V = 1 \text{ cm/s}$.

3.3.6 Comparison with experiments and scale law

The simulation results are shown with dashed lines in Figure 3.4. They match well the experimental data for both xanthan gels (at 0.4 and 0.9 w%) and without any adjustable parameter. This confirms the scaling law and validates the prefactor used. Deviations are observed for high values of l_w (e.g. xanthan at 0.4 w% for $l_w \geq 18 \text{ mm}$) and they will be discussed in the next chapter (see section 4.1.3). We believe that they are due to a poor description of the shape of the back meniscus when l_w is large.

3.4 Comparison of shear-thinning and Newtonian fluids

From an industrial perspective, it is interesting to be able to compare fluids of different kinds to see which one will give better spreading results. The evaluation can be done, for example, on the shape of the fluid film. The fluid that provides the most uniform profile in thickness will be preferred in many industrial applications. The energy required to spread the fluid can also be an evaluation criterion. This can impact the user experience in the case of cosmetics, with a product that may feel more or less easy to spread. At a time when a lot of research is being done to reduce the energy consumption of industrial processes, these comparisons may also be relevant for other application areas (building materials, coating).

To compare the spreading of a shear-thinning and a Newtonian fluid the question that arises is on which ground to compare them. Indeed, by definition, the shear-thinning fluids have a variable viscosity depending on the shear rate. Unlike a fluid sheared between two parallel plates at a constant velocity, a fluid spread in the flexible blade geometry is not subject to a uniform shear rate (Fig. 3.7). This means that if the fluid under consideration is shear-thinning, the viscosity is variable under the blade.

Newtonian fluids by definition have a constant viscosity. The question that arises then is what should be the viscosity of an equivalent Newtonian when comparing these two fluids? Several approaches are possible and are discussed in the following paragraphs.

3.4.1 Choice of the equivalent Newtonian fluid

First case: Zero shear rate viscosity

One possibility is to take the viscosity of the Newtonian fluid to be equal to the zero shear rate viscosity of the shear-thinning fluid [74]. This is equivalent in our case to writing $\mu = \eta_0$ (with μ the notation used in this paragraph to distinguish the Newtonian viscosity). This viscosity is very high: for instance $\eta_0 = 21$ Pa.s for a 0.4 w% xanthan solution and $\eta_0 = 56$ Pa.s at 0.9 w%. In this case, the shear-thinning fluid film is significantly thinner than the Newtonian film, similarly to what was demonstrated in dip-coating experiments by Ashmore *et al.* [74].

Another approach consists in increasing n until $n = 1$. This is equivalent to considering that the viscosity of the Newtonian equivalent corresponds to $\mu = k$, i.e. 4 Pa.s for xanthan solution at 0.9 w%. Even though the viscosity is not as high as the zero shear rate viscosity, it is equal to the viscosity at $\dot{\gamma} = 1 \text{ s}^{-1}$ which still might not be representative of the shear rates experienced by the system. The maps of shear rates under the blade shown in Figure 3.7a show that the experimental values are typically greater in magnitude than 1 s^{-1} . Similar conclusions are obtained: the thickness increases with n by 4.4 times going from $n = 0.3$ to $n = 1$, all other parameters being kept identical to the xanthan at 0.9w% case (Fig. 3.8).

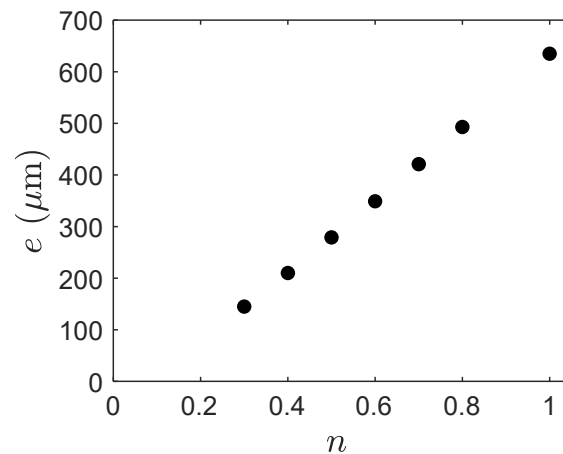


Fig. 3.8 – Thickness as a function of the shear-thinning index n . Results of the numerical calculation for a shear-thinning fluid with $k = 4 \text{ Pa.s}^n$, $V = 10 \text{ mm/s}$ and $l_w = 14 \text{ mm}$. The n value varies from 0.3 to 1 (Newtonian case). The surface tension and contact angles correspond to those of xanthan at 0.9 w%.

However Newtonian fluids (such as silicon oils) with such high viscosities (estimated at $\dot{\gamma} \rightarrow 0$ or $\dot{\gamma} = 1$) are difficult to handle and spread: they do not appear to be a good Newtonian equivalent to

the xanthan gel. The comparisons made between these two situations are not very relevant from an application point of view.

Second case: Viscosity evaluated at a "representative" shear rate

A more natural choice might be to select a Newtonian fluid with a viscosity equal to the viscosity of the shear-thinning fluid at a typical shear rate. This typical shear rate can be chosen in several ways: for example, at the exit of the geometry $\dot{\gamma}^* \sim \frac{V}{h_L}$ [76, 106] or in the coated film $\dot{\gamma}^* \sim \frac{V}{e}$ [73]. The latter choice leads to an equivalence between the scaling law of a Newtonian fluid (Equation 2.4) and a complex fluid (Equation 3.1). However, it is important to note that this coincidence is only pointwise. Contrary to what is observed in dip-coating experiments [73], the film thickness e varies during spreading, so that $\dot{\gamma}^* \simeq \frac{V}{e}$ cannot be uniquely defined. This implies that the viscosity of such a "perfect" Newtonian equivalent changes for each value of e , and thus with the reservoir size l_w . Similarly, it is not possible to define a representative shear rate based on the gap of the geometry defined at the blade tip, h_L , as this value is not fixed but evolves with time with the emptying of the fluid reservoir. For example, with a 0.9% xanthan solution, the scaling laws give viscosities in the range 45 mPa.s to 300 mPa.s (or 150 mPa.s to 380 mPa.s if h_L is used in the shear rate definition instead of e) for l_w varying between 4 and 20 mm. The range of viscosity is quite large and we lack another comparison point to choose one over another and to consider that the chosen viscosity represents the shear-thinning fluid behavior over the entire spreading experiment.

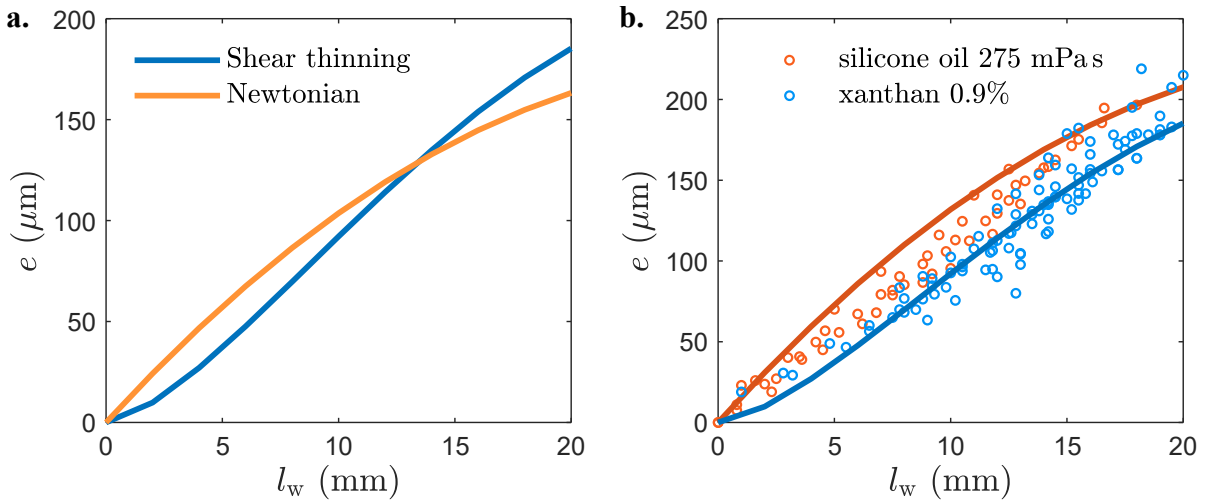


Fig. 3.9 –**a.** Comparison of the scaling laws predicting the film thickness $e(l_w)$ for a Newtonian fluid with viscosity $\eta = 170$ mPa.s (Eq. 2.4) and a shear-thinning fluid, a 0.9% xanthan solution (Eq. 3.7) with a prefactor of 0.17 and 0.06 respectively. **b.** Comparison of the scaling laws and experimental data for a Newtonian fluid with viscosity $\eta = 275$ mPa.s and the 0.9% xanthan solution.

An example is given in Figure 3.9a which compares the evolution of thickness as a function of wetting length l_w for a shear-thinning fluid and for a Newtonian fluid spread at $V = 1$ cm/s. The viscosity chosen for the Newtonian fluid is estimated for $l_w^* = 12$ mm. The corresponding thickness of the shear-thinning

film is computed numerically: $e = 112 \mu\text{m}$. The typical shear rate under the blade is approximated by $\dot{\gamma}^* \simeq V/e(l_w^*) \simeq 90 \text{ s}^{-1}$ and the corresponding viscosity $\eta = 170 \text{ mPa s}$ is obtained from the rheological curves (Fig. 3.2). We observe that the deposition curves coincide only at one point. The rest of the time, a deviation (of less than 20%) is seen between the two curves. Another example is presented in Figure 3.9b, this time the viscosity of the Newtonian fluid was chosen equal to 275 mPa.s, which is close to the value obtained by estimating the viscosity for $l_w^* = 18 \text{ mm}$. There is no crossing between the two curves and $e = f(l_w)$ is always higher for the Newtonian fluid. The experimental data confirm this difference in the deposition law.

With this approach, the choice of the viscosity for the Newtonian fluid remains arbitrary and depends on the wetting length chosen as representative. Another important drawback of the scaling law is to estimate that the shear rate within the fluid is uniform, which might lead to neglecting some effects of the shear-thinning property.

Third case: Viscosity defined to get the same volume spread in a given time

This time we consider the definition of the equivalent Newtonian from a more applicative point of view, assuming that in the industry, if someone were to compare the spreading of two types of fluids for a given application he might initially formulate them in such a way that they give comparable spreads. We will not choose the Newtonian fluid whose viscosity corresponds to that of the shear-thinning fluid taken at the shear rate most representative of the spread, but rather the one that will give a comparable final deposit (thickness, length, volume, deposition time ...).

We do the following thought experiment: starting from identical initial conditions (ie same l_{wi} and same spreading velocity V), it should take the same time t_d to spread a volume Ω_d of the equivalent Newtonian fluid as of the shear-thinning fluid of interest. Indeed, if the mechanical properties of the blade are known, for a fixed V and l_{wi} , there is a bijective relation between the spreading time and the viscosity of the Newtonian fluid.

Concretely we calculate for a xanthan solution the time t_d necessary to spread a given volume Ω_d starting from a given l_{wi} by integrating the following equation:

$$\Delta t_d|_{e_j \rightarrow e_{j+1}} = \frac{\Delta \Omega_d}{\bar{e}V} = \frac{\int_{x_j}^L h_j dx - \int_{x_{j+1}}^L h_{j+1} dx}{\bar{e}V} \quad (3.33)$$

This equation describes the mass conservation during the emptying of the fluid reservoir from l_{wj} and $l_{w(j+1)}$, with $\int_{x_j}^L h_j dx$ and $\int_{x_{j+1}}^L h_{j+1} dx$ the volumes of liquid under the blade at l_{wj} and $l_{w(j+1)}$ respectively. The difference of volumes is entirely found in the deposited film and can be written $\bar{e}V\Delta t_d|_{e_j \rightarrow e_{j+1}}$ with $\bar{e} = (e_j + e_{j+1})/2$ the averaged deposited thickness and Δt_d the corresponding deposition time. Note that the lowest l_w taken as input of the numerical calculation are typically 4 mm. There is a lack of discretization to finely represent the behavior at the end of the spreading. Instead, the end of the

deposited profile is approximated by a triangular shape: $\Delta t_d|_{e_{l_w=4} \rightarrow 0} = 2 \frac{\int_{l_w=4}^L h_{l_w=4} dx}{e_{l_w=4} V}$. In Figures 3.10 and 3.12 the dotted lines at the end of each curves are used to highlights this final part.

We then estimate the viscosity of the Newtonian fluid which has the same spreading characteristics, i.e the same time t_d required to spread the same volume Ω_d at the same velocity and starting from the same l_w . Figure 3.10.a shows the curves $t_d = f(\Omega_d)$ obtained with xanthan at 0.9% (continuous blue line) and some Newtonian fluids of viscosity $\eta = 150, 300, 500$ and 1000 mPa.s (dashed lines). The spreading velocity is $V = 10$ mm/s and the initial wetting length is $l_{wi} = 18$ mm. The equivalent Newtonian fluid has a viscosity equal to 300 mPa.s: a volume of $\Omega_d = 0.4$ cm³ is spread in $t = 6$ s for both this fluid and the xanthan solution. More generally, the two curves overlap almost perfectly allowing the 300 mPa.s solution to be considered as a broad Newtonian equivalent to the xanthan for most of the spreading experiment and not just pointwise. This definition of Newtonian equivalent is used in the following sections to compare shear-thinning and Newtonian spreading.

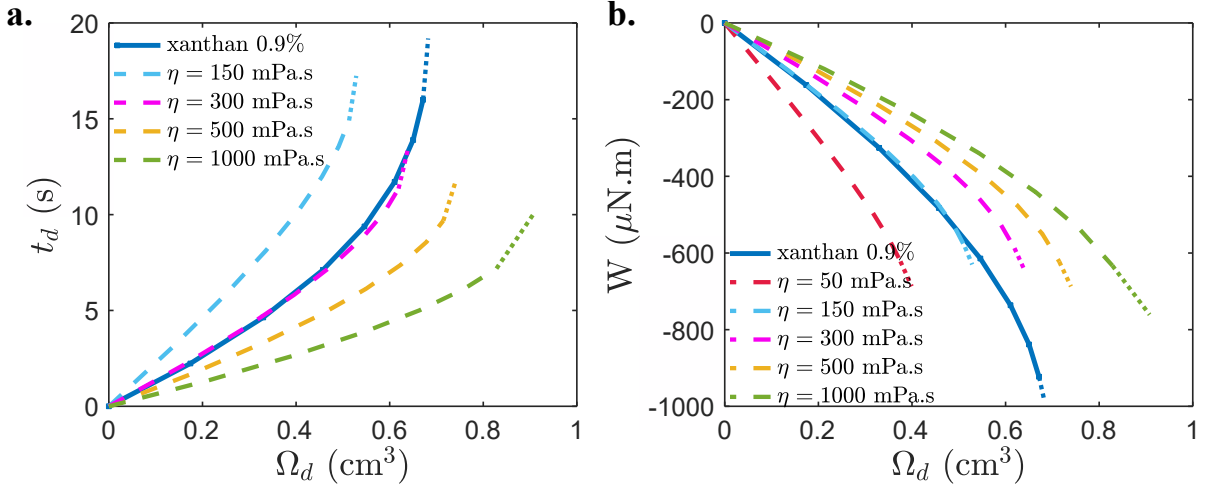


Fig. 3.10 – **a.** Deposition time t_d as a function of the deposited volume Ω_d for xanthan at 0.9% (dark blue) and Newtonian fluids with viscosity from top to bottom: 1000 mPa s (green), 500 mPa s (yellow), 300 mPa s (pink) and 150 mPa s (cyan). Initially $l_{wi} = 18$ mm, and $V = 10$ mm/s. **b.** Mechanical work of the viscous forces during the spreading of volume Ω_d for the fluids of figure 3.10a) and the supplementary case 50 mPa s (red). The xanthan fluid dissipates more energy than the Newtonian fluid with $\eta = 300$ mPa s ($-W$ is 30% higher for $\Omega_d = 0.2$ cm³, 34% for $\Omega_d = 0.4$ cm³ and 26% for $\Omega_d = 0.64$ cm³).

3.4.2 Mechanical work

The mechanical work dissipated by the fluid when emptying the reservoir from l_{wj} to $l_{w(j+1)}$ is defined by:

$$\Delta W = \bar{F} V \Delta t_d \quad (3.34)$$

with $\bar{F} = (F_j + F_{j+1})/2$ the average force. Here we denote F_j the force exerted by the fluid under the blade on the PMMA surface and calculated by integrating the shear stress at the liquid/substrate interface

in the x and z directions, for l_{wj} :

$$F_j = \int_{x_{wj}}^{x_L} \tau(x) b dx \quad (3.35)$$

The force exerted by the liquid under the free surface, and particularly in the meniscus zone, is neglected. By integrating Eq. 3.34 from $l_w = 18$ to $l_w = 0$ mm it is thus possible to access the mechanical work $-W$ needed to spread the fluid present under the blade entirely. Figure 3.10b shows the value of W as a function of the deposited volume for the 0.9 w% xanthane, its Newtonian equivalent ($\eta = 300$ mPa.s), and other Newtonian fluids with $\eta = 50, 150, 500$ and 1000 mPa.s. We observe that the energy required to spread a shear-thinning fluid is typically 30% higher than its Newtonian equivalent according to the "3rd case" definition (e.g. 34% for $\Omega_d = 0.40$ cm³). This is consistent with the comparison of shear stress extracted from the simulations of the shear-thinning fluids (Fig. 3.11a) and the Newtonian fluids (Fig. 3.11b). The stress is distributed more evenly under the blade in the shear-thinning case, which is expected of a Stokes flow since $\frac{\partial \tau}{\partial y}$ is constant at a given x (Eq. 3.8). But more importantly, we also observe that the shear stress at the moving interface (the substrate) is significantly higher in the shear-thinning case. The fact that more energy is needed to spread a shear-thinning fluid than the equivalent Newtonian fluid might seem counter-intuitive: indeed, in industrial applications, the addition of polymer to a product is often seen as a way to make the liquid easier to spread. Here we show that the opposite may be true: shear-thinning fluids resist more to the spreading than the equivalent Newtonian fluid.

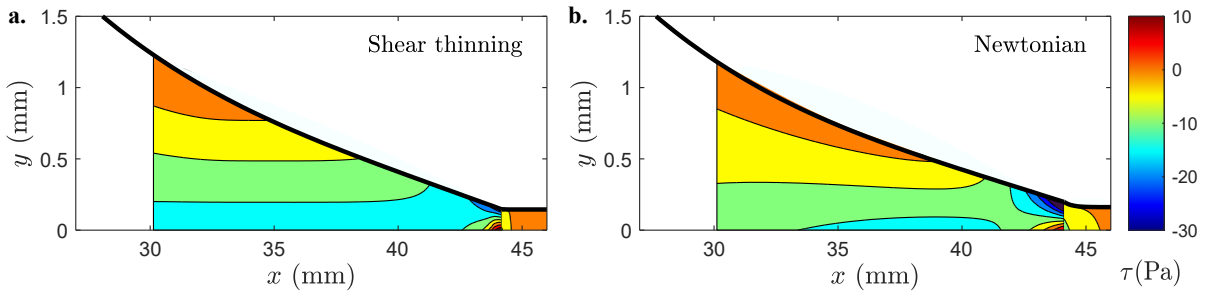


Fig. 3.11 – Numerical computation of the stress distribution, for $l_w = 14$ mm in **a.** a shear-thinning fluid (xanthan 0.9%) and **b.** in an equivalent Newtonian fluid (same $t_d = f(\Omega_d)$) with viscosity $\eta = 300$ mPa.s spread at $V = 1$ cm/s. The color scale indicates the shear stress τ .

If we look at the problem from the opposite angle, we see that to deposit the same volume of fluid without increasing its energy expenditure, we must then choose a Newtonian fluid of lower viscosity, $\eta = 150$ mPa.s. Indeed, in Figure 3.10b, the xanthan curve is superimposed on the 150 mPa.s curve. However, the deposition time (or the deposition length) is longer for the fluid of viscosity 150 mPa.s than with xanthan (Fig. 3.10a). The choice was made to define the equivalent Newtonian as the fluid that allows the same volume to be deposited in the same time (at the same velocity and l_{wi}). Other definitions are possible. For example, the equivalent fluid could be the one that allows to deposit the same volume of fluid by providing the same work. The choice between these different definitions depends on the final application. In the case of cosmetics, the surface concentration is often the most important parameter. A

classic example is the application of a sunscreen: it is essential to ensure the same coverage to maintain the same level of sun protection. In the context of energy-intensive industrial coating processes, one can imagine the case where reducing (or keeping constant) energy expenditure is the main criterion for comparison between different types of fluids.

3.4.3 Shape of the fluid deposit

Going back to our definition of the Newtonian equivalent, the spreading of the same volume over an identical length does not presume the shape of the deposited fluid film. To obtain the profile of the fluid film, the same calculation is performed as with the Newtonian fluid (see section 2.5.4). Figure 3.12b displays the deposition profile, $e = f(l_d)$, calculated numerically for both categories of fluid with $V = 10 \text{ mm/s}$ and $l_{wi} = 18 \text{ mm}$. In the situation of Newtonian fluids ($\eta = 150, 300$ and $500 \text{ mPa}\cdot\text{s}$), the deposited thickness decreases more and more sharply to reach zero at the end of the film. This situation is particularly visible for $150 \text{ mPa}\cdot\text{s}$. In the xanthan situation, the deposited thickness decreases more strongly at the beginning than at the end. In other words, shear-thinning fluids thin out almost linearly in contrast to Newtonian fluids whose thickness tends to drop abruptly after some point. The curvature is opposite in these two situations. This difference in slope between the two types of fluid is validated in Figure 3.12a by comparing the experimental data to the numerical data (in red, a Newtonian fluid, silicon oil at $480 \text{ mPa}\cdot\text{s}$ –from Fig. 2.18a– and in blue, a shear-thinning fluid, 0.9% xanthane). The experimental data were initially offset (see section 2.5.4) to account for the fact that the length of the deposited fluid is only modeled in the steady-state. Back on Figure 3.12b, when l_d reaches 80% of the total deposited length, the thickness has dropped by 90% for xanthan versus 68% for the

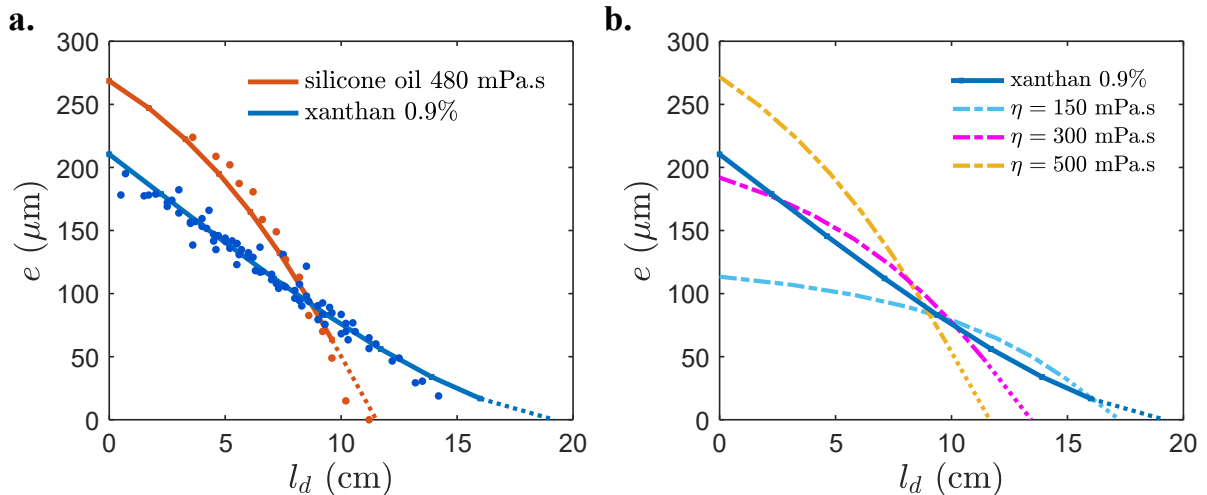


Fig. 3.12 – **a.** Evolution of the deposited thickness e as a function of the deposited length l_d for a $480 \text{ mPa}\cdot\text{s}$ silicone oil (red) and 0.9% xanthan (dark blue). The dots are experiments, and the lines are computations without fitting parameters. The experiments are carried with a velocity of $1 \text{ cm}\cdot\text{s}^{-1}$. **b.** Shape of the deposit for xanthan and Newtonian fluids of viscosity: $500 \text{ mPa}\cdot\text{s}$ (yellow), $300 \text{ mPa}\cdot\text{s}$ (pink) and $150 \text{ mPa}\cdot\text{s}$ (light blue)

Newtonian equivalent with 300 mPa.s. The spreading of the equivalent Newtonian fluid results in a more homogeneous deposit than for the shear-thinning fluid.

3.4.4 Disentangle the effect of the rheological parameters n and k

To better understand the impact of the shear-thinning properties on the deposited film shape, the values of n and k have been varied. Figure 3.13 shows the film profile resulting from different combinations of values of these parameter.

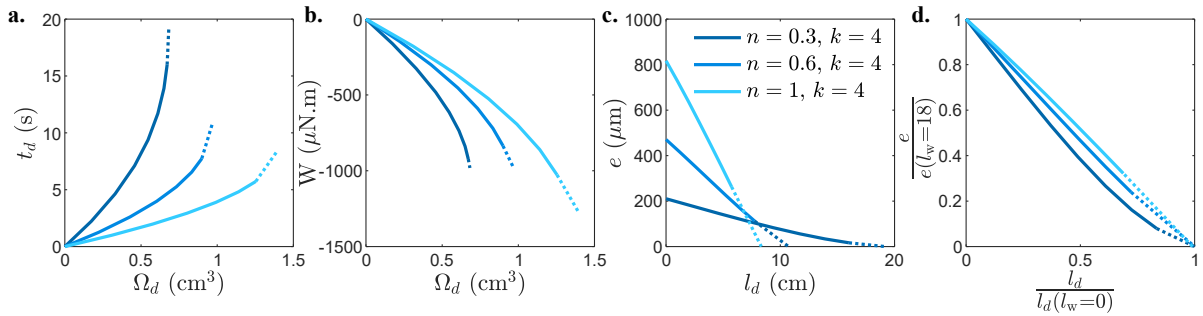


Fig. 3.13 – Study of the influence of the rheological parameter n on spreading. Three fluids with increasing shear-thinning index are compared: $n = 0.3$ (dark blue), 0.6 (blue) and 1 (light blue), while k is kept constant at $4 \text{ Pa}\cdot\text{s}^n$ ($V = 1 \text{ cm/s}$ and $l_{wi} = 18 \text{ mm}$). Note that $n = 0.3$ corresponds to xanthan at 0.9% , and $n = 1$ describes the case of a Newtonian fluid. **a.** Deposition time t_d as a function of the deposited volume Ω_d . **b.** Mechanical work $-W$ provided during the spreading of volume Ω_d . **c.** Evolution of the thickness of the deposit e as a function of the deposited length l_d . **d.** Deposited thickness normalised by its initial value ($e(l_w = 18)$) as a function of the deposited length normalised by its final value ($l_d(l_w = 0)$).

By increasing n , the relation $t_d = f(\Omega_d)$ is modified, a same volume of fluid is deposited in a shorter time thus on a shorter distance. For example for $\Omega_d = 0.5 \text{ cm}^3$ the deposited lengths are 8.2 , 3.2 and 1.7 cm for $n = 0.3$ to 0.6 and 1 respectively. The work required to deposit this volume is decreased by a factor of 1.5 and 2 . Figure 3.12c shows the shape of the corresponding fluid profiles. Increasing n while keeping k constant results in initially thicker profiles, but the thickness decreases more rapidly. By normalizing the deposited thickness (by its maximum value $e(l_w = 18)$) and the deposited length (by its maximum value $l_d(l_w = 0)$) we can thus highlight the difference in curvature previously observed while comparing the deposited shapes between xanthan and silicone oil (Fig. 3.12). By increasing n from 0.3 to 1 the curvature goes from negative to a slightly positive testifying to a slightly better thickness homogeneity in the Newtonian case. This difference in curvature is controlled by the value of n but can be amplified to some extent by varying k .

When k is reduced by a factor 8 in the Newtonian fluid case ($n = 1$, $\mu = k$) then the curvature increases (Fig. 3.14d) and the thickness homogeneity improves as discussed in Chapter 2. This effect is also observed in Figure 3.12. However, for shear-thinning fluids multiplying k by 3 or 5 (dashed lines), does not appear to have an significant impact on the curvature of the film profile. In particular, we observe a superposition of the curves of $\frac{e}{e(l_w=18)} = f\left(\frac{l_d}{l_d(l_w=0)}\right)$ as presented in the Figure 3.14d. It

can also be noticed that the work required to deposit a given volume remains almost the same while the time required to deposit this given volume decreases when k increases. These results suggest that n is the dominant parameter controlling the amount of work needed to deposit a volume of shear-thinning fluid. It would be interesting to complement these results with shear-thinning fluids featuring k less than $4 \text{ Pa}\cdot\text{s}^n$ to verify to what extent k has such a small effect on the shape of the deposit and the energy necessary to spread it.

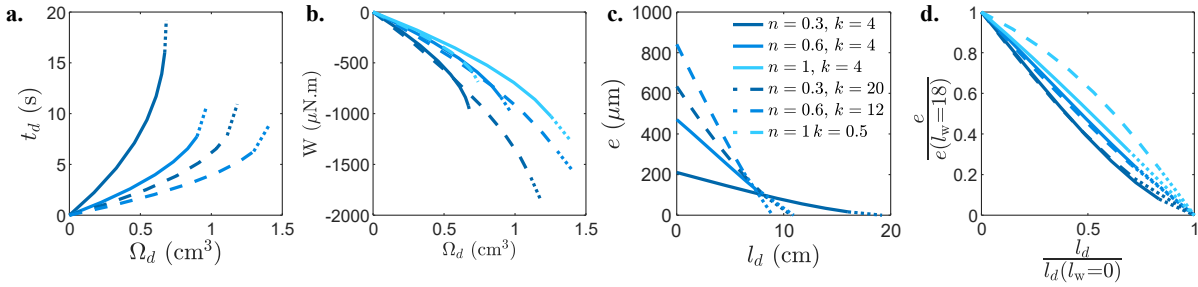


Fig. 3.14 – Study of the influence of the rheological parameter k on the spreading. Its reference value $4 \text{ Pa}\cdot\text{s}^n$ (solid lines) is multiplied (dashed lines) by 5 for $n = 0.3$ (dark blue), by 3 for $n = 0.6$ (blue) and divided by 8 for $n = 1$ (light blue). $V = 1 \text{ cm/s}$ and $l_{wi} = 18 \text{ mm}$. **a.** Deposition time t_d as a function of the deposited volume Ω_d . **b.** Mechanical work $-W$ provided during the spreading of volume Ω_d . **c.** Evolution of the thickness of the deposit as a function of the deposited length l_d . **d.** Deposited thickness normalised by its initial value ($e(l_w = 18)$) as a function of the deposited length normalised by its final value ($l_d(l_w = 0)$). The curves corresponding to $n = 1$ are presented only in **b.** and **d.** for clarity.

Conclusion – Chapter 3

In this chapter, we have studied the film thickness of a shear-thinning fluid spread by a soft blade and compared it to a Newtonian fluid:

1. We extended the scaling law to model the soft blade coating of shear-thinning fluids. We showed that the thickness of the deposit can be predicted as a function of the rheological parameters of the fluid when modelled as a power law fluid following the Ostwald and de Waele equation.
2. Numerical calculations were also adapted to the shear-thinning equations. They were in good agreement with the experimental data and validated the scaling law.
3. In order to compare the soft blade coating of Newtonian and shear-thinning fluids, we discussed the main possible definitions of a Newtonian "equivalent". In this work we decided to define as a Newtonian equivalent a fluid for which the same volume can be spread in the same time (at an identical spreading velocity and initial wetting length) as the shear-thinning fluid of interest.
4. In this context, we evidenced numerically that shear-thinning fluids require more energy to be spread than Newtonian fluids. This is related to an increase in interfacial stress, which can either be an advantage (allowing a better control of the movement, for example) or a drawback (since more energy is needed to move the solid at the same velocity).
5. The shapes of the deposited film were also found to be different. The shear-thinning fluid thins more linearly, making the deposit less homogeneous in thickness. This difference in curvature has been related essentially to the shear-thinning index n . The parameter k was observed to impact the curvature only in the Newtonian case ($\mu = k$). These results will be valuable in applications, for example to determine whether a polymer needs to be added to a product, or to choose the polymer depending on the expected effect: a thicker or a more regular film or a fluid that is more easy to spread.

Shear-thinning fluids are one type of fluid among many. In particular, it is rare to have pure shear-thinning fluids, but this property is often combined with others, such as the presence of a yield-stress at low shear rates or the generation of normal stresses at high shear rates. In the next chapter, we discuss the soft blade coating of two polymer solutions chosen to model these rheological behaviors.

Chapter 4

Normal stress and Yield stress shear-thinning fluids

In this chapter, we consider the spreading of complex fluids with a soft blade and focus on shear-thinning fluids that additionally generate normal stresses at high shear rates, or exhibit a yield stress at low shear rates. In the first part, the experiments are compared to the pure shear-thinning case presented in Chapter 3 in order to discuss the effect of first normal stress difference over the deposited thickness. We perform a dimensional analysis to explain the results obtained and we propose a new dimensionless number to predict the impact of the normal stress for this coating geometry. This number also helps to understand the results obtained in the literature on dip coating of normal stress fluids.

In the second part, the spreading experiments are finally performed with yield stress fluids. The scaling law approach no longer describe the experimental results. A lateral follow-up of the spreading experiment is used to obtain a qualitative understanding of the observed discrepancies. A theoretical study of the flow under the blade partially explain the behavior of the fluid during spreading.

The results presented in this chapter about the role of the normal stresses have been published in Physical Review Fluids [2]. The article can be found in Appendix D.

Contents

4.1	Normal stress fluid coating	82
4.1.1	HPAM solutions	82
4.1.2	Spreading experiment	84
4.1.3	Comparison with xanthan	85
4.1.4	Comparison with other coating geometry described in the literature	89
4.2	Yield stress fluid coating	90
4.2.1	Carbopol gels	90
4.2.2	Expectations for spreading dynamics by dimensional analysis	92
4.2.3	Huge variation of $e = f(l_w)$ relationship	92
4.2.4	Impact of Carbopol elasticity	93

4.2.5 Fluid partially stuck under the blade	95
4.3 Conclusion	98
4.4 Perspectives	99

4.1 Normal stress fluid coating

Normal stress fluids generate normal stress when sheared, usually at high shear rate. In the case of polymers, this is due to the stretching of the polymer chains. When spreading with a soft blade, one would expect the polymer chains to experience this stretching at the blade tip, where the shear rate is at its highest. Thus, one would imagine that normal stresses would contribute to the lifting of the blade and result in a different deposition law and film profile. To determine if the addition of polymers, when aimed to generate these normal stresses, has a positive impact, we studied the spreading of a model fluid.

4.1.1 HPAM solutions

We focus on partially hydrolyzed polyacrylamide (HPAM). This polymer is often used for its viscosifying properties that help to improve oil recovery (fossil fuel industry). But the property of most interest to us in this work is its ability to generate high normal stresses at high shear rates, which is why it is often used to illustrate the Weissenberg effect. The effect is observable for the highest molecular weights (e.g. 18×10^6 g/mol in [107]) and varies with the concentration [107].

From a structural point of view, this polymer is linear and it consists of a succession of acrylamide monomers. A fraction of these monomers is hydrolyzed, i.e. the amide groups are replaced by carboxylate groups (in water at pH= 7). For the HPAM studied (from SNF), with a molecular weight $M_w = 18 \times 10^6$ g/mol, around 25 to 30% of the functions are hydrolyzed.

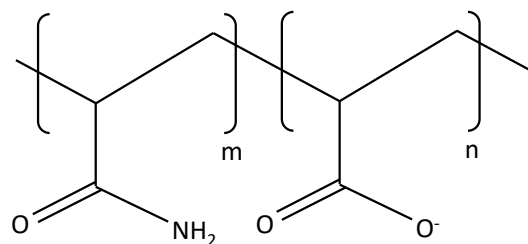


Fig. 4.1 – Chemical formula of HPAM.

Preparation of HPAM solutions

HPAM solutions were prepared by dissolving the powder in Milli-Q water at room temperature by gentle magnetic stirring, for up to 24 hours. The choice of a gentle agitation was motivated by the concern

to avoid polymer chain breakage. The samples were left to rest for 24 hours after preparation. Due to potential bacterial contamination and polymer oxidation, the samples were stored in a refrigerator (5°C) and their rheological properties were checked before each measurement campaign.

Three concentrations were studied: 0.1 w%, 0.3 w% and 0.5 w%. According to Beaumont's work [107], HPAM is expected to be in a semi-dilute entangled regime for all these concentrations as he estimated the critical entanglement concentration to be below 40 ppm.

Rheology in flow

Rheological measurements of HPAM solutions were performed with a cone and plate geometry at 25°C. The limit of detection for the normal force by the rheometer is 5 mN, which correspond to 8 Pa for the normal stress N_1 . The shear rate was imposed and was varied from 10^{-2} to 1000 s^{-1} .

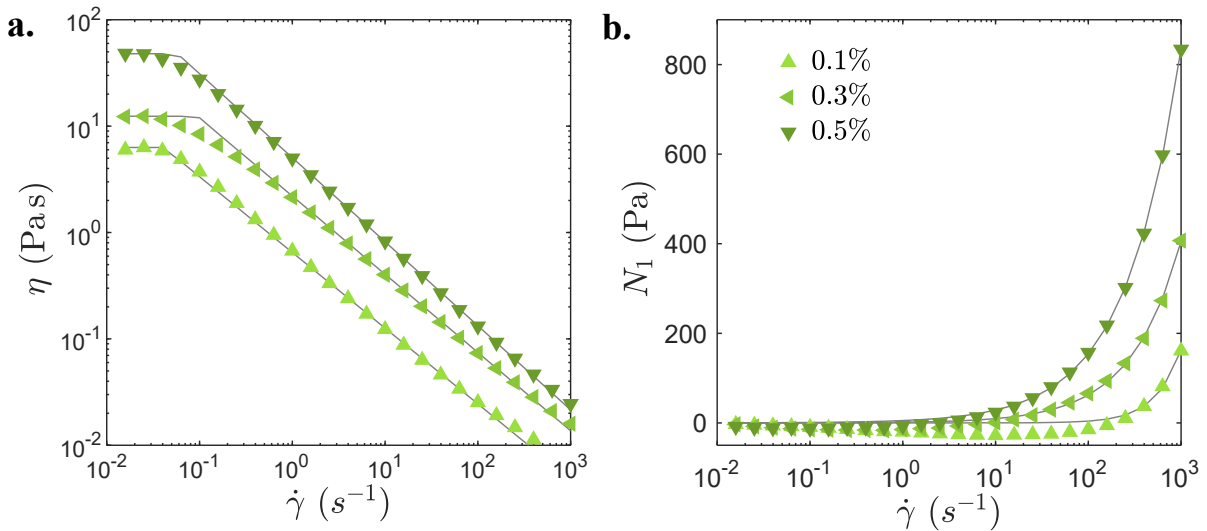


Fig. 4.2 – Rheological curves of HPAM solutions with a concentration of 0.1 (light green), 0.3 (green) and 0.5 w% (dark green). **a.** Viscosity η as a function of the shear rate $\dot{\gamma}$. **b.** First normal stress difference N_1 as a function of $\dot{\gamma}$. The grey lines represent the fits obtained with the parameters from the Table 4.1.

HPAM solutions exhibit strong shear-thinning behaviour after a Newtonian plateau (Fig. 4.2a). The shear-thinning behavior can therefore be described by a power law equation similar to that of xhantan (Eq. 3.1). The rheological parameters n , k and η_0 are given in Table 4.1. The shear-thinning behavior is more pronounced as the concentration increases (n decreases).

The first normal stress difference, N_1 is measured as a function of the shear rate in Figure 4.2b. Note that this value has been corrected for inertia which is not negligible at high angular velocity (typically $\dot{\gamma} > 100 \text{ s}^{-1}$). For cone-plate (and parallel plates) geometry, the inertia contributes to the value of N_1^{exp} through $N_1^{\text{inertia}} = -\frac{3}{20}\rho\omega^2R^2$ [45]. The corrected value of N_1 is hence $N_1^{\text{exp}} - N_1^{\text{inertia}}$. N_1 increases as a power law for high shear rates: $N_1 = \alpha\dot{\gamma}^m$. The values of the first normal stress coefficients α and m are given in Table 4.1. The normal stress difference increases with the concentration: at $\dot{\gamma} = 10^3 \text{ s}^{-1}$ it

reaches more than 800 Pa for 0.5% concentration against less than 200 Pa at 0.1 %. Consequently, the impact of normal stresses is likely to be greater for 0.5 % concentration.

Table 4.1 Rheological properties of HPAM solutions.

	0.1%	0.3%	0.5%
η_0 (Pa s)	6.3	12.4	48
k (Pa s ^{<i>n</i>})	0.65	2.2	5.1
n	0.29	0.27	0.21
α (Pa s ^{<i>m</i>})	2e-3	1.44	5.24
m	1.62	0.82	0.73

4.1.2 Spreading experiment

The spreading experiment is performed with the HPAM at different concentrations under the same experimental conditions as in Chapter 3. It again appears that $e(t)$ is a function of $l_w(t)$ (Fig. 4.3) and, at first glance, no obvious difference can be seen with the $e = f(l_w)$ of xanthan solutions presented in Chapter 3. The deposited thickness was calculated numerically for HPAM using the code developed for xanthan, thus considering only a shear-thinning behavior. There is a good agreement at low l_w between the experimental and numerical data. The discrepancies observed at high l_w are explained in section 4.1.3.

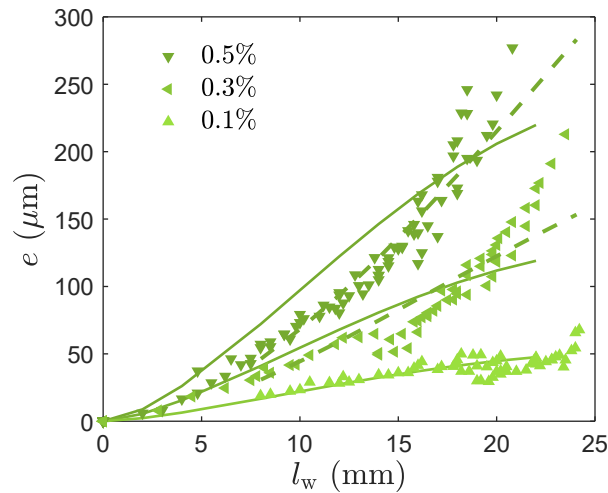


Fig. 4.3 – Evolution of fluid thickness e with wetting length l_w for HPAM at 0.1 (light green), 0.3 (green) and 0.5 (dark green) w%. The markers represent the experimental data. The numerical calculations describing shear-thinning fluids (without considering the normal stresses) are shown as dashed lines. The solid lines depict the scaling laws written in the previous chapter (Eq. 3.7) with a prefactor of 0.06.

4.1.3 Comparison with xanthan

In order to investigate the effect of normal stresses and disentangle it from shear-thinning, HPAM is compared with a pure shear-thinning fluid (without normal stresses).

Rheological properties

In practice, HPAM at 0.5 w% was compared to xanthane at 0.9 w%. As evidenced in Figure 4.4a, the comparison of these two specific fluids is particularly relevant. Indeed, the shear rheology of the two solutions is almost identical: the viscosity $\eta(\dot{\gamma})$ of HPAM (green triangles) overlaps with that of xanthan (blue circles) as shown in Figure 4.4a. However, the normal components of the stress tensor are fundamentally different. In particular, the first normal stress difference in HPAM reaches several hundred Pascals under high shear (as visible in Figure 4.4b) while N_1 is always less than 80 Pa in xanthan (Fig. 4.4b). For instance, for $\dot{\gamma} = 400 \text{ s}^{-1}$, N_1 is 5 times higher with HPAM.

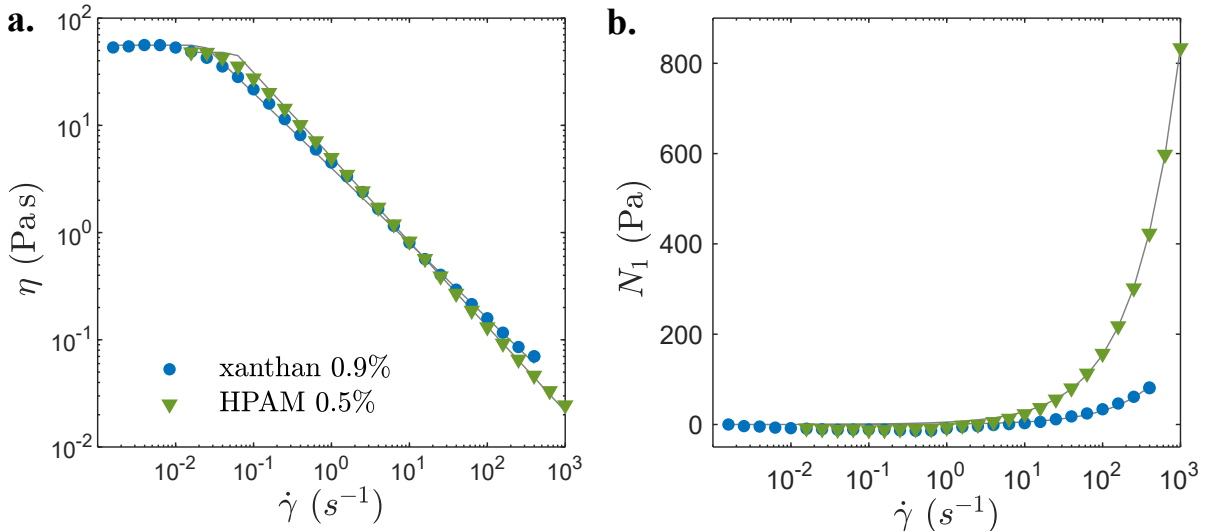


Fig. 4.4 – Comparison of the flow curves of 0.5% HPAM solution (green) and 0.9% xanthan solution (blue). **a.** Viscosity as a function of shear rate. **b.** First normal stress difference N_1 as a function of the shear rate $\dot{\gamma}$.

Following a classification used by Ashmore *et al.* [74], xanthan is in the weakly elastic limit (it is an almost purely shear-thinning fluid) while HPAM is in the strongly elastic limit, since it develops large normal stresses. To be more precise, the boundary between weakly and strongly elastic situations is often set by the Weissenberg number $Wi = \frac{N_1}{\tau}$, which compares the normal stress N_1 to the shear stress τ . For the HPAM solution considered here, Wi is much larger than one: using our notations, and a characteristic shear rate $\dot{\gamma} = \frac{V}{e} \simeq 100$, it writes: $Wi = \frac{\alpha}{k} \dot{\gamma}^{m-n} \simeq \frac{\alpha}{k} \left(\frac{V}{e}\right)^{m-n} \simeq 10$. On the contrary, the Weissenberg number in the xanthan gel is less than 2 (for 0.9 w% xanthan, $\alpha = 0.99$ and $m = 0.74$).

This difference in Weissenberg number is large enough to see effects on the behavior of these fluids. For example, when looking at the jet of these two polymer solutions coming out of a capillary tube, a noticeable difference can be observed: in the case of HPAM, the jet swells after exiting the capillary tube (Fig. 4.5). This experiment is performed with a capillary tube of 0.65 mm outer diameter and a flow rate of $0.5 \text{ mL}\cdot\text{s}^{-1}$. Thus, under the conditions of the spreading experiments, one would reasonably expect normal stresses to play a role.

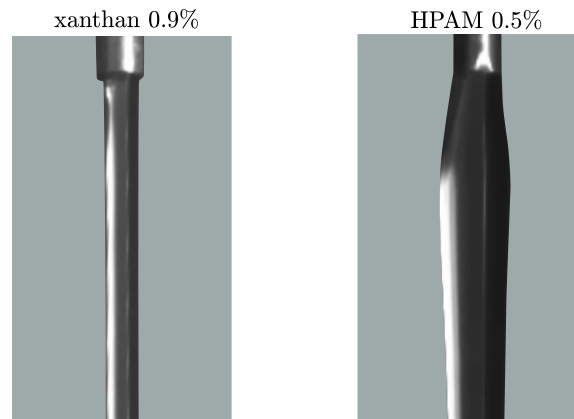


Fig. 4.5 – Comparison of a polymer jet outside a capillary tube for a 0.9% xanthan (left) and 0.5% HPAM (right) solution. The polymer jet clearly swells in the case of HPAM while the liquid jet remains straight with xanthan.

Similar spreading dynamics between shear-thinning and normal stress fluids

Surprisingly, the spreading experiments shows that the normal stresses do not impact the film deposition law. In Figure 4.6, the film thicknesses e , obtained by the spreading of a 0.5 % HPAM solution (green triangles) and a 0.9% xanthan solution (blue circles) are compared. The spreading conditions are strictly identical, with $V = 1 \text{ cm/s}$. Intriguingly, the two sets of experimental data overlap almost perfectly, suggesting that, within the experimental error, normal stresses do not affect the film thickness.

This is further confirmed by the simulation: in Figure 4.6, the thicknesses calculated numerically for *purely shear-thinning* fluids are shown in dashed lines. The simulation matches the experimental data points for HPAM particularly well, even though the effects of normal stresses were not taken into account in the calculation. If the normal stresses were to have an effect, there would be a discrepancy between the numerical and experimental data.

It can be noted that there is some deviation at high l_w , but if normal stress effect were to occur it would rather be at low l_w since it corresponds to higher shear rates on average and would maximize the potential effect. This deviation is not attributed to normal forces and an explanation of its origin is presented in the next paragraph.

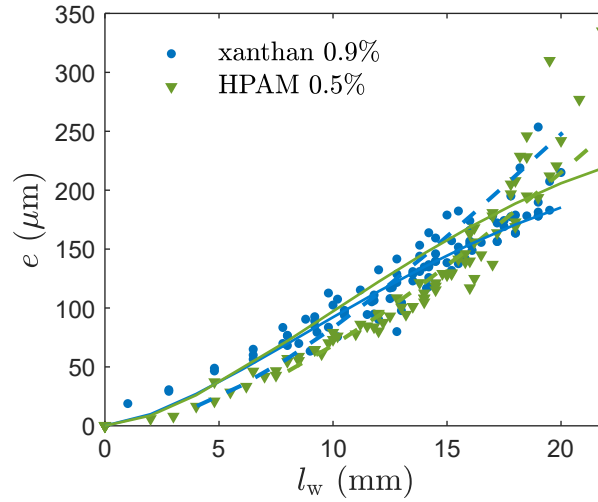


Fig. 4.6 – Film thickness of 0.9% xanthan (blue) and 0.5% HPAM (green) solutions as a function of the wetting length l_w . The markers correspond to the experimental data. The solid lines represent the scaling law (Eq. 3.7) with a prefactor 0.06. The dashed lines show the results of numerical simulations of the film thickness in both cases. The numerical computation correspond to the one presented in Chapter 3, and it does not take into account N_1 .

Deviation with the numerical computation at large l_w

With HPAM, the deviation between the experimental data and the numerical computation is highly evidenced for $l_w \geq 18$ mm. Similar deviation had already been observed but to a lesser extent with xanthan at 0.4 w%. In order to investigate the origin, a sensitivity analysis was performed for shear-thinning fluids (xanthan solution at 0.9%), with spreading conditions $l_w = 14$ mm and $V = 10$ mm/s. It shows that e is very little affected by variations in γ , η_0 and δ_b but varies by about 6–8% with δ_s and k and 13% with n (the parameters were varied by $\pm 10\%$ to perform this sensitivity study). The contact angle of the fluid on the substrate, δ_s , if badly estimated, can be at the origin of a significant deviation from the experimental results. For large fluid reservoir, the shape of the meniscus at the back of the reservoir can no longer be described as a circular arc but takes a S-shape (Fig. 4.7). As a consequence the approximation of the pressure p_{sw} by the Laplace equation (Eq. 2.11) does not properly describe the experimental situation anymore, hence the divergence. The pressure p_{sw} is underestimated in the numerical computation leading to an underestimated thickness which is consistent with the observed deviation. However, it is difficult to estimate the actual value of p_{sw} to correct it with confidence.

Now that we have shown that there is no evidence of the effect of normal stresses from the experimental data, how can we explain such a small effect of normal stresses on the spreading, even though they are dominant over shear stress in the highly elastic limit?

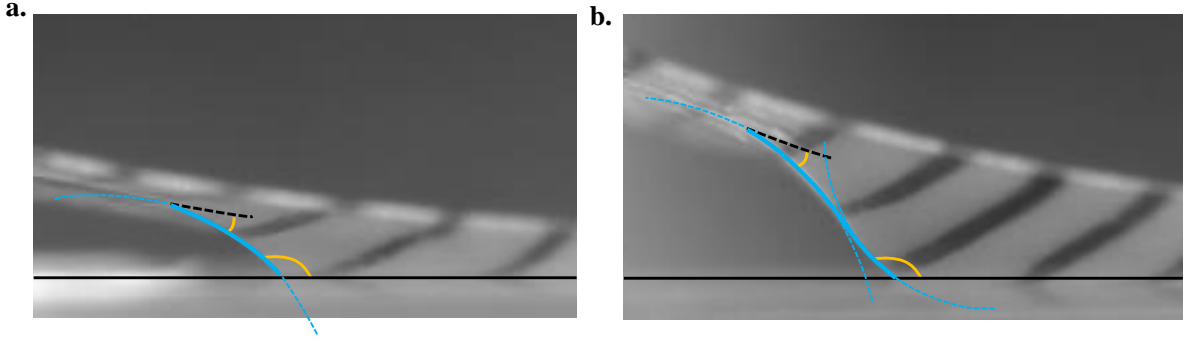


Fig. 4.7 – Pictures of the meniscus at the back of the fluid reservoir for HPAM 0.5 w% spread at $V = 10$ mm/s. **a.** Case 1: the shape correspond to a circular arc implying $p_{sw} < 0$ ($l_w = 15.5$ mm). **b.** Case 2: The shape can no longer be fitted by a circle arc but instead shows a positive and a negative curvature. The associated pressure becomes potentially $p_{sw} \geq 0$ ($l_w = 21.8$ mm).

Discussion in light of a dimensional analysis

To understand why normal stresses do not have a significant impact on the deposition law, a dimensional analysis is performed from the Equation 3.5, recalled here for ease of reading :

$$-\frac{\partial p}{\partial x} + \frac{\partial}{\partial x} \left(\frac{2}{3}N_1 + \frac{N_2}{3} \right) + \frac{\partial \tau_{xy}}{\partial y} + \frac{\partial \tau_{xz}}{\partial z} = 0$$

This time, the N_1 term is kept. As often for polymer solutions, the influence on the flow of the second normal stress N_2 is neglected. It is typically ten times smaller than N_1 for dilute systems [32, 108]. This approximation is done by de Ryck & Quéré [73] and by Ashmore *et al.* [74] (using a more complex polymeric model). It further simplifies the flow equation which writes :

$$\frac{\partial p}{\partial x} = \frac{\partial \tau}{\partial z} + \frac{2}{3} \frac{\partial N_1}{\partial x} \quad (4.1)$$

The total pressure p can therefore be expressed as the sum of two terms: $p = p_{lub} + p_N$. The first term is the usual lubrication pressure which scales, as before with the Newtonian and shear-thinning fluids, as $p_{lub} \sim \tau \frac{l_w}{e}$. The second term corresponds to the additional pressure p_N due to the normal stresses, which is simply proportional to N_1 . The ratio of the two pressures gives an estimate of the relative importance of the two terms in the spreading:

$$\frac{p_N}{p_{lub}} \sim \frac{2}{3} \frac{N_1}{\tau} \frac{e}{l_w} \sim \frac{2}{3} Wi \frac{e}{l_w}. \quad (4.2)$$

As shown in Eq. 4.2, a new dimensionless number $\mathcal{E} = \frac{2}{3} Wi \frac{e}{l_w}$ can be defined. It compares the two terms of the total fluid pressure p , and characterizes the effect of normal stresses in spreading experiments. For $\mathcal{E} \ll 1$, only shear-thinning effects are visible, while for $\mathcal{E} \gg 1$, the elastic effects of the fluid become dominant. In practice, $\mathcal{E} \ll 1$ is always verified for xanthan in our experiment. Interestingly, even though

the Weissenberg number is close to 10 in the 0.5% HPAM solution – indicating that the first normal stress difference dominates over the shear stress – \mathcal{E} is of the order of 0.1 due to the geometric factor $\frac{e}{l_w} \simeq 10^{-2}$.

For $\mathcal{E} \ll 1$ the N_1 term can simply be neglected, and the Equation 4.1 simply reduces to the Equation 3.6. Thus the scaling law equation (Eq. 3.7) describing the deposited film thickness as a function of the wetting length written for xanthan is also valid for HPAM. The condition $\mathcal{E} \ll 1$ can be rewritten $\frac{2}{3} \frac{\alpha}{k} \left(\frac{V}{l_w}\right)^{\frac{m}{n+1}} \left(1 - \frac{l_w}{L}\right)^{\frac{2(1-m+n)}{n+1}} \left(\frac{kL^2 b l_w}{E^* I}\right)^{\frac{1-m+n}{n+1}} \ll 1$. This expression is used to determine that $\mathcal{E} \ll 1$ is true as long as $l_w > 0.05$ mm for 0.5% HPAM. This condition is always verified in our experiments. This is consistent with the fact that the scaling law expressed for shear-thinning fluids is in good agreement with the experimental data of the HPAM spreading experiment (Fig. 4.3). This dimensional analysis explains why the effect of normal stresses is negligible in soft blade coating. The Weissenberg number is not the appropriate characteristic number to predict the effects of normal stress in this geometry.

4.1.4 Comparison with other coating geometry described in the literature

The geometric factor e/l_w is central to explain the difference with other experiments. For example, de Ryck *et al.* [73] found a very strong effect of the normal stresses when dip-coating a fiber. They used a 1% PAA solution whose properties are similar to those of the 0.5% HPAM solution, so that the Weissenberg number is also close to 10. However, in dip-coating, the characteristic length scale in the flow direction parallel to the rod is an internal length $l \sim \sqrt{e(r+e)}$ with r the fiber radius. In Ref. [73] the ratio e/l varies between 0.2 and 1, so that \mathcal{E} is always greater than 1. In our experiment, however, the presence of the blade imposes the wetting length l_w as the relevant length scale. Since $l_w \simeq 100e$, we cannot observe any effect of the normal stresses unless the Weissenberg number is greater than 100, a situation that cannot be obtained with the fluids used here and which will be difficult to achieve.

4.2 Yield stress fluid coating

Most cosmetic and pharmaceutical creams present a yield stress. This means that at rest the fluid does not flow and behaves like a solid. In practice, this property is useful to deposit patches of a sunscreen or a foundation without being in a hurry to spread them. The user can thus better control the deposition and the spreading of the product. In this context, extending our study to yield stress fluids seemed relevant. We encountered difficulties to predict the deposited thickness, at first sight it was even difficult to observe a tendency in the experimental results which were very poorly reproducible. Our objective was then to find the origins of these discrepancies in a qualitative way.

4.2.1 Carbopol gels

Carbopol is a polymer often chosen as a model of a yield-stress fluid in many academic researches [25], and it is also widely used in cosmetics and pharmaceutical products for its mechanical properties (thickener and yield stress fluid). Carbopol is the brand name given to carbomers. It is part of the family of water-swallowable microgels. Carbopol are hydrophilic polymers of polyacrylic acid with a low crosslink density (Fig. 4.8a). In water, the molecules swell due to the dissociation of the acrylic acid. By adding a base (e.g. NaOH) to the solution, the carboxylate groups are deionized and the polymer chains repel each other electrostatically (Fig. 4.8b). The microgels can increase in volume 200 to 1000 times in water [25, 26] and up to 8 times in polar solvent such as glycerol [27]. Above the jamming concentration, the microgel particles are compressed and the polymer-chain ends of different Carbopol particles can become entangled [25–27]. This jamming is at the origin of the yield stress: if the stress applied to the solution is not high enough, the space-filling structure is not mobile and instead behaves like an elastic solid. It can be considered as a glass of sponges [109]. The jamming concentration depends on the Carbopol type (structure and crosslink density) as well as the pH [110]. In water this value is between 0.05-0.1 w% [26, 109, 110], and in glycerol it is comprised between 0.8 and 1.1 w% [27]. In this work, we use Carbopol 940 from Lubrizol. This Carbopol is one of the most cross-linked carbomers.

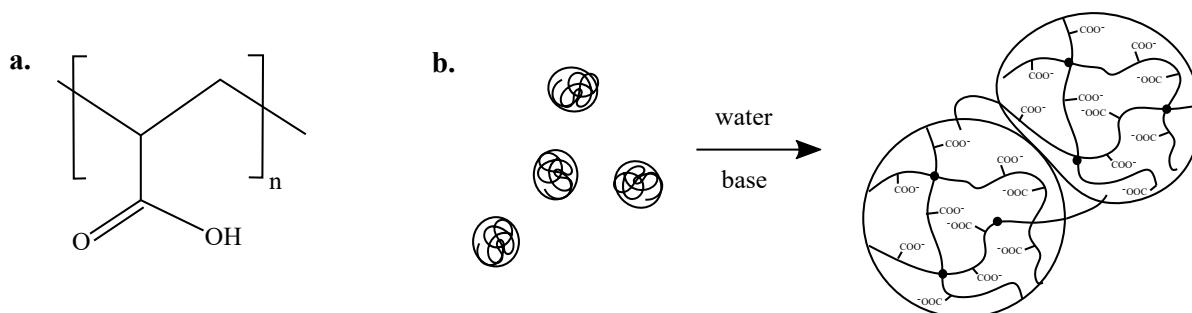


Fig. 4.8 – **a.** Chemical formula of the Carbopol polymer **b.** Microgel swelling after neutralization in alkali aqueous solution. The solid circles represent the crosslinks.

Preparation of the solutions

The Carbopol is initially in powder form. Gels are prepared by dissolving Carbopol in MilliQ water. The powder is added little by little to avoid large agglomerates under mechanical stirring at 500 rpm. After one hour of stirring, the polymer is completely hydrated and a solution of sodium hydroxide is added to the mixture. The amount should be sufficient to adjust the pH between 6 and 7. In practice, the mass of NaOH solution (at 1 mol/L) added is 8 times the mass of Carbopol. As soon as the NaOH comes into contact with the solution, gelation occurs. The Carbopol gel is then stirred at 900 rpm for 2 hours. It is important not to apply a higher stirring speed and time, to avoid breakage of Carbopol polymer in small chains. These small chains can create depletion forces between the large polymers, resulting in thixotropic behavior, that translates in practice into hysteresis between the upward and downward flow curves [111]. Sometimes, at the highest concentration in Carbopol, air bubbles can be trapped in the gel during the preparation. For some applications (as in Chapter 6) it is not a problem but for the spreading experiment described here the gels are centrifuged for 2 minutes.

We prepared Carbopol gel with concentrations of 0.2, 0.15 and 0.1 w%. For all these concentrations, the system is jammed.

Rheological characterization

The rheology of Carbopol gels was measured using a parallel plate geometry on an Anton Paar rheometer (MCR 302). The sample was tested in the non-linear regime with a 1 mm gap at 20°C. The shear rate $\dot{\gamma}$ was swept from 200 to 10^{-1} s^{-1} . Going from high to low shear rate allows avoiding to measure the elasticity effect at the beginning of the flow due to the high elasticity of the Carbopol gels [112]. For each value of the shear rate, the effort was maintained for 30 s on the sample. The Rabinowitsch correction was applied on the data [35].

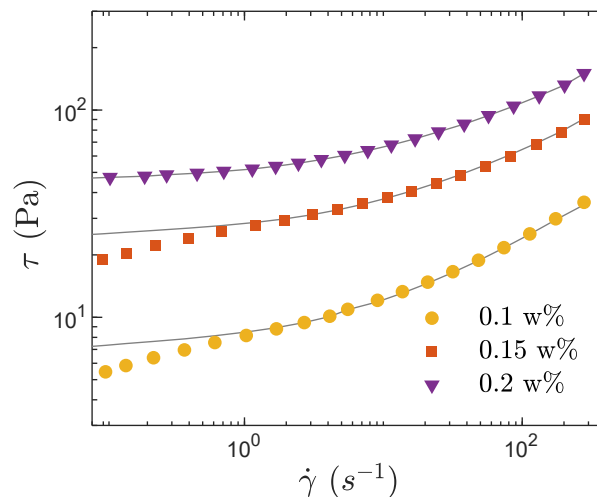


Fig. 4.9 – Stress τ as a function of the shear rate $\dot{\gamma}$ for Carbopol formulated at 0.1 0.15 and 0.2 w%. The grey line corresponds to the Herschel-Bulkley fit with rheological parameters given in Table 4.2.

Table 4.2 Rheological properties of Carbopol gels.

	0.1%	0.15%	0.2%
τ_y (Pa)	6.7	23.2	44.4
k (Pa s ^{<i>n</i>})	2.6	7.7	12.7
n	0.45	0.41	0.4

The flow curves are presented in Figure 4.9. The Carbopol gels are yield stress fluids: their rheological behavior can be described by Herschel-Bulkley model [22]. The fits corresponding to $\tau = \tau_y + k\dot{\gamma}^n$ are shown in grey lines, with τ_y the yield stress, k the consistency index and n the shear-thinning index. The values extracted from these fits are given in Table 4.2. They are in the range of the values reported in the literature [25] but these values vary widely. For instance for Carbopol 940 at 0.2 w% and pH ~ 7 , Aktas reports $\tau_y = 20$ Pa, $k = 5.8$ Pa.s^{*n*} and $n = 0.42$ [113] and Gomez, $\tau_y = 91$ Pa, $k = 46.8$ Pa.s^{*n*} and $n = 0.33$, with more uncertainty on the pH value (pH = 6.2 – 7) [114].

4.2.2 Expectations for spreading dynamics by dimensional analysis

The stress is described by the Herschel-Bulkley model $\tau = \tau_y + k\dot{\gamma}^n$, it scales as $\tau \sim \tau_y + k\left(\frac{V}{e}\right)^n$. The yield stress τ_y could be neglected only if:

$$\tau_y \ll k\left(\frac{V}{e}\right)^n \quad (4.3)$$

In this case, the shear stress could be expressed simply as $\tau \approx k\dot{\gamma}^n$ and the scaling law giving the deposited thickness would correspond to the Equation 3.7 describing a pure shear-thinning fluid. An example is given in Figure 4.11a (dashed curve).

However, for most of our spreading experiments, τ_y is of the order of $k\left(\frac{V}{e}\right)^n$ and therefore cannot be neglected. In this situation, a consequent part of the fluid behaves like a solid and the spreading process corresponds to a fracture process [75]. Therefore, we expect discrepancies between the scaling law and the experimental data.

4.2.3 Huge variation of $e = f(l_w)$ relationship

The soft blade coating experiments were performed on Carbopol gels. Spreading conditions such as velocity and blade rigidity were varied. However, contrary to what was expected from the scaling law, no clear tendency seems to emerge when plotting $e = f(l_w)$ for a given set of parameters. Examples are given in Figure 4.10 for Carbopol at 0.15 w% spread at 5 and 10 mm/s. The initial volumes, Ω_0 , were varied and the corresponding results are represented with different tones. The data do not overlap on a single curve but rather appear to be sensitive to initial conditions. Two types of behavior can be noticed: at high l_w , the series are nearly vertical showing that the deposited thickness is nearly independent from the wetting length, whereas for the lower l_w values a more usual quasi-linear trend is observed, however bounded to low values of the deposited thickness. Even at low yield stress (e.g. 6.7 Pa for Carbopol

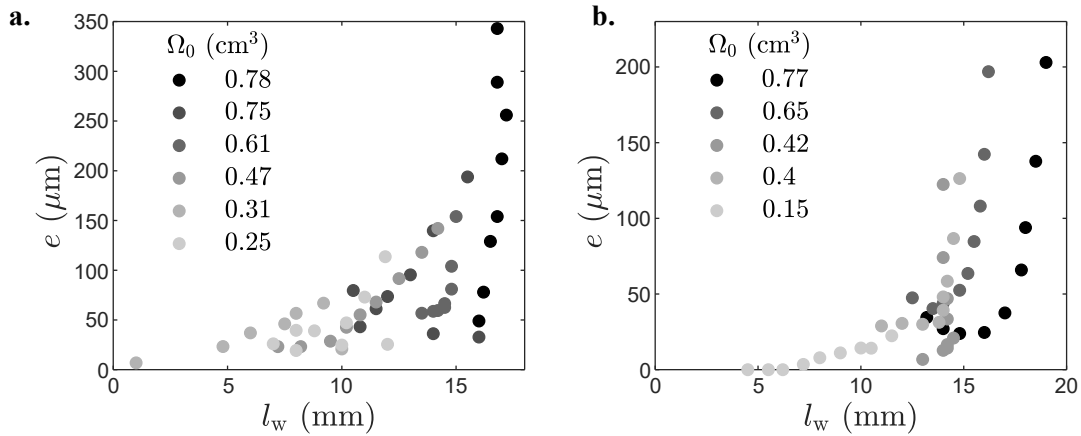


Fig. 4.10 – Deposited fluid thickness as a function of the wetting length for 0.15 w% Carbopol gel spread at **a.** $V = 10$ mm/s, and **b.** $V = 5$ mm/s. The initial volumes Ω_0 are varied as indicated on the plots. In both cases, the data appear to be experiment-dependent; the points do not merge into a single line.

at 0.1 w%) such types of behavior have been observed. One can also note, during the spreading, the increase in e for $\Omega_0 = 0.77$ and 0.65 cm³ (Fig. 4.10b) and in l_w for $\Omega_0 = 0.75$, 0.31 and 0.25 cm³ (Fig. 4.10a). When spreading yield stress fluids, more complex phenomena occur than expected, leading to surprising and inconsistent results.

Two effects, thereafter discussed, have been found to explain, at least partially, the high dispersion of the experimental points and the fact that the scaling law does not allow describing them.

4.2.4 Impact of Carbopol elasticity

In Figure 4.11, a representative example of unexpected behavior is presented. When spreading 0.78 cm³ of Carbopol 0.2 w% at 2.5 mm/s, the deposited thickness decreases from 220 to 50 μm but the wetting length only slightly varies from 20.5 to 18.2 mm (Fig 4.11a). We call this situation a "blocking" situation. The pictures of the blade taken from above at $t = 12$ and 32 s (corresponding to the orange and blue circles of Fig. 4.11a) confirm the small variation of the wetting length during this spreading experiment (Fig. 4.11b). One might wonder where does the deposited volume comes from as the volume of the fluid reservoir seems to remain constant (l_w varies very little), except for a slight emptying on the sides but that cannot account for all of the deposited volume. Looking at the blade from the side, it appears that it gradually moves down during the experiment (Fig. 4.11c). This variation of the blade position is underlined by the zoom in the inset showing the difference in blade positions at $t = 12$ s (orange) and 32 s (blue). The decrease in the height of the blade makes sense to explain where the volume of the deposited film comes from.

We hypothesize, to explain this situation, that due to the yield stress of the fluid, the initial equilibrium of the blade result not only from the balance between viscous stress and blade elasticity but also involves the elasticity of the fluid. At the beginning of an experiment, a finite amount of fluid is deposited with a

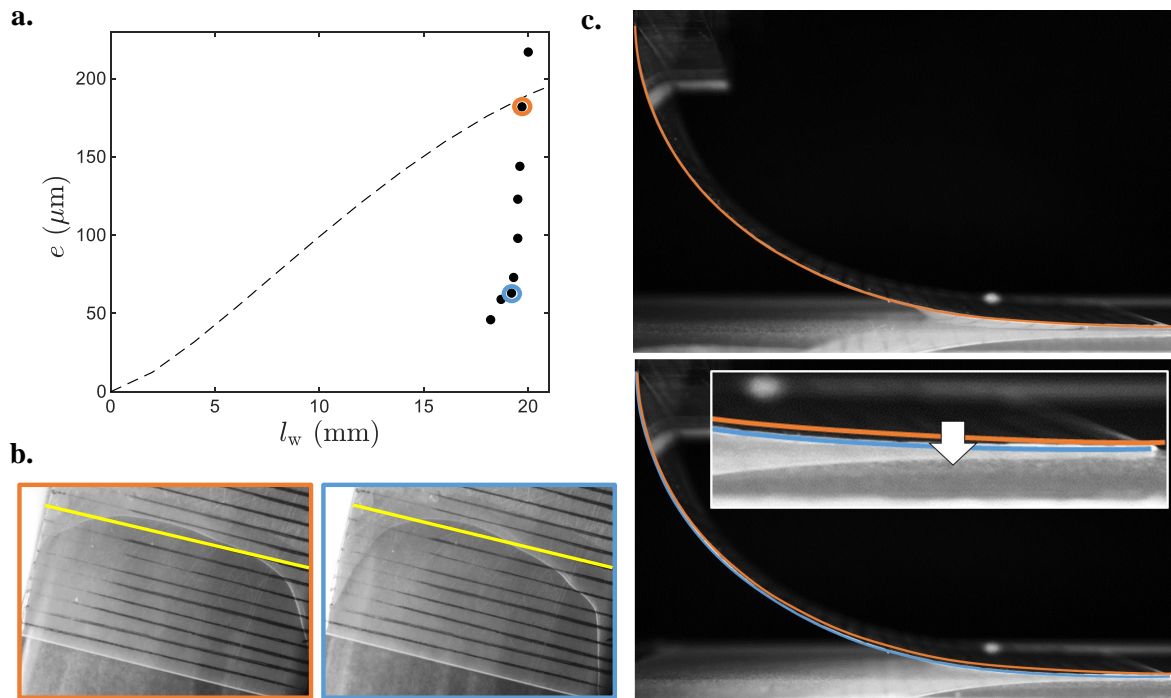


Fig. 4.11 – **a.** Deposited film thickness e as a function of the wetting length for a spreading experiment of Carbopol at 0.2 w% ($k = 12.7 \text{ Pa}\cdot\text{s}^n$, $n = 0.40$) at $V=2.5 \text{ mm/s}$ (dots). The dashed line correspond to the equation 3.7, the numerical prefactor has been chosen so that $e(l_w = 0 - 20) \in [0, 200] \mu\text{m}$. This equation is plotted to highlight the difference in shape with the experimental data. The orange and blue circles corresponds to $t = 12$ and 32 s . **b.** Top pictures of the blade during the experiment at 12 s (top) and 32 s (bottom). The yellow line is drawn at $s = 39 \text{ mm}$ to facilitate comparison. **c.** Side pictures of the blade taken at 12 s (left) and 32 s (right). The shape of the blade is highlighted by orange and blue lines respectively. The two shapes are compared in the bottom image. The inset is a zoom at the end of the blade. The blade goes down between $t = 12 \text{ s}$ and 32 s .

syringe at the estimated position of the blade end, and then the blade is set on top. Without a yield stress, the blade elasticity compresses the fluid underneath until a corner is formed. With a yield stress fluid, the fluid acts as an elastic solid and the blade can stay on top of it, leaving a gap of a few millimeters between the tip of the blade and the substrate. To get a situation where the fluid fills a corner between the blade end and the surface, the blade end is manually pressed down on the fluid. This is source of reproducibility issues as it is difficult to ensure an equivalent initial state. During the spreading experiment, after an initial decrease of l_w linked to the setting in motion of the system, l_w varies very little during several seconds, the situation is "blocked". This situation is schematized in Figure 4.16a. The blade goes down until a certain point where we assume the fluid elasticity becomes second order compared to the viscous stress. From that moment l_w starts to decrease significantly with e as expected theoretically.

4.2.5 Fluid partially stuck under the blade

Experimental observations

When looking at some of the deposition profiles, $e = f(t)$, independently, we can observe quite often small bumps. The thickness no longer decreases continuously in phase II, but increases temporarily before decreasing again. An example is given in Figure 4.12. Note that using Carbopol with a higher yield stress amplifies this phenomenon, as reported by C. Kusina (Fig. 1.10), and that not only one, but several consecutive bumps are observed for $\tau_y \geq 60$ Pa and high spreading velocities [3]. Kusina postulated these bumps were the manifestation of instabilities arising when the fluid is no longer able to recirculate under the blade. To evaluate this assumption experimentally, one must closely examine what happens under the blade during spreading.

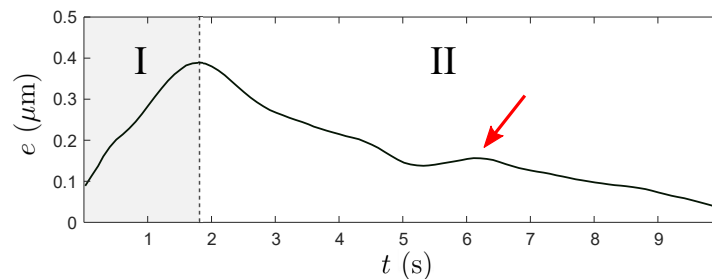


Fig. 4.12 – Average thickness over the film width as a function of time, during the spreading at $V = 10$ mm/s of 0.83 cm^3 of Carbopol 0.2 w%. Instead of a continuous decrease in phase II, at $t = 5.3$ s the thickness is observed to increase temporarily.

Using an optical camera, it can be determined that some of the fluid remains stuck under the blade in a triangular shape as evidenced in Figure 4.13. We call it a "passive volume" because it does not participate anymore in the formation of the fluid film. The rest of the fluid ("active volume") is spread: the triple contact line moves towards the blade tip. As a consequence, the length of the liquid supporting the blade decreases and the blade progressively goes down.

At some point, the fluid stuck under the blade can enter in contact with the moving substrate, as observed in Figure 4.13b and illustrated in Figure 4.16b. It starts to be partially sheared and a part of it is spread. Experimentally, this area of fluid appears as a dark spot as shown in Figure 4.14. This increase in "active" volume is thought to be the cause of the increase in thickness and explain the presence of bumps in the deposition profile. In such situations, l_w can no longer be defined and the fluid stuck under the blade has an additional weight that should be taken into account in the scaling law balance.

It should be noted that, even for low yield stresses (e.g. 6.3 and 23 Pa), a part of the fluid remains stuck under the blade. Most of the time, the conditions for the passive volume of fluid to be redeposited are not met and this does not lead to bumpy profiles. However, ignoring this volume in the deposition models would lead to divergences.

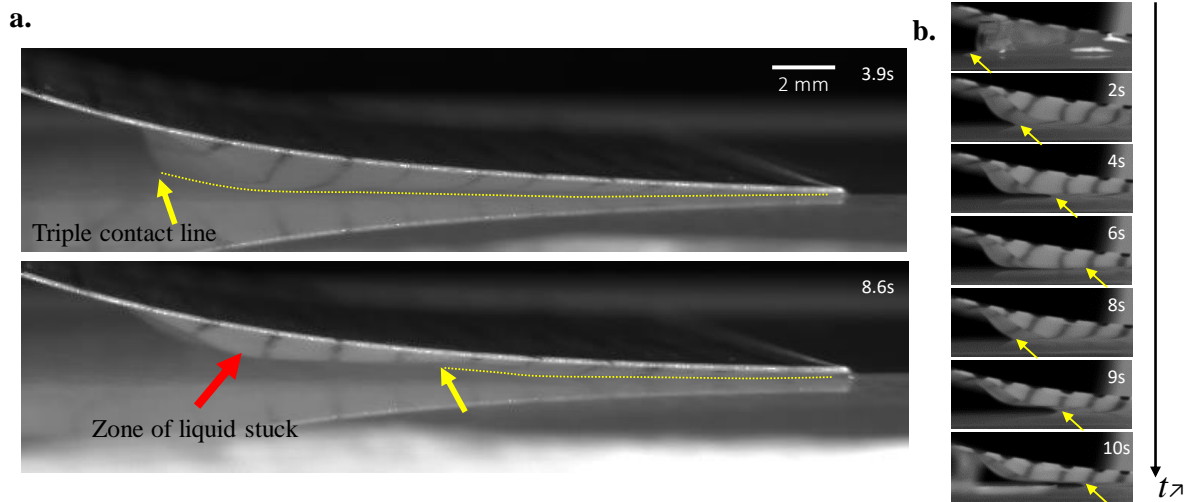


Fig. 4.13 – Two examples of partial deposition of liquid under the blade for an initial volume Ω_0 of 0.2 w% Carbopol spread at $V = 10$ mm/s with **a.** a 125 μm thick blade ($B = 1.0$ mN m) and $\Omega_0 = 0.91$ cm³, or **b.** a 250 μm thick blade ($B = 7.1$ mN m) and $\Omega_0 = 0.78$ cm³. At the back of the reservoir, the triple contact line on the substrate represented in **a.** (in yellow) moves to the right. However the triple contact line on the blade does not move. Note that there is a small perspective effect on the pictures. In **b.** the liquid stuck under the blade enters in contact with the substrate at $t = 8$ s and a re-deposition is observed.

In addition, experiments with solid particles tracers did not allow to observe any recirculation near the blade. The existence of negative velocity near the blade is not questioned but we think that it is a marginal effect that does not allow an efficient recirculation of the fluid.

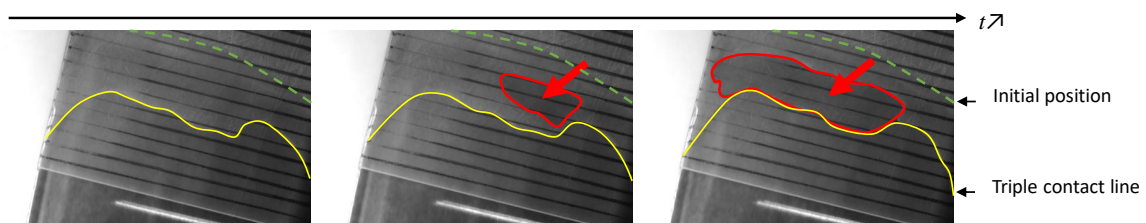


Fig. 4.14 – Top view of the spreading experiment of 0.2 wt% Carbopol gel ($\Omega_0 = 0.69$ cm³, $V = 10$ mm/s, $B = 1.0$ mN m). The pictures taken at 0.5 s of interval evidence the redeposition of a part of the fluid stuck under the blade (circled in red). The initial l_w is shown in green dashed line and the positions of the triple contact lines with the substrate are shown in solid lines. In the zone where the liquid is in contact with both substrate and blade, it appears in dark grey. When the fluid is stuck under the blade is not visible from the top. It appears only when it enters in contact with the substrate and is redeposited.

Prediction of the fluid residual under the blade

The behaviour observed under the blade that has been described before can be explained by stating that a part of the fluid under the blade is not sheared enough to be considered liquid-like, i.e. $|\tau(y)| < \tau_y$.

Consequently, when the fluid is deposited, part of it does not flow and gets stuck under the blade as a solid would. This is predicted by Kusina and coworkers [3]. They adopted the same assumptions as those made in this manuscript: gravity was neglected and they assumed laminar flow. They defined $\lambda_i(x)$ and $\lambda_o(x)$ as the two positions where $\tau(\lambda_i) = -\tau_y$ and $\tau(\lambda_o) = \tau_y$ (Fig. 4.15). Three regions can be distinguished based on the number of liquid-like and solid-like regions under the blade. In the first one, both λ_i and λ_o are defined in the fluid, meaning liquid with negative velocity is expected near the blade surface. In the second region, only λ_i is defined: a liquid region in contact with the substrate is overlaid with a solid region in contact with the blade. And in the third region, the fluid is liquid-like over its entire height.

To obtain the λ_i and λ_o positions, we use the calculations proposed by Kusina [3]. They are recalled in Appendix F.

In region I, λ_i and λ_o are defined by a system of two equations:

$$\frac{1+n}{n} \left[\frac{k(\lambda_o - \lambda_i)}{2\tau_y} \right]^{\frac{1}{n}} V = \lambda_i^{1+\frac{1}{n}} - (h - \lambda_o)^{1+\frac{1}{n}} \quad (4.4)$$

$$\frac{(1+n)(1+2n)}{n} \left[\frac{k(\lambda_o - \lambda_i)}{2\tau_y} \right]^{\frac{1}{n}} eV = n\lambda_i^{2+\frac{1}{n}} - (h + nh + n\lambda_o)(h - \lambda_o)^{1+\frac{1}{n}} \quad (4.5)$$

In region II, only λ_i is defined in the fluid and happens to be independent of x :

$$\lambda_i = \frac{1+2n}{n} e \quad (4.6)$$

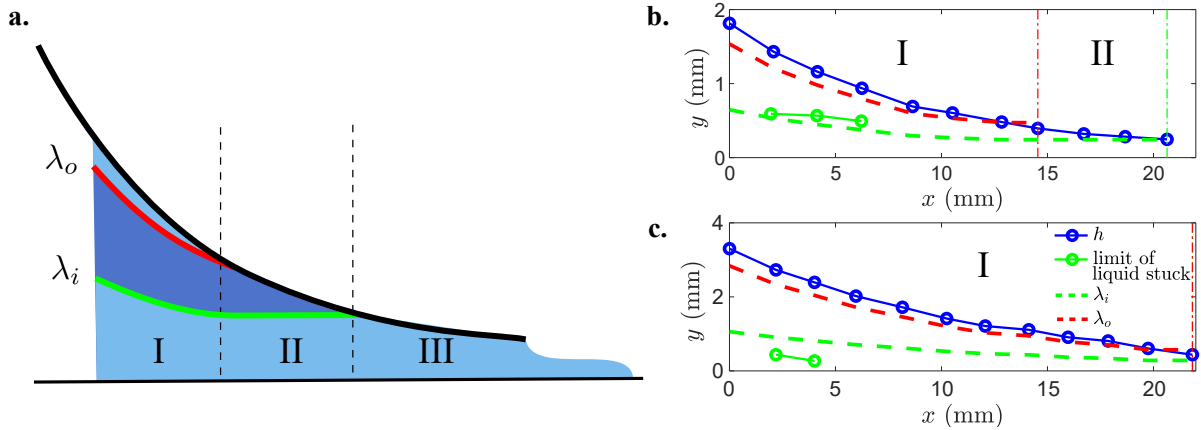


Fig. 4.15 – **a.** Schematic representation of the blade and the flow regions beneath it (adaptated form Kusina [3]). **b.** and **c.** Evaluation of $\lambda_i(x)$ (green dashed line) and $\lambda_o(x)$ (red dashed line) from Equation 4.4, 4.5 and 4.6 using experimentally measured $h(x)$ (blue markers). λ_i is compared to the height at which the liquid is stuck under the blade (green markers). The experimental data used in **b.** correspond to Figure 4.13a at $t_g = 8.6$ s, and in **c.** to Carbopol at 0.2 w% spread with a thicker blade ($B = 7.1$ mN.m, $V = 10$ mm/s, $\Omega_0 = 1.12$ cm³) at $t_g = 7.5$ s.

It is possible to evaluate the value of λ_i (and λ_o) in our experiments at a given time t_g . The pictures taken during the spreading from the side give access to the experimental value of $h(x, t_g)$ and the profilometer measured the corresponding deposited thickness $e(t_g)$. Equations 4.4, 4.5 and 4.6 are then solved. Two examples are plotted in Figure 4.15. In some cases, the calculated boundary height between the solid-like and liquid-like regions (λ_i) matches quite well with the experimentally measured shape of the fluid stuck (Fig. 4.15b). For other situations, the volume of fluid stuck is more important than predicted by computing the interface position (Fig. 4.15c).

This can be explained by several factors. First, the camera axis is sometimes slightly above the blade. Second, it images well what happens on the side, the measurements are therefore sensitive to the edge effects. Furthermore using particle tracers, the fluid velocity at the back of the reservoir showed a visible component along y in addition to the one along x for the large fluid volumes, which questions the lubrication approximation used to write the equations. Performing these measurements with a rigid fixed blade would help conclude if the fluid stuck precisely corresponds to the solid-like region.

Here we have highlighted at least two limiting phenomena that may explain the variation of the experimental data when spreading yield stress fluids with a soft blade. They are summarized in Figure 4.16.

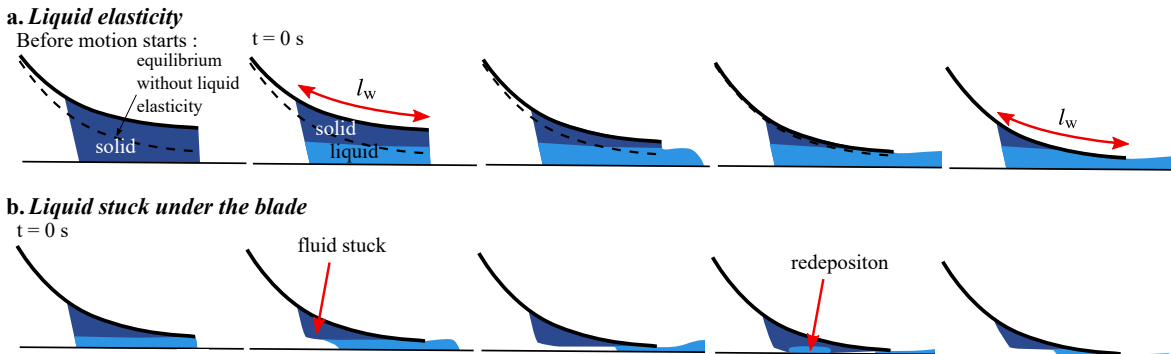


Fig. 4.16 – Schematic representation of the two limiting effects that were observed. **a.** The blade equilibrium is affected by the fluid elasticity due to the yield stress and l_w does not significantly vary during the deposition process. **b.** Some of the fluid is stuck under the blade and might be deposited later on, resulting in bumps in the deposit.

Conclusion – Chapter 4

In this chapter, we studied the film thickness of a shear-thinning fluid that additionally exhibits either yield stress or positive first normal stress difference:

1. We showed that normal stresses plays a little role with this spreading geometry even for a Weissenberg number of order of 10. Experimentally, no significant difference was observed in the deposition law between a shear-thinning fluid and a fluid that additionally generates normal forces. The normal stress fluid could be satisfactorily described by the scaling law and the numerical computations presented in Chapter 3 for shear-thinning fluids.
2. We proposed a new dimensionless number, involving a geometric factor, to predict whether or not normal stresses have an effect on the deposited thickness.
3. These results further confirm that soft blade coating of a finite reservoir of fluid is not analogous to dip-coating as the two processes do not involve the same characteristic length scale: an externally imposed length in blade coating (the wetting length l_w), versus an internal length (the meniscus deformation) in dip-coating, which explains why normal stresses have an effect on thickness with dip-coating and not with soft blade coating geometries.
4. The study of soft blade coating of a yield stress fluid like Carbopol showed some limitations and no model was found to predict the thickness deposited in this situation. This is mainly due to the fact that the presence of yield stress leads to an emptying of the reservoir which can no longer be described by a decrease of l_w . Either because the initial equilibrium of the blade also involves the elasticity of the fluid which results in a reservoir emptying preferentially from bottom to top rather than from left to right during the spreading. In this case l_w is no longer a measure of the change in reservoir volume. Or because part of the fluid remains stuck under the blade and can sometimes be deposited afterwards creating bumpy profiles. In most experiments, both situations are combined, leading to a large scattering of the data.

4.4 Perspectives

The fact that the gap is not fixed and that the blade can move vertically make the measurement sensitive to the problems described above. We believe that in the case of a rigid blade (whose shape and position are fixed) it would be possible to study and predict the deposited thickness by adapting the model proposed by C. Kusina [3]. In this case, the blade position would no longer be defined by an equilibrium involving changing contributions. And even if part of the liquid could remain stuck under the blade, it would not redeposit during the process (fixed blade), therefore this effect could be estimated and taken into account in the model. However, the use of a rigid blade with a fixed gap takes us away from the

model of the cosmetic spreading by a finger. It was therefore decided not to pursue further this line of research, but rather to study cosmetic spreading from another angle. So far, we have studied really simple cosmetic fluid models, consisting only of polymer solutions. In practice, most cosmetics such as moisturizers, foundations, nail polishes, mascaras... contain solid particles in suspension. Focusing on cream type formulas, we sometimes observe the appearance of particle aggregates when the product is spread on the skin. In this second part, the problematic is the following: ***Why defects such as aggregates appear during the application of some formulations?***

To study these defects, model formulations containing solid particles are used and new spreading set-ups are developed. In Chapter 5, the different physical concepts needed afterwards to understand the aggregate formation are presented. In Chapter 6, the spreading experiments performed and their results are described. We then propose a model to explain the formation of these defects. And finally we give a formulation criterion to be respected to limit their appearance.

Part II

Suspensions

Chapter 5

Introduction - Part II

In this second part of the manuscript we study the effect of solid particles, present in cosmetic formulations, on spreading defects, with particular interest in the formation of aggregates. In comparison to the first part we will not study "simple" fluids but suspensions of solid particles. Moreover, in order to get closer to the real conditions of use of cosmetic products, we wish to use a soft substrate reproducing the mechanical properties of the skin, and make the spreading gesture more complex.

This chapter presents the bibliographical analysis carried out on suspensions, their rheological behavior, and their drying, which might lead to a granulation. Notions about adhesion and cohesion are also described. Then we present the characteristics of the human skin and the experimental models that have been developed in the literature to reproduce its mechanical and surface properties.

Contents

5.1	Suspension of particles	104
5.1.1	Phase diagram	104
5.1.2	Rheology of dense suspensions	107
5.1.3	Suspensions of particles in a yield stress fluid	111
5.2	Drying	112
5.2.1	Drying of a sessile droplet	112
5.2.2	Drying of complex fluids	112
5.3	Adhesion and cohesion	114
5.3.1	Differentiation between tackiness, stickiness, adhesion, and cohesion	114
5.3.2	Main categories of material adhesives	115
5.3.3	Adhesion tests	116
5.3.4	Results of a tack test	117
5.3.5	Link with rheological properties	119
5.4	Soft substrate: the skin	121
5.4.1	Skin structure	121
5.4.2	Mechanical characteristics	123

5.4.3	Surface properties	126
5.4.4	Skin Models in the literature	126
5.4.5	Focus on PDMS	128
5.5	Goals of this thesis - Part II	128
5.6	Conclusion	129

5.1 Suspension of particles

A suspension is a particular case of dispersion where the continuous phase is liquid and the suspended elements are solid. The flow of a suspension depends on the flow of the liquid around the solid particles, so it is more difficult to make a suspension flow than the pure liquid because the particles create a disturbance. The volume fraction in a suspension is therefore a fundamental parameter for understanding its flow properties.

5.1.1 Phase diagram

The different regimes

The solid volume fraction of a suspension (often called concentration) is defined as the volume occupied by the solid particles, v_p , in the total volume (volume of the particles and the interstitial liquid v_{il}):

$$\phi(v\%) = \frac{v_p}{v_p + v_{il}} \quad (5.1)$$

Porosity and particle swelling must be taken into account to evaluate the effective volume fraction (see section 6.6.2).

When increasing the volume fraction of particles in a liquid, they pack more and more closely until there is not enough liquid to embed all particles. Above that point several objects are formed: it corresponds to the granulation regime. A schematic representation is given in Figure 5.1 and illustrative experiments are shown in Figure 6.30.

Several regimes can be defined regarding the suspension:

- *the diluted regime*: the concentration is low enough for the particles to behave as if they were alone in the liquid, they do not interact hydrodynamically.
- *the semi-diluted regime*: at a volume fraction beyond a few percent, the particles interact hydrodynamically, by their presence they disturb the flow over distances greater than the distance which separates them from their neighbors.
- *the concentrated regime*: the hydrodynamic interactions are not necessarily predominant, the contacts between the particles play a role and the behavior of the system reflects the evolution of particles network under shear. The system begins to have great difficulty flowing because particle

jamming can occur under shear through the formation of continuous chains of particles in contact with one another and opposing the induced motion. The viscosity, which measures the ability of a material to flow, begins to diverge.

- *the compact regime*: it corresponds to the maximum packing fraction of the particles in a liquid. The system is no longer able to flow. At this volume fraction the viscosity diverges.

The transition from the purely hydrodynamical regime to the one where contacts play a role is around 35 v% [115].

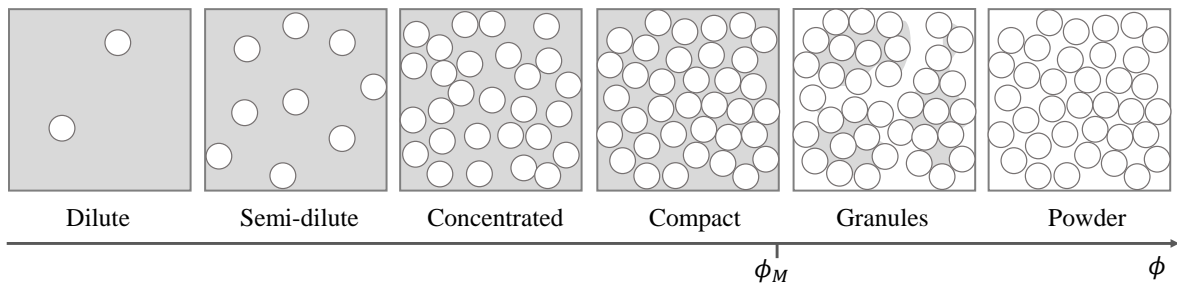


Fig. 5.1 – Phase diagram of solid particles in a solvent (adapted from [116])

Maximum packing fractions

The transition from compact regime to granules occurs at the maximum packing fraction ϕ_M , at which the viscosity diverges (see section 5.1.2). For monodisperse hard spheres, in frictionless contact ($\mu = 0$), ϕ_M is called the random close packing fraction ϕ_{RCP} . Empirically, computations and experiments have given $\phi_{RCP} \approx 64$ v% [117, 118]. It can be noted that this value is lower than the maximum "organized" packing fraction which is 74 v% for face-centered cubic and hexagonal compact packings.

In practice, the value of ϕ_M is strongly affected by the shape, polydispersity and friction of the particles, as well as by the interactions between particles. With non-spherical particles, the packing is less efficient, the particles do not organize easily when they are angular or have asperities, leading to jamming situations at lower volume fraction [119]. Particles with high friction (sliding or rolling friction) have difficulty moving relative to other particles, which is also a decay factor of ϕ_M as shown in Figure 5.2 [21, 120, 121]. Conversely, having polydisperse particles increases the attainable value of ϕ_M . The small particles can fill some of the interstitial space left between the large particles. McGeary showed in an idealized experimental study it is possible to reach a solid fraction as high as 95 v% for a quaternary system of spheres with diameter ratio up to 316 [122]. Without attaining such level of space optimization, binary systems have been shown to significantly increase the maximum packing fraction [123–125]. At equivalent mass fraction of solid particles, a polydisperse system has a lower viscosity than a monodisperse one. Finally, in presence of attractive forces the particles can form aggregates and agglomerates that prevent packing optimization: this creates structures full of voids that reduce the ϕ_M .

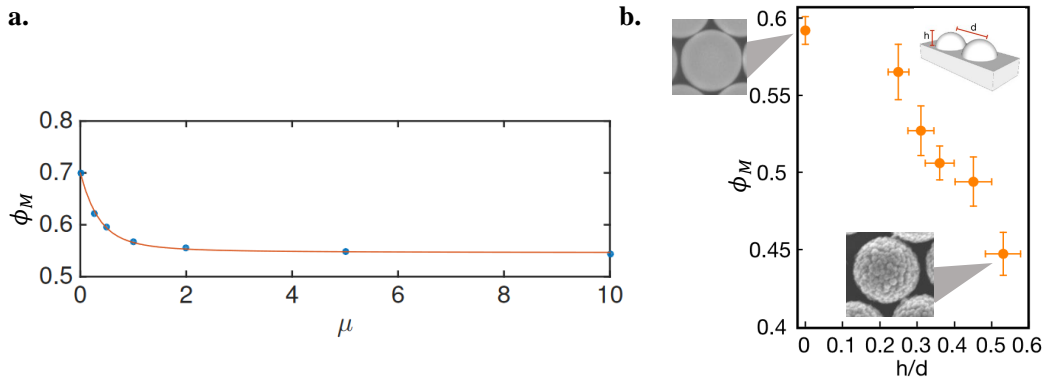


Fig. 5.2 – **a.** Numerical evaluation of ϕ_M as a function of the friction coefficient μ (from [121]). **b.** Experimental measurement of ϕ_M as a function of the roughness parameter h/d defined in the schematic representation (adapted from [21]).

Granulation

Above ϕ_M , shearing the suspension makes it granulate (Fig. 5.1). Conducting rheological measurements in this range of volume fractions is irrelevant because the material is inhomogeneous and more like a solid than a liquid. As the solid content increases, the granules are smaller and more numerous until at a some point a dry granular media is obtained. The granules belong to the wet granular materials, they are cohesive due to the capillary forces that generate suction between the beads. Closer examination shows that several states allow cohesion between beads: the capillary, the funicular and the pendular states (Fig. 5.3a). The force at a neck of a capillary bridge can be written: $F_{\text{bridge}} = 2\pi r_2 \gamma + \pi r_2^2 \Delta P$ with the surface tension γ , the radius of the neck r_2 and the suction $\Delta P = \gamma \left[\frac{1}{r_1} - \frac{1}{r_2} \right]$ derived from the Young-Laplace equation (Fig. 5.3b). The suction increases as the liquid content decreases, while the overall cohesion goes through a maximum in the funicular state [126]. Granules can also be formed at volume fractions slightly below ϕ_M . Cates observed the formation of a matt granule by shearing a droplet from a very dense shear-thickening suspension [127]. Under the effect of shear, the material wants to expand (dilatancy), which leads to partial emergence of the beads on the surface of the droplet (Fig. 5.3c). The system is jammed and can be maintained in this state by the capillary forces created at the surface [128].

Cosmetic creams are suspensions of solid particles initially in the diluted or semi-diluted regime. However, during the drying stage, most of the liquid volume is evaporated since the first ingredient in most products is water. This is like going through the phase diagram from left to right until reaching the particle volume fraction in the non-volatile phase (Fig. 5.1). The final stage of the cosmetic product on the skin is often a dense suspension. We focus here on the rheology of concentrated suspensions and only briefly address the case of diluted suspensions.

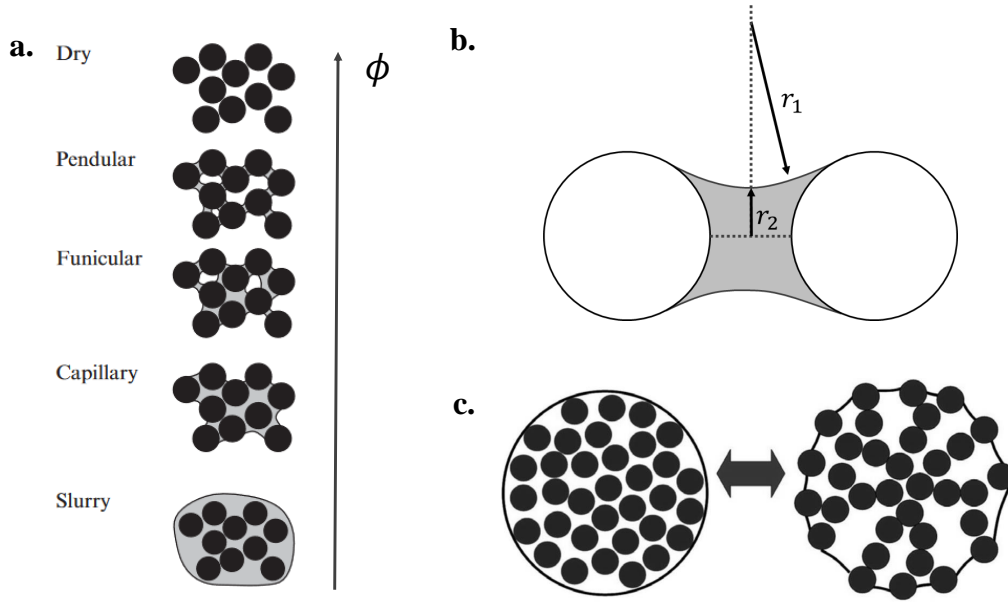


Fig. 5.3 – **a.** Diagram of granular media when varying ϕ . In the capillary state the pores are filled with liquids while in pendular state the liquid bridges are located between the grains. **b.** Schematic representation of a liquid bridge between two particles. (**a.** and **b.** adapted from [126]) **c.** A fluid (left) and the solid droplet (right) obtained after shearing. Under the effect of vibration, it returns to its liquid state (from [127]).

5.1.2 Rheology of dense suspensions

Dimensional analysis

In the general situation, the viscosity of a suspension is a function of several independent variables: the solid fraction ϕ (or the particle pressure P), the particle diameter d_p , the particle density ρ_p , the fluid density ρ_f , the fluid viscosity η_f , the shear rate $\dot{\gamma}$ (or the shear stress τ) and the thermal energy $k_B T$.

$$\eta = f(P, d_p, \rho_p, \rho_f, \eta_f, \dot{\gamma}, k_B T) \quad (5.2)$$

These variables can all be expressed in mass, length and time dimensions. According to the Buckingham- π theorem, four dimensionless parameters are needed to fully describe the system.

$$\eta = f(I_v, St, Pe, Sh) \quad (5.3)$$

where $St = \frac{\rho_p \dot{\gamma} d_p^2}{\eta_f}$ is the Stokes number which characterizes the interplay between viscous and inertial flow, $Pe = \frac{3\pi\eta_f \dot{\gamma} d_p^3}{4k_B T}$ is the Péclet number which compares the advective and diffusive transport, $Sh = \frac{\eta_f \dot{\gamma}}{\Delta\rho g d_p}$ is the Shield number which quantifies buoyancy or sedimentation, and I_v is a number comparing the microscopic time of rearrangement η_f/P with the macroscopic time $1/\dot{\gamma}$ [129].

Non-Brownian suspensions

The number of dimensionless parameters can be reduced if we consider that the particles are large enough to be considered non-Brownian ($Pe \rightarrow \infty$), that the system is density matched and/or the fluid is highly viscous ($Sh \rightarrow \infty$), and that the viscous forces are much larger than inertial forces ($St \rightarrow 0$). Experimentally, we evaluated for the "dry" formulation (see Chapter 6): $St < 10^{-10}$, $Pe > 10^7$, and $Sh > 10^7$, using $\eta_f \in [10^2, 10^4]$ Pa.s, $\dot{\gamma} \in [10^{-1}, 10^2]$ s $^{-1}$, $d_p = 5$ μm , $T = 298$ K, $\rho_p = 2.15 \cdot 10^3$ kg.m $^{-3}$, and $\rho_f = 1.26 \cdot 10^3$ kg.m $^{-3}$. Therefore, the viscosity can be considered to depend only on four dimensional parameters $\eta = f(P, d_p, \eta_f, \dot{\gamma})$ and thus on a unique dimensionless number I_v . The constitutive laws can be expressed as functions of I_v : $\phi = g(I_v)$ and $\tau = \mu(I_v)P$ [129]. Using the definition of $I_v = \eta_f \dot{\gamma} / P$, we can write $\tau = \mu[g^{-1}(\phi)] \frac{\eta_f \dot{\gamma}}{g^{-1}(\phi)}$ with μ the effective friction law. This expression can be rewritten in terms of viscosity:

$$\tau = \eta(\phi) \dot{\gamma} \quad \text{with} \quad \eta(\phi) = \eta_f \frac{\mu[g^{-1}(\phi)]}{g^{-1}(\phi)} \quad (5.4)$$

This equation means that a suspension of spherical and rigid non-Brownian particles with low Stokes and Shield numbers behaves as a Newtonian fluid: assuming the volume fraction is homogeneous, the viscosity is therefore constant in the fluid and does not vary with the shear rate.

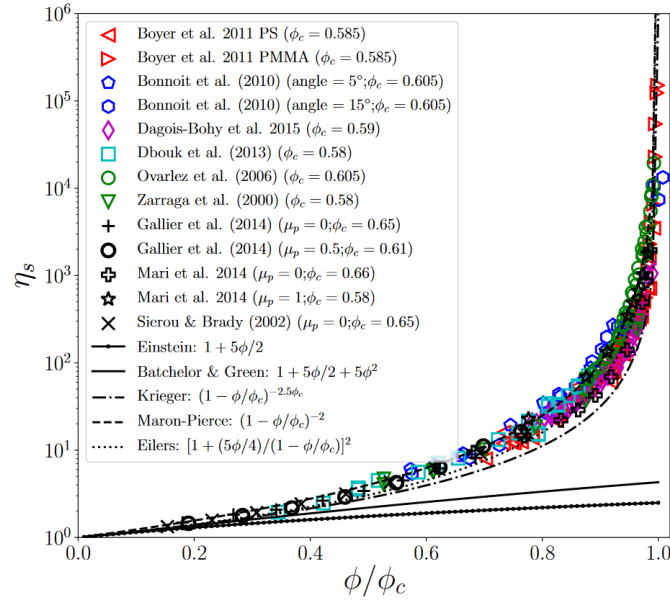


Fig. 5.4 – Relative viscosity $\eta_s = \eta/\eta_f$ as a function of the reduced volume fraction ϕ/ϕ_c . ϕ_c is the notation used here for the maximum packing fraction ϕ_M . The black markers correspond to numerical simulations and color markers to experiments with poly(methylmethacrylate), polystyrene and glass spheres suspensions. The lines shows the different laws $\eta_s = f(\phi)$ and in particular the Einstein and Krieger laws (reproduced from [130]).

$\eta(\phi)$ for the different concentration regimes:

In the diluted regime, $\eta(\phi)$ can be expressed as an affine function of ϕ [131]:

$$\eta = \eta_f(1 + [\eta]\phi) \quad (5.5)$$

with $[\eta]$ the Einstein coefficient or "intrinsic viscosity" often considered to be $[\eta] = 2.5$ even though different values have been reported in practice in the literature [132].

In the concentrated regime, the interparticle distances become lower than the particle size. The spacial arrangement of the particles and their interaction (lubrication and friction) makes modeling and experimentation more delicate. Empirical correlations have been proposed but there is no general consensus. The most popular model has been proposed by Krieger and Dougherty [133]:

$$\eta = \eta_f \left(1 - \frac{\phi}{\phi_M}\right)^{-[\eta]\phi_M} \quad (5.6)$$

The others models often differ in the value of the exponent, sometimes taken simply as 2 [43]. Figure 5.4 compares the different laws with experimental and numerical data reported in the literature. The Krieger Dougherty model is often used to estimate the value of ϕ_M from rheological measurements of viscosity.

In practice, most of the suspensions studied in the literature do not show the expected Newtonian behavior. This is due to discrepancies with the monodisperse rigid sphere model. Note that small deviations from the model assumptions often have a negligible effect in the dilute regime but can have a noticeable effect in the concentrated regime, which is why different models are used to fit the experimental data. Such non-Newtonian behaviors result for example from the presence of colloidal forces, a change in the nature of the contact under shear, a certain polydispersity, the presence of roughness, or an inhomogeneity of the concentration or the shear rate.

Colloidal forces

Colloidal forces are attractive or repulsive forces exerted by particles on their neighbors. These forces impact the microstructure and compete with the particle pressure which leads to non-Newtonian mechanical behaviors when they are predominant. Attractive and repulsive forces can have various origins such as: van der Waals interactions, electrostatic forces, adsorbed polymers layers and depletion [116]. We do not detail these aspects here, but focus on the associated rheological behaviors.

Attractive suspensions

Attractive particles tend to aggregate (Fig. 5.5). When a percolating network is created it corresponds to an attractive colloidal gel. At rest, the structure does not flow, it is a yield stress fluid [14, 24].

For $\tau > \tau_y$, the stress is sufficient to break the aggregate network and the mixture starts to flow. As the shear rate goes up, the clusters are broken into smaller pieces, resulting in a decrease in viscosity,

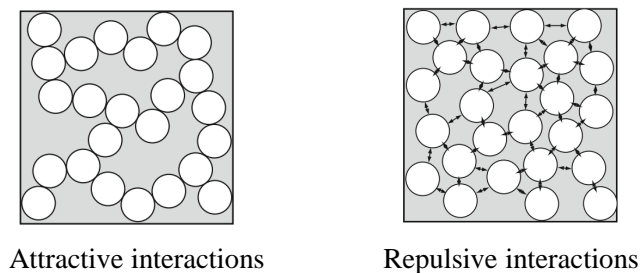


Fig. 5.5 – Attractive and repulsive suspensions in the concentrated regime (from [116])

characteristic of shear-thinning behavior [14, 18]. These systems can be complex to study because their rheological properties are strongly dependent on the aggregate network, itself dependent on the preparation steps, rest times and aggregation dynamics.

Repulsive suspensions

Repulsive particles can be thought of as soft particles with a larger effective radius, resulting in a larger effective volume fraction. At high concentrations, a network of interactions can jam the suspension, even if no direct contact exists between the particles, as long as the interaction potential is stronger than the thermal agitation (Fig. 5.5). In that case, the mixture is a yield stress fluid [134].

Under flow, the particle pressure increases with the shear rate leading to lower effective volume fraction. As a result, the viscosity is reduced, the suspension is shear-thinning [135].

A shear-thickening behavior can be observed when the particle pressure force becomes dominant over the repulsive forces. The contact between the particles shifts from lubricated to frictional [19, 136, 137]. The law $\eta = f(\phi)$ is modified since it depends on the friction between the particles. Thus, at a given volume fraction, the viscosity increases (Fig. 5.6b) [136]. Shear-thickening amplifies with the volume fraction of the particles: by increasing ϕ , the jump from one curve to the other is higher (Fig 5.6a).

These systems can again be shear-thinning at higher shear rate, which corresponds to high particle pressure. It has been shown that the friction coefficient μ of particles in frictional contact decreases with applied normal force [135, 138], resulting in enhanced flow and reduced viscosity. This behavior is observed both when the suspension is initially frictional at $\dot{\gamma} = 0 \text{ s}^{-1}$ [138], and when it is initially in the lubricated state and brought to the frictional regime by shearing the solution sufficiently strongly [135]. The decrease of μ with the normal force can have various origins: it can result as the transition from an elastic to a plastic contact due to the presence of surface asperities [138] or be linked to the formation of a soft layer induced by the swelling of the particles [15].

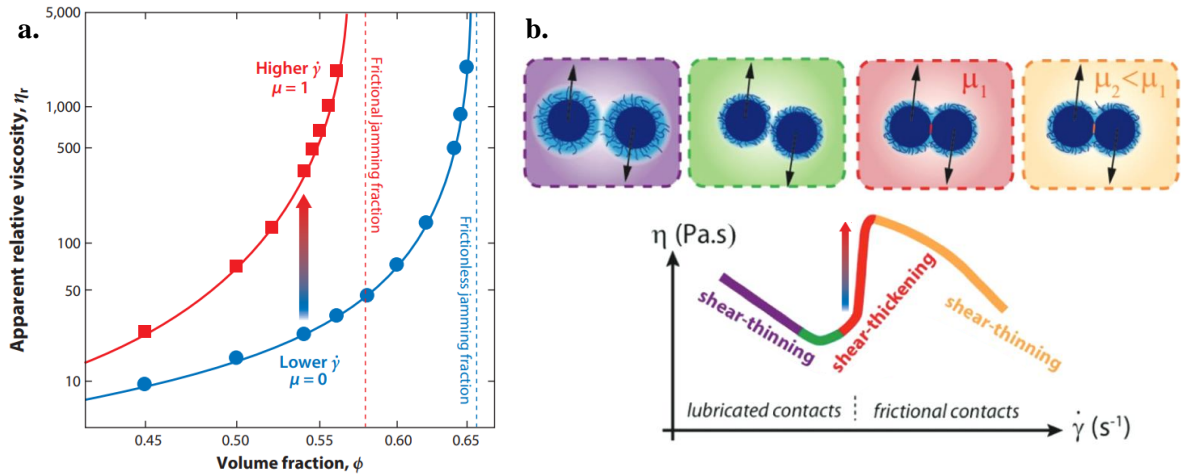


Fig. 5.6 – **a.** Relative viscosity η_r as a function of ϕ for the limit of lubricated ($\mu = 0$) and frictional ($\mu = 1$) situations. By increasing the shear rate the friction increases and the viscosity transitions from the low to high curve (from [20]). **b.** Schematic representation of the flow curve $\eta = f(\dot{\gamma})$ showing the different behaviors encountered for a repulsive system made of beads with polymer brushes at the surface. It is first shear-thinning, then shear-thickening, then shear-thinning again (adapted from [135]).

5.1.3 Suspensions of particles in a yield stress fluid

At rest

In a yield stress fluid at rest, the suspended particles need to overcome a critical force F_c to be set in motion: $F_c = 14\pi R^2 \tau_y$ for a spherical object [139]. This drag force does not tend towards zero when the particle moves infinitely slowly, contrary to the Newtonian case. In fact a significant deformation needs to be applied to the surrounding yield stress fluid to make it transition from a solid to a liquid in a sphere of twice the radius of the particle. This property is useful to obtain stable suspensions of particles that are not density matched with the fluid. If the particles are small enough and the yield stress is high enough, sedimentation is prevented. The stability condition at rest is: $\Delta\rho g \Omega_p < F_c$ with $\Delta\rho$ the density difference and Ω_p the particle volume [116].

Under shear

Under shear the yield stress fluid behaves as a liquid and the suspended particles sediment if their density is higher than that of the fluid. Adding particles to a yield stress fluid does not change its overall behavior: it is still a yield stress fluid with only a higher apparent viscosity [140]. In the solid regime, the fluid can be assumed to be purely elastic, the particles can be considered to have an analogous effect on the elastic modulus than on the viscosity of a Newtonian fluid. Thus, in a first approximation for the concentrated regime, $G = G_0(1 - \frac{\phi}{\phi_M})^{-2.5\phi_M}$ with G_0 the elastic modulus without particles [140].

5.2 Drying

An important phenomenon occurring during the application of a cosmetic is drying. Indeed, the first ingredient of a hydrating cream is water, this solvent facilitates the transport of non-volatile cosmetic principles (solid particles, polymers, emulsion droplets) during spreading and is used to give a desired texture to the product. Giorgiutti-Dauphiné and Pauchard recently published a review describing the drying of drops with a solute [141]. We present here the main mechanisms applicable to the drying of cosmetic creams.

5.2.1 Drying of a sessile droplet

The drying of a liquid droplet is limited by the vaporization kinetics, the diffusion in the vapor phase, and the heat transfer. The evaporation of a cosmetic product corresponds approximately to conditions of calm atmosphere, it is thus considered that the limiting factor is the diffusive transport of water molecules in the ambient air. This diffusion determines the evaporation rate. Generally, the droplet evolves in two modes: *i*) its contact line with the substrate can be pinned, i.e. the contact surface remains constant, *ii*) or it retracts with a constant contact angle (Fig. 5.7b and a). Pinned situations can occur for example because of surface roughness [51], if the contact angle is not small enough [142] or when solutes are present in the composition.

The presence of non-volatile constituents in the cosmetic formulation (such as solid particles, oil emulsion droplet, polymers), makes the drying mechanism more complex and we present below two classical effects.

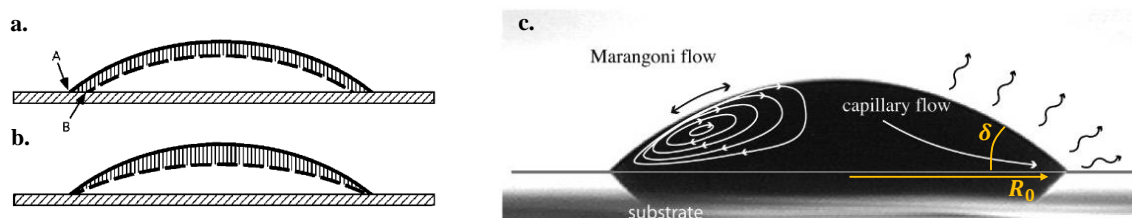


Fig. 5.7 – **a.** Unpinned contact line associated with uniform evaporation: the contact area decreases progressively while the contact angle remains constant. **b.** Pinned contact line leading to advective current: the contact angle progressively decreases (from [143]). **c.** Illustration of capillary and Marangoni flows (from [141]).

5.2.2 Drying of complex fluids

Pinned contact line

When non-volatile compounds are present in solution, they deposit near the triple line that is pinned to the substrate [143, 144]. Unlike the evaporation of a pure water droplet [141], the radius R_0 of a

pinned droplet does not decrease during the drying, only the droplet thickness, and the contact angle δ decreases (Fig 5.7b). Sometimes, stick-slip motions are observed with an alternation of pinned and unpinned steps [145]. In the particular case of a cosmetic cream, they often present a yield stress (e.g. carbopol gel or dense emulsions) which is another factor known to pin a contact line [146].

For a pinned sessile drop (droplet lying on a surface) such that R_0 is less than the capillary length, the local evaporation flux close to the contact line, J scales as [143]:

$$J \sim \left(\frac{1}{R_0 - r} \right)^{\frac{\pi - 2\delta}{2(\pi - \delta)}} \quad (5.7)$$

with r the distance from the center to the triple line. For $\delta < \pi/2$ (wetting scenario), the evaporation flux is maximal (it diverges) at the contact line. This inhomogeneity in evaporation flux leads to internal flows that have an impact on the solute distribution.

Inhomogeneity of particles concentration

In the presence of non-volatile species, such as solid particles, a crust or "skin" may form at the surface of the droplet [141, 143, 147] (Fig 5.8). Evaporative flux causes particles to accumulate near the surface of the droplet if advection dominates particle diffusion [148]. The effect is enhanced at the edges by inner radial flows (Fig 5.7c). Indeed, since drying is faster at the edges when $\delta < 90^\circ$ (Eq 5.7), a strong outward capillary flow inside the drop is produced to replenishing the corner [143]. This flow transports the solid particles which creates a zone of high particle concentration at the edge. Marangoni convection flow, originating from surface tension gradient related to surfactant concentration or temperature gradients, creates recirculation loops. The Marangoni flow can oppose the capillary flow and transport the solutes in the center [143, 149], however, most of the time (and particularly for thin drop edge), it is the capillary flow that dominates, leading to the well know coffee ring effect.

Due to this particle accumulation, a solidification front is observed: it separates a fluid domain from a porous region where solid particles are stacked. The formation of a particle crust corresponds to a "vertical drying" process which is present when the evaporation rate or solute concentration is high (Fig. 5.8). For small value of δ , horizontal drying can become dominant which leads to a liquid droplet surrounded by a disc of solid particles.

Similar crust formation occurs when drying a suspension of solid particles in a beaker near the air/liquid interface [150].

The composition (volume fraction) varies resulting in non-uniform rheological properties. Note that the evaporation can continue, despite this crust made of solid particles, as it can be considered as a porous media where permeation occurs. This is not the case for soft deformable particles that can lead to a blockage of the evaporative flux [141].

Mechanical instabilities such as buckling [151] and crack formation in the solid layer of particles can occur due to the relaxation of stresses built up during drying [150, 152]. For example, during

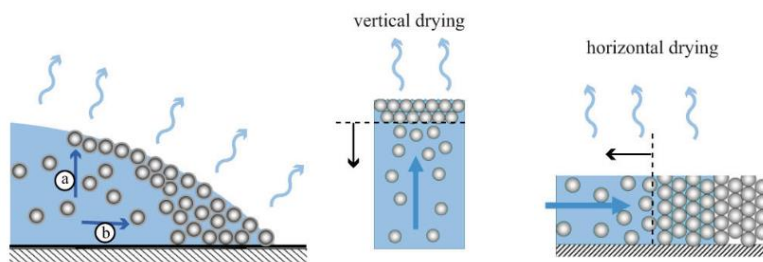


Fig. 5.8 – Schematic representation of solid particle accumulation at the drop surface (by vertical drying) and at the drop edge (by horizontal drying) leading to an envelope formation or a solid drop edge respectively (from [141]).

evaporation, the capillary meniscus formed at the liquid interface between neighboring solid particles creates a pressure gradient and strong stress. If the adhesion to the substrate is not high enough cracks may appear.

5.3 Adhesion and cohesion

In this section, we give some background information to understand the concepts of adhesion and cohesion that are used in Chapter 6. These properties have been extensively studied for elastomeric films for use in adhesive tapes and labels. In other fields, such as food [153, 154], building material [155, 156], and cosmetics [157], these properties are also important, being desired or unwanted properties for processors and customers.

5.3.1 Differentiation between tackiness, stickiness, adhesion, and cohesion

Before going any further in the description of adhesion and cohesion, we felt it was necessary to clarify the terminology as various terms - tackiness, stickiness, adhesion - are used in different research fields, sometimes without distinction, which can create some confusion. The review by Noren *et al.*, focused on distinguishing between the different terminologies previously used in the literature [154]. We use their definitions in this work.

When an adhesive and an adherend are brought into contact, they can bond either by covalent or non-covalent bonds (e.g. van der Waals interactions) at the interface: this is called *adhesion*. For the adhesion to be effective, a certain amount of time and pressing force are required. *Cohesion* describes the particular case where these two objects are made of the same material. If no force is required to separate the two objects after bringing them into contact, then they are not adhesive (or cohesive).

Several definitions have been proposed in the literature regarding tackiness and stickiness, both of which describe situations where cohesion and adhesion are involved. Two situations are usually observed when pressing an adhesive material between two surfaces before separating them: either it leaves residues on both surfaces, or it detaches from one of them (Fig. 5.9). The first case is called

cohesive failure: the adhesive forces are stronger than the cohesive forces. The opposite scenario is called *adhesive failure*. The general idea that emerges from Noren’s review is that tackiness refers to a material that undergoes adhesive failure while stickiness refers to a material that undergoes a cohesive debonding [154]. A material is said to be *tacky* if it has a high cohesion and a large energy is needed to obtain adhesive failure. For instance, a soft PDMS gel is tacky while honey is considered sticky as cohesion is very low and leads easily to cohesive failure. Of course, in practice, intermediate behavior between adhesive failure and cohesive one can be observed [153, 158], which reinforces the difficulty of categorizing the material behavior.

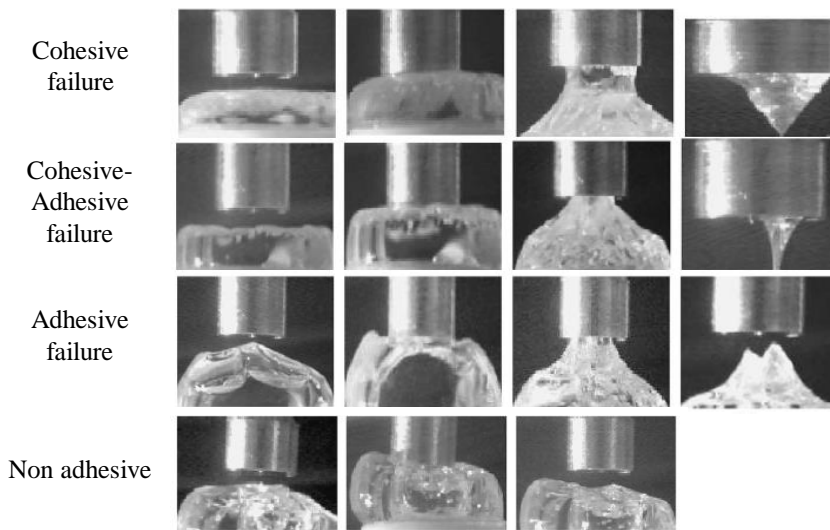


Fig. 5.9 – Several debonding mechanisms have been identified for sugar solutions (adapted from [153]). The first situation is not perfectly a cohesive failure but, for simplicity, we consider it here as such.

5.3.2 Main categories of material adhesives

Tacky and sticky materials are numerous and common. Here we present the main categories of material with these properties.

We leave aside the case of adhesive materials whose mechanism is based on covalent bonding, such as UV-curable resins, or epoxy glue, which transition from a liquid to a solid state upon curing.

Pressure sensitive adhesives (PSA) are elastomers designed to bond under light pressure on most surfaces without any activation and are not supposed to leave residuals when withdrawn. They rely on van der Waals interactions. Numerous theoretical and experimental work exists in the literature to describe the debonding mechanism of these products due to their wide range of applications. The objective is generally to require a large force to separate the adhesive and substrate surfaces while dissipating a large amount of energy during the process.

Newtonian and non-Newtonian liquids can also be sticky if they have good wetting properties with the surface. They might generate sometimes quite similar behavior than observed with PSA (e.g. cavitation and fingering instability [159]).

Colloidal and granular pastes which correspond to concentrated suspensions of particles in simple or complex fluids are also studied. The reported morphological debonding behavior most often corresponds to cohesive failure with large plastic deformation [155, 156].

5.3.3 Adhesion tests

There are different experimental techniques for analyzing the adhesive properties of a material, and they give access to different information (Fig. 5.10).

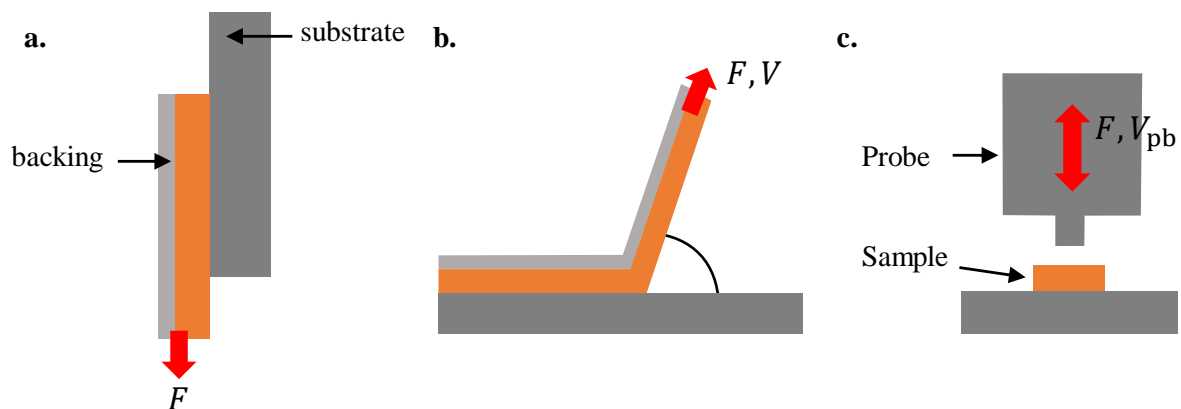


Fig. 5.10 – a. Shear test b. Peel test c. Probe tack test

- **The shear test** (Fig 5.10a). It measures the resistance of the material to shear. A strip of adhesive is brought into contact with a substrate and subjected to a constant shear stress. The time taken to reach the failure of the assembly indicates the shear holding power of the adhesive, it is a measure of the material's ability to resist creep.
- **The peel test** (Fig 5.10b). It evaluates long-term adhesion and is often use in industry because it mimics the removal of an adhesive tape. A strip of adhesive material is peeled away from a substrate at a fixed peeling rate and peeling angle (usually held at 90° or 180°). The peeling force is recorded. During peeling, the fracture propagates progressively and is often accompanied by bulk fibrils.
- **The tack test** (Fig 5.10c). It assesses the material's ability to quickly create an interaction with the surface upon light contact, and its ability to resist debonding. Several tack tests exist, such as the rolling ball test and the loop tack test, but in the vast majority of studies the *probe tack test* is performed, as it is more rigorous and provides access to more data. In this case, a probe (flat or spherical) is brought into contact with the material until a set force is reached. Contact is maintained for a period of time during which the material is allowed to relax, and then the probe

is pulled back at a constant speed V_{pb} . The force and displacement are recorded throughout the process. They are used to plot characteristic nominal stress - nominal strain curves for the traction step. After reaching some displacement, the material ultimately undergoes a cohesive or adhesive failure.

In this work, we used a probe tack test because we wanted to discern which samples were subject to cohesive or adhesive failure and it is simple to set up with a rheometer.

5.3.4 Results of a tack test

The tack curve

The force-displacement curve is transformed into a nominal stress ($\sigma_N = \frac{F}{\pi a^2}$) versus nominal strain ($\varepsilon = \frac{h-h_0}{h_0}$) curve, h_0 being the initial thickness of the material before probe removal. The three main parameters can be extracted whatever the type of material: the peak stress σ_{max} , the maximum extension ε_{max} , and the work of debonding, generally defined as $W_{deb} = h_0 \int_0^{\varepsilon_{max}} \sigma_N(\varepsilon) d\varepsilon$ (Fig. 5.11). In Chapter 6, we prefer to use instead the volumetric work of debonding written $W_{deb} = \int_0^{\varepsilon_{max}} \sigma_N(\varepsilon) d\varepsilon$ because the volume of the different samples varies greatly through h_0 . In the case of a fracture occurring strictly at the interface without dissipation, the energy per unit area required to separate the two surfaces is called the thermodynamic work of adhesion and is given by Dupré's equation: $\Delta\gamma = \gamma_A + \gamma_B - \gamma_{AB}$ calculated by adding the two free surface energy and subtracting the interaction free energy [160]. When the two materials are identical, the equation simplifies to $\Delta\gamma = 2\gamma$. In practice W_{deb} is greater than the thermodynamic work of adhesion for adhesive failure mechanism, as it is a combination of both the energy needed to separate the two surfaces and the energy involved in the bulk deformation:

$$W_{deb} = W_{interface} + W_{bulk} \quad (5.8)$$

In other words, the tack curve and the debonding work derived from it include the contributions of both adhesion and cohesion. We will come back to this in the section 5.3.5.

Several experimental limitations can affect the measurements performed by probe tack test. In particular, the lack of parallelism leads to uneven material confinement and non homogeneous contact. This can lead to different results as exposed by Crosby *et al.* [161] who highlighted the role of confinement in elastomer debonding. Instrument compliance can play a role on the real velocity and displacement imposed [162]. For instance, when performing the tack test at the highest pull-back velocity on our rheometer, the velocity increases from 0.08 to 3.2 mm/s during the 0.6 seconds that last the experiment instead of rapidly reaching the 10 mm/s set value (and in theory applicable by the rheometer).

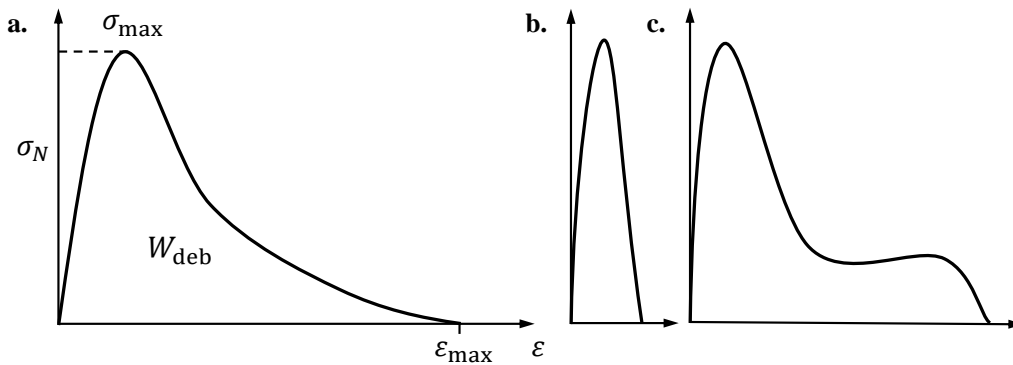


Fig. 5.11 – Typical probe tack test curves for **a.** liquid-like behavior (e.g. paste) **b.** solid-like behavior (brittle failure) **c.** adhesive debonding of a PSA with large bulk deformation (fibrils).

Effect of test parameters

The contact time, the contact force, the temperature and the retracting velocity are known to have an influence on the results of the probe tack test.

- Increasing the load allows the sample to achieve a greater contact with the probe surface which improves the adhesion [163, 164].
- Increasing the contact time augments the ability of the material to relax and make close contact with the surface [163]. Once the material has had time to relax completely, increasing the contact time has no effect [165].
- Increasing the retracting velocity, V_{pb} , shifts the debonding from cohesive to adhesive for PSA [166]. Lakrout *et al.* also evidenced that the peak stress is proportional to the elastic modulus G' at the debonding frequency V_{pb}/h_0 . In case of Newtonian fluids, the increase of the debonding velocity also has an impact: it changes the debonding mechanism from fingering to cavitation [159].
- Temperature often has an effect, particularly with polymers, as it can strongly modify their rheological properties, and particularly G' and G'' , making the material more flowable or more rigid.

Failure mechanism

Depending on the type of material being studied, its properties, and the surface of the probe, the debonding can occur in the bulk or at the interface (Fig. 5.12).

In bulk, cohesive failure can occur after the formation of fibrils that result from the growth and merging of cavities within the bulk, and can withstand a sometimes long deformation before breaking [158]. Another mechanism relies on a radial flow that creates a central neck that thins and eventually ruptures (with potential fingering) [159]. A combination of the mechanisms can be observed for instance with granular paste where inward flow is combined with internal void growth [156].

At the interface, the adhesive failure can result from fracture propagation. Cavities appear at the interface and quickly merge without much deformation of the material. Another potential mechanism is the formation of fibrils that ultimately prefer to detach at the interface rather than in the middle due to strain hardening [158].

Several models use the rheology to determine when systems transition from interfacial crack propagation to bulk deformation mechanisms.

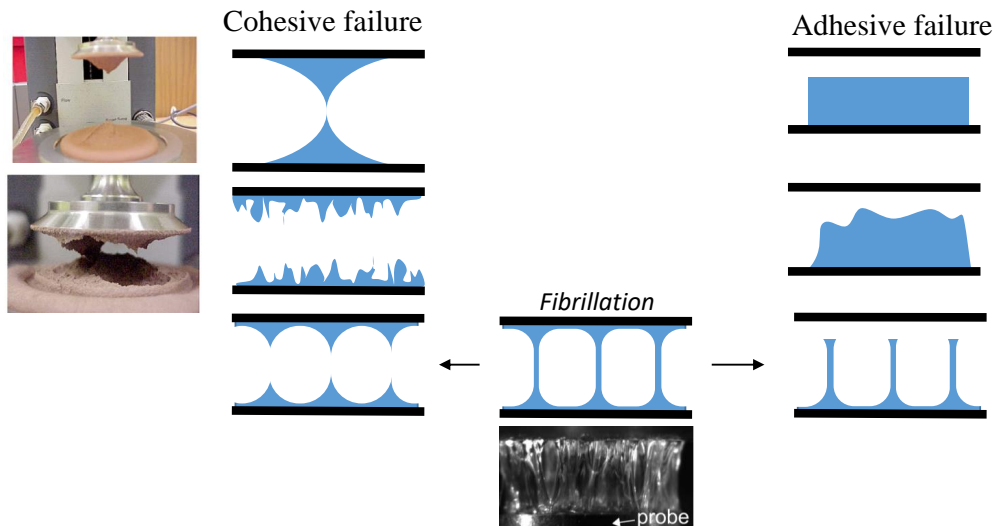


Fig. 5.12 – Illustration of several debonding mechanisms occurring in bulk or at the interface and leading to cohesive or adhesive failure. The pictures are from [155] (left) and [167] (middle).

5.3.5 Link with rheological properties

Dahlquist criterion

The first criterion often used to predict the adhesiveness of a material is the Dahlquist criterion: the storage modulus G' at the bonding frequency must be less than 0.1 MPa for the material to make sufficient contact. This ensures that the material is energetically favored to deform along a rough surface and creates bonding not just at the peaks. This value can be explained with a simple formula giving the modulus needed for a material to spontaneously flow in a roughness: $G'_c = \Delta\gamma\sqrt{\frac{R_r}{h_r^3}}$ with R_r the radius of the roughness and h_r its height above the mean level [158, 168]. By taking $h_r = 1 \mu\text{m}$, $R_r = 5 \mu\text{m}$ and a work of adhesion $\Delta\gamma = 50 \text{ mJ/m}^2$ the value of 0.1 MPa for G'_c is obtained. Of course, this critical value of the storage modulus varies with the level of roughness and surface energy, but it has been experimentally shown to be a good criterion for various materials [169], and is largely used in the adhesive community. When the Dahlquist criterion is not met, the tack curve is sharp (Fig. 5.11b) [170], the material is rapidly subjected to an adhesive failure without bulk deformation.

Linear viscoelastic properties and debonding mechanisms

Based on thermodynamic considerations, the Griffith criterion expressing the equilibrium of a crack inside an inelastic material writes [158]:

$$\mathcal{G}_c = \Delta\gamma \quad (5.9)$$

with \mathcal{G}_c the strain energy release rate corresponding to the energy necessary to make the interfacial crack move and $\Delta\gamma$ the thermodynamic work of adhesion.

In case of deformable material, several debonding mechanisms can be observed occurring either at the interface or in the bulk. To predict the transition between interfacial and bulk mechanism for elastomers, \mathcal{G}_c the critical strain energy release rate is compared to Eh_0 the energy needed to deform the bulk (with E the elastic modulus and h_0 the thickness of the adhesive layer) [171]. When $\frac{\mathcal{G}_c}{Eh_0} < 1$ the initial defects will expand at the interface of the adhesive layer. When a crack propagates in a viscoelastic material, viscoelastic dissipation limits the crack velocity to a maximum value v . Maugis and Barquins proposed an empirical equation for the critical energy release rate [172]:

$$\mathcal{G}_c = \mathcal{G}_0(1 + \Phi(a_T v)) \quad (5.10)$$

With Φ the dissipation function, a_T the time-temperature coefficient, v the crack velocity and \mathcal{G}_0 the threshold fracture energy for zero rate of crack growth ($v \rightarrow 0$). In case of reversible separation: $\mathcal{G}_0 = \Delta\gamma$. In the high velocity and dissipation approximation, the second term becomes predominant and Eq. 5.10 is simply:

$$\mathcal{G}_c \approx \mathcal{G}_0 \Phi(a_T v) \quad (5.11)$$

The dissipation term is proportional to $\tan \delta = \frac{G''}{G'}$ for a simple elastomer having only van der Waals interactions with the surface [172]. Moreover, the elastic modulus E is of the order of the storage modulus G' . Hence, the ratio $\frac{\mathcal{G}_c}{Eh_0}$ can be rewritten only as a function of rheological parameters and \mathcal{G}_0 :

$$\frac{\mathcal{G}_c}{Eh_0} \approx \frac{\mathcal{G}_0 \tan \delta}{G'h_0} \quad (5.12)$$

Using this ratio, Nase et al. proposed for elastic rubbers a mechanism map, plotting $\mathcal{G}_0 \tan \delta = f(G'h_0)$, which allows to distinguish samples that undergo interfacial crack propagation from the ones subjected to fibrillation and bulk deformation mechanism [173]. When the energy cost to deform the bulk is high, interfacial crack propagation is expected: $\mathcal{G}_0 \tan \delta < G'd$. In the opposite situation, crack propagation requires high energy, which leads to bulk mechanism (deformation, fibrillation). In practice, $G'(\omega_f)$ and $\tan \delta(\omega_f)$ are measured experimentally at the angular frequency $\omega_f = 2\pi V_{pb}/h_0$ [166, 170] and G_0 is obtained by measuring the debonding work with a tack test performed at low V_{pb} [173]. Deplace also proposed a close representation, following the same reasoning, separating the viscoelastic parameters from the the fracture parameters (Fig. 5.13) [170]. An important point here, is that, with elastomers, having crack growth in bulk or at the interface does not necessarily mean that the failure type is different. For instance Deplace always observed adhesive failures.

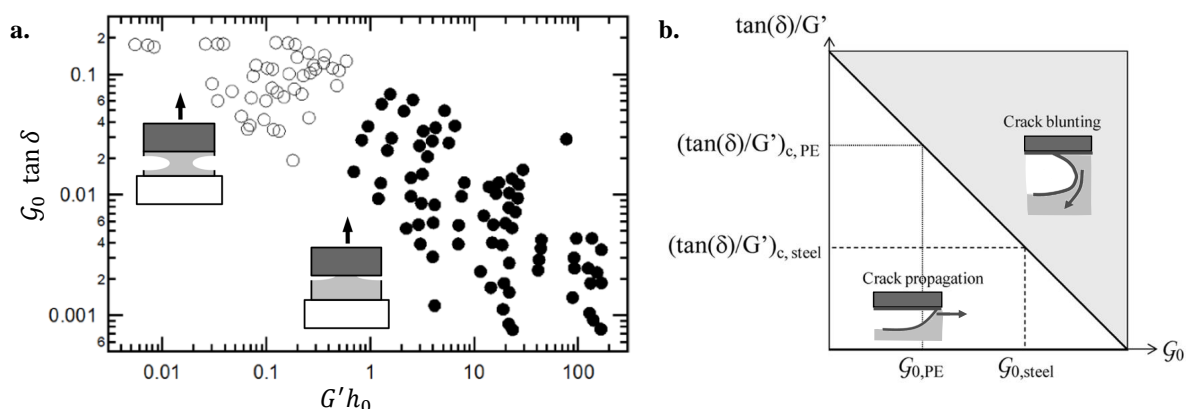


Fig. 5.13 – Prediction of the debonding mechanisms as function of the rheological parameters for viscoelastic fluids **a**. Open symbols represent bulk deformation and black full symbols interfacial crack propagation for PolyDiMethylSiloxane systems (adapted from [173]). **b**. Another quite similar representation adapted from [170]. Increasing G_0 leads to lower the critical value of $\tan \delta / G'$ above which bulk deformation occurs.

The number of studies dealing with pastes is quite low compared to those dealing with elastomers. In addition, the pastes are usually tested in a range of concentration where only deformation in bulk and cohesive debonding occur. We did not find any study proposing a suitable map to distinguish the bulk mechanism from the interface mechanism in the case of pastes.

5.4 Soft substrate: the skin

So far, we have described the aspects related to cosmetic formulations (rheology, drying, adhesion). When modelling the defects that appear during the spreading of cosmetic fluids, the choice of the support can play an important role through its surface and mechanical properties.

In this bibliographic report we seek to describe the structure and properties of the skin to propose a model that is relevant for our study.

5.4.1 Skin structure

The skin has a multilayered structure (Fig. 5.14a). It is composed of three main layers, the epidermis, the dermis and the hypodermis, which are themselves subdivided into sub-layers. These distinctions are based on differences in cell populations and structures that allow for appropriate mechanical and physiological functions.

The skin also has elements such as hairs, sebaceous glands and nerves that we have decided to ignore in our model for obvious reasons of simplification and which are therefore not presented here.

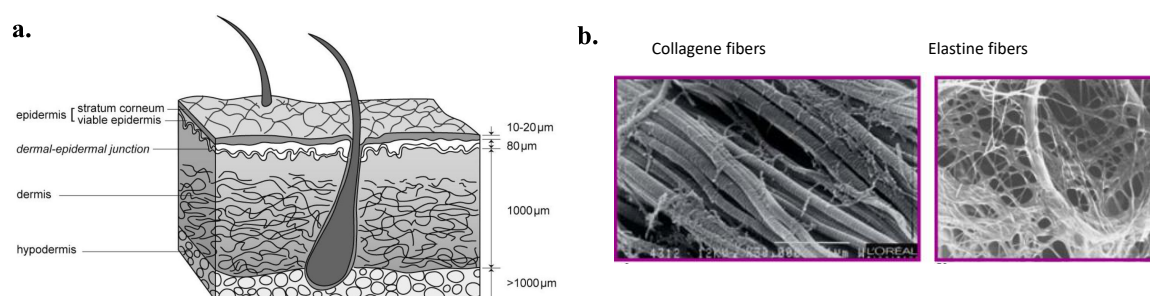


Fig. 5.14 – **a.** Schematic representation of the different skin layers (from [174]). **b.** Collagen fibers (from L'Oréal) and elastin fibers (from [175]) of the reticular dermis observed by electron microscopy.

The epidermis

The epidermis corresponds to the external part of the skin. It is the thinnest layer of the skin; it measures from a few tens of micrometers to 100 μm [176, 177]. It is made up of five sub-layers: the cells, which are constantly renewed, migrate towards the surface by passing through the different layers successively and end up in the cornea. This last layer is about 15 μm thick [175], and corresponds to a layer of dead cells. The cornea provides protection against biological, chemical and mechanical aggressions. It is mainly made up of keratin which gives its very specific mechanical properties compared to the rest of the epidermis. Its properties varies greatly depending on the level of hydration. Nevertheless, to simplify the mechanical models of the skin, the cornea and the epidermis have long been considered to have a negligible impact, particularly in traction, in comparison with the dermis [178]. However, the epidermis has been recently studied as a bilayer with the cornea on the one hand, and the viable epidermis on the other hand in order to make the models more representative [174, 179]. Indeed the viable epidermis enhances the rigidity of the cornea and should not be overlooked [8].

The dermis

The dermis is a connective tissue, i.e. it is characterized by the presence of fibers, cells and fundamental substances. The dermis is measured between 1 and 4 mm thick depending on the area of the body [180]: on the face, it is around 1.2 mm thick [181]. The reticular dermis stands for 90% of this thickness and is composed of elastin and collagen fibers at respectively 2 to 4% and 60 to 80% of the dry weight of the skin (Fig. 5.14b) [182, 183]. Elastin fibers play a role in small deformations, by allowing the elasticity of the skin, while collagen fibers provide tensile strength at large deformations and prevent tearing. Due to the presence of this densely intertwined network of fibers parallel to the skin surface, the reticular dermis is often considered to be solely responsible for the mechanical properties of the skin in the most simplified models.

The hypodermis

The hypodermis is a highly vascularized connective tissue made of adipose tissue. The thickness varies greatly according to the morphology, for example on the upper arm it is around 5 mm thick for men and twice that for women [184]. The hypodermis is regularly considered not to be part of the skin, and is rarely taken into account in mechanical models despite its role as a shock absorber. This very loose tissue also allows the skin to move en bloc over the underlying areas.

5.4.2 Mechanical characteristics

Skin is a material with a complex mechanical behavior. It is non-linear, viscoelastic, anisotropic and pre-stressed.

Mechanical behavior

Non-linearity

As early as 1861, Langer showed by in vitro tests that the force-elongation relationship is not linear by in vitro test [185], which was later confirmed in vivo by Evans and Siesennop [186].

In the first phase, the skin is very extensible with a low modulus of elasticity. From a microscopic point of view, this corresponds on the one hand to the unfolding of collagen fibers, which occurs practically without effort, and on the other hand to the extension of elastin fibers, which contribute to the beginning of traction (Fig. 5.15).

In the second phase, some collagen fibers, by unfolding and orienting themselves, begin to play a role in tensile strength. As the number of collagen fibers involved increases, the stiffness of the skin increases, as they have a much higher Young's modulus than elastin fibers.

Then, in the last phase, all collagen fibers are aligned in the direction of traction and participate in the tensile strength, the behavior is again linear with a very steep slope.

The transition from the initial linear to non-linear regime is found around 20-40% deformation [187–189]. The transition from the second to the last phase occurs around 60% deformation [188]. In the case of spreading, we are on limited deformation ranges that mainly belong to the linear regime as the maximum deformation achievable in vivo without creating pain and trauma is about 25% [8].

Viscoelasticity

The skin has a viscoelastic behavior [188, 190–192]. This behavior is due to the flow of the fundamental substance between the fibers of the dermis. Due to the density of the fiber network, this behavior is only visible for strains <30% [193] and low tensile speeds [175].

Anisotropy and prestressing

The anisotropy of the skin was first demonstrated by Dupuytren, in 1836, by cutting the skin with tools of circular section. The shapes obtained were not round but oval, which showed differences between

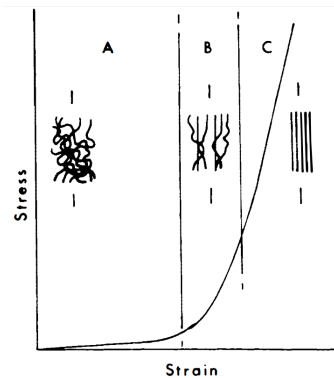


Fig. 5.15 – Stress-strain curve and organisation of the associated collagen network. A = fibers straightening out but not yet carrying load; B = some fibers are straight and collagen starts to carry load; C = all fibers are carrying load (from [188]).

the tensions at rest according to the directions. A difference in Young's modulus can be measured [182, 194].

All these characteristics, to which we can add the structural heterogeneity of the skin, make this material very difficult to characterize and model. We will now review the measurements made on the mechanical and physico-chemical properties of the skin.

Quantification of mechanical characteristics

In vivo or *in vitro*

Depending on the measurement techniques used, the tests are carried out *in vivo* or *in vitro* on cadaveric tissue.

In vitro measurements allow to scan wider ranges of stresses and deformations [195] and makes it possible to study separately the different layers of the skin [174]. This method raises several problems: the separation of the tissues can affect the properties of the tissues, dead tissue may not be representative of living tissue [196], and fixing the sample means prestressing in a way that is not necessarily representative of *in vivo* situation.

In vivo measurements are intended to be closer to the actual characteristics, but it is very tricky to separate the response of the skin from the underlying tissues, or within the skin itself, to determine whether one is measuring the response of the skin as a whole or only certain layers [197].

Method of measurements

A wide variety of measurements have been presented in the literature: the four main ones are suction, tension, torsion, and indentation. Traction is most often carried out *in vitro* by fixing the sample between jaws to stretch it parallel to its surface, whereas suction and indentation, which involve small deformations in a non-invasive way, are suitable for *in vivo* measurements. In the case of suction, the skin is sucked by depressurization in a tube, the resulting shape allows to trace the mechanical properties.

Indentation is a technique that uses an indenter to apply a compressive deformation to the skin. Finally, torsion can be carried out *in vivo* or *in vitro* by applying a rotation to a disc attached to the skin. These different measurements do not stimulate the skin in the same way and do not measure the same elements.

Results present in the literature

A very wide variety of elastic moduli are proposed for skin in the literature. The values are reported in Figure 5.16. Moduli ranging from a few kPa to several tens of MPa are listed, i.e. almost 5 orders of magnitude of differences.

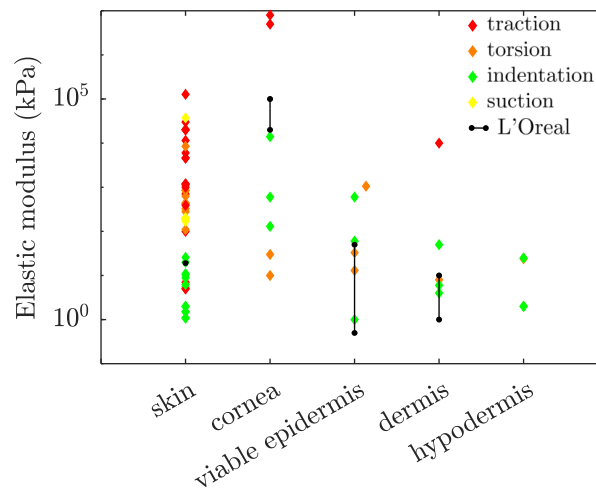


Fig. 5.16 – Elastic moduli reported in the literature for the human whole skin and its different layers measured *in vivo* or *in vitro*. The colors correspond to the main categories of measurement. The black bars correspond to the range of values considered by L'Oréal. The data have been extracted from the literature reviews and the experimental data shown in the thesis of Hendricks [196], Jacquemoud [195], Geerligs [174], Tran [198] and the articles of Abellan [179], Dai [199] and Nicolle [197].

The studies that have tried to give distinct moduli according to the layers are less numerous but the variability of the moduli is just as important. We find that the cornea is quite rigid compared to the other layers. There is little difference between the epidermis, dermis and hypodermis, but this may be the result of the type of test performed. Most of the time, for these layers, indentation or torsion tests are reported in the literature, these tests do not highlight the strength of the dermal fibers as much as a tensile test would, for example, which can lead to a bias.

Factors affecting the measured mechanical properties

Several factors intrinsic to the skin explain the variability of the moduli reported in the literature.

Intrinsic factors of the skin

First of all, within the same individual, the layers of skin do not have the same thickness nor the same relative thickness according to the places of the body which causes different properties. The anisotropy

of the skin presented before generates different measurements for the same sample depending on the axis in which it was stimulated. There is also variability between individuals, particularly related to age [200] linked with microstructural changes.

Factors related to the measurements

First of all, depending on the technique used, the reported measured moduli are not the same, they can be elastic or shear moduli. The notion of elastic modulus itself varies according to the mode of stress: tension, compression or bending. Within the same type of mechanical stimulation, the results vary greatly depending on the protocol and the conditions of the measurements. As mentioned, there will be differences between *in vitro* and *in vivo* measurements. The impact of the hydration of the sample is also determinant, particularly for the study of the cornea for which the modulus can be decreased by an order 1 or 2 [201–203]. Depending on the tool used to hold the sample, additional pre-stressing may occur and disturb the measurement. Finally, the measured moduli are not the same from one experiment to another if parameters such as frequency, amplitude, deformation are varied, due to the non-linearity of the skin.

5.4.3 Surface properties

As for the mechanical properties, the physico-chemical properties depend on the areas of the body considered. This is due to differences in the composition of the lipidic film at the skin surface. For example, the production of sebum is very strong on the forehead and the face and less on the rest of the body. This fatty body impacts the hydrophobic/hydrophilic character and the surface energy [204, 205]. Skin is highly hydrophobic due to the presence of keratin and lipids on the surface. The contact angle method gives angle values of $91 - 140^\circ$ [204, 206]. On areas with high sebum production hydrophobicity is (surprisingly) decreased, angles of 60 to 85° are measured [204]. It is also characterized by a fairly low surface energy: on average on the body it is $38 - 39$ mN/m [205, 207] while for the forehead it is higher, $42 - 46$ mN/m [205]. The skin surface has a roughness of $17-20$ μm [206]. This point, although important in spreading processes, is neglected in the following to simplify the model.

Now that we have presented the properties of the skin, we discuss the synthetic skin models that have been developed to reproduce these properties.

5.4.4 Skin Models in the literature

The skin has a large number of properties and there are therefore a large number of models that are very different from one another and that seek to reproduce one or more of its properties. Biological models of human skin are currently being developed but they are very restrictive and are most often intended for tissue reconstruction. "Physical models" are made of inert materials and intend to reproduce certain properties of the skin (thermal, electrical, mechanical, chemical, optical, surface properties, etc.). Dabrowska wrote an interesting review on the various physical models developed so far [180].

Within the framework of the spreading of cosmetics, two groups of properties were identified as having a fundamental role: the mechanical properties and the physico-chemical properties of surface. The transpiration also impacts the spreading but it has been neglected in this study in order not to make the system too complex.

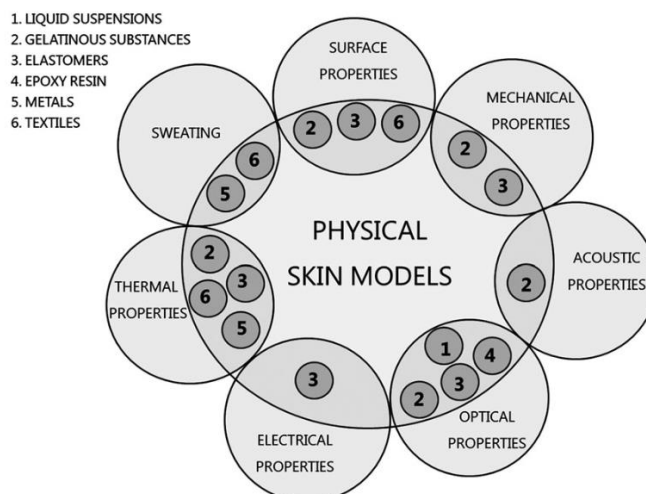


Fig. 5.17 – Materials used to simulate skin functions and properties (from Dabrowska's review [180])

The materials used in the literature to reproduce the mechanical and surface properties of the skin correspond to gelatinous substances and elastomers (Fig. 5.17):

- Gelatinous substances:

They refer in the case of skin models to gelatin agar, collagen, and polyvinyl alcohol (PVA). As they are gels, their properties are very flexible by playing on the concentration of water but also on temperature or on pH for example. Gelatin is one of the components of the skin. This protein, put in gel, allows to reproduce the density and the viscosity of the skin. This model is widely used to study impacts and injuries but it can also be used to test creams. Agar and PVA are used mainly for imaging applications, the recent development of cryogel PVA opens up greater opportunities as the mechanical properties of the skin are achieved with this material.

- Elastomers:

These are viscoelastic polymers at room temperature. The most used elastomers for skin models are silicones and polyurethane. PolyDiMethylSiloxane (PDMS), sometimes combined with fillers, is used to reproduce the skin surface state, optical, acoustic, electrical and mechanical properties. Studies that reproduce the mechanical properties aimed at model skin wound [208, 209], needle penetration [210] or tactile behavior [211–213]. Polyurethanes are regularly used as mechanical models, they can reproduce skin friction, injection and wounding behavior, tactile evaluation and optical properties.

Multilayer models (2 or 3 layers) have been studied in order to better model the skin by combining layers with different properties. Thus the epidermis (or stratum corneum) is often modelled separately

from the rest of the skin as its friction properties are important and its mechanical properties differ from the rest of the skin [209, 212].

5.4.5 Focus on PDMS

The PolyDiMethylSiloxane is a silicon material that can be reticulated with a cross-linker agent to form a gel structure.

Mechanical properties

Different grades of PDMS exist to achieve very different elastic moduli. For the same type of PDMS it is possible to reach elastic moduli ranging from a few kPa to about ten MPa, by playing on the polymer/crosslinking agent ratio as well as on the curing time and temperature [214, 215]. This effect can also be obtained by mixing several types of PDMS [216, 217] which can even allow to reproduce the non-linearity of the skin [218]. Such range of moduli makes it possible to reproduce with PDMS both the properties of the stratum corneum (of the order of MPa) and the lower layers (of the order of tens of kPa).

Surface properties

The contact angle of water deposited on PDMS is around 110° [216, 219]. The surface energy reported is $19 - 21 \text{ N}\cdot\text{m}^{-1}$ [219]. These values are close to those reported for the skin of the body, but are far from those reported for areas with high sebum production (face). In this last case, PDMS is more hydrophobic than the skin.

Various values of the coefficient of friction have been reported in the literature, with silicone rubber having a lower [211] or higher [213] coefficient than real skin ($\mu \simeq 0.2 - 1.3$).

5.5 Goals of this thesis - Part II

As soon as a cosmetic cream is applied, or later when rubbing a "dry" cosmetic deposit, aggregates might appear. They look like small cylindrical objects that eventually fall off the skin under the action of gravity. An example is shown in Figure 5.18. These aggregates are very detrimental because they cause unpleasant sensations and prevent a homogeneous and uniform coverage of the cosmetic product. Consumer feedback is often variable, and surprisingly dependent on the region of the world, which suggests a complex problem that is not solely dependent on the product formulation. In the switch to biobased products, the use of some new materials has led to an increased occurrence of these defects. It is therefore essential to address these issues, which, although they have always existed, are coming back to the forefront with the shift to biobased particles.

A review of the literature has shown that this problem and possible solutions have not yet been reported. Based on this state of the art, dealing on the one hand with suspensions, their drying, adhesion and cohesion mechanisms, and on the other hand with the skin and its synthetic models, we are going to build an experiment that allows us to study the formation of aggregates. Our goal is first to identify the different parameters involved in their formation in order to understand the mechanisms involved



Fig. 5.18 – Picture illustrating the cylindrical aggregates formed during the rubbing of a dried cosmetic deposit on a forearm.

and to propose a model to explain the formation of aggregates. The final objective, in the perspective of industrial application and consumer benefit, is to propose advice to avoid the formation of aggregates in practice. It is mainly on the formulation aspects that we are looking for these guidelines, because it is the point on which the industrial has the most impact, as opposed to the gesture and technique of application of the product by the consumer.

Conclusion – Chapter 5

From its application and throughout all its life on the skin, a cosmetic cream goes through many states and is submitted to many different mechanisms. Therefore we presented in this chapter a quite broad literature review related to the following aspects. Initially a cosmetic cream can be assimilated to a semi-diluted suspension of particles whose properties mainly depend on the suspending phase. When drying, the volume fraction of particles increases and we have shown it is often accompanied by non-Newtonian behaviors related to the particle contacts and interactions. During drying at rest, studies also reported a crusting phenomenon leading to a non-uniform distribution of particles in the deposit. Finally when shearing a dried cosmetic deposit, adhesion and cohesion start playing a decisive role. This point which has been mostly studied in the context of pressure sensitive adhesives, but not in the context of spreading of thin layers of complex fluids, will be discussed in detail in the next Chapter.

In light of this literature review we seek to understand: *How to explain the aggregate formation? What are the parameters and mechanisms involved in their occurrence? How to avoid them?*

In Chapter 6, to answer these questions, we first develop a set-up allowing to reproduce in a controlled way the aggregates observed in practice on the skin. Then we identify the main parameters involved in the emergence of these defects. These observations are completed by characterization tests, which allow us to propose a model of the aggregate formation mechanism that explains why instead of smoothly spreading, the fluid deposit generates those defects. Finally, we propose a criterion based on the volume fraction of the particles to reduce the risk of aggregate formation.

Chapter 6

Impact of fillers in the formation of aggregates in cosmetic deposit

In this chapter, we study a common problem encountered with fillers in cosmetics: the formation of macro-aggregates during the spreading on the skin, or after drying, of the formulation. We develop a back and forth spreading experiment to mimic the formation of these aggregates *in vitro*. The choice of applicator and substrate has proven to be crucial to reproduce these defects. We study the effect of filler concentration and polymer on their appearance. Finally, we propose a mechanism for the formation of cylindrical aggregates. The jamming volume fraction of fillers in the non-volatile phase should not be exceeded to limit aggregation, which implies a good knowledge of the filler properties such as porosity or swelling.

Contents

6.1	Context and evaluation	132
6.1.1	Industrial context	132
6.1.2	Industrial evaluation of defects	133
6.1.3	Problem definition and scope	134
6.2	Mimic the spreading of cosmetics	135
6.2.1	Proposition of a new skin model	135
6.2.2	New applicator	137
6.2.3	Protocol	138
6.2.4	Water-based formulations	139
6.3	Factors that influence the formation of aggregates	140
6.3.1	Discontinuity in the dry deposit	140
6.3.2	Solid particle concentration in the non-volatile phase	142
6.3.3	Normal force and velocity dependency	144
6.3.4	Carbopol role	146
6.4	Rheology of the dried formulations	147

6.4.1	Flow properties in the non-linear region	147
6.4.2	Viscoelastic properties in the linear region	149
6.4.3	Impact of Carbopol on rheology	150
6.5	Formation mechanism	151
6.5.1	Nucleation of the cylindrical shape	152
6.5.2	Proposal for a microscopic mechanism	153
6.5.3	Validation of the model with experimental results	155
6.5.4	Comparison of the different tests	164
6.5.5	How to favor spreading ?	165
6.6	Link with ϕ_M	166
6.6.1	Formulation tested	167
6.6.2	Evaluation of ϕ_M and calculation of volume fractions	168
6.6.3	Results on the industrial skin model	170
6.6.4	Origin of defects formation when $\phi < \phi_M$	172
6.6.5	Reducing aggregates formation by increasing ϕ_M	172
6.7	Conclusion	173
6.8	Perspectives	175

6.1 Context and evaluation

6.1.1 Industrial context

Most cosmetic formulations are much more complex than those presented in the first part. Indeed, they are composed of a large number of ingredients. In particular, in addition to water, oils and polymers, there are usually solid particles which are called fillers. They are most of the time micrometric (or even nanometric). They are used, for example, for sun protection (titan or zinc oxide particles), as an optical agent (silica), as a covering agent (mica), to make the formulation more adherent, to modify its density or its texture (wax). However, they are often considered as responsible for defects that appear during the spreading and drying of the formulation. Thus, some particles can create a squeaky feeling, others generate macro-aggregates. These defects have a double negative impact on the consumer: *i*) on the sensory perceptions and *ii*) on the effectiveness of cosmetic products. Aggregates concentrate the formulation locally, leaving large areas of the skin uncovered, which is highly detrimental to the covering effect or sun protection for example.

To narrow the scope of the study, we have chosen to focus on a single type of defect: the formation of aggregates. This defect is of major importance because it is reported for classic type of cream with high content of particles (especially foundation and blur). In addition, some bio-based products (such as micrometric cellulose beads), which are strategic for the cosmetic transition to sustainability, have

shown a strong tendency to form aggregates. This represents a barrier to their large-scale use and makes this topic a critical one.

The formation of macro-aggregates in the cosmetic deposit is a complex phenomenon whose very definition can be debated. We present how it is described and evaluated in the industry, then propose a more precise definition and perform a scope-specific analysis.

6.1.2 Industrial evaluation of defects

Product evaluation is a key step during the development of new cosmetic formulations. It can be conducted *in vivo* either on expert panels, or directly with consumers. However, this process is costly and is often implemented only in the last phase of product development. Moreover, the spreading parameters, such as the velocity and force applied during the movement, are not controlled and therefore cannot be studied rigorously. For the initial research and development phases, it is therefore necessary to use *in vitro* test protocols. The challenge is to find quantitative and reproducible methods that are representative of real-life conditions of use.

In the example of aggregates formation, a test was developed in industry to identify the formulations that produce them. A commercial artificial skin made of a PDMS matrix, covered with a polyurethane film, and which presents the topography of a human skin (pores and lines) is used as a skin model. To perform a test, a mass of fluid is deposited to obtain a final surface concentration of 2 mg/cm². The artificial skin is maintained at 35°C. Then a protocol consisting in a succession of spreading by hand and drying steps is followed:

- Spreading: 15 rotations during 15s.
- Drying: for 15s
- Spreading: 15 rotations during 15s.
- Drying: for 2 minutes and 15s
- Spreading (or shearing): by making 5 strong rotations (the normal force F_N targeted is 5N) on the dry deposit (meaning only the particles and the non-volatile phase, such as glycerol, are still present).

A rating is given between 1 and 5, by looking at the aspect of the final deposit. This rating reflects the likelihood of a formulation to generate defects, 1 corresponds to the case where no defects are observed and 5 to the case where aggregates are numerous. Three references, rated 1, 3 and 5, are tested first to calibrate the way of rating. The defects usually encountered are macro-aggregates in rolls, in sheets, but also the appearance of powdery zone where the particles are visible by creating white areas. Sometimes, the deposit, instead of generating aggregates on the sample, forms residues in the papillary folds of the fingers, leading to delicate rating. To have more robust results, these tests are performed by a panel of 3 to 5 people.

This evaluation tool is a quick way to test formulations but has several limits:

- It is not very reproducible because of differences in applied force, spreading velocity, and characteristics of the skin of the fingers (dry, oily...) that can differ between experiments.

- The polyurethane film covering the substrate shows rapid deterioration when high pressing force is used (tears and partial delamination of the film lead to the formation of particle "traps" between the PDMS and the film, film flaps can form and act as aggregate nucleator).
- The cleaning is difficult due to the presence of folds and holes (related to skin topography).

These limits motivated us to develop a new setup to study in a more controlled and quantitative way the formation of these aggregates.

6.1.3 Problem definition and scope

Definition of the object of study

The previously described test is used not only to quantify the presence of macro-aggregates but also other defects, such as white powdery deposit, that do not have the same physical origin (Fig. 6.1b and c respectively). In our study, we focus ourselves on macro-aggregates, by defining them as assemblies of solid particles that are sufficiently aggregated and cohesive to be handled with a pair of tweezers for example (Fig. 6.1b). We call them macro-aggregates but also cylindrical, rolling or simply aggregates. We thus exclude from our study the clusters of particles, the powdery deposits, or other heterogeneities in concentration, which do not constitute the formation of a new object. The physical question we ask ourselves is: why, instead of spreading, some parts of the dry deposit create macro-structures that roll under shear?

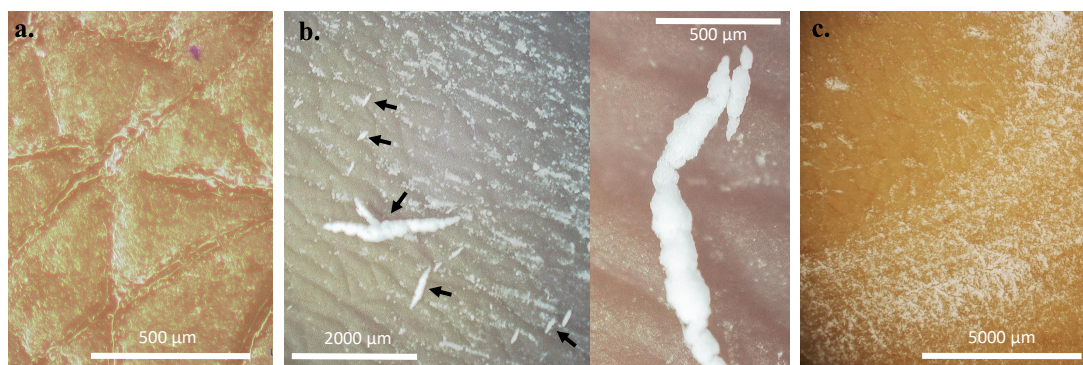


Fig. 6.1 – Picture from Hirox microscope showing typical results obtained after the test on the commercial artificial skin. **a.** Spreading situation obtained for starch at 1.3 w%. The residual liquid and the solid particles are visible in the skin folds. **b.** Cylindrical aggregates of various size are observed (dark arrows) for cellulose beads at 5.0 w% in water based formulation (Carbopol gel and glycerol at 10w%). The lost of focus highlights the three-dimensionality of these objects compared to the powdery areas. The picture of a macro-aggregate of approximately 1.2 mm long and 100 μm wide is shown. This object is cohesive and can be manipulated. **c.** White powdery deposit obtained with starch 35.9 w% in oil based formulation (isododecane and silicone oil 100 cSt at 10 w%).

Scope of the study

Several elements involved in aggregates formation can be identified: the applicator, the substrate and the formulation. For example, the roughness and the softness of the applicator and substrate influence defects formation [3]. Additional interactions with the deposit (wetting, electrostatic effect...) might also have an impact. The normal force [3], the motion, and the shearing velocity applied by the applicator are other parameters at stake. Figure 6.2 presents a summary of the different elements and their main parameters supposedly involved in the formation of aggregates. The main lever of action of the cosmetic industry being the formulation, we seek to set the parameters related to the substrate and the applicator in a configuration that reproduces fairly the results obtained on natural skin to focus on the parameters related to the deposit.

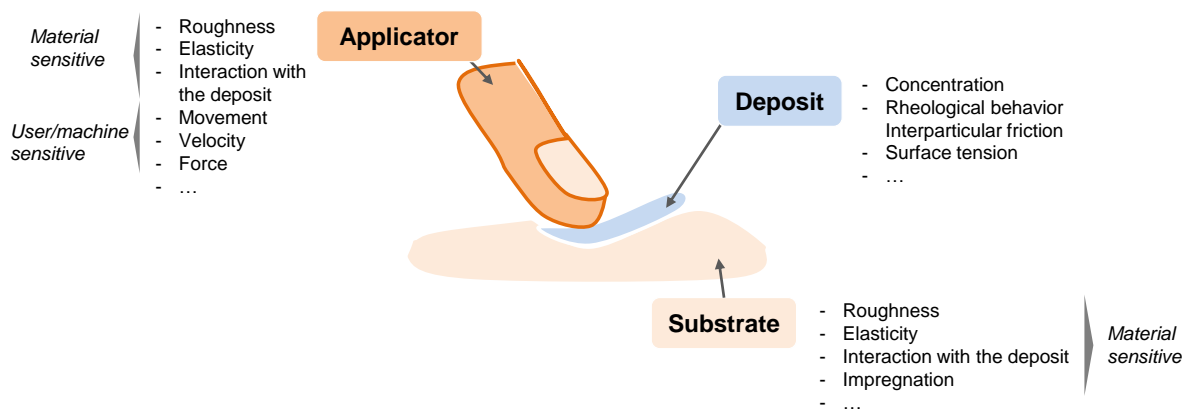


Fig. 6.2 – Representation of the different elements of the problem and the related factors that might play a role in the formation of aggregates. The list is not meant to be exhaustive but gives a first overview.

6.2 Mimic the spreading of cosmetics

In the first chapters (2–4), a flexible blade coating set up has been used to spread the liquid on a rigid surface. This system does not allow to realize complex movements, such as back and forth, or circular motions. Moreover, the rigid surface does not reproduce the elastic properties of the skin and pre-tests have shown that the use of a soft support favors very strongly the appearance of these aggregates. To study the formation of aggregates, we wanted to develop a *new set-up* that more closely reproduces the conditions under which aggregates appear.

6.2.1 Proposition of a new skin model

To model the skin a PDMS (PolyDiMethylSiloxane) bilayer was used (Fig. 6.3). The lower layer is the thickest and the softest; it mimics the dermis and hypodermis part of the skin. The upper layer is thinner and more rigid; it tends to reproduce the corneum. This layer also prevents the artificial skin to be too sticky. In practice the lower layer is made first by casting about 4.5 cm thick of soft PDMS

(Dowsil™ CY52-276 from Dow Chemicals) in a PMMA mold handled in a grey room. After degassing under vacuum, it is cured at 70°C for 30 minutes. Then a layer of about 0.5 cm thick of hard PDMS (Sylgard™ 184 from Dow Chemicals) is cast on top. A quick degassing is again performed if necessary. It is cured again at 70°C for 30 minutes. The weight ratio of hard versus soft PDMS is 1:9 (Fig. 6.3 a). The PDMS CY52-276 is mixed in a 1:1 ratio of polymer chains and curing agent, to obtain an elastic modulus of around 10 to 25 kPa [220–222]. The PDMS Sylgard is mixed in a 4:1 ratio of polymer chains and curing agent to obtain an elastic modulus of around 2 to 5 MPa depending on the curing conditions and type of test (compression [214] or traction [215]). The effective longitudinal Young modulus of the bilayer can be estimated using the Voigt model, known as the "Rule of Mixtures":

$$E_{\text{bilayer}}^{\text{long}} = f_s E_s + f_h E_h$$

with E_s and E_h the elastic modulus, and f_s and f_h the volume fraction, of the soft and hard layer respectively. The effective transverse Young modulus $E_{\text{bilayer}}^{\text{trans}}$ is obtained, using the Reuss model $E_{\text{bilayer}}^{\text{trans}} = \left(\frac{f_s}{E_s} + \frac{f_h}{E_h} \right)^{-1}$. Using, $E_s = 17 \pm 7$ kPa [220–222], $E_h = 3.5 \pm 1.7$ MPa [214, 216] and for the geometric parameters, $f_s = 0.9$ and $f_h = 0.1$, the value of the effective Young moduli is estimated to be: $E_{\text{bilayer}}^{\text{long}} = 365 \pm 157$ kPa and $E_{\text{bilayer}}^{\text{trans}} = 19 \pm 8$ kPa. The estimated moduli are of the order of those reported in the literature, generally of the order of a few tens to several hundred kPa for the linear region.

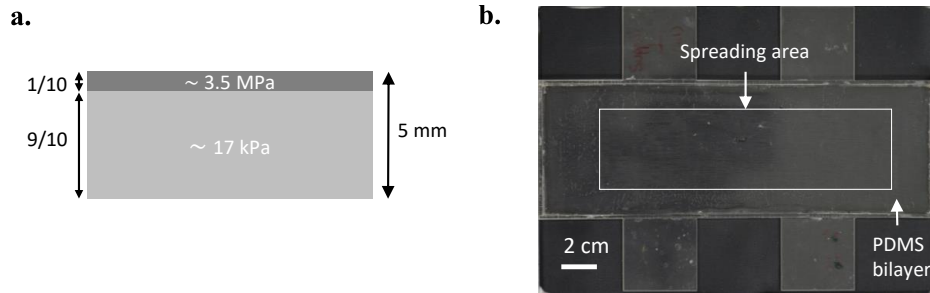


Fig. 6.3 – **a.** Schematic representation of the PDMS bilayer. **b.** Top view picture of the PDMS bilayer in a PMMA mold used as a substrate for the spreading experiment. The white rectangle delimits the spreading area. The square cut-outs on the sides are shims.

With this skin model, the hard layer, mimicking the corneum, is way thicker than the real thickness of the corneum, around 15 μm [8]. Thinner layers of hard PDMS (typically 5 to 25 μm) lead to wrinkling pattern due to stress relaxation. These stresses are thought to be generated during the fabrication process, coming either from the difference in thermal expansion of the two types of PDMS, or resulting from the stacking of the two layers if cured separately. The buckling theory predicts the wavelength of the wrinkling pattern $\lambda = 2\pi h_h \left(\frac{E_h^*}{3E_s^*} \right)^{\frac{1}{3}}$, with E^* the plane strain modulus including the Poisson's ratio and h_h the thickness of the thin film [223, 224]. The soft substrate is considered infinite in thickness in this model. We consider this assumption holds in our case as $h_h \ll h_s$. The measure of the wrinkling

wavelength in a prestressed sample ($\lambda_{\text{exp}} = 1.2 \pm 0.2$ cm) was in agreement with the theoretical one ($\lambda_{\text{theo}} = 1.3$ cm), thus confirming the ratio of the two elastic moduli. To avoid wrinkling pattern the easiest solution was to make thicker the hard layer, even if it meant having a more approximate skin pattern.

Regarding the wetting properties, the PDMS tends to be more hydrophobic than the skin (section 5.4.5) but it was decided not to try to correct it with a coated film to avoid potential tearing and degradation. A picture of the skin model is presented in Figure 6.3b.

6.2.2 New applicator

The applicator used to spread the dry deposit (see section 6.2.3 for the protocol) is a PMMA cylinder, 40 mm long and 15 mm in diameter (Fig. 6.4a). It is covered with a latex film, cut from a non-powdered latex glove (VWR) and glued by its inner side with double-sided tape. This material was chosen because it is sometimes used in the industry, instead of bare fingers, to evaluate the tendency to make aggregates. Its surface presents a certain roughness (Fig. 6.4b) and ensures a good grip, via its frictional character, with the dry deposit. In fact, rubbers such as latex are known to present high friction coefficients due to their adhesive and viscoelastic properties [225]. Without this latex covering, all other conditions being equal, it was not possible to generate aggregates. The characteristic size of the roughness ($5 \mu\text{m}$) corresponds to the size of the spread particles, which allows us to consider a non-slip situation at the applicator wall.

The cylindrical shape is chosen to mimic a finger shape and, as it is symmetric, it allows for equivalent back and forth movements. The applicator degrees-of-freedom are only vertical and horizontal translations. It is not free to rotate. The PMMA cylinder is fixed to a mounting, itself fixed to a robotic arm. The robotic arm is a Cobot UR3e from Universal Robots. The robot is used to perform the back and forth movements at a controlled velocity. A system of masses and ball bearings allows to apply a constant normal force during an experiment, as the cylinder is free to move up and down (Fig. 6.5a). The applied normal force F_N can be varied by changing the masses.

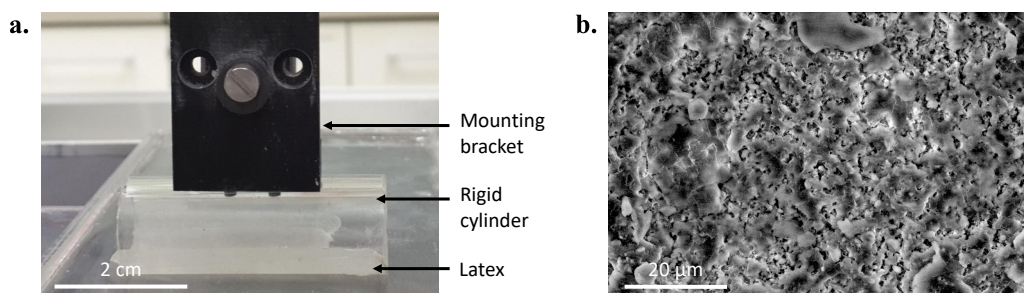


Fig. 6.4 – **a.** Picture of the applicator used for the spreading experiment. The rigid cylinder cannot roll. It is covered with latex. **b.** SEM picture of the latex glove showing the roughness of the surface in contact with the dry deposit. The characteristic in-plane length describing the surface heterogeneities is around $5 \mu\text{m}$.

6.2.3 Protocol

Although the general idea of the test is similar to the industrial procedure, some notable differences exist. We start by spreading between 0.1 and 0.16 g of the sample using the latex-coated cylinder first handled by hand. This initial spreading is performed with a linear motion along the y-axis, perpendicularly to that performed later by the robot (along the x-axis). Figure 6.7b shows an example of the initial deposit after drying; it is discontinuous due to dewetting. Dewetting occurs during the initial spreading movement; during drying the deposit does not further dewet, the contact lines are pinned (see section 5.2.2). Small droplets and line of fluids are observed, most often ranging in size from 100 μm to several centimetres along the y-axis, and from 100 μm to 500 μm along the x-axis. Spreading the initial formulation perpendicularly to the direction of the test results in small objects along the x-direction which favors the generation of aggregates. The effect of the initial deposit discontinuity over aggregates formation is discussed in section 6.3.1.

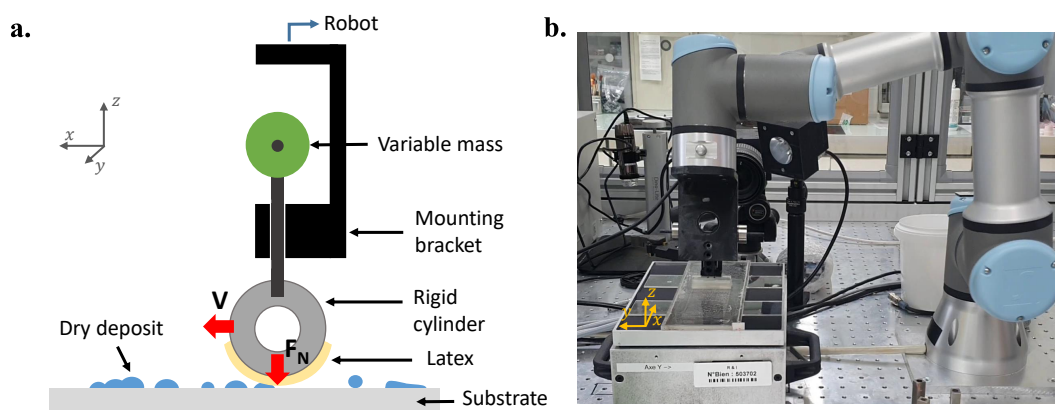


Fig. 6.5 – **a.** Schematic illustration of an experiment and **b.** image of the robotic set-up.

The deposit is dried on a hot plate at 40°C for 20 minutes, a time sufficient to ensure complete drying regardless of particle concentration. Then it is placed on a force sensor. This sensor is used to record, during the test, the forces applied to the substrate in the x, y and z directions. A picture of the set-up is presented in Figure 6.5b). Two back and forth movements are performed, by the robot, at a constant velocity ($V = 0.01$ to 200 mm/s) and constant normal force ($F_N = 0.20$ to 1.37 N). A picture of the deposit is taken initially, and after each linear movement, with a Nikon camera hanged above the set-up.

The velocity range is chosen to include typical spreading velocities, estimated around 50 to 150 mm/s. For the industrial test (presented in section 6.1.2) the value is estimated around 125 mm/s. The normal force range chosen is 10 times lower than for the industrial test. With an artificial skin that mimics the topography of the skin (like the one used industrially) particles are drawn into the pores and foldings during the first spreading step. A high pressing force is then required to push out the particles and observe the formation of aggregates. In the case of the PDMS bilayer, the dry deposit remains above

the flat surface and a high pressing force, like the one applied in the industrial test, would lead to a complete scraping of the deposit. Unlike the industrial test the substrate is not heated during the test (room temperature).

With this protocol, the drying and spreading steps are fully dissociated which is a main difference compared to a real application. This choice is motivated by the desire to simplify the study of aggregates formation.

6.2.4 Water-based formulations

The studied formulations are simplified versions of a cosmetic cream, made with solid particles dispersed in a formulation base.

Formulation base

It can be of two categories: water or oil based. We mainly studied the water-based formulation but some results with oil-based formulation are presented in section 6.6.

For water-based system, the formulation base is made of a Carbopol gel commonly used in cosmetics. It is a yield stress fluid, namely it is solid-like at rest, and fluid-like when a sufficient shear stress is applied ($\sigma > \sigma_y$). This behavior is sought to allow an easier use of the cosmetic product. Carbopol is prepared at 0.3 w% in water. The corresponding yield stress is $\sigma_y = 72$ Pa. It is associated with a biocide used to prevent contamination of the formulation (2-phenoxyethanol at 0.5 w%). Glycerol at 10 w% completes this formulation base. Since it is non-volatile, it is used to maintain a residual fluid film containing the other ingredients of the cream after water evaporation.

Solid particles

The formation of aggregates has been observed for different types of particles such as cellulose, starch, wax and silica. We decided to focus on silica microbeads (NP30, Sunsphere). They are referred to as NP. They present a spherical shape, with no porosity and no swelling, which makes them great model particles. Their density is 2.15. Their diameter is of the order of 4 μm , with some polydispersity that has

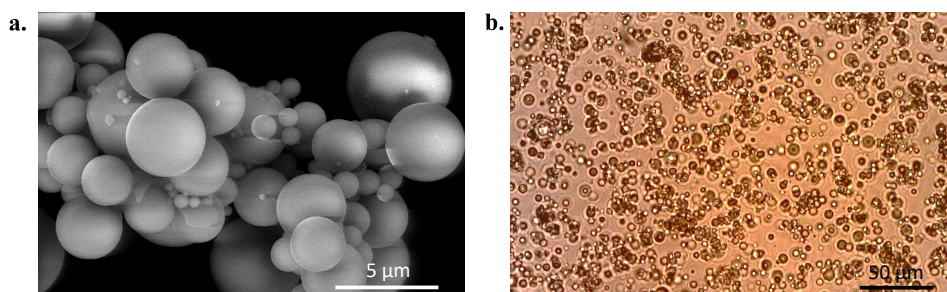


Fig. 6.6 – **a.** SEM picture of silica beads (named NP). **b.** Dispersion in a formulation with 10v% of NP in the non-volatile phase.

not been quantified (Fig. 6.6a). These particles are pretty well dispersed in the formulation base (Fig. 6.6b). In the following, the different formulations are distinguished by the volume fraction, c_v , of the particles in the *non-volatile phase* (i.e. glycerol). The Carbopol is excluded from the calculation of the volume fraction. In the initial formulation (i.e. before drying), the Carbopol is highly swelled in water (due to the neutralization step with NaOH), by 200-1000 times its original volume [25]. During drying, the volume of the Carbopol microgels decreases, but they are expected to remain swollen up to more than 8 times their initial size since the glycerol can also act as a swelling agent thanks to its polarity [27]. This is confirmed by the observation of the sample after drying: only one fully transparent phase is observed. Thus we consider the Carbopol as a modifier of the interstitial fluid properties and not as a solid particle.

In the last section, we extend our study to cellulose, corn starch and silica microbeads which are more complex to study because of their porosity, swelling, roughness or angular shape for instance.

6.3 Factors that influence the formation of aggregates

In this section we describe several factors influencing the formation of aggregates such as the continuous or discontinuous nature of the deposit, the concentration of solid particles, and the presence of Carbopol.

6.3.1 Discontinuity in the dry deposit

The experiment described before is carried out on two types of deposits: a continuous one of about 100 μm thickness, and a discontinuous one due to the dewetting of the formulation. To obtain a continuous deposit, the mass of deposited fluid per square centimeter has been multiplied by 10. The thickness of the film becomes sufficient for gravity to stabilize it with respect to the capillary forces. Both types of samples are left overnight to dry due to the longer drying duration of the continuous deposit. It is possible that a particle crust forms on the surface of the deposits during the drying process (section 5.2.2), but this would apply to both continuous and discontinuous deposits. Then the spreading experiment is performed. Pictures of the two deposits are shown before and after the test for a formulation at $c_v = 65\%$ (Fig. 6.7a and b). We observe the formation of rolling aggregates only for the discontinuous deposit. For the continuous deposit, we observe a slight footprint left by the passage of the cylinder, as it removed only few particles away. However, if we initially generate a defect (i.e. discontinuity) in the continuous deposit, such as a scratched line, we observe that rolling aggregates resulting from this defect can be formed (Fig. 6.7c). From these observations, we can state that aggregate formation is linked to the inhomogeneity of the deposit. This inhomogeneity originates in our system from the dewetting of the formulation on the PDMS.

How does this compare to the real situation? The skin topography also presents inhomogeneities: the pores and skin lines act as particle traps during the first phase of the spreading (Fig. 6.8a). A top view of the skin shows patches and lines of particles quite similarly to what is observed with our artificial skin

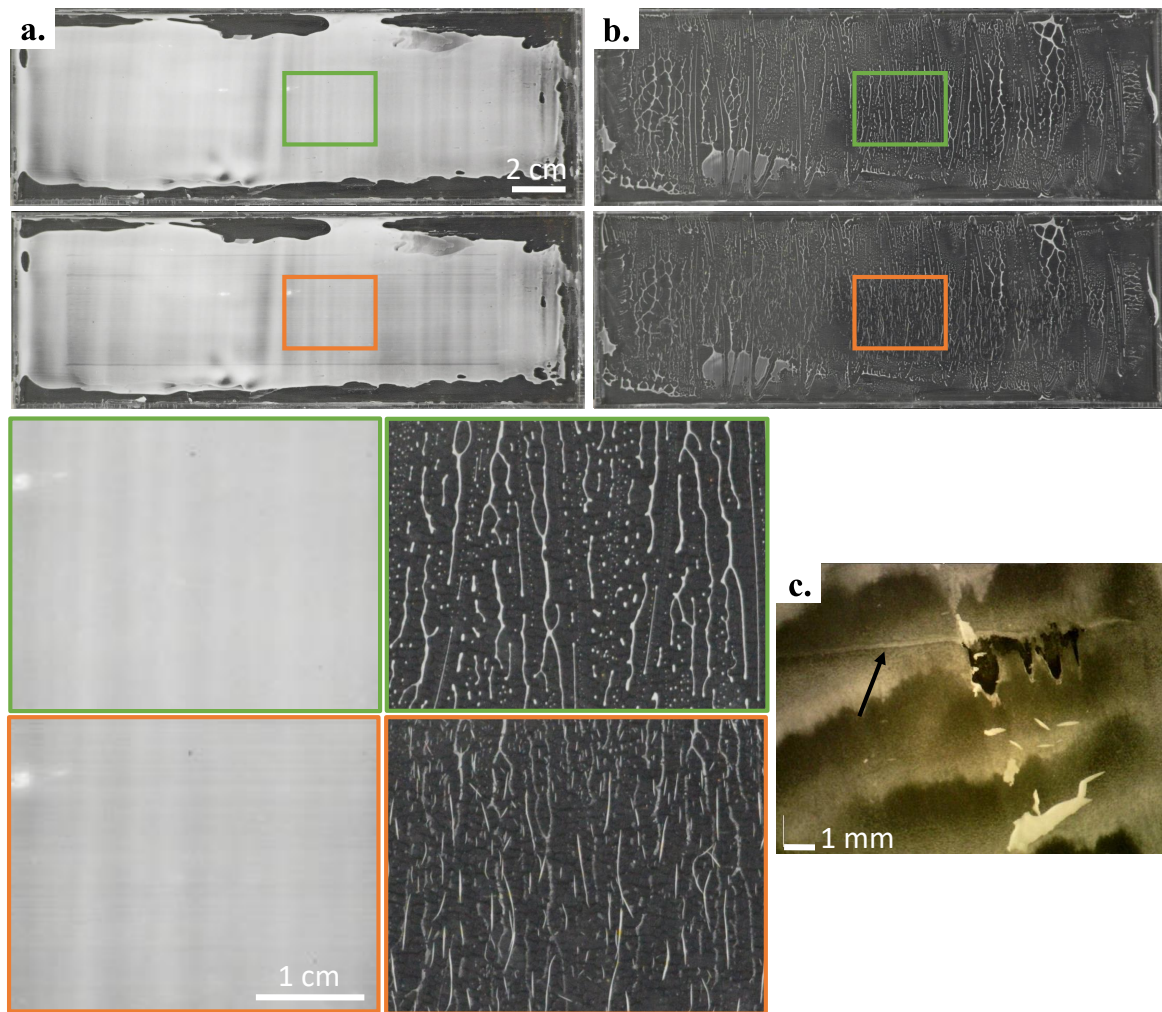


Fig. 6.7 – **a**. Continuous dry deposit, and **b**. discontinuous dry deposit of NP at $c_v = 65 \text{ v}\%$ in the glycerol phase. First line: Pictures of the initial continuous deposit, Second line: Pictures of the final deposit after spreading, and Bottom: Zoom of the initial (green) and final (orange) deposits. Cylindrical aggregates are observed after the test for the discontinuous deposit. The parameters of the spreading test are $F_N = 0.6 \text{ N}$ and $V = 50 \text{ mm/s}$. **c**. Macro-aggregates obtained after a fracture (dark arrow) had been made in the continuous deposit (manual movement of the applicator).

(Fig. 6.8b). The main difference is that these deposits are more easily sheared off by an applicator in the case of PDMS, as they are protruding, whereas with a skin topography, greater forces must be applied to push these particles out of the holes and see aggregates build up.

Thereafter all the results presented were obtained from discontinuous deposits.

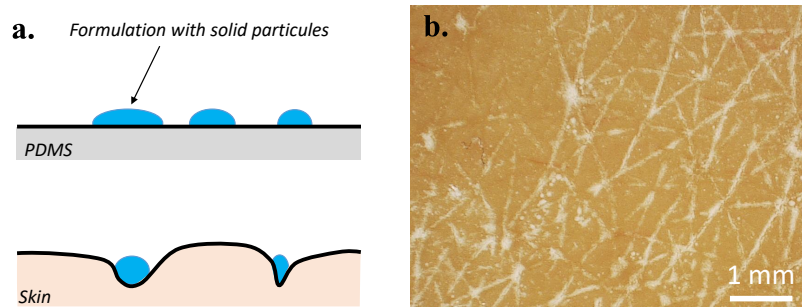


Fig. 6.8 – **a.** Schematic representation of the deposit inhomogeneity on a PDMS substrate (top) and on the skin (bottom). The formulation is not deposited with a homogeneous thickness on the whole surface but is concentrated at the bottom of the folds and holes. **b.** Hirox microscope picture of a commercial artificial skin on which a formulation has been spread using the industrial protocol. During the drying and spreading steps, the particles are not evenly distributed on the surface but concentrate at the bottom of the folds and holes, forming white lines (porous silica H51 in an oil formulation base at 21 w%, see section 6.6).

6.3.2 Solid particle concentration in the non-volatile phase

To study the effect of the particle concentration, samples with various volume fractions of solid particles in the non-volatile phase ($c_v \in [10, 90]$ v%) were formulated.

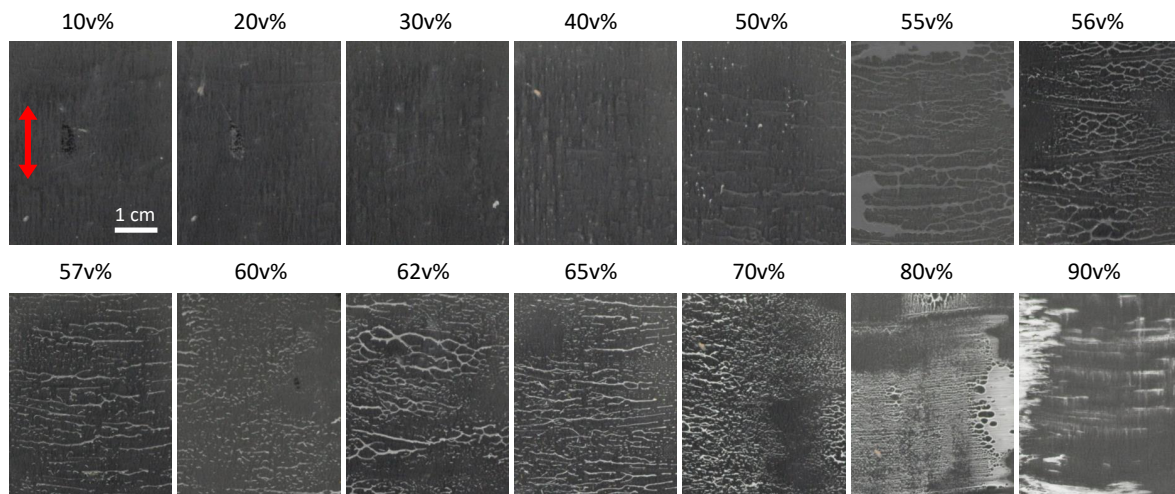


Fig. 6.9 – Pictures of the central part of the deposit, taken after the *first* spreading movement of the robot. From left to right, top to bottom, increasing volume fraction of NP from 10 to 90 v%. The deposits are initially discontinuous. The parameters used for the spreading test are $V = 50$ mm/s and $F_N = 0.6$ N. The spreading direction is vertical (red arrow). The white areas indicate the presence of NP particles. At low particle concentration, $c_v \leq 55$ v% the dry deposit is spread and appears light grey.

The pictures of the dry deposits, obtained after the 1st and 4th spreading movement, are presented in Figure 6.9 and 6.10 respectively. For, $10 \leq c_v \leq 55$ v%, the deposit is spread as a viscous fluid would be. Elongated patches of deposit are observed in the spreading direction. For volume fractions $c_v \in [65, 80]$

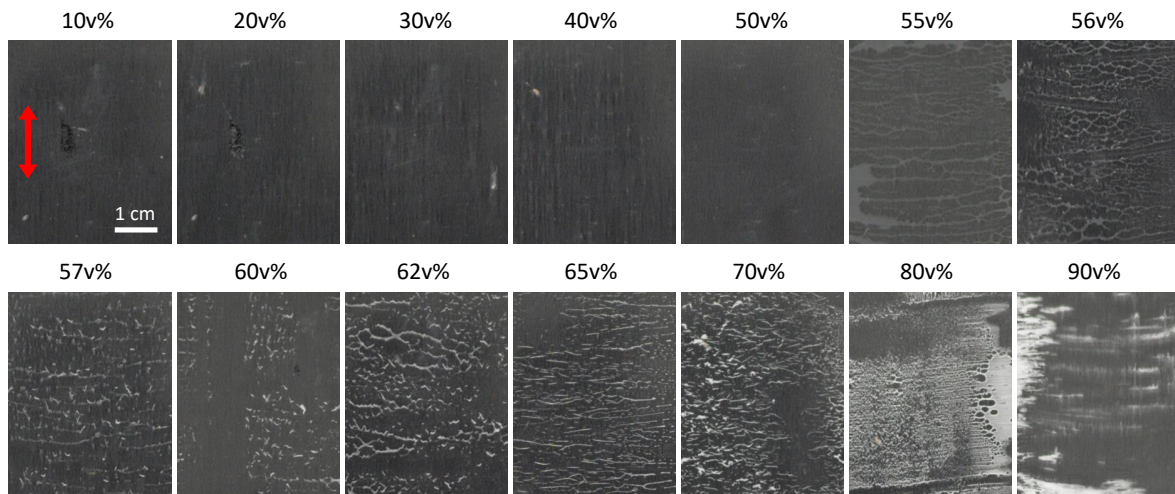


Fig. 6.10 – Same as Figure 6.9 except that the pictures are taken after the 4th spreading movement of the robot.

$v\%$, rolling aggregates are clearly observed. They present an elongated (\sim cylindrical) shape aligned on the mean perpendicularly to the spreading direction. They are well defined and fully detached from the initial dry deposit. They tend to grow in size, particularly in length, after each run. This is due to the merging of several aggregates together (Fig. 6.11).

When increasing the volume fraction from 65 to 80 $v\%$, we observe a decrease of the aggregate size. In fact, the volume of interstitial liquid is no longer sufficient to ensure the cohesion of all the particles by capillary bridges. Consequently, it tends toward a powdery deposit as seen for 90 $v\%$. At this volume fraction the deposit is considered as "spread" again, while it could have been considered as a defect in the industrial test and rated 5/5. For c_v ranging from 55 to 62 $v\%$ we observe an intermediate situation: aggregates tend to form after the first run (Fig.6.9) but they are spread little by little in the following runs.

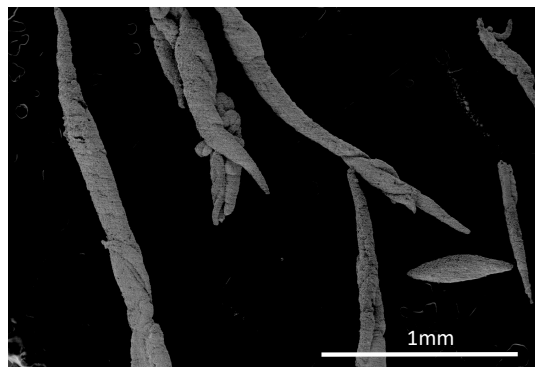


Fig. 6.11 – SEM image of aggregates of NP ($c_v = 65 v\%$). SEM conditions : low pressure vacuum 100 Pa, voltage 10 kV, and current 0.18 nA. The aggregates are cylindrical with various length. Their diameter is around 50 to 200 μm and can reach several millimeters. The bigger ones are obtained by the merging of smaller ones.

Wave-like pattern can be observed by looking carefully at the shapes of the deposits (Fig. 6.10). This is an indication of anchor points on the PDMS substrate causing the aggregates to spread. This behavior will be further discussed in section 6.5.3.

The results for the intermediate volume fraction ($c_v \in [55, 62]$ v%) are not always reproducible, leading sometimes to full spreading (as with $c_v = 50$ v%), or aggregates that grow larger run after run (as with $c_v = 65$ v%). We believe the humidity of the air can modify the properties of the dry deposit, and thus its behavior under shear.

6.3.3 Normal force and velocity dependency

We use the robot to map the effect of velocity and normal force applied at a given concentration. Figure 6.12 shows the results for three volume fractions: 57 v%, 60 v% and 65 v%. The velocity typically ranges from 1 to 200 mm/s, and the applied normal force from 0.2 to 1.37 N. The points at high velocity and low normal force ($F_N = 0.2$ N, $V = 200$ mm/s) are not shown because we are concerned that the contact is not assured and that disturbances such as bumping might occur under these conditions. Three types of behavior are observed: either aggregates appear and grow, the deposit is scraped, or the deposit

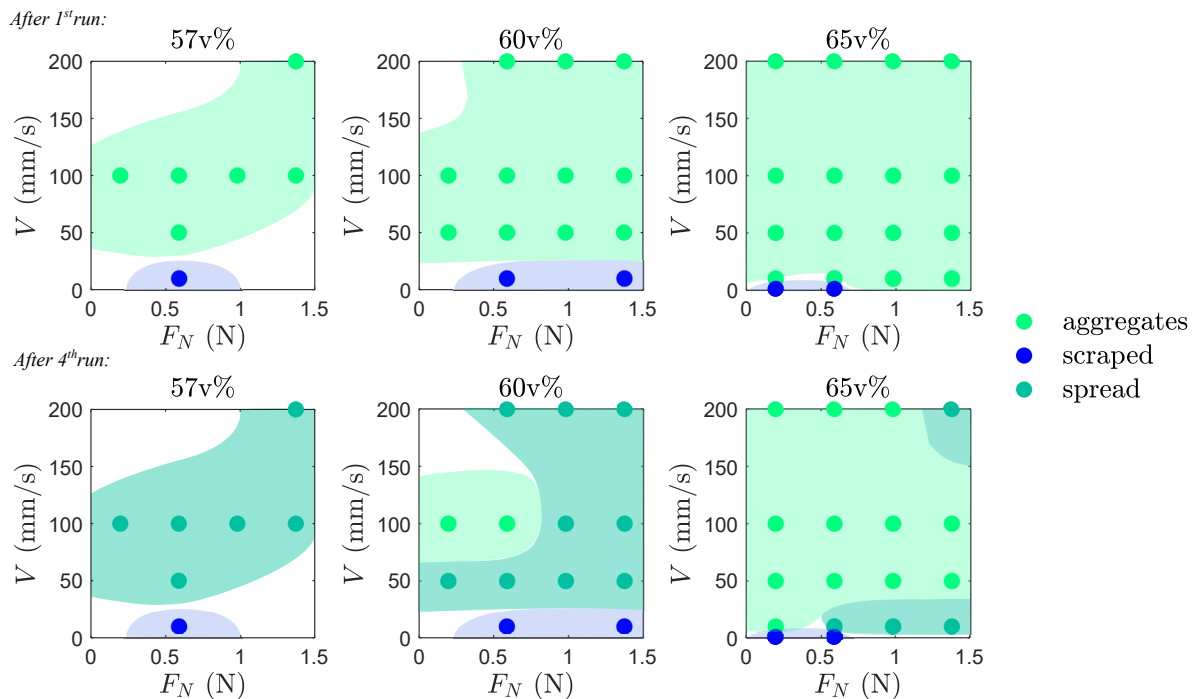


Fig. 6.12 – Map representing the spreading test results after the 1st (top line) and 4th run (bottom line) for different velocities $V \in [1, 10, 50, 100, 200]$ mm/s and normal forces F_N , for formulations at 57 v%, 60 v% and 65 v% (from left to right). The dots correspond to samples tested experimentally. Three behaviors are observed: aggregates formation (light green), spreading (dark green) and scraping of the deposit (blue). The areas with common behavior have been colored with associated colors. For some test conditions (F_N, V) the aggregates are spread after the first run, this is represented by a color change from light to dark green.

is spread. Figure 6.13 shows the three types of results. When the deposit is scraped, this corresponds to a situation where there is no material left in the test area, instead it can be seen agglomerated on the applicator cylinder. It is equivalent to say that there is slip at the bottom wall. The results of both the 1st and the 4th run are presented; if it happens that aggregates appear in the first run but eventually spread, then the sample is described as "spread".

Velocity dependency

Whatever the concentration chosen, if the spreading velocity is too low, there is no formation of aggregates and the deposit is instead directly spread or scraped (even when applying a low normal force). A critical velocity V_c must be exceeded to form aggregates that will not be spread (e.g. $V_c \in]50, 100[$ mm/s at 60 v% and $V_c \in]10, 50[$ mm/s at 65 v%). This means that some kind of dynamics is involved.

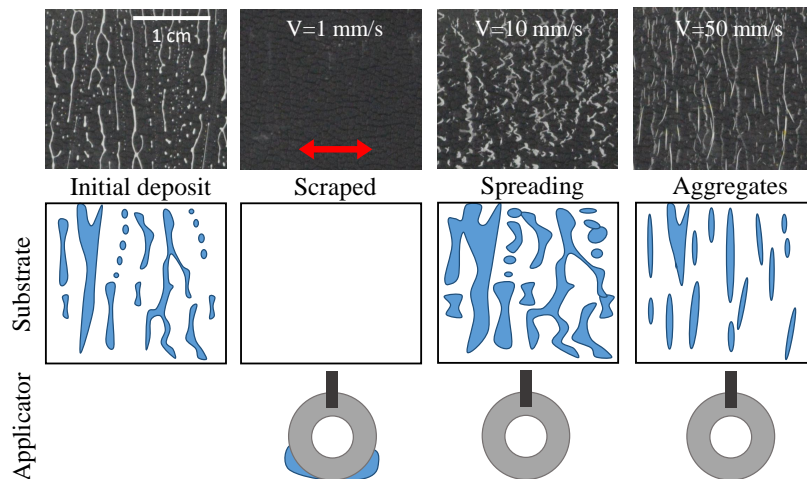


Fig. 6.13 – Pictures and schematic representations of the different behaviors observed after the 4th run by varying the velocity V ($c_v = 65$ v%, $F_N = 0.6$ N). The spreading direction correspond to the horizontal (red arrow). The deposit is scraped off the surface and agglomerates on the applicator at $V = 1$ mm/s. At $V = 10$ mm/s, the sample spreads (widening and wavy shapes). Finally at $V = 50$ mm/s, cylindrical aggregates are observed. Note that the skin pattern (particularly visible for $V = 1$ mm/s) comes from the fact that a synthetic leather has been placed under the substrate to obtain contrasted images.

Normal force dependency

There is little effects of the normal force over the range studied. However, in some cases ($c_v = 60$ v%, $V = 100$ mm/s, and $c_v = 65$ v%, $V = 200$ mm/s) the increase in normal force changes the situation from aggregation to spreading. The increase of the normal force goes hand in hand with the increase of the tangential force (\sim shear stress) which becomes sufficient enough to spread the aggregates.

6.3.4 Carbopol role

To test the impact of the Carbopol we formulate the particles directly in a water-glycerol mixture, keeping the same proportions of solid particles in the non volatile phase as before. Due to the low viscosity of the mixture, and the high density of the particles, sedimentation occurs. To limit this effect the solutions are homogenized just before spreading. Without Carbopol the deposit is inherently different, it dewets more in small droplets, but we managed to obtain equivalent characteristic sizes of the liquid islands by thorough spreading of the initial deposit. By comparing formulations with and without Carbopol (top and bottom line of Fig. 6.14), we observe that, without Carbopol, the deposit is spread whatever the concentration is. The picture from Figure 6.10 are reproduced for ease of comparison. No cylindrical aggregates of particles are seen, instead we observe dry deposit trails along the spreading direction without Carbopol. These results suggest that the Carbopol plays an important role in the formation of rolling aggregates for this type of formulation base. Complementary tests were performed to validate the absence of impact of the biocide (2-phenoxyethanol), alone or in interaction with Carbopol, on aggregates formation (study not shown here).

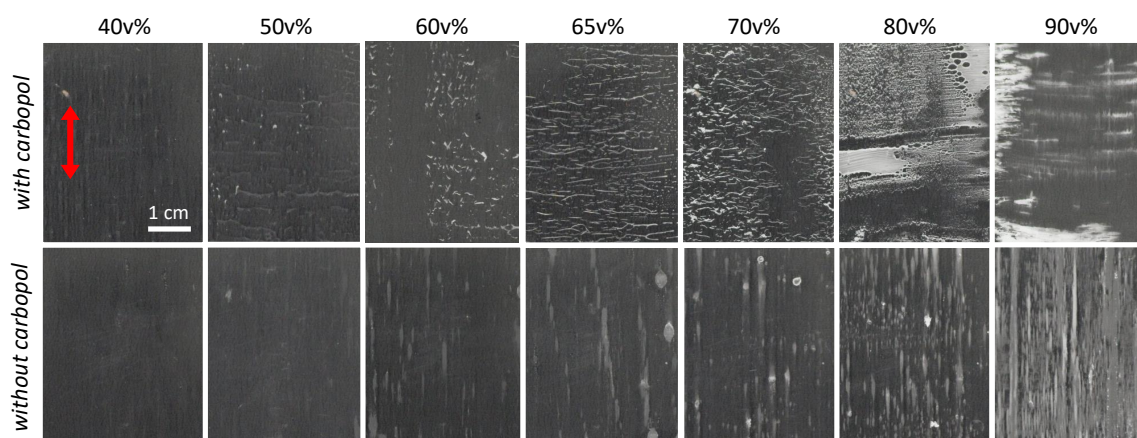


Fig. 6.14 – Picture of the deposit obtained after the 4th run for various concentration of particles in the glycerol phase ($c_v = 40$ to 90 v% from left to right) with Carbopol (top line), and without Carbopol and 2-phenoxyethanol (bottom line). The spreading is materialized by gray lines parallels to the motion direction while when aggregates are formed, they align perpendicularly.

The potential sedimentation of the particles during the 20 minutes of drying would lead to heterogeneities of concentration along the z-direction. The particles (of density $d = 2.15$) are expected to accumulate at the bottom leaving a layer of pure glycerol ($d = 1.26$) at the top. However, for large concentration of particles, as 65 v% and 70 v%, the volume of particles is sufficiently high compared to the interparticular liquid volume to consider there is only one region with particles and glycerol present over the full height of the deposit. We consider that the situation in that case can be compared without restriction to the one with Carbopol. The absence of macro-aggregates at these concentrations confirms the importance of Carbopol.

To understand the differences in behavior observed by varying the composition of the deposit, the applied normal force, and the spreading velocity, we characterized the rheology of these formulations (with and without carbopol when indicated) in their dried state.

6.4 Rheology of the dried formulations

To study the rheology of the dried deposits, we dry the formulations (concentration ranging from $c_v = 40$ to 59 v%) in bulk in an oven at 50°C for at least 48 hours. Evaporation monitoring shows that, after this time, the samples masses vary very little, and that more than 99 w% of the water content has been evaporated. Note that the samples are not homogenized by mixing during drying in order to more closely replicate the spreading experiment for which the sample is left at rest to dry for 20 minutes. This opens the possibility for heterogeneity in particle concentration to occur during drying (see section 5.2.2). At low particle concentrations, the dried formulations are sticky and elastic, while at high concentrations, the formulations become stiffer pastes. At 65 v% and above, the dried formulations are no longer liquids and become brittle. In fact, experiments and computer simulations predict a random close packing of around 64 v% for hard spherical monodispersed particles [226]. The exact value is driven by the polydispersity, the swelling, the roughness, the particle shape, the colloidal interactions etc. Beyond this volume fraction, there is not enough liquid to consider a continuous phase and granulation occurs. This is the reason why rheological measurements were limited to volume fractions $c_v \leq 60$ v%. A piece of the dry formulation is collected and deposited on the rheometer plate, still without previous mixing. The geometry used is parallel plate with 1 mm gap and plane diameter of 20 mm. To avoid slippage, sandpaper (Grit P800, grain diameter 22 μm) is glued on both surfaces with double-sided tape. The temperature is fixed with a Peltier plate at 25°C.

6.4.1 Flow properties in the non-linear region

Typical results

A constant stress is applied to the sample for 120 seconds. The shear rate and the axial force are recorded as a function of time. This experiment is repeated for increasing values of stress on the same sample. We observe that for most stress levels, the measured shear rate value is not constant but evolves with time (Fig. 6.15). We can identify four different regions:

- Region I: For the lowest stresses (red), the angular velocity required to apply these setpoints is too low compared to the limit of the device. Therefore, these values are not reliable and are not considered in the following. Note that this limit is reached for quite high absolute stress values (4 to 8 kPa in this example) due to the very high viscosity of the sample.
- Region II: For $11 \leq \sigma \leq 17$ kPa (light green), the shear rate, after a sharp drop, continues to decrease without reaching a plateau. The flow gradually slows down while the viscosity continues to increase with time.

- Region III: At $\sigma = 20$ kPa (dark green), a more usual behavior is observed. After a few seconds, the shear rate reaches a constant value over time. Steady state viscous flow is reached: only the viscous response is measured on the plateau.
- Region IV: For $\sigma \geq 22$ kPa (orange), we observe an increase in the shear rate over time with occasional fluctuations. This corresponds experimentally to the onset of edge fracture, and the formation of formulation ridges outside the geometry (see *Edges fractures* in section 1.2.4).

In all cases, the shear rate starts by decreasing quickly, which corresponds to the instantaneous elastic response of the material.

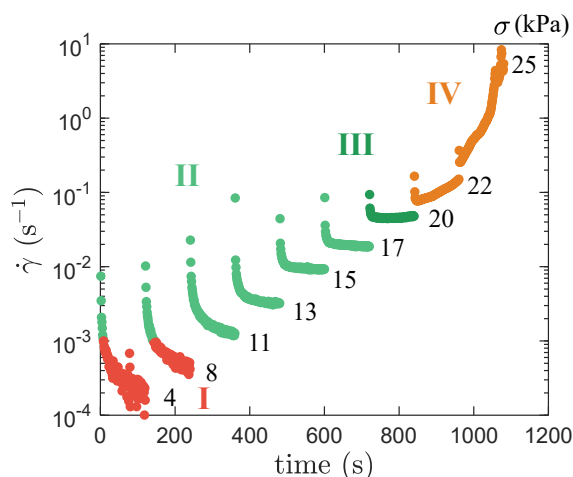


Fig. 6.15 – Change in shear rate over time for different stress levels applied successively for 120 s over the same sample. The sample is a dried formulation of NP at $c_v = 56$ v%. Colors are used to distinguish four different regions (see text).

This figure illustrates how difficult it is to measure the flow properties of such a material. The sample barely reaches steady state before undergoing instabilities that prevent further measurements. This bifurcation behavior between the second and third region means that there is a critical shear stress under which shearing leads to a non-flow condition in the steady state [227]. This critical stress corresponds to a yield stress. Thus, in this example, we define the yield stress around $\sigma_y = 18.5 \pm 1.5$ kPa. This value has been confirmed by the determination of the yield stress from the oscillation experiments (data in section 6.4.2). For $\sigma < \sigma_y$ the rheology measures the elasticity of the material. Note that as the steps are successively applied to the same sample, kinetics might be hindered by the history experienced by the sample.

In the following parts, the data from region II and III are kept, although region II do not give access to proper rheological characterization (out of equilibrium data); it is used to show some tendency only.

Yield stress

From the rheological curves, we identify the yield stress at different concentrations as the critical stress where steady flow is reached. The corresponding values are indicated by dashed lines in Figure 6.16a.

The yield stress increases strongly with particle concentration (Fig. 6.16b). The error bars represent the uncertainty associated with this definition of yield stress.

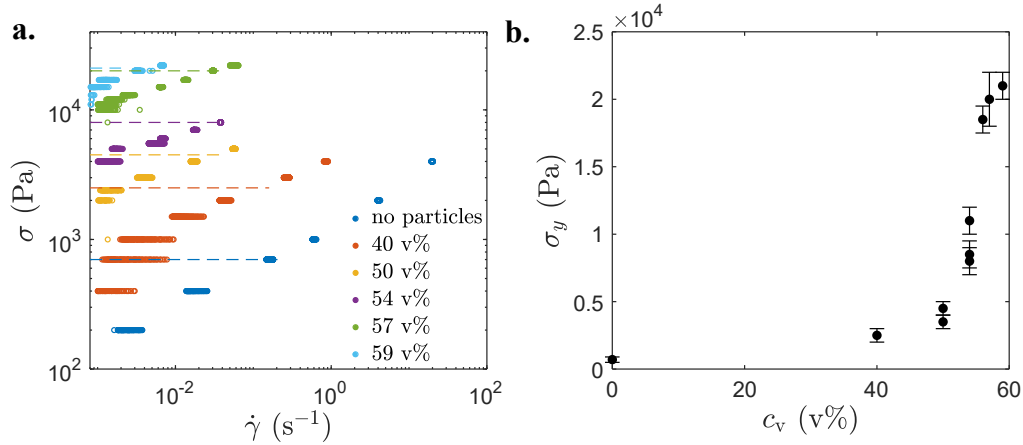


Fig. 6.16 – **a.** Stress as a function of the shear rate for dried samples at different volume fractions of NP in glycerol. The dashed lines represent the estimated yield stresses. Only the stress levels in regions II and III, defined in section 6.4.1, are shown. **b.** Yield stress as a function of particle concentration in the non-volatile phase.

6.4.2 Viscoelastic properties in the linear region

Oscillatory stress at a constant frequency (1 Hz) is imposed on the material using strains, $\hat{\gamma}$, comprised between 0.01 and 1000%. The elastic and loss moduli are recorded. This experiment shows the behavior of the dried formulation in the linear regime (G' and G'' constant) and its transition to the non-linear regime (G' and G'' with non-zero slope) where the curves even cross. The curves are characteristics of yield stress material with G' above G'' in the linear regime before changing order in the non linear regime (Fig 6.17a). However, edge fractures are observed for samples with particles at the end of the elastic regime ($\hat{\gamma} \simeq 50\%$) which prevents us from studying the high strains above this value.

We estimated the deformation of aggregates around 20% (dotted line in Figure 6.17), which corresponds to the elastic behavior region. To probe the viscoelastic properties of the material at this amplitude, an oscillatory stress at various frequencies (ranging from 0.01 to 10 Hz) is applied to the sample.

We observe that the storage modulus, related to the elastic properties of the material, increases with the concentration of particles and the frequency of sollicitation. For 56 v% NPs in the glycerol phase, G' increases by 54% over two decades of frequency (Fig 6.17b).

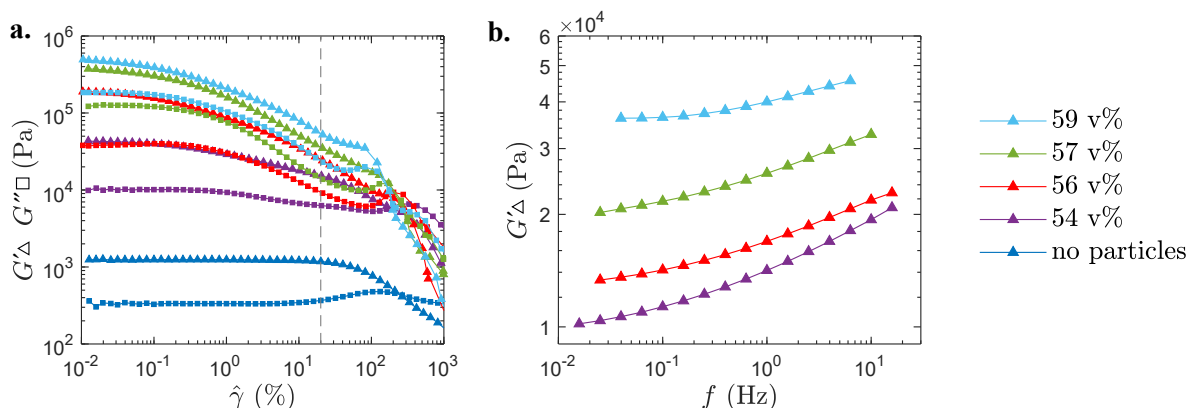


Fig. 6.17 — **a.** Evolution of the storage G' and loss modulus G'' as a function of oscillation strain $\hat{\gamma}$ of dried formulation of NP at various volume fractions in glycerol. **b.** Evolution of the storage modulus G' as a function of the oscillation frequency at a constant strain of 20% (dashed line in plot **a.**). The sample with no particles is not shown.

6.4.3 Impact of Carbopol on rheology

To estimate the effect of Carbopol on aggregates formation, we compared the dried formulations with a mixture of particles formulated at the same volume fraction directly in glycerol. We observe a totally different rheological behavior. The results are presented in Figure 6.18 for NPs at 57 v% in the glycerol.

Flow behavior

Different levels of constant stress are applied to the samples as described previously. In this section, all the regions are shown for the sample with Carbopol and the regions II and III are highlighted by the green rectangle (Fig. 6.18a). We observe that for this range of shear rates, the viscosity of the formulation is 5 orders of magnitude lower without Carbopol. In fact, in the absence of Carbopol, there is no yield stress ($\sigma_y(\text{no Carbopol}) \approx 0$) and instead the sample is shear-thickening after a Newtonian plateau. The situation in which the applied stress is lower than the yield stress no longer exist for the samples without Carbopol.

We note that the onset of shear-thickening measured for the sample without Carbopol occurs at the same shear rate, $\dot{\gamma} \approx 0.2 \text{ s}^{-1}$ as edge fracture and expulsion of the sample with Carbopol. The shear-thickening is related to the frictional contact chain of particles [19, 20]. Since the particle concentration is the same relative to the interparticular fluid, it is logical to expect that interparticle contacts would appear at the same shear rate with Carbopol. This is consistent with the appearance of edge defects because these are generally associated to a high value of the second normal stress difference N_2 , and N_2 is itself related to the contact between spheres [32]. Interplay between shear-thickening and increased normal stress differences has been reported previously by Cwalina & Wagner [228].

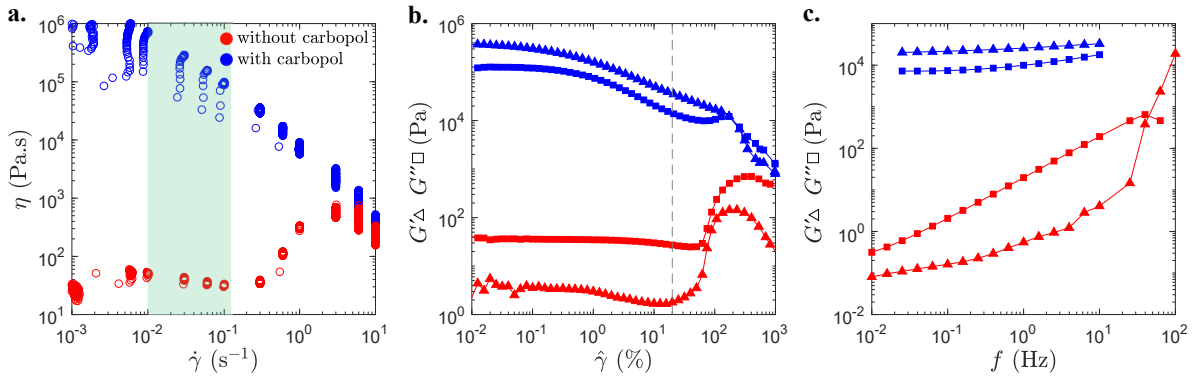


Fig. 6.18 – Comparison of the rheological curves obtained for NPs at 57 v% in glycerol, with (blue) and without Carbopol (red). **a.** Viscosity η as a function of the shear rate $\dot{\gamma}$ obtained by applying different stress levels for 120 s. The green area represents the region II and III. **b.** Storage G' and loss G'' moduli obtained for amplitude oscillations at 1 Hz, **c.** or frequency oscillations at $\hat{\gamma} = 20\%$. The amplitude chosen corresponds to the dashed line in **b.** G' increases by 55% with Carbopol and by more than a decade without Carbopol when increasing the frequency from 0.02 Hz to 10 Hz.

Behavior in oscillation

The comparison of the oscillation curves also shows strong differences between the two situations. For example, the storage modulus G' is more than 4 orders of magnitude lower in the absence of Carbopol for most strains (Fig 6.18b). The storage modulus is also lower than the loss modulus in this case. Hence, at e.g. 20% strain and 1 Hz, the sample with Carbopol behaves like an elastic solid while the sample without Carbopol behaves like a viscous liquid. The frequency oscillations (Fig. 6.18c) show that these observations are valid for most frequencies. The sharp increase observed in the storage modulus for a frequency $f \geq 30$ Hz is linked to shear-thickening behavior.

In both cases, G' increases with the frequency: by 55% with Carbopol and by more than a decade without Carbopol (when increasing the frequency from 0.02 Hz to 10 Hz).

Based on the spreading experiments and rheological measurements performed on the dried formulations, we propose, in the following section, a mechanism to explain the formation of aggregates.

6.5 Formation mechanism

In this section, we first attempt to understand how aggregates are initiated from the dry deposits, and then propose a mechanism and a model to explain why some samples spread while others generate rolling aggregates. We use the experimental results from the sections 6.3 and 6.4 as well as some additional results on tackiness and millimeter-sized aggregates to support them.

6.5.1 Nucleation of the cylindrical shape

After drying, the deposit consists mainly of small sessile drops due to the dewetting. When the aggregates appear they take the shape of cylindrical rods. To go from a disk geometry to a cylinder geometry, we can imagine two mechanisms (Fig. 6.19c). First, we can imagine a rolling of the deposit like a snail shell. Second, we can have a rolling without slipping of the entire deposit like a treadmill. To decide between these two potential mechanisms, we examine the formation of an aggregate from a sessile drop. Since the substrate is transparent (PMMA and PDMS bilayer), it is possible to follow what happens to a sessile drop during shearing by the applicator. Figure 6.19a shows a drop being deformed by the passage of the applicator and fractured before forming an aggregate visible from $t = 0.2$ s. We notice that the aggregate appears at the back of the cylinder whose center axis is highlighted by the gray line. This suggests a treadmill type of driving mechanism whose steps are now illustrated with a macroscopic system. Thus, to test this hypothesis, we studied the shearing of a glue pad disk between a sheet of sandpaper and a transparent PMMA cylinder (Fig. 6.19b). The glue pad (UHU Patafix) is a pressure

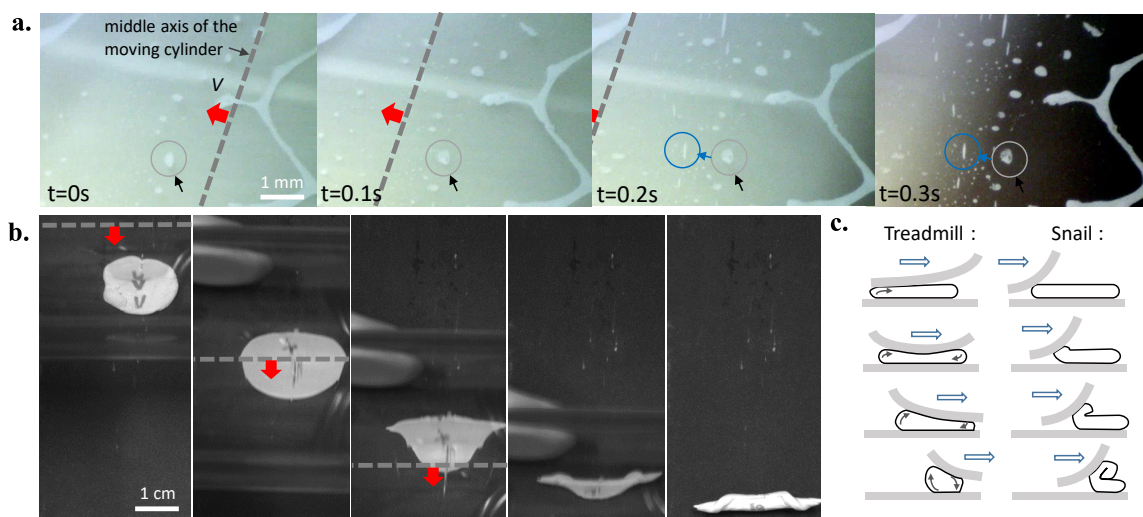


Fig. 6.19 – **a.** Bottom view, through the transparent substrate (PDMS bilayer), of the formation of aggregates. The central axis of the applicator is shown as a dashed line. It moves from right to left according to the direction indicated by the red arrow. Looking at the particular case of the circled dry deposit we observe at $t = 0.1$ s a deformation of the deposit then at $t = 0.2$ s the formation of a cylindrical "child" aggregate circled in blue. The formulation used was $c_v = 65$ v%, the motion was done by hand and did not allow to control V and F_N . **b.** Top view of a transparent PMMA cylinder shearing a Patafix disk deposited on a sandpaper. The disk has been pre-marked with chevrons on its upper side and crosses on its lower side. Spacers of $125 \mu\text{m}$ are used to avoid scratching the cylinder on the sandpaper. It is observed during the experiment that the disk is first deformed by the cylinder before contracting on itself at the back of the cylinder to form a rod-like aggregate. The crosses are visible in the second and third picture, indicating a treadmill-like mechanism. **c.** Schematic representation of two types of cylinder formation, either through a treadmill type mechanism (left) or through a "snail shell" type mechanism (right).

driven adhesive, yield stress, and viscoelastic material. There are no strong chemical bonds between the glue pad and the walls, but there are strong (cohesive) forces that allow it to roll easily. The materials of the substrate and applicator were chosen to allow a good grip, and the transparency of the PMMA applicator cylinder allows to follow the mechanism from above. We observe a deformation of the disc which extends perpendicularly to the movement. A rod is formed at the back of the applicator. Moreover, the observation of the marks, made prior to the experiment on the two faces of the disc, testify of a mechanism of treadmill type as all markers remain (deformed) on the surface of the rod. The glue pad experiment is a proof of concept that treadmill-like motion is possible with highly cohesive and adhesive materials and results in a cylindrical rod formed at the back of the applicator. In this case, no fracture is observed, unlike in Figure 6.19a (for a better understanding of the fracture in a treadmill mechanism, reference should be made to Fig. 6.26c). Tests performed on dried formulation at 65 v% also evidenced a treadmill motion when a millimeter sized deposit was sheared between two sandpaper plates (see section 6.5.3).

To conclude, we consider that a *rolling without slipping motion accompanied by a treadmill-like motion is at the origin of the cylindrical shape of the aggregates.*

6.5.2 Proposal for a microscopic mechanism

To get a treadmill motion, as described above, two parameters seem critical: a strong *cohesion* inside the material, which prevents it from deforming too much (being spread) while still being able to deform to roll, and a certain *adhesion* to the walls that allows the material to be driven in this rolling motion. We propose that *aggregates formation occurs when the cohesion within the material is greater than the adhesion on the walls.* Otherwise, the sample spreads until a fracture within the material occurs.

The illustration of this model is shown in Figure 6.20. It should be noted that some level of adhesion is always required to ensure aggregates formation. If this is not the case, the deposit is scraped, or remains in place on the substrate without perturbation depending on how the applicator enter in contact with the deposit (from the side or the top). This situation is represented in the top line of the figure. It is equivalent to say slip can occur at one or both walls. We make the assumption of non-slip at the walls. The main difference between the spreading and rolling situations lies in the behavior of the particles colored in red and green :

- In the first case (middle line of Fig. 6.20), they remain stuck to the walls: this corresponds to the spreading situation. The deposit stretches in the spreading direction, which is accompanied by a movement of the upper and lower walls towards each other, and finally, by a fracture of the deposit if the material cannot be deformed sufficiently. Fracture can occur in the sample (a picture of the two fractured parts is shown in Figure 6.26d) or near the interface between the sample and one of the walls (bottom or top). The cohesion in the material is not high enough compared to the adhesion to the walls to prevent stretching and/or fracture. When fracture takes place in the sample, it is considered as "spread".

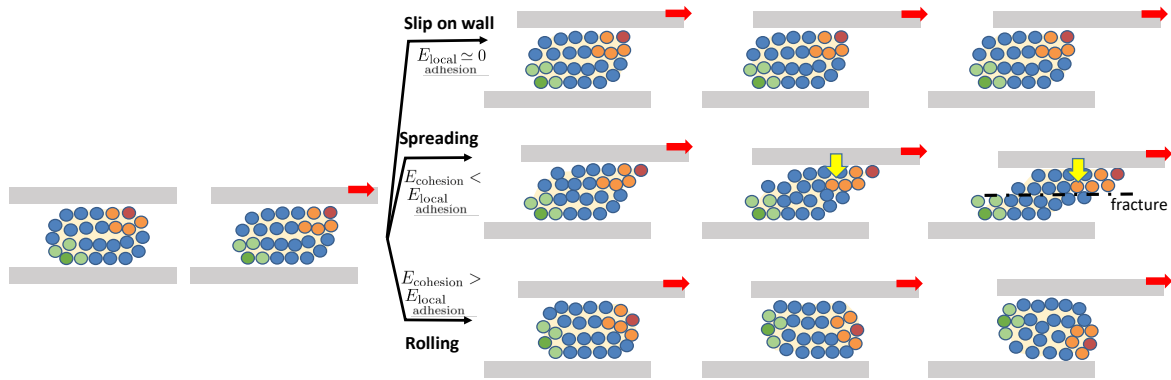


Fig. 6.20 – Illustration of the competition between adhesion and cohesion and the resulting behavior of the sheared deposit: either spread (middle) or undergoing a rolling motion (bottom). The latter situation describes the formation of rolling aggregates. The spheres represent the solid particles inside the glycerol/Carbopol matrix (pale yellow). Some are colored (red and green) to easily follow their displacement. The first line corresponds to a situation where the slip occurs at the top interface. The yellow arrows indicate the vertical movement of the top plate caused by the deformation of the droplet.

- In the second case, the cohesion within the material prevents a strong stretching of the material. The adhesive force between the colored particles and the walls is overcome by the cohesive force, causing them to detach. The rolling without slipping motion starts.

Experimentally, the adhesion on the top and bottom walls are not equivalent as the materials used (PDMS and latex) are not the same. If the cohesion is greater than the adhesion on one wall but less than the adhesion on the other wall, fracture and consequently slip is expected to occur at the low adhesion interface, even though the adhesion is not zero in absolute terms.

The term describing the adhesion energy is written $\Delta\gamma S$ with $\Delta\gamma$ the Dupré energy which corresponds to the work per unit area necessary to move two surfaces apart: $\Delta\gamma = \gamma_1 + \gamma_2 - \gamma_{12}$ expressed in $\text{J}\cdot\text{m}^{-2}$ (see section 5.3.4). Multiplied by the surface of contact between the material and the wall, S , it gives the energy needed to separate the two surfaces. However to start a rolling motion it is not the whole surface of contact that has to detach but only a fraction corresponding to the surface of few particles. The quantity is denoted $E_{\text{local adhesion}}$ and is expressed as $\Delta\gamma r\alpha$ with r the surface of contact between one particle and the substrate, and α the number of particles involved in the detachment, $r\alpha < S$ as only a fraction of the top and bottom surfaces must be detached to perform rolling. To take into account the dissipation that occurs during crack propagation, a dissipation function Φ should be added similarly as in Eq. 5.10. Note here that to simplify this model we consider the top and bottom walls are made of the same material.

The cohesion energy can be written as $G'\Omega$ with G' the storage modulus, Ω the volume of the material.

Aggregates form if :

$$E_{\text{cohesion}} > E_{\text{local adhesion}} \quad (6.1)$$

which can be rewritten as :

$$G'\Omega > \Delta\gamma r\alpha\Phi \quad (6.2)$$

The inequality 6.2 is similar to the criterion used in the adhesive field to describe the transition between interfacial and bulk deformation $\frac{\mathcal{G}_c}{Ed}$ [158, 171], where $Ed \approx \frac{G'\Omega}{S}$ and \mathcal{G}_c represent the energy to propagate a crack at the interface. Using the reasoning of Deplace [170] and Nase [173] we would be tempted to consider $\Phi \approx \tan(\delta)$ with δ the phase shift between stress and strain. This approximation is applicable to elastomers, and has been studied in this framework. The transposition to the case of dense suspensions may not be straightforward. Further work needs to be done on this question in order to refine and validate the expression of $E_{\text{local adhesion}}$, in particular the dissipative term.

To validate the model (Eq. 6.1) we want to check the dependency of aggregates formation over the storage modulus (G') and the adhesion to the walls.

6.5.3 Validation of the model with experimental results

In light of this model, we propose explanations to the results obtained in section 6.3 by combining the rheological measurements with probe tack test, used to assess the cohesion/adhesion balance.

Aggregates and particle concentration

The formation of aggregates was found to be related to the concentration of particles in the non-volatile phase. This increase in concentration leads to an increase in viscosity, yield stress and storage modulus. In Figure 6.21, we observe that the samples that generate aggregates on the first run (red rectangle) correspond to those with the highest storage modulus G' and yield stress σ_y . We estimate that the applied stress σ_a is higher than σ_y in all spreading situations. Indeed, the deformations undergone during the spreading are very large. The pictures in Figure 6.26d show that the sample has undergone at least 200% deformation before fracturing, this level of deformation corresponds to the non-linear regime above

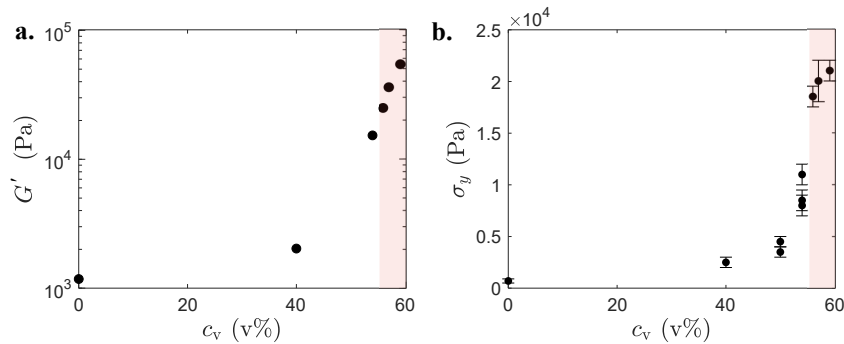


Fig. 6.21 – **a.** Storage modulus G' (value at $\hat{\gamma} = 20\%$ extracted from amplitude sweep test performed at 1 Hz) and **b.** yield stress σ_y as a function of particle concentration c_v . The red area highlights the concentrations at which aggregates can be observed.

the yield stress (Fig. 6.17). For samples that generate aggregates, the expected strain is less, between 10 and 50%. To know whether the applied stress is above the yield stress or not in this situation, we tried to estimate the value of σ_a . It can be expressed as $\sigma_a = \frac{F_x}{S'}$, with F_x the tangential force measured in the x-direction by the force sensor, and $S' = S\beta$ the area on which this force is applied ($\beta < 1$ is a factor applied on the evaluated area without any deposit, S , to take into account the fact that the deposit is discontinuous and does not cover the whole area). The main difficulty is the determination of S' because the initial deposit is discontinuous and the substrate is soft. An estimate for $c_v = 57$ v% gives $\sigma_a \approx 45000$ Pa with $S' = 4 \text{ cm} \times 1 \text{ mm} \times 0.5$ and $F_x = 0.9$ N corresponding to a situation where half the surface of contact effectively shears the deposit. Although the value cannot be given precisely, it turns out that it is of the order of the yield stress, $\sigma_y(57\text{v}\%) = 20000 \pm 2000$ Pa. The uncertainty on β prevents us from concluding that $\sigma_a > \sigma_y$ for 100% of the situations, but it is likely to be the case as the deposit is highly discontinuous and height variations might further reduce the area sheared. In any case, since the system is not in a stationary flow, but is solicited over short periods of time, it reacts elastically. In the first moments of the shear, the system is initially at low deformations ($\hat{\gamma} = \dot{\gamma}t$), it starts from 0% and increases until the system starts to roll or until it fractures. *The yield stress is therefore not the determining factor here in the understanding of the aggregates, motivating the choice of a model relying on the cohesion through G' .*

G' increases with particle concentration (Fig. 6.21a), which implies elasticity and cohesion are greater for materials with high content in solid particles. It can be assumed that the cohesion becomes greater than the adhesion from a certain concentration. *Probe tack experiments are performed to test this assumption and investigate how concentration might also affect adhesion.*

Probe tack test:

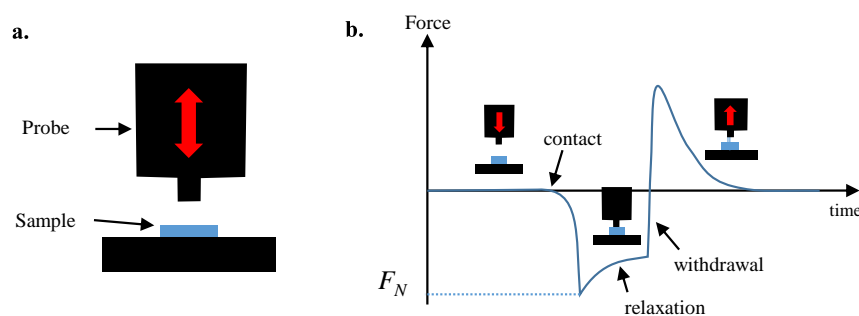


Fig. 6.22 – **a.** Illustration of the probe tack test. **b.** Typical force profile obtained during an experiment. After an approach phase, the probe comes into contact with the sample and compresses it until it reaches the target value F_N . The system is left at rest for a few seconds during which a relaxation of the force is observed. Then the probe is withdrawn which applies a tension on the sample: a strong increase of the force is measured up to a maximum. At this point, the adhesive contact begins to break and the force gradually returns to zero as the probe is removed.

To evaluate the tackiness, related to both cohesion and adhesion, a probe tack test is performed (Fig. 6.22a and b). A sample with a lateral dimension of 8 mm and a thickness of 1 to 2 mm is cut from the dry deposit and placed on the plane of the rheometer as such or after manual pre-mixing. The probe is a 6 mm diameter cylinder. The rheometer is used to control the movement of the probe and measure the axial force. The plane of the rheometer and the surface of the probe are covered with sandpaper (grit P800 $\sim 20 \mu\text{m}$ roughness). For a typical experiment, the probe enters in contact at controlled speed (0.1 mm/s) until the pressure reaches $F = 1.5 \text{ N}$, then pauses for 2 s at the same position, and then pull-backs at $V_{\text{pb}} = 0.5 \text{ mm/s}$ (Fig. 6.22b).

The two classic types of behavior are observed: either the material undergoes a cohesive failure or an adhesive failure. The two situations are illustrated in Figure 6.23a by circles and crosses respectively. In the first case, the adhesion is stronger than the cohesion, and necking of the material or filaments are observed, leaving at the end some material residuals on the probe. In the second case, the detachment occurs at the interface, indicating the existence of strong cohesive forces. Different situations are observed if the samples are previously mixed or not, we focus here on unmixed samples, the impact of mixing is discussed in the next paragraph. For samples tested directly after drying (unmixed), if $c_v \geq 56 \text{ v\%}$ an adhesive failure is observed, while for $c_v \leq 50 \text{ v\%}$ a cohesive failure occurs. At 54 v% a combination of both situations is observed, called cohesive-adhesive failure. The curves of nominal stress

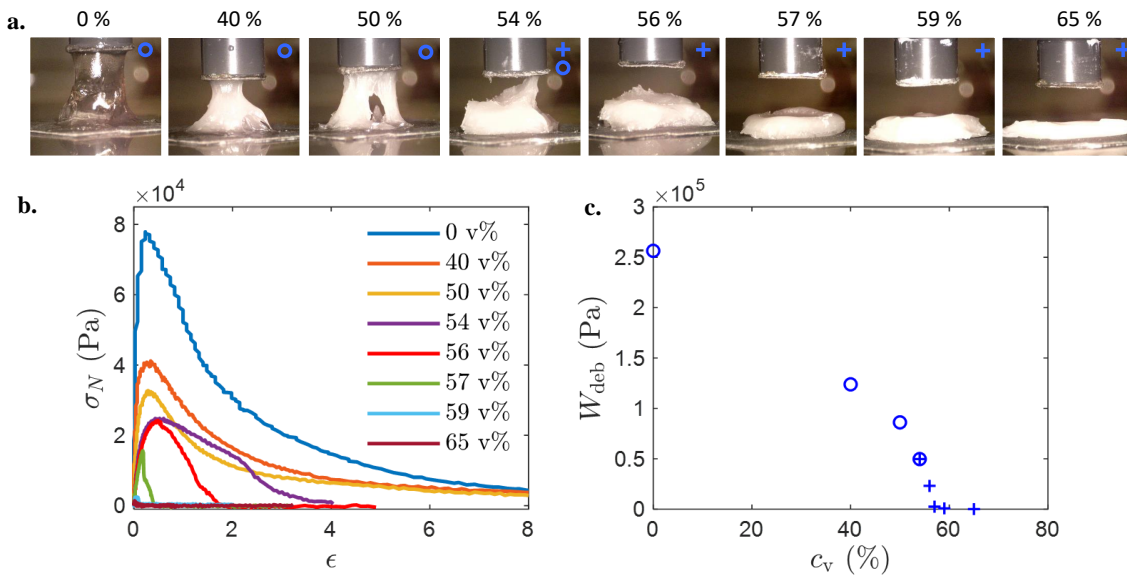


Fig. 6.23 – **a.** Pictures of the tack tests for samples at different particle concentrations c_v . Two situations are observed: the failure occurs inside the sample (circle) or at the interface (cross). The cohesion energy becomes lower than the adhesion energy for $c_v \leq 54 \text{ v\%}$. **b.** Normalized force-displacement curve $\sigma_N = f(\epsilon)$ for unmixed samples. $\sigma_{N\text{max}}$ and ϵ_{max} decrease when the concentration of particles increases. **c.** Volumetric work of debonding W_{deb} as a function of the concentration for unmixed samples. W_{deb} increases as the particle concentration decreases. The pull-back velocity is 0.5 mm/s and $F_N = 1.5 \text{ N}$.

($\sigma_N = \frac{F}{\pi a^2}$) versus nominal strain ($\epsilon = \frac{h-h_0}{h_0}$) obtained in the pull-back step for different concentrations are plotted in Figure 6.23b, with h_0 is the initial thickness of the material before the probe withdrawal. The maximum deformation experienced by the sample before failure, as well as the $\sigma_{N\max}$, increase strongly for materials undergoing a cohesive failure. Overall, the volumetric work of debonding, defined as $W_{\text{deb}} = \int_0^{\epsilon_{\max}} \sigma_N(\epsilon) d\epsilon$, increases when the particle concentration decreases (Fig 6.23c). This increase of W_{deb} results from an increase in adhesion, since cohesion is known to reduce (G' decreases with particle concentration, in Fig. 6.21). At a really high concentration, almost no adhesion is observed (for $c_v = 59$ and 65 v%). This could be directly explained by the Dahlquist criterion which specifies that adhesion cannot occur if $G' > 10^5$ Pa [229] at the bonding frequency. This is because the material is not able to deform sufficiently to ensure good contact with the probe surface. Figure 6.17a shows that such ranges are attained for 57 and 59 v% at 1 Hz for $\hat{\gamma} \leq 4\%$.

This experiment allows to measure the balance between cohesion and adhesion. The parallel can be drawn with the results of this test and the formation of aggregates, if we consider that the problem can be considered isotropic. If the rupture occurs in the material, it corresponds to a situation where $E_{\text{adhesion}} > E_{\text{cohesion}}$ and spreading is expected. If the rupture occurs at the interface with a small deformation of the sample ($\sigma_N = f(\epsilon)$ returns quickly to 0), this corresponds to the situation: $E_{\text{adhesion}} < E_{\text{cohesion}}$ and the formation of aggregates is expected. A fairly good agreement is obtained with the spreading experiments: in the first run (no pre-mixing) the aggregates are observed from $c_v \geq 56$ v% (Fig. 6.9), it is also the lowest concentration at which a clear adhesive failure is observed in Figure 6.23a. This comparison is further discussed in section 6.5.4.

In summary, increasing particle concentration is equivalent to increase cohesion and reduce adhesion, leading to a situation where $E_{\text{cohesion}} > E_{\text{local adhesion}}$ and aggregates appear.

Change in properties with pre-shear and link to aggregates spreading

In this section, we seek to explain the observation made in section 6.3.2 on the spreading of aggregates. Indeed, we have seen, at some concentrations, that aggregates can be observed after the first run but they spread during the following runs by forming wave-like shapes. This situation is observed for example at 62 v%. In Figure 6.24b, we highlight the formation of well-defined, cylindrical, rolling aggregates after the 1st run and their spreading leading to a wave shape in the subsequent runs.

By performing rheological experiments, we realized that the dried formulations had a modified behavior in case of prior shearing at high $\dot{\gamma}$. Note that due to fracture and ejection of the sample even at quite low shear rates, the pre-shear is applied manually by mixing the sample with a spatula. On the one hand, the viscosity, yield stress and storage modulus decrease ($G'(\text{mixed}) < G'(\text{unmixed})$). On the other hand, the tackiness measured after mixing increases significantly, for instance, for $c_v = 57$ v% the sample goes from adhesive failure to cohesive failure by premixing (Fig. 6.24a). The volumetric work of debonding is multiplied by 24 when the sample is premixed. Therefore, a greater adhesion to the walls is expected: $E_{\text{adhesion}}(\text{mixed}) > E_{\text{adhesion}}(\text{unmixed})$. Both effects increase the weight of adhesion

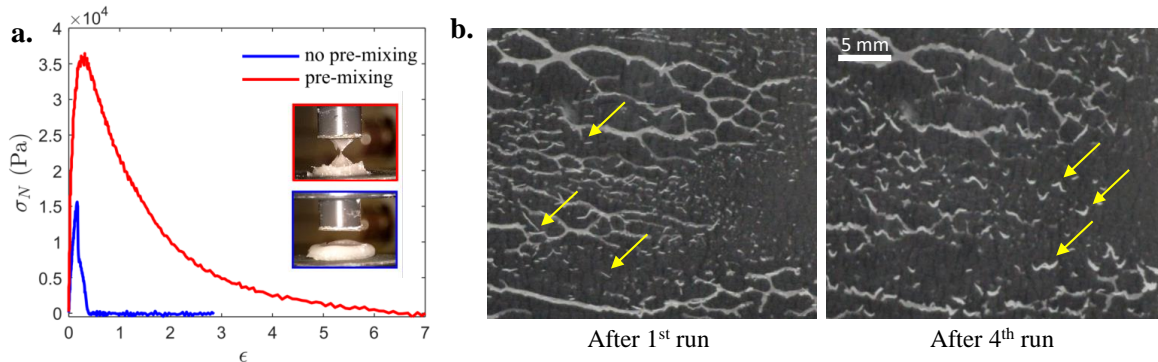


Fig. 6.24 – **a.** Normalized force-displacement curves for a 57 v% sample that has been previously mixed (red) or not (blue). The pictures illustrate the cohesive and adhesive debonding that occurs with and without premixing, respectively. **b.** Picture of the sheared deposit of the 62 v% formulation after the 1st run (left) and the 4th run (right). Arrows indicate rolling cylindrical aggregates (left) or spread aggregates with a wave-like shape suggestive of adhesion points (right).

relative to cohesion. Note that this increase in tackiness is observed for all concentrations as highlighted in Figure 6.25.

Such change in properties can explain the spreading test results. In the first run of the spreading test, the sample has not yet been pre-sheared and generates aggregates for $c_v \geq 56$ v%. This first run acts as a pre-shearing of the deposit and consequently, during the following runs, the adhesion increases and the cohesion decreases leading to a spreading of the aggregates for $c_v \in [56, 62]$ v%. Once the aggregates have been spread, they cannot be formed again. Their wavy shape is evidence of adhesive anchoring at given locations.

It can be noted that adhesive failure is observed with the tack test from 59 v% which is in contradiction with the observation of spread aggregates up to 62 v% (Fig. 6.24b). An exact parallel cannot be drawn between these different situations: it has been shown that the velocity plays a role (see section 6.3.3) and the choice of V_{pb} might not reflect the conditions of the aggregate formation in the spreading test. In addition, the materials used are not the same in the tack test and in the spreading test, which probably modifies the adhesion. The tendency remains correct and further studies should be performed to refine these observations.

To explain this shift in properties with pre-shearing, we suspect that a structuring of the material occurs as the formulation dries: the measured viscosity is one decade higher for a sample directly tested after drying as compared to a sample that was previously mixed. A first hypothesis could be that this results from the formation of a particle crust (see section 5.2.2). This hypothesis is supported by the tack measurement carried out on the samples showing that they are less adhesive before mixing. Another mechanism involving potentially drying-induced consolidation could be at play [230] but we lack information on how Carbopol deswells in the presence of particles.

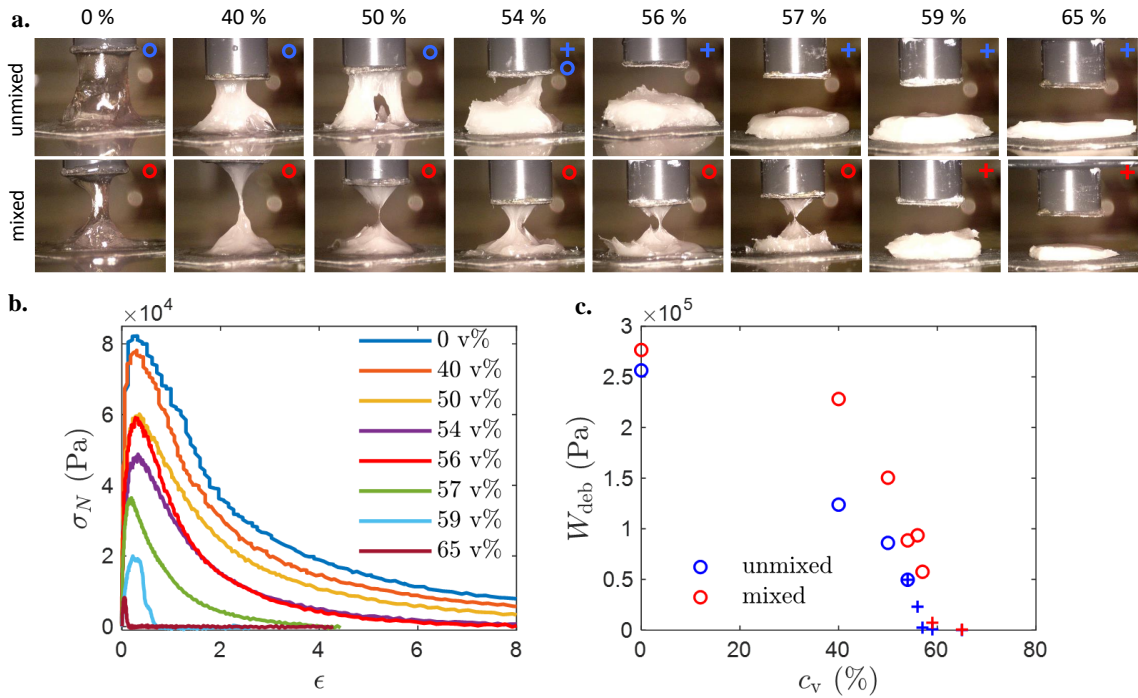


Fig. 6.25 – **a.** Pictures of the tack tests for premixed samples (bottom line) at different particle concentrations c_v . The unmixed samples from Fig. 6.23 are given in the top line for ease for comparison. The concentration at which the failure occurs inside the sample (circle) instead of the interface (cross) is shifted. The cohesion energy becomes lower than the adhesion energy for $c_v < 59$ v% with premixing (instead of 54 v% without). **b.** Normalized force-displacement curve $\sigma_N = f(\epsilon)$ for mixed samples. **c.** Volumetric work of debonding W_{deb} as a function of the concentration for mixed (red) and unmixed (blue) samples. W_{deb} increases when performing a pre-mixing. The pull-back velocity is 0.5 mm/s and $F_N = 1.5$ N.

Effect of the normal force applied

It was previously shown that increasing the applied force allows to go from a situation where the deposit forms aggregates to a situation where the deposit is spread (section 6.3.3). In our model, aggregates are generated if $E_{\text{cohesion}} > E_{\text{local adhesion}}$. By increasing the applied normal force, $E_{\text{local adhesion}}$ is expected to increase. This dependency is usually seen with pressure driven adhesive [164]. In fact, by applying a greater force on the deposit, the contact area increases. In our case, this translates in Eq. 6.2 by an increase in α value. Therefore, the cohesion term can become smaller than the adhesion term, $E_{\text{cohesion}} < E_{\text{local adhesion}}$, and spreading is expected for fairly high F_N in agreement with the observations (see Fig. 6.12).

Effect of the velocity

A clear effect of the velocity has been observed experimentally (section 6.3.3). For a given concentration and normal force, we observe sometimes situations where the sample is scraped at low velocity, spread

at medium velocity and forms aggregates at high velocity (see Fig. 6.12 and 6.13). Increasing the spreading velocity is equivalent to increase the rolling frequency of potential aggregates. In Figure 6.17b, dried formulations were shown to be viscoelastic and G' increases with the frequency. However, it is questionable whether the range of frequencies studied is really representative of the frequencies of solicitation experienced by the aggregates.

Limits of the rheological measurements

In oscillatory mode, the frequency range is limited at its lower and upper end by the inability of the rheometer to track the target strain value. The frequencies at which a rolling soft body is stimulated are diverse and associated with rolling, contact zone deformation, roughness solicitation ... The smallest frequency at stake is the rolling frequency. For $V = 50$ mm/s and $R = 50$ μm , which are typical values of shearing velocity and aggregate radius, the rolling frequency is $f = \frac{V}{2\pi R} \simeq 160$ Hz. Higher velocities and lower radius lead to even higher values of the frequency. The rheometer does not allow to reach this frequency range. We decided, instead of trying to characterize the material at high frequencies, to decrease the frequency range of interest by studying millimeter-sized aggregates at smaller velocities. Thus, if $R = 1$ mm and $V = 0.1$ to 10 mm/s, the rolling frequency becomes on the order of 10^{-2} to 1 Hz which corresponds to the frequency range of rheological measurements.

Millimeter-sized aggregates and link to rheology

A quadrilateral of typical dimensions 10 mm is cut from the dried formulation and placed between two parallel plates covered with sandpaper (grit P800 $\sim 20\mu\text{m}$ roughness). The lower plate moves at a constant velocity V (ranging from 0.1 to 10 mm/s) along the x-axis for 47 mm, while the upper plate is free to move along the z-axis. A constant mass of 69 g is applied by the upper plate. The displacement of the sample is tracked laterally by a high speed camera. This gives access to the velocity of its barycenter V_s and the relative velocity \tilde{v} is defined as $\tilde{v} = \frac{V_s}{V}$. The results are given for different solid particle concentrations in Figure 6.26a. Two types of situations are observed :

- $\tilde{v} \simeq 0.5$: This value corresponds to the theoretical prediction for a rolling without slipping. This type of behavior is depicted by the pictures presented in Figure 6.26c for $c_v = 57$ v% and $V = 1$ mm/s. At the end of the experiment, a rod-shaped object is obtained.
- $\tilde{v} \simeq 1$ or $\tilde{v} \simeq 0$: The sample moves at the same velocity as the lower or upper plates respectively. This situation is more difficult to observe because the upper and lower plates tend to move closer and closer together, as shown in Figure 6.26d. At the end of the experiment, two objects are usually obtained, one on each plate, testifying to a fracture that occurred in the middle of the sample during the experiment. The shapes of the two deposits show that the sample is partially spread before the fracture.

Rolling without slipping is obtained for *high particle concentrations*. Furthermore, this experiment highlights the velocity influence on the behavior of the sheared deposit since either rolling or spreading

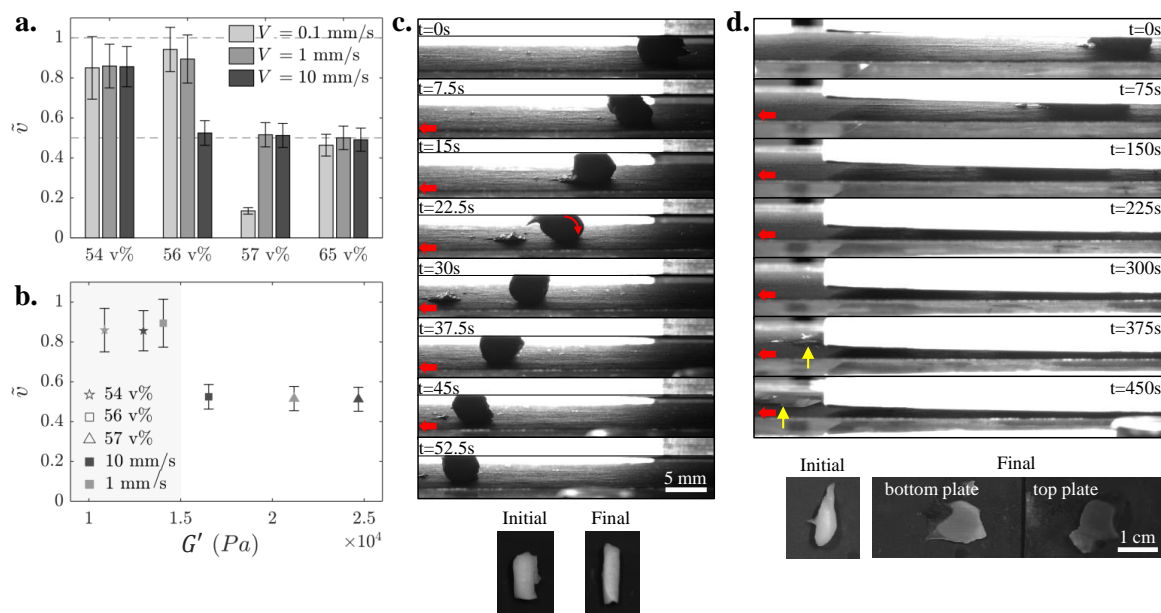


Fig. 6.26 – **a.** Relative velocity of the millimeter-sized object \tilde{v} as a function of the NP concentration in the dried formulation. The substrate velocity is varied : $V = 0.1, 1$ or 10 mm/s. **b.** Relative velocity as a function of storage modulus measured at the expected rolling frequency (around 0.6 and 0.06 Hz for velocity of $V = 10$ and 1 mm/s and an initial diameter of 5 mm). The values of G' are extracted from Fig. 6.17a. Picture taken from the side view for a shear experiment showing: **c.** the rolling of a sample at $c_v = 57$ v%, $V = 1$ mm/s, with the initial and final shapes of the deposit at the bottom, **d.** the spreading and fracturing of a sample at $c_v = 54$ v% and $V = 0.1$ mm/s. The yellow arrows indicate the presence of the sample. The pictures at the bottom show the sample is elongated before fracturing in two parts during the process. The upper plate is the white rectangle and the lower plate is light gray. The upper plate can move freely along the vertical and in **d.** it descends.

is obtained by varying the velocity at a given concentration (e.g. at 56 v% and 57 v%). By examining the value of the elastic modulus G' at the rolling frequency, we observe that we can define a critical value $G'_v \approx 15$ kPa above which the sample rolls instead of spreading (Fig. 6.26b).

This study on millimeter-sized samples highlights the dependency of aggregate formation (rolling behavior) on shearing velocity. This can be related to the viscoelastic properties of the material: a higher velocity means a higher rolling frequency which leads to a higher storage modulus. In other words, the elasticity and thus cohesion of the material increases with the velocity applied to shear it, until, beyond a critical value, it becomes sufficiently large relative to the adhesion so that the material can no longer be spread but starts to roll.

An example of mixed behavior can be observed in Figure 6.26c: in the picture at $t = 22.5$ s, we can see a filament of the material that has been stretched and broken in the middle. The cohesive forces are not high enough to avoid some fracture of the material, leaving a deposit on the substrate. However, when looking at the deposit as a whole, it rolls, indicating cohesion and elasticity that are nevertheless

strong.

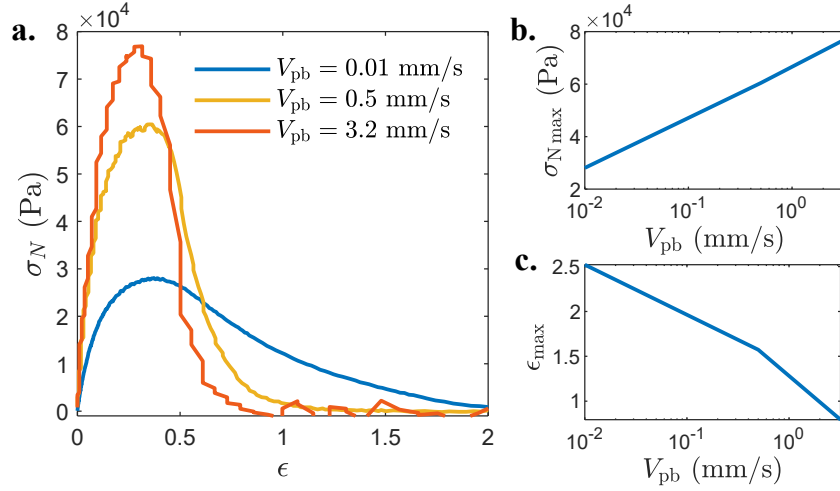


Fig. 6.27 – Effect of the pull-back velocity on tack measurements **a.** Normalized force-displacement curve for a premixed 60 v% sample with $V_{pb} = 0.01$ (blue), 0.5 (yellow) and 3.2 mm/s (red). **b.** Peak stress $\sigma_{N,max}$ as a function of V_{pb} (logarithmic scale). **c.** Maximum extension as a function of V_{pb} .

Confirmation of the velocity effect by tack measurements

The probe test is carried out at various pull-back velocity ($V_{pb} = 0.01, 0.5$ and 3.2 mm/s) on *premixed* samples at 60 v% for which velocity has been shown to have a wider impact on the spreading test results (Fig 6.12 bottom line). Reducing the pull-back velocity leads to lower and wider peaks: σ_N decreases while ϵ_{max} increases (Fig. 6.27). In all cases, detachment occurs at the interface level but some residuals are visible on the probe and their amount increases when the velocity is reduced. Concretely, the sample deforms more for lower pull-back velocities. This can be understood as the solicitation frequency f_{pb} reduces when V_{pb} diminishes: Lakrou *et al.* proposed to approximate f_{pb} by V_{pb}/h_0 [166]. With $h_0 \simeq 1$ mm, $f_{pb} = 0.01, 0.5$ and 10 Hz respectively. Reducing the velocity therefore implies to reducing G' and thus reducing the cohesion of the sample. Reducing the pull-back velocity can also have an impact on the adhesion as the surfaces are kept longer in contact and relaxation and rearrangements are favoured. Although we did not observe cohesive failure at low velocity, this measurement suggests that as velocity increases, the material is less able to deform and should form rolling aggregates more readily. This is confirmed by the millimeter sized aggregate spreading test. Sheared between the two plates the premixed samples are spread for $V = 1$ mm/s and a hybrid situation is observed at $V = 10$ mm/s (rolling frequency $f \approx 0.7$ Hz): part of the sample remains stuck on the upper plate while the rest starts to roll. One would have expected to observe rolling aggregates at both $V = 1$ and 10 mm/s since the tack test gave quite good adhesion failure (very few residuals left on the probe). This reasoning is too direct and it does not take into account the fact that the pull-back or spreading velocity correspond to different solicitation frequencies. A factor 10 is present between the two, the rolling frequency (f) being lower than the pull-back frequency (f_{pb}) for a given velocity. The tack curve that should be used to interpret

the millimeter aggregates spreading at $V = 1$ mm/s, thus would lie in between the yellow and blue curve: it describes a sample that tends to deform (ϵ_{\max} high), which shows a tendency to be spread.

The tack test measures the change in properties due to the change in velocity which is another confirmation of the impact of velocity.

Carbopol role

The study of the Carbopol (c) role revealed that without Carbopol (nc) the formulation did not generate aggregates (see section 6.3.4). The rheology shows that the removal of Carbopol leads to a very strong decrease in the value of G' so: $G'_c \gg G'_{nc}$ (4 orders of magnitude for $c_v = 57$ v% at 1 Hz and $\hat{\gamma} = 20\%$ in Fig. 6.18). The cohesion of the material is strongly reduced without Carbopol, which favors spreading. When performing the tack test on 60 v% in pure glycerol, the sample behaves as a shear-thickening liquid, a capillary bridge forms during the pull-back and finally breaks leaving residuals on the probe. The adhesion is hence stronger than the cohesion of the material which explain why Carbopol-free formulations spread.

Substrate dependency

To further confirm the importance of adhesion, aggregates formation was tested on a wide range of substrates. A range of sticky PDMS was prepared by changing the ratio of polymer to curing agent (50:1, 35:1 and 25:1) with Sylgard 184. These samples were both soft and sticky because there is no thin hard layer unlike our bilayer PDMS. We observed that the sticky PDMSs did not allow aggregates to form while the smooth PMMA led to complete scraping of the deposit. This highlights the importance of material selection (substrate and applicator) for the test. If the substrate is too sticky, the adhesion is greater than the cohesion of the material and the formulation is spread, whereas if the adhesion is really weak (smooth PMMA), it is scraped off. Adhesion also partly explains differences in concentration at which the first aggregates are observed when comparing real skin, industrial skin, and PDMS bilayer.

6.5.4 Comparison of the different tests

The following is a summary of how the different tests carried out - spreading test with the robot, tack test, and spreading of millimeter-sided objects - compare with each other in terms of results. In the Figure 6.28, are recalled the results obtained for these three tests according to the quantity of solid particles, on samples previously mixed or not. We show for unmixed samples, that the appearance of aggregates (in the spreading test), the observation of adhesive failure (tack test), and the rolling of millimeter sized aggregates are observed for nearly the same concentration which is around 56 v%, with more or less uncertainty depending on the tests. Less agreement is observed for premixed (or presheared) samples when comparing the spreading test with the tack test and the spreading of millimeter-sized objects; the latter two underestimate the concentration at which aggregates appear. In general, the values at which aggregates, adhesive failure, and rolling are first observed are in 8% range. Of these three tests, the tack

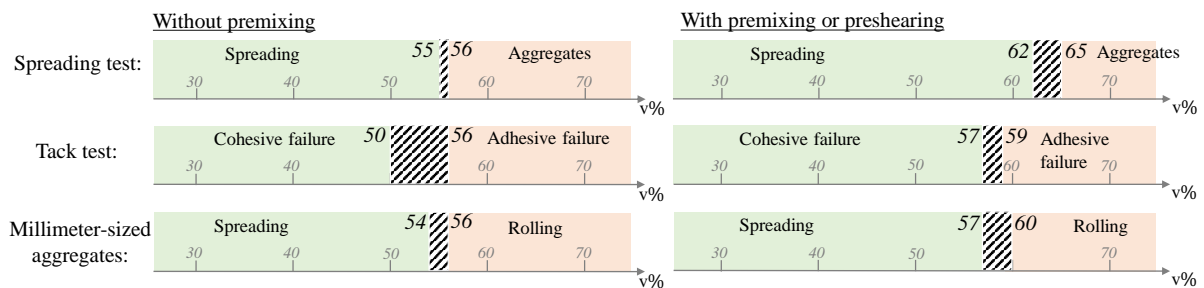


Fig. 6.28 – Comparison of the results observed when performing: the spreading tests with the Cobot (after the 1st run (left) or 4th run (right), $V = 50$ mm/s, $F_N = 0.6$ N), the tack tests ($V_{pb} = 0.5$ mm/s) and the spreading of millimeter-sized aggregates ($V = 10$ mm/s, $F_N = 0.7$ N). Samples were pre-mixed or pre-sheared prior to the experiments in the right column. The hatched areas correspond to the uncertainty range.

test seems to be a promising and easy-to-implement test for predicting whether or not aggregates will appear.

6.5.5 How to favor spreading ?

Here is a summary of the different lever of action that have been shown to be relevant to reduce the incidence of aggregates.

The balance between adhesion and cohesion can be shifted in favor of spreading by:

- *Decreasing the solid particle concentration (for $c_v < \phi_M$).* The adhesion becomes larger than the cohesion as the particle concentration decreases: the storage modulus decreases and the adhesion energy is increased.
- *Increasing the concentration of solid particles (for $c_v > \phi_M$).* There is not enough interparticular fluid to provide capillary bridges over the entire sample. In this case, the overall cohesion becomes weaker and weaker and the spreading starts to be important again (e.g. 90 v%).
- *Removing the Carbopol from the formulation.* The cohesion is greatly reduced: the storage modulus is strongly decreased, resulting in a viscous fluid.
- *Pre-shearing of the dried deposit.* It leads to an increase in adhesion energy relative to cohesion energy, especially through a decrease in the modulus of elasticity.
- *Modifying the substrate* to increase its adhesion to the material.
- *Increasing the normal force applied during the spreading* to increase its adhesion by maximizing the contact surface.
- *Reducing the spreading velocity.* As seen previously, a decrease in velocity can be associated with a decrease in the frequency of material sollicitation, which is accompanied by a decrease in storage modulus. This leads to a decrease in the cohesion of the material, which can become lower than the adhesion. The latter might be enhanced by longer contact time.

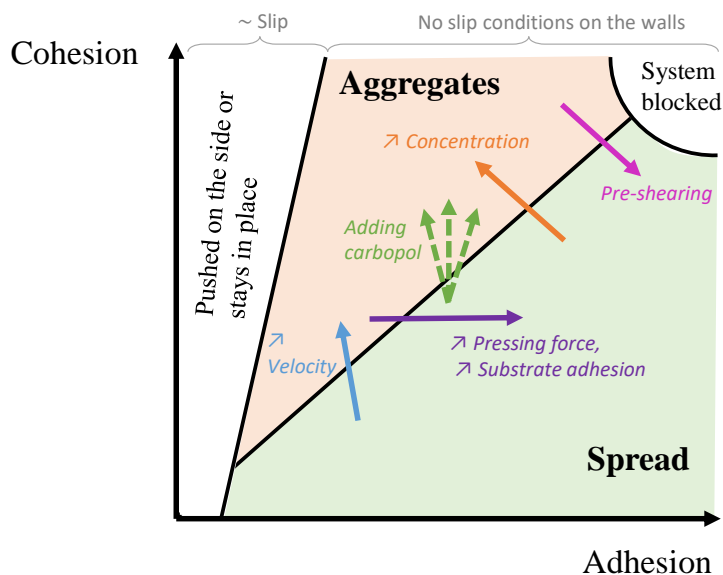


Fig. 6.29 – Illustration summarizing the model and representing the different behaviors observed as a function of the balance between adhesion and cohesion. The adhesion is assumed to be equivalent with the upper and lower surfaces. If the adhesion is too low, the deposit remains at rest or is mechanically pushed aside by the applicator. In the case where there is no slip on the walls: if the cohesion is higher than the adhesion, the deposit forms aggregates, otherwise it is spread (with potential fracturing of the material). When both adhesion and cohesion are very important, the whole system can be blocked. The color arrows represent qualitatively the influence of the different factors on the adhesion/cohesion ratio and consequently on the emergence or disappearance of aggregates.

6.6 Link with ϕ_M

In this last part we look for a simple formulation criterion to avoid aggregate formation, that can be easily assessed and followed by formulators. In the previous sections, it was shown that aggregates are particularly present from 65 v%. This volume fraction is close to the jamming fraction measured at $\phi_M = 64 \pm 1\%$ in pure glycerol. Kusina studied aggregates formation with corn starch and concluded that having a volume fraction of particles above ϕ_M systematically leads to systems that form aggregates [3]. Above this volume fraction, there is not enough liquid to maintain a continuous phase. In bulk, this situation is equivalent to granulation (Fig. 6.30). He proposed to consider ϕ_M as a criterion to avoid aggregation. Here, we verified this criterion by testing other particles and other formulation systems (oil-based) and showed that it is not a "strict" limit. Some aggregates can appear below this threshold as long as the cohesion is greater than the adhesion as stated in the previous section.

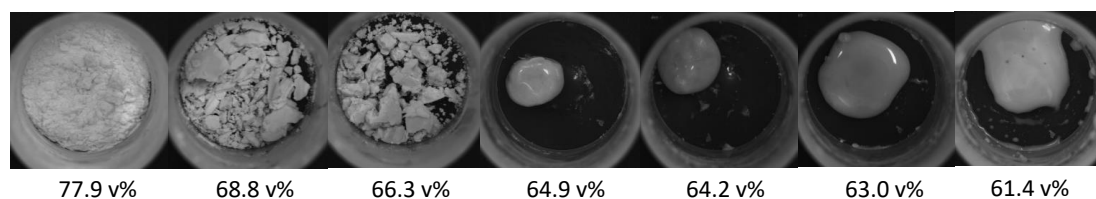


Fig. 6.30 – NP in pure glycerol at various volume fraction. Glycerol is progressively added from left to right. ϕ_M correspond to the volume fraction where a unique ball is formed, here around 64.9 v%.

6.6.1 Formulation tested

In this section, the different types of particles and formulation bases used to validate the role of ϕ_M are presented.

The particles studied are:

- Porous silica (H51, Sunsphere). The volume porosity is 0.74 mL/g, giving a density of 0.82 (true density of 2.15). The pore diameter is 5.5 ± 1 nm. It was measured by the nitrogen adsorption method allowing the measurement of interconnected and semi-interconnected pores.
- Cellulose beads (Cellulobeads USF, Daito Kasei). These particles are porous: the volume porosity is 0.58 mL/g and the pores diameter is around 9.4 nm. The true density is 1.56 and it becomes 0.82 when the porosity is taken into account. In addition, the cellulose beads show roughness (in air) and strong swelling in lots of different solvents. Using an optical microscope, we observed that the particles swell by a factor of 1.3 in pure glycerol, of 2.3 in water. In a water/glycerol mixture at 10wt% in glycerol, the particles swell and remain swollen (factor 2 in volume) even after evaporation of the water.
- Corn starch (Beauté by Roquette® ST 005, Roquette). These particles are angular and are well known to present strong shear-thickening behavior. The density is 1.54. They present a slight swelling both in water and in glycerol: the volume increases by a factor 1.26.

They are all rather spherical and of comparable size (about $5 \mu\text{m}$). Swelling and porosity are important to evaluate: they must be taken into account to properly assess the volume fraction of the particles.



Fig. 6.31 – SEM images from L'Oréal of **a.** Porous silica (H51) **b.** Cellulose beads (USF) **c.** Corn starch (ST 005).

In addition to the water-based formulation system used so far (water/Carbopol/glycerol), an oil-based formulation system is also studied. It consists in a mixture of isododecane (volatile phase) and 100 cSt silicone oil (non-volatile phase) at 10 wt%. Isododecane (2,2,4,6,6-Pentamethylheptane from Ineos Oligomers) was chosen because it is commonly used in cosmetics and evaporates quickly (0.803 mg/cm²/minute at 25° and 50% relative humidity [231]). Silicone oil (Sigma Aldrich) is also a cosmetic material, the one used is 7 times less viscous than glycerol in the water-based system.

6.6.2 Evaluation of ϕ_M and calculation of volume fractions

Measurement protocol

The principle of the measurement is to scan the phase diagram to find the volume fraction at which the system changes from a granular state to a concentrated liquid (Fig. 6.30). The liquid is added progressively (almost drop by drop) to a known quantity of powder (~ 1 g) while homogenizing with the spatula between each addition, until a single ball is formed that does not flow at rest and is not soft. ϕ_M corresponds to the fraction in particle at which this ball is formed. To increase the measurement accuracy, the phase diagram can be run back and forth several times (addition of liquid until $\phi < \phi_M$, then powder until $\phi > \phi_M$).

Equations used to calculate volume fractions

The general equation of the volume fraction (5.1) is recalled here:

$$\phi(\text{v}\%) = \frac{v_p}{v_p + v_{il}} = \frac{m_p/d_p}{m_p/d_p + m_l/d_l}$$

with m_p , m_l the weights and d_p , d_l the densities of the particles (true density) and the interstitial liquid respectively. Note here that v_{il} represents the volume of interstitial liquid, and that in the following v_l is used to denote the total volume of liquid. These two volumes correspond the non-volatile phase.

Case of porous particles: we define d_{pp} the density corrected by the pore volume v_{pores} (in cm³/g of powder), $d_{pp} = \frac{1}{v_{pores} + 1/d_p}$. There are two extreme cases:

- Either the liquid does not enter the pores:

$$\phi(\text{v}\%) = \frac{v_p}{v_p + v_{il}} = \frac{m_p/d_{pp}}{m_p/d_{pp} + m_l/d_l}$$

- Or it enters the pores (volume v_{lp}), then $v_{il} = v_l - v_{lp}$:

$$\phi(\text{v}\%) = \frac{v_p}{v_p + v_l - v_{lp}} = \frac{m_p/d_{pp}}{m_p/d_{pp} + m_l/d_l - v_{pores} \cdot m_p}$$

Case of swollen particles: the effective volume of the particle increases (increase factor g) while the volume of the interstitial liquid is reduced by v_{lg} (volume of the fluid involved in the swelling).

$$\phi(v\%) = \frac{v_p \cdot g}{v_p \cdot g + v_l - v_{lg}} = \frac{m_p/d_p \cdot g}{m_p/d_p \cdot g + m_l/d_l - (g-1)m_p/d_p} = \frac{m_p/d_p \cdot g}{m_l/d_l + m_p/d_p}$$

Case of porous particles that swell: the two effects must be combined.

$$\phi(v\%) = \frac{m_p/d_{pp} \cdot g}{m_p/d_{pp} \cdot g + m_l/d_l - v_{pores} \cdot m_p - (g-1)m_p/d_{pp}} = \frac{m_p/d_{pp} \cdot g}{m_l/d_l - v_{pores} \cdot m_p + m_p/d_{pp}}$$

It is quite difficult to calculate the actual value of the volume fractions because particle swelling can be difficult to measure and many uncertainties remain about the pore volume actually accessible to the fluid.

Choice of the fluid

For the oil-based systems ϕ_M is measured in the non-volatile phase, i.e. pure silicone oil.

For the water based systems the choice of the fluid is debatable. The options considered for a direct measurement were pure water, pure glycerol, mixture of glycerol in water (at 10 w%) and dried formulation (Carbopol in glycerol). None of these allow direct comparison with the spreading experiment as they correspond, at the best, to the environmental media of the solid particles at a specific moment of the experiment (e.g. before or after drying). For non-porous and non-swelling particles such as NP, the ϕ_M values obtained in water, glycerol, and dried formulation, are 76.3, 73.2, and 72 w% respectively. The volume fractions corresponding are quite close, 60, 64, and 60 v%. In this case the choice of the liquid has little impact on the value of ϕ_M . The best compromise seems to be the glycerol: the dried formulation has to be prepared in advance (with 2 days of drying) and the yield stress resulting from the carbopol presence makes the ϕ_M measurement difficult. Additionally, measuring ϕ_M in glycerol is preferred to pure water, as it is closer to the final conditions in which the aggregates are formed.

However, in the case of porous or swelling particles, the history experienced by the particles is important. Fluid penetration into the pores and/or its participation in swelling may be initially favoured by the presence of water, while it may be prevented in case of highly viscous fluid, high yield stress or unfavourable interactions between the particles and the remaining solvent. Consequently, neither the measurement in pure water, nor in pure glycerol, or in the dried formulation is fully satisfactory. The best practice would be to prepare samples with increasing particles concentration in the water, glycerol and carbopol mixture, let them dry and test whether the dry samples flow or granulate. This technique was not chosen because it is time consuming and would not be easily transferable to industry. Instead, the choice was made to perform the measurements in glycerol for the porous particles, as glycerol is expected to enter the porosity as easily as water (molecular diameter 0.5 nm). For the swelling particles, the presence of water is primordial to promote the swelling (section 6.6.1) so the measurements were made in pure water.

Table 6.1 Summary the fluid chosen to measure ϕ_M

Particles	Type	Water-based systems	Oil-based systems
Non porous silica (NP30)	hard sphere	glycerol	silicone oil
Porous silica (H51)	porous	glycerol	silicone oil
Cellulose (USF)	porous and swelling	water	silicone oil
Starch	swelling	water	silicone oil

Note that we expect a few percent of error from these choices since they are not fully representative of the reality undergone by the formulation during a spreading experiment. However as it will be shown later this approach is still useful to give guidance to formulators.

6.6.3 Results on the industrial skin model

The industrial spreading tests, described in section 6.1.2, were performed for at least three different concentrations for each [particles, formulation base] combination. We assumed that the interstitial liquid penetrates the pores of the H51 silica, and the cellulose beads. For the water-based systems, the non-volatile liquid is considered to also participate in the swelling of the cellulose bead particles (swollen by a factor of 2 in volume) and starch (by a factor 1.26). Grades are given according to industrial criteria, meaning both white powdery deposit and aggregates will be graded 5. The results are displayed in Figure 6.32.

We observe that all samples formulated above ϕ_M generate defects and are graded 5, as expected. This observation is valid for both water-based and oil-based systems. Below ϕ_M , most samples are well spread. However, we can observe that some samples, close to, but below ϕ_M , can show aggregates. This effect is particularly important with starch where defects are observed from $c_v = 30$ v%, while ϕ_M is evaluated at 62 v%. For non-porous silica, defects are also observed from $c_v = 50$ v% which is comparable with the results obtained with the new set-up presented in section 6.3 (defects were observed from $c_v = 55$ v%). It is interesting to note that the same observation can be made for oil-based systems. Consequently, ϕ_M is a *one sided limit*: it should not be exceeded to avoid defects such as aggregates (or others), but formulations below this fraction are not necessarily defect-free as some aggregates can be formed at an intermediate fraction.

An important point highlighted in Figure 6.32 is that *for particles that swell or have porosities, the jamming fraction is reached at very low mass fractions*. This is the case for cellulose beads for which we estimate ϕ_M around 66 v% which corresponds to a mass fraction of particles of only 22 w%. This shows that it is very important for formulators to adapt their mixtures according to the ϕ_M of each particle. Determining whether a particle is porous or swollen is interesting to understand the physics behind the values measured, but from a practical point of view, one can mostly focus on the mass fractions. For instance, with the porous silica, the limit is 35 w%, and to determine this, one only needs to know the mass of the particles and the liquid. The density and porous volume values are not involved, which reduces measurement and approximation errors and it is not necessary to make assumptions about the

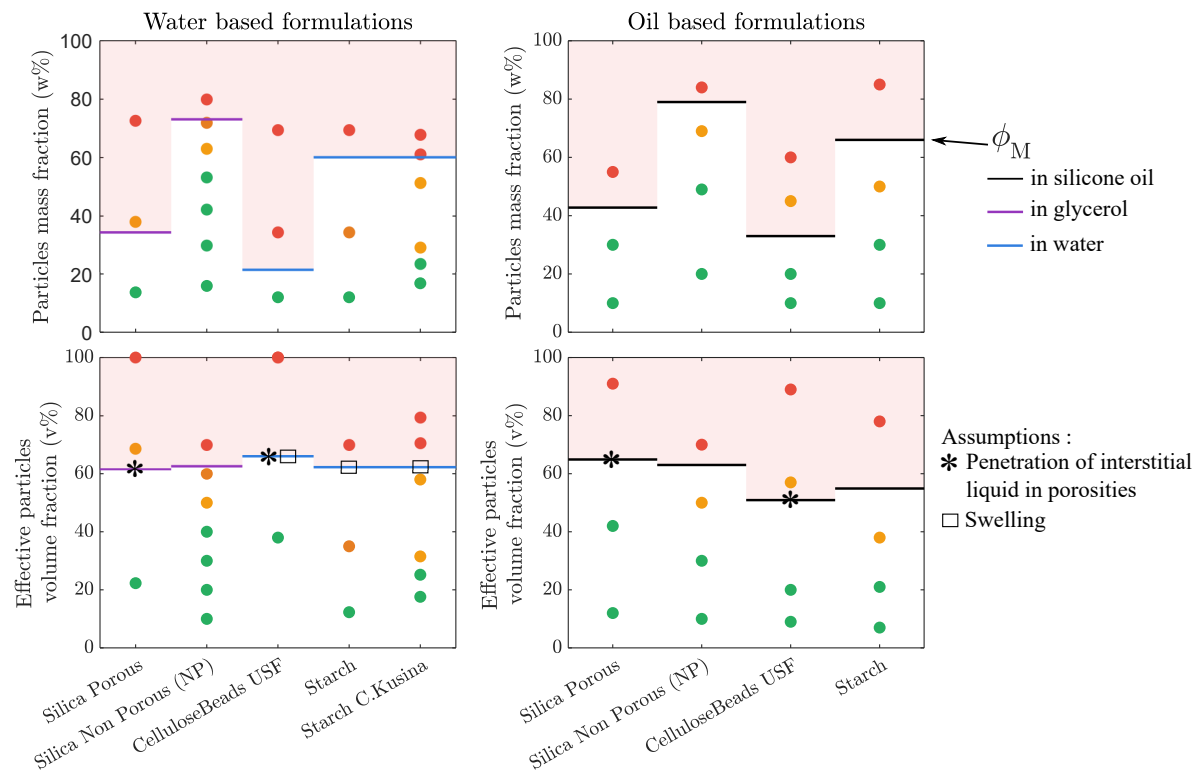


Fig. 6.32 – Evaluation of the defects obtained during the spreading of water-based (left), or oil-based (right) formulation on the industrial skin model. On each graph are represented the ϕ_M values (continuous line) delimiting the areas where defects are expected (red zone). The ϕ_M values correspond to measurements in silicone oil (black), glycerol (purple) or water (blue). The tested samples are represented by dots. The colors correspond to their grade (green=1 or 2, orange=3 or 4, red=5). The particle concentration in the non-volatile phase is expressed either by mass fraction (top) or by effective volume fraction (bottom). The hypotheses used for the calculation of the effective volume fraction are signaled by markers. For cellulose beads and starch, the liquid participates in the swelling (square) in water-based systems. For porous silica and cellulose beads, the liquid (water, glycerol, or silicone oil, depending on the situation considered) is assumed to enter the porosities (star).

presence of liquids inside the pores. The cosmetic formulations should have mass fraction of solid particles in the non-volatile phase below this value. For greater confidence, the measurements should be performed in the non-volatile phase and the main liquid phase (e.g. water) if the particle is suspected to swell and if there is a difference, further investigation is required.

The assumptions made about the role of the fluid in swelling and pore filling are supported by the fact that the values of ϕ_M obtained are all around 64 v%, which is the theoretical value expected for spherical monodispersed hard spheres. In oil-based system the range of values is wider than for water based systems. For instance ϕ_M for cellulose beads in silicone oil is estimated around 51 v%. This could be related to the surface roughness (Fig. 6.31). In water-based formulation the swelling is thought to smooth the surface which is consistent with a value closer to 64 v%.

The defects observed with silicone oil are mostly white powdery deposits, or flake-like clusters of particles with very low cohesion. The situation can be compared to the particle formulated in pure glycerol: the viscosity of the silicone oil is lower, and the potential capillary bridges are weaker (lower surface tension: $63.4 \text{ mN}\cdot\text{m}^{-1}$ for glycerol [232] and typically three times less for silicone oil [84]). Therefore, the dried deposits are not cohesive enough to generate rolling aggregates.

6.6.4 Origin of defects formation when $\phi < \phi_M$

When $\phi < \phi_M$, the formation of cylindrical aggregates is no longer a granulation problem but can be explained by a cohesion larger than adhesion (see section 6.5). Thus this is expected to have aggregates below ϕ_M in most of the systems studied.

Another rheological factor that has not been explored in depth here, but which could explain the peculiarity of starch, is the strong shear-thickening behavior. Doing the same study with starch directly formulated in pure glycerol (no drying phase), we obtained aggregates that have the peculiarity of flowing at rest for $c_v \geq 35 \text{ v\%}$. The rheology of these formulations shows a continuous shear-thickening above this concentration. It is conceivable that in the presence of Carbopol, which ensures the solid behavior at rest, the aggregates are maintained in their shape. A parallel can be drawn with Cates's study about the granulation from suspensions undergoing brittle fracture, with capillary forces stabilizing the granule shape and maintaining a jammed state [127, 128].

Other experimental factors that could play on the emergence of these aggregates below ϕ_M are the potential deterioration of the substrate that plays a role of nucleator of aggregates, and the difficulty to ensure a perfect cleaning of the substrate (in particular at the level of holes and folds).

If we now return to the problem of the application of cosmetics on the skin, the presence of hairs, dead skin, as well as the possible penetration of glycerol in the skin are likely to be amplifying factors for the appearance of aggregates below ϕ_M .

6.6.5 Reducing aggregates formation by increasing ϕ_M

We presented ϕ_M as a limit that should not be crossed by the formulators in order to largely avoid the formation of aggregates.

To avoid this problem one can also change the approach and try to increase ϕ_M (the value in volume and mass) to widen the concentration range available to the formulator. Several methods are possible, some of which were described in the previous chapter:

- Improving the dispersion of particles to avoid aggregated systems that do not optimize particle stacking [233]. This can be achieved by using a dispersant to reduce attractive colloidal interactions [234].
- Using polydisperse systems. The interparticle space can be optimized in this way. Smaller particles will be able to fit into the spaces left by the larger particles [122, 123].

- Reducing the friction coefficient. This can be done by reducing the roughness of the particles, which can more easily slide but also roll on one against another [21]. Another technique is to use polymer coating. The polymer brush fixed on the particles can facilitate their sliding. In the work carried out by Poon and collaborators, the lecithin was used to reduce the coefficient of friction of chocolate [120], and the polyacrylic acid added to calcite resulted in ϕ_M increase of about 10% [24]. These works seem promising but it is difficult to disentangle the effect of the polymer as a dispersant or a friction modifier.

It is difficult to demonstrate experimentally that increasing ϕ_M by any of these methods increases the range of concentrations at which no aggregation occurs with our systems. This is due to two factors. First, the expected variations in ϕ_M are overall quite small in the case of conventional particles. For instance, modifying the coefficient of friction of 34% (by urea sorption) only resulted in an increase in ϕ_M by 1% [234]. Otherwise, when the variations are significant, this is often not really accessible in the usual situations. For example Hsu et al [21] who reports increases in ϕ_M of 15 points, which is very large, have model systems that have extreme characteristics (smoothness and roughness), which does not give a good idea of the variations expected for more conventional systems. Identically with polydispersity, the largest variation in ϕ_M corresponds to extremely well-defined quaternary systems with a diameter ratio that reaches more than 300 between the smallest and largest spheres [122]. This difference in diameter is not feasible in cosmetic products where nanoscale particles raise toxicity issues and only a small diameter range generally gives the desired properties. Secondly, it was previously shown that ϕ_M is not an absolute limit: aggregates are visible below this value and even with the robotic spreading setup on PDMS bilayer there is a range of concentration for which it is difficult to determine if aggregates are formed or not ($c_v = 55 - 62$ v% with NP). This uncertainty is greater than the expected variations of ϕ_M in the case of mixing of bidisperse systems for example, so we could not validate these proposals.

For an equivalent volume fraction of particles, it is also possible to increase the maximum mass fraction (the value of ϕ_M in w%) and consequently the number of particles:

- By using non-swelling particles. Thus it is possible to put a larger number of particles in the same volume.
- By using non-porous particles, or particles with closed pores. This avoids that a part of the liquid does not participate in the interstitial liquid phase. One solution would be to use highly cross-linked polymer particles.

The interest of these methods depends on the effect sought by the presence of these particles. In cosmetics, it is often preferable to have a large number of small particles to ensure good covering.

Conclusion – Chapter 6

In this chapter, we studied the formation of rolling cylindrical aggregates that appear at the end of the spreading of a cosmetic deposit (after evaporation of the volatile phase):

1. We proposed a new set-up to study the formation of aggregates with back and forth movements performed by a robot on a skin model made of a PDMS bilayer.
2. We investigated the factors having an impact on the formation of aggregates. We observed that they form from discontinuities in the deposit. We also pointed out that the formation of aggregates is related to the particle volume fraction in the non-volatile phase and the presence of Carbopol. The application parameters such as the velocity and, to a lesser extent, the applied strength, affect the development of aggregates.
3. Rheological measurements of the dried formulations revealed the presence of a strong yield stress associated with high storage modulus, the latter increasing with the frequency. However we highlighted the limit of classic rheology to study the formulations in the right range of solicitation due to partial ejection, fracture and slip of the sample.
4. We proposed a model to explain their formation as a competition between the cohesion of the material and its adhesion on the substrate and applicator surfaces. Under the condition of no slip at the walls, if cohesion is greater than adhesion then the material tends to detach and start to roll rather than deform and spread.
5. We validated this model and particularly understood the role of particle concentration, Carbopol and velocity in light of this model. In addition to the spreading test results and rheological measurements, probe tack tests were used to assess the cohesion/adhesion balance, and larger scale systems enabled to study the rolling or spreading of macro-sized aggregates. As a perspective, we think it would be interesting to further investigate the link between tack test results and aggregates formation.
6. Focusing on the formulation lever, we have shown, in agreement with the work of C. Kusina [3], that the volume fraction of particles should not be higher than ϕ_M in the non-volatile phase to partly avoid the presence of aggregates but also other defects such as white powdery deposits. For formulations at higher volume fraction the non-volatile phase amount is too low to ensure a continuous media.
7. This limit is a one-sided limit, which means that some aggregates can also be observed below it, especially if cohesion is stronger than the adhesion, and shear-thickening might also play a role.
8. For swelling and porous particles, ϕ_M corresponds to low mass fractions of solid particles in the non-volatile phase. Evaluation of ϕ_M should help formulators to avoid preparing samples that are doomed to generate aggregates.

6.8 Perspectives

This exploratory study presented in the manuscript about aggregates formation in the presence of solid particles is a first step in the understanding of this phenomenon. Further work needs to be accomplished to refine and validate quantitatively the model proposed to describe and match closer the application case.

For instance, our substrate (the PDMS bilayer) is smooth and does not present folds and holes like those encountered on skin. This geometrical difference implies that the experimental conditions for the formation of aggregates, in particular the normal force applied, are not the same. An important force (about 5 N) is applied to form the aggregates on the skin while in our experimental device it is 10 times weaker. This difference in geometry implies more complex phenomena in the case of the skin as the material has to be extracted from the bottom of the folds and limits the parallels that can be made when comparing the results. Studying the formation of aggregates on wrinkled substrates, used to better represent the skin, would be interesting to compare the effect of topography.

The most promising way to predict the formation of aggregates and to move towards a quantitative approach in order to validate the model, is from our perspective the tack test. In particular, it would be relevant to perform this test by covering the probe and the substrate with surfaces that are more representative of the skin. A first step would be to use PDMS and latex surfaces to make a better parallel with the robot spreading test.

Quantifying the adhesion part of the model is challenging. Nase and Deplace have shown that, by using rheological and tack test at small pull-back velocity, it was possible to evaluate the adhesion term with the dissipation factor [170, 173]. We did not have enough time to try to extend their approach to our materials but it seems to be an interesting way to go towards a better quantification of aggregates formation.

Conclusion and perspectives

In this thesis, we studied the spreading of complex fluids in order to better understand the phenomena involved in the application of cosmetics and pharmaceuticals. By modeling the first movement of a cream application using a soft blade coating of a finite amount of liquid, we came to the conclusion that the deposited thickness was not constant and decreased as the reservoir emptied. We proposed, by balancing the elastic and viscous forces, a scaling law that gives the deposited thickness for a shear-thinning or a Newtonian fluid as a function of the blade wetting length l_w , a parameter allowing to follow the filling level of the fluid reservoir. This scaling law successfully explains how the finite reservoir of fluid affects the thickness of the deposit. It was confirmed with a numerical model whose scope was extended (compared to the previous literature) in particular by taking into account large deformations and the presence of a meniscus at the back of the reservoir. The deposited thickness increases with spreading velocity and fluid viscosity and decreases as blade rigidity increases. Capillary effects are second order and, when the wettability of the fluid on the surfaces decreases, the deposited thickness increases slightly. Our work leads us to believe that the analogy with dip coating, where elastic forces are considered to replace capillary forces, does not hold in the case of a finite reservoir.

In order to compare the spreading of a shear-thinning fluid with that of a Newtonian fluid, we have defined a so called Newtonian "equivalent" fluid (and the corresponding viscosity) such that the same amount of fluid is deposited in the same amount of time. In this context, it is necessary to provide more energy to spread a shear-thinning fluid than a Newtonian fluid. We also observed that the deposited film is more homogeneous if a Newtonian fluid is spread compared to a shear-thinning one, and this effect can be amplified by reducing the viscosity of the Newtonian fluid.

The presence of normal forces did not experimentally show any effect on the deposition law. Normal force fluids can be satisfactorily described by considering only their viscous properties. This result is linked to the geometry used. In order to predict whether normal forces have an effect in this situation, one should not rely on the Weissenberg number which compares viscous and normal stresses but on a dimensionless number which compares the pressures resulting from these stresses. Thus a geometric factor, which is the ratio of the deposited thickness over the wetting length, is introduced. In our situation, this term is small, which explains the absence of normal stress effects, contrary to what has been reported in the literature for dip coating experiments, where normal forces lead to a swelling of the deposited film.

Yield stress fluids spreading with a flexible blade gave very scattered results. We identified two reasons for this discrepancy in the data. First, due to the yield stress, the blade may be initially out of equilibrium which may lead to a draining of the reservoir from bottom to top, thus at constant wetting length, which is not taken into account in our model. Secondly, a part of the fluid present in the reservoir remains stuck under the blade and can lead to successive redeposition cycles, producing patchy deposit of fluid. These two phenomena prevent us from modelling easily the coating of yield stress fluids with a flexible blade.

By judiciously combining the different types of fluids, we highlighted the impact (or absence of impact) of the different rheological properties studied over the deposited thickness.

This model of spreading in linear motion using a flexible blade on a rigid substrate is somewhat far from real cosmetic applications. At best, it represents the first movement realized during the spreading of a cream which is then followed by complex circular and back and forth movements. However, this study provides leads for cosmetic formulations by showing that the fluid which spread in the most homogeneous way with the least energy is a Newtonian fluid of low viscosity spread slowly.

An interesting avenue to pursue would be to see the effect of substrate elasticity using a soft material as a substrate, such as PDMS. In the case of an infinite reservoir, Corvalan predicts that the deposited thickness is thinner, all other conditions being equal [7]. The measurements with an optical profilometer will not be straightforward because the reference level corresponding to the skin position before spreading will be modified in the presence of liquid.

In a second part, we have made the formulations, materials and gestures more complex to get closer to a more representative spreading situation. These modifications allowed us to study the formation of particle aggregates which may appear when the cosmetic deposit is sheared after drying. Normally, the presence of a non-volatile phase should ensure a continuous medium capable of spreading. When the particle volume fraction is higher than the maximum packing fraction ϕ_M , aggregates formation is expected and is similar to granulation. Taking into account the swelling and the porosity of the particles is essential to correctly evaluate this limit which should not be exceeded by the formulators. However, aggregates can also be observed below this threshold. Aggregates are considered to form when the cohesion of the dried formulation prevails over the adhesion on the walls of the applicator and substrate, otherwise the dry deposit is spread. We managed to show that one can switch between these situations by changing: the volume fraction of the particles, the presence of polymers, the spreading speed, the applied force and the adhesive properties of the walls. While rheology was very limited to evaluate the properties of dried formulations with high particle content, the tack test allowed to evaluate the adhesion/cohesion balance according to the observed failure mode. Thanks to this study and the proposed model we are able to better understand the formation of aggregates and therefore better prevent their occurrence.

From our point of view, the tack test represents a way to pursue the study of the formation of these aggregates and in particular to allow a quantitative validation of the model that we propose. It would be interesting to use the same surface as in the spreading test to improve the similarity of conditions

between these tests. It also seems relevant as an industrial test because it is easy to set up and could allow a quick evaluation of the risk of aggregates formation that is not user dependent.

An important part of the cosmetic formulations being emulsions, it would be interesting to study the role that the second phase can have in aggregates formation in light of this model.

References

- [1] M. Krapez, A. Gauthier, H. Kellay, J-B. Boitte, O. Aubrun, J-F. Joanny, and A. Colin. Impact of the wetting length on flexible blade spreading. *Physical Review Letters*, 125(25):254506, 2020.
- [2] M. Krapez, A. Gauthier, J-B. Boitte, O. Aubrun, J-F. Joanny, and A. Colin. Spreading of complex fluids with a soft blade. *Physical Review Fluids*, 7(8):084002, 2022.
- [3] C. Kusina. *Behaviour, properties and structure of complex fluids upon spreading*. PhD thesis, Université Paris Sciences et Lettres, 2019.
- [4] J. Seiwert, D. Quéré, and C. Clanet. Flexible scraping of viscous fluids. *J. Fluid Mech.*, 715:424–435, 2013.
- [5] K. Warburton, D.R. Hewitt, and J.A. Neufeld. The elastic landau–levich problem on a slope. *J. Fluid Mech.*, 883, 2020.
- [6] H.N. Dixit and G.M. Homsy. The elastic landau–levich problem. *J. Fluid Mech.*, 732:5–28, 2013.
- [7] C.M. Corvalán and F.A. Saita. Blade coating on a compressible substrate. *Chem. Eng. Sci.*, 50(11):1769–1783, 1995.
- [8] P. Agache, T. Lihoreau, S. Mac-Mary, F. Fanian, and P. Humbert. *Agache’s Measuring the Skin: Non-invasive Investigations, Physiology, Normal Constants*. Springer International Publishing, 2017.
- [9] R. Kleiman, S. Koritala, and J.C. Hill. Method for improving spreading properties of cosmetic ingredients, 2007. Patent number: US7304177B2.
- [10] T. Morávková and P. Stern. Rheological and Textural Properties of Cosmetic Emulsions. *Applied Rheology*, 21(3):6, 2011.
- [11] E. Gore, C. Picard, and G. Savary. Spreading behavior of cosmetic emulsions: Impact of the oil phase. *Biotribology*, 16:17–24, 2018.
- [12] L. Gilbert, G. Savary, M. Grisel, and C. Picard. Predicting sensory texture properties of cosmetic emulsions by physical measurements. *Chemometrics and Intelligent Laboratory Systems*, 124:21–31, 2013.
- [13] M.D Contreras and R. Sanchez. Application of a factorial design to the study of the flow behavior, spreadability and transparency of a Carbopol ETD 2020 gel. Part II. *International Journal of Pharmaceutics*, 234(1):149–157, 2002.
- [14] N. Koumakis and G. Petekidis. Two step yielding in attractive colloids: transition from gels to attractive glasses. *Soft Matter*, 7(6):2456–2470, 2011.

- [15] A.V.N. Le, A. Izzet, G. Ovarlez, and A. Colin. Solvents govern rheology and jamming of polymeric bead suspensions. *hal-03601873*, 2022.
- [16] H.A. Barnes, J.F. Hutton, and K. Walters. *An Introduction to Rheology*. Elsevier Inc, 1989.
- [17] M. Kroupa, M. Soos and J. Kosek. Slip on a particle surface as the possible origin of shear thinning in non-Brownian suspensions. *Physical Chemistry Chemical Physics*, 19(8):5979–5984, 2017.
- [18] J.B. Hipp, J.J. Richards, and N.J. Wagner. Direct measurements of the microstructural origin of shear-thinning in carbon black suspensions. *Journal of Rheology*, 65(2):145–157, 2021.
- [19] M. Wyart and M.E. Cates. Discontinuous Shear Thickening without Inertia in Dense Non-Brownian Suspensions. *Physical Review Letters*, 112(9):098302, 2014.
- [20] J.F. Morris. Shear Thickening of Concentrated Suspensions: Recent Developments and Relation to Other Phenomena. *Annual Review of Fluid Mechanics*, 52(1):121–144, 2020.
- [21] C-P. Hsu, SN. Ramakrishna, M. Zanini, ND. Spencer, and L. Isa. Roughness-dependent tribology effects on discontinuous shear thickening. *Proceedings of the National Academy of Sciences*, 115(20):5117–5122, 2018.
- [22] V.W.H. Herschel and R. Bulkley. Ronsistenzmessungen von Gummi-Benzolloesungen. *Kolloid-Zeitschrift*, 39:291–300, 1926.
- [23] R. Wessel and R.C. Ball. Fractal aggregates and gels in shear flow. *Physical Review A*, 46(6):R3008–R3011, 1992.
- [24] J.A. Richards, R.E. O’Neill, and W.C.K. Poon. Turning a yield-stress calcite suspension into a shear-thickening one by tuning inter-particle friction. *Rheologica Acta*, 60(2-3):97–106, 2021.
- [25] Z. Jaworski, T. Spychaj, A. Story, and G. Story. Carbomer microgels as model yield-stress fluids. *Reviews in Chemical Engineering*, 2021.
- [26] F.K. Oppong and J.R. de Bruyn. Microrheology and jamming in a yield-stress fluid. *Rheologica Acta*, 50(4):317–326, 2011.
- [27] S. Migliozzi, G. Meridiano, P. Angeli, and L. Mazzei. Investigation of the swollen state of Carbopol molecules in non-aqueous solvents through rheological characterization. *Soft Matter*, 16(42):9799–9815, 2020.
- [28] L. Becu, S. Manneville, and A. Colin. Yielding and flow in adhesive and non-adhesive concentrated emulsions. *Physical Review Letters*, 96(13):138302, 2006.
- [29] E.K. Hobbie and K.B. Migler. Vorticity Elongation in Polymeric Emulsions. *Physical Review Letters*, 82(26):5393–5396, 1999.
- [30] A.A. Montesi, A. and Pena and M. Pasquali. Vorticity Alignment and Negative Normal Stresses in Sheared Attractive Emulsions. *Physical Review Letters*, 92(5):058303, 2004.
- [31] C.O. Osuji and D.A. Weitz. Highly anisotropic vorticity aligned structures in a shear thickening attractive colloidal system. *Soft Matter*, 4(7):1388–1392, 2008.
- [32] O. Maklad and R.J. Poole. A review of the second normal-stress difference; its importance in various flows, measurement techniques, results for various complex fluids and theoretical predictions. *Journal of Non-Newtonian Fluid Mechanics*, 292:104522, 2021.

- [33] B.K. Aral and D.M. Kalyon. Viscoelastic material functions of noncolloidal suspensions with spherical particles. *Journal of Rheology*, 41(3):599–620, 1997.
- [34] J.G. Oldroyd and A.H. Wilson. On the formulation of rheological equations of state. *Proceedings of the Royal Society of London.*, 200(1063):523–541, 1950.
- [35] R.S. Lenk. The Hagen-Poiseuille Equation and the Rabinowitsch Correction. The Pressure Drop in Tapered Channels. In *Polymer Rheology*, pages 75–85. Springer, Dordrecht, 1978.
- [36] H.A. Barnes. A review of the slip (wall depletion) of polymer solutions, emulsions and particle suspensions in viscometers: its cause, character, and cure. *Journal of Non-Newtonian Fluid Mechanics*, 56(3):221–251, 1995.
- [37] S.P. Meeker, R.T. Bonnecaze, and M. Cloitre. Slip and flow in pastes of soft particles: Direct observation and rheology. *Journal of Rheology*, 48(6):1295–1320, 2004.
- [38] J. Persello, A. Magnin, J. Chang, J.M. Piau, and B. Cabane. Flow of colloidal aqueous silica dispersions. *Journal of Rheology*, 38(6):1845–1870, 1994.
- [39] R.I. Tanner and M. Keentok. Shear Fracture in Cone-Plate Rheometry. *Journal of Rheology*, 27(1):47–57, 1983.
- [40] R.I. Tanner and S. Dai. Edge fracture in non-colloidal suspensions. *Journal of Non-Newtonian Fluid Mechanics*, 272:104171, 2019.
- [41] E.J. Hemingway, H. Kusumaatmaja, and S.M. Fielding. Edge Fracture in Complex Fluids. *Physical Review Letters*, 119(2):028006, 2017.
- [42] A. Fall, H. de Cagny, D. Bonn, G. Ovarlez, E. Wandersman, J.A. Dijksman, and M. van Hecke. Rheology of sedimenting particle pastes. *Journal of Rheology*, 57(4):1237–1246, 2013.
- [43] G. Ovarlez, F. Bertrand, and S. Rodts. Local determination of the constitutive law of a dense suspension of noncolloidal particles through magnetic resonance imaging. *Journal of Rheology*, 50(3):259–292, 2006.
- [44] G. Ovarlez, F. Mahaut, S. Deboeuf, N. Lenoir, S. Hormozi, and X. Chateau. Flows of suspensions of particles in yield stress fluids. *Journal of Rheology*, 59(6):1449–1486, 2015.
- [45] W.M. Kulicke, G. Kiss, and R.S. Porter. Inertial normal-force corrections in rotational rheometry. *Rheologica Acta*, 16(5):568–572, 1977.
- [46] P.G. de Gennes. Wetting: statics and dynamics. *Reviews of Modern Physics*, 57(3):827–863, 1985.
- [47] W.D. Harkins and A. Feldman. Films. the spreading of liquids and the spreading coefficient. *Journal of the American Chemical Society*, 44(12):2665–2685, 1922.
- [48] H. Dobbs and D. Bonn. Predicting Wetting Behavior from Initial Spreading Coefficients. *Langmuir*, 17(15):4674–4676, 2001.
- [49] D. Bonn, J. Eggers, J. Indekeu, J. Meunier, and E. Rolley. Wetting and spreading. *Reviews of Modern Physics*, 81(2):739–805, 2009. Publisher: American Physical Society.
- [50] F. Brochard-Wyart, J.M. Di Meglio, D. Quere, and P.G. De Gennes. Spreading of nonvolatile liquids in a continuum picture. *Langmuir*, 7(2):335–338, 1991.

- [51] B. Sobac and D. Brutin. Triple-Line Behavior and Wettability Controlled by Nanocoated Substrates: Influence on Sessile Drop Evaporation. *Langmuir*, 27(24):14999–15007, 2011.
- [52] L. Landau and B. Levich. Dragging of a liquid by a moving plate. *Acta Physicochimica U.R.S.S.*, 17(1-2):42–54, 1942.
- [53] G. Delon, M. Fermigier, J H. Snoeijer, and B. Andreotti. Relaxation of a dewetting contact line Part 2: Experiments. *Journal of Fluid Mechanics*, 604:55–75, 2008.
- [54] J. Eggers. Existence of receding and advancing contact lines. *Physics of Fluids*, 17(8):082106, 2005.
- [55] T.D. Blake and K.J. Ruschak. A maximum speed of wetting. *Nature*, 282:489–491, 1979.
- [56] S.F. Kistler and P.M. Schweizer, editors. *Liquid Film Coating*. Springer Netherlands, 1997.
- [57] F.R. Pranckh and L.E. Scriven. Elastohydrodynamics of blade coating. *AIChE J.*, 36(4):587–597, 1990.
- [58] A.E. Hosoi and L. Mahadevan. Peeling, healing, and bursting in a lubricated elastic sheet. *Phys. Rev. Lett.*, 93(13):137802, 2004.
- [59] P.H. Trinh, S.K. Wilson, and H.A. Stone. An elastic plate on a thin viscous film. *arXiv:1410.8558*, 2014.
- [60] F. Saita. Simplified models of flexible blade coating. *Chem. Eng. Sci.*, 44(4):817–825, 1989.
- [61] A.J. Giacomini, J.D. Cook, L.M. Johnson, and A.W. Mix. Flexible blade coating. *J. Coat. Technol. Res.*, 9(3):269–277, 2012.
- [62] A. Deblais, R. Harich, A. Colin, and H. Kellay. Taming contact line instability for pattern formation. *Nature communications*, 7(1):1–7, 2016.
- [63] B. Derjaguin. Thickness of liquid layer adhering to walls of vessels on their emptying and the theory of photo-and motion-picture film coating. In *CR (Dokl.) Acad. Sci. URSS*, volume 39, pages 13–16, 1943.
- [64] J. Seiwert. *Entraînements visqueux*. PhD thesis, Ecole Polytechnique, 2010.
- [65] J.H. Snoeijer. Analogies between elastic and capillary interfaces. *Phys. Rev. Fluids*, 1(6):060506, 2016.
- [66] S.S. Hwang. Hydrodynamic analyses of blade coaters. *Chemical Engineering Science*, 34(2):181–189, 1979.
- [67] T. Sullivan, S. Middleman, and R. Keunings. Use of a finite-element method to interpret rheological effects in blade coating. *AIChE journal*, 33(12):2047–2056, 1987.
- [68] P.H. Trinh, S.K. Wilson, and H.A. Stone. A pinned or free-floating rigid plate on a thin viscous film. *J. Fluid Mech.*, 760:407–430, 2014.
- [69] L. Chen. An integral approach for large deflection cantilever beams. *International Journal of Non-Linear Mechanics*, 45(3):301–305, 2010.
- [70] N.B. Rao and V.G. Rao. Large deflections of a cantilever beam subjected to a rotational distributed loading. *Forschung im Ingenieurwesen A*, 55(4):116–120, 1989.

- [71] C. Gutfinger and J.A. Tallmadge. Films of non-Newtonian fluids adhering to flat plates. *AIChE Journal*, 11(3):403–413, 1965.
- [72] R.P. Spiers, C.V. Subbaraman, and W.L. Wilkinson. Free coating of non-newtonian liquids onto a vertical surface. *Chemical Engineering Science*, 30(4):379–395, 1975.
- [73] A. de Ryck and D. Quéré. Fluid Coating from a Polymer Solution. *Langmuir*, 14(7):1911–1914, 1998.
- [74] J. Ashmore, AQ. Shen, HP. Kavehpour, HA. Stone, and GH. McKinley. Coating flows of non-newtonian fluids: weakly and strongly elastic limits. *Journal of Engineering Mathematics*, 60(1):17–41, 2008.
- [75] W.J. Smit, C. Kusina, A. Colin, and J.F. Joanny. Withdrawal and dip coating of an object from a yield-stress reservoir. *Physical Review Fluids*, 6(6):063302, 2021.
- [76] T. Sullivan and S. Middleman. Film thickness in blade coating of viscous and viscoelastic liquids. *Journal of non-newtonian fluid mechanics*, 21(1):13–38, 1986.
- [77] E. Mitsoulis. Numerical simulation of viscoelastic effects in blade-over-roll coating forming flows. *Computer Methods in Materials Science*, 10(3):156–166, 2010.
- [78] Y. Greener and S. Middleman. Blade-coating of a viscoelastic fluid. *Polymer Engineering & Science*, 14(11):791–796, 1974.
- [79] M. Maillard, C. Mézière, P. Moucheront, C. Courrier, and P. Coussot. Blade-coating of yield stress fluids. *Journal of Non-Newtonian Fluid Mechanics*, 237:16–25, 2016.
- [80] I. Iliopoulos and L.E. Scriven. A blade-coating study using a finite-element simulation. *Phys. Fluids*, 17(12):127101, 2005.
- [81] L. Mahadevan and J.B. Keller. Periodic folding of thin sheets. *Siam Rev.*, 41(1):115–131, 1999.
- [82] L. Landau, E. Lifchitz, and A. Kosevich. *Physique théorique. Théorie de l'élasticité*, volume 7. MIR, Moscou, 1990.
- [83] H. Becker. Elastic modulus of mylar sheet. *J. Appl. Polym. Sci*, 9(3):911–916, 1965.
- [84] Bluestar. Rhodorsil Oils 47. *Technical information*.
- [85] L. Zhang, L. Tong, and J.A. Gal. *Applied Mechanics: Progress and Applications : Proceedings of the Third Australasian Congress on Applied Mechanics*. World Scientific, 2002.
- [86] O.V. Voinov. Hydrodynamics of wetting. *Fluid Dyn.*, 11(5):714–721, 1976.
- [87] R.G. Cox. The dynamics of the spreading of liquids on a solid surface. part 1. viscous flow. *J. Fluid Mech.*, 168:169–194, 1986.
- [88] J-J. Marigo. *Mécanique des Milieux Continus I*, page 340. Ecole Polytechnique, 2014.
- [89] S.P. Timoshenko and J.M. Gere. *Theory of elastic stability*. Courier Corporation, 2009.
- [90] Non-linear boundary value problem, numerical methods, 2020. https://encyclopediaofmath.org/wiki/Non-linear_boundary_value_problem,_numerical_methods, Accessed: 2022-07-28.
- [91] M. Kubíček, V. Hlaváček, and M. Holodniok. Solution of nonlinear boundary value problems—X. *Chemical Engineering Science*, 31(8):727–731, 1976.

- [92] Ł. Płociniczak, G.W. Griffiths, and W.E. Schiesser. ODE/PDE analysis of corneal curvature. *Computers in Biology and Medicine*, 53:30–41, 2014.
- [93] G.D. Mallinson and G. de Vahl Davis. The method of the false transient for the solution of coupled elliptic equations. *Journal of Computational Physics*, 12(4):435–461, 1973.
- [94] G.D. Smith. *Numerical solution of partial differential equations: finite difference methods*. Oxford university press, 1985.
- [95] S.J. Ruuth. Implicit-explicit methods for reaction-diffusion problems in pattern formation. *J. Math. Biol.*, 34(2):148–176, 1995.
- [96] P.D. Lax and R.D. Richtmyer. Survey of the stability of linear finite difference equations. *Commun. Pure Appl. Math.*, 9(2):267–293, 1956.
- [97] E.R. Morris. Molecular Origin of Xanthan Solution Properties. In *Extracellular Microbial Polysaccharides*, volume 45 of *ACS Symposium Series*, pages 81–89. American chemical society edition, 1977.
- [98] P.J. Whitcomb and C.W. Macosko. Rheology of Xanthan Gum. *Journal of Rheology*, 22(5):493–505, 1978.
- [99] K-W. Song, Y-S. Kim, and G-S. Chang. Rheology of concentrated xanthan gum solutions: Steady shear flow behavior. *Fibers and Polymers*, 7(2):129–138, 2006.
- [100] P.D. Oliveira, R.C. Michel, A.J.A. McBride, A.S. Moreira, R.F.T. Lomba, and C.T. Vendruscolo. Concentration Regimes of Biopolymers Xanthan, Tara, and Clairana, Comparing Dynamic Light Scattering and Distribution of Relaxation Time. *PLoS ONE*, 8(5):e62713, 2013.
- [101] O. du Roure, A. Lindner, EN. Nazockdast, and MJ. Shelley. Dynamics of flexible fibers in viscous flows and fluids. *Annual Review of Fluid Mechanics*, 51(1):539–572, 2019.
- [102] F. García-Ochoa, VE. Santos, JA. Casas, and E. Gimes. Xanthan gum: production, recovery, and properties. *Biotechnology Advances*, 18(7):549–579, 2000.
- [103] Í.G.M. Silva and E.F. Lucas. Rheological Properties of Xanthan Gum, Hydroxypropyl Starch, Cashew Gum and Their Binary Mixtures in Aqueous Solutions. *Macromolecular Symposia*, 380(1):1800070, 2018.
- [104] R.K. Prud'Homme and R.E. Long. Surface tensions of concentrated xanthan and polyacrylamide solutions with added surfactants. *Journal of Colloid and Interface Science*, 93(1):274–276, 1983.
- [105] R. Abdulla, E. Chan, and P. Ravindra. Biodiesel production from *Jatropha curcas*: A critical review. *Critical reviews in biotechnology*, 31:53–64, 2011.
- [106] A.B. Ross, S.K. Wilson, and B.R. Duffy. Blade coating of a power-law fluid. *Physics of Fluids*, 11(5):958–970, 1999.
- [107] J. Beaumont. *Écoulements de fluides viscoélastiques en géométries confinées -Application à la récupération assistée des hydrocarbures*. PhD thesis, Université Bordeaux I, 2013.
- [108] A. Gauthier, M. Pruvost, O. Gamache, and A. Colin. A new pressure sensor array for normal stress measurement in complex fluids. *Journal of Rheology*, 65(4):583–594, 2021.
- [109] J.M. Piau. Carbopol gels: Elastoviscoplastic and slippery glasses made of individual swollen sponges: Meso- and macroscopic properties, constitutive equations and scaling laws. *Journal of Non-Newtonian Fluid Mechanics*, 144(1):1–29, 2007.

- [110] I.A. Gutowski, D. Lee, John R. de Bruyn, and B.J. Frisken. Scaling and mesostructure of Carbopol dispersions. *Rheologica Acta*, 51(5):441–450, 2012.
- [111] M. Dinkgreve, M. Fazilati, M. M. Denn, and D. Bonn. Carbopol: From a simple to a thixotropic yield stress fluid. *Journal of Rheology*, 62(3):773–780, 2018.
- [112] M. Dinkgreve, M.M. Denn, and D. Bonn. “Everything flows?”: elastic effects on startup flows of yield-stress fluids. *Rheologica Acta*, 56(3):189–194, 2017.
- [113] S. Aktas, D.M. Kalyon, B.M. Marín-Santibáñez, and J. Pérez-González. Shear viscosity and wall slip behavior of a viscoplastic hydrogel. *Journal of Rheology*, 58(2):513–535, 2014.
- [114] C. Gomez, B. Derakhshandeh, S.G. Hatzikiriakos, and C.P.J. Bennington. Carbopol as a model fluid for studying mixing of pulp fibre suspensions. *Chemical Engineering Science*, 65(3):1288–1295, 2010.
- [115] F. Peters, G. Ghigliotti, S. Gallier, F. Blanc, E. Lemaire, and L. Lobry. Rheology of non-Brownian suspensions of rough frictional particles under shear reversal: A numerical study. *Journal of Rheology*, 60(4):715–732, 2016.
- [116] Philippe Coussot. *Rheophysics. Soft and Biological Matter*. Springer Cham, springer edition, 2014.
- [117] A.R. Kansal, S. Torquato, and F.H. Stillinger. Diversity of order and densities in jammed hard-particle packings. *Physical Review E*, 66(4):041109, 2002.
- [118] G.D. Scott. Packing of Spheres: Packing of Equal Spheres. *Nature*, 188(4754):908–909, 1960.
- [119] J.L. Willett. Packing Characteristics of Starch Granules. *Cereal Chemistry Journal*, 78(1):64–68, 2001.
- [120] E. Blanco, D.J.M. Hodgson, M. Hermes, R. Besseling, G.L. Hunter, P.M. Chaikin, M.E. Cates, I. Van Damme, and W.C.K. Poon. Conching chocolate is a prototypical transition from frictionally jammed solid to flowable suspension with maximal solid content. *Proceedings of the National Academy of Sciences*, 116(21), 2019.
- [121] L. Lobry, E. Lemaire, F. Blanc, S. Gallier, and F. Peters. Shear thinning in non-Brownian suspensions explained by variable friction between particles. *Journal of Fluid Mechanics*, 860:682–710, 2019.
- [122] R.K. McGearry. Mechanical Packing of Spherical Particles. *Journal of the American Ceramic Society*, 44(10):513–522, 1961.
- [123] R.J. Farris. Prediction of the Viscosity of Multimodal Suspensions from Unimodal Viscosity Data. *Transactions of the Society of Rheology*, 12(2):281–301, 1968.
- [124] A. Dörr, A. Sadiki, and A. Mehdizadeh. A discrete model for the apparent viscosity of polydisperse suspensions including maximum packing fraction. *Journal of Rheology*, 57:743–765, 2013.
- [125] P.M. Mwasame, N.J. Wagner, and A.N. Beris. Modeling the effects of polydispersity on the viscosity of noncolloidal hard sphere suspensions. *Journal of Rheology*, 60(2):225–240, 2016.
- [126] N. Mitarai and F. Nori. Wet granular materials. *Advances in Physics*, 55(1-2):1–45, 2006.
- [127] M.E. Cates, R. Adhikari, and K. Stratford. Colloidal arrest by capillary forces. *Journal of Physics: Condensed Matter*, 17(31):S2771–S2778, 2005. Publisher: IOP Publishing.

- [128] M.E. Cates, M.D. Haw, and C.B. Holmes. Dilatancy, jamming, and the physics of granulation. *Journal of Physics: Condensed Matter*, 17(24):S2517–S2531, 2005.
- [129] F. Boyer, E. Guazzelli, and O. Pouliquen. Unifying Suspension and Granular Rheology. *Physical Review Letters*, 107(18):188301, 2011.
- [130] E. Guazzelli and O. Pouliquen. Rheology of dense granular suspensions. *Journal of Fluid Mechanics*, 852:P1, 2018.
- [131] A. Einstein. Berichtigung zu meiner Arbeit. *Annalen der Physik*, 339(3):591–592, 1911.
- [132] S. Mueller, E.W. Llewellyn, and H.M. Mader. The rheology of suspensions of solid particles. *Proceedings of the Royal Society A*, 466(2116):1201–1228, 2010.
- [133] I.M. Krieger and Thomas J. Dougherty. A Mechanism for Non-Newtonian Flow in Suspensions of Rigid Spheres. *Transactions of the Society of Rheology*, 3(1):137–152, 1959.
- [134] Y. Lin, N. Phan-Thien, J.B.P. Lee, and B.C. Khoo. Concentration Dependence of Yield Stress and Dynamic Moduli of Kaolinite Suspensions. *Langmuir*, 31(16):4791–4797, 2015.
- [135] G. Chatté, J. Comtet, A. Niguès, L. Bocquet, A. Siria, G. Ducouret, F. Lequeux, N. Lenoir, G. Ovarlez, and A. Colin. Shear thinning in non-Brownian suspensions. *Soft Matter*, 14(6):879–893, 2018.
- [136] R. Mari, R. Seto, J.F. Morris, and M.M. Denn. Shear thickening, frictionless and frictional rheologies in non-Brownian suspensions. *Journal of Rheology*, 58(6):1693–1724, 2014.
- [137] J. Comtet, G. Chatté, A. Niguès, L. Bocquet, A. Siria, and A. Colin. Pairwise frictional profile between particles determines discontinuous shear thickening transition in non-colloidal suspensions. *Nature Communications*, 8(1):15633, 2017.
- [138] M. Arshad, A. Maali, C. Claudet, L. Lobry, F. Peters, and E. Lemaire. An experimental study on the role of inter-particle friction in the shear-thinning behavior of non-Brownian suspensions. *Soft Matter*, 17(25):6088–6097, 2021.
- [139] A.N. Beris, J.A. Tsamopoulos, R.C. Armstrong, and R.A. Brown. Creeping motion of a sphere through a Bingham plastic. *Journal of Fluid Mechanics*, 158:219–244, 1985.
- [140] X. Chateau, G. Ovarlez, and K.L. Trung. Homogenization approach to the behavior of suspensions of noncolloidal particles in yield stress fluids. *Journal of Rheology*, 52(2):489–506, 2008.
- [141] F. Giorgiutti-Dauphiné and L. Pauchard. Drying drops: Drying drops containing solutes: From hydrodynamical to mechanical instabilities. *The European Physical Journal E*, 41(3):32, 2018.
- [142] T.W.G. van der Heijden, A.A. Darhuber, and P. van der Schoot. Macroscopic Model for Sessile Droplet Evaporation on a Flat Surface. *Langmuir*, 34(41):12471–12481, 2018.
- [143] R.D. Deegan, O. Bakajin, T.F. Dupont, G. Huber, S.R. Nagel, and T.A. Witten. Contact line deposits in an evaporating drop. *Physical Review E*, 62(1):756–765, 2000.
- [144] F. Parisse and C. Allain. Shape Changes of Colloidal Suspension Droplets during Drying. *Journal de Physique II*, 6(7):1111–1119, 1996.
- [145] E. Adachi, A.S. Dimitrov, and K. Nagayama. Stripe Patterns Formed on a Glass Surface during Droplet Evaporation. *Langmuir*, 11(4):1057–1060, 1995.

- [146] Q. Barral, G. Ovarlez, X. Chateau, J. Boujlel, B. Rabideau, and P. Coussot. Adhesion of yield stress fluids. *Soft Matter*, page 10.1039.b922162j, 2010.
- [147] Y. Zhang, X. Gao, H. Chu, and B.P. Binks. Various crust morphologies of colloidal droplets dried on a super-hydrophobic surface. *Canadian Journal of Physics*, 98(11):1055–1059, 2020.
- [148] T. Okuzono, K. Ozawa, and M. Doi. Simple Model of Skin Formation Caused by Solvent Evaporation in Polymer Solutions. *Physical Review Letters*, 97(13):136103, 2006.
- [149] H. Hu and R.G. Larson. Marangoni Effect Reverses Coffee-Ring Depositions. *The Journal of Physical Chemistry B*, 110(14):7090–7094, 2006.
- [150] R.W. Style and S.S.L. Peppin. Crust formation in drying colloidal suspensions. *Proceedings of the Royal Society A: Mathematical, Physical and Engineering Sciences*, 467(2125):174–193, 2011.
- [151] L. Pauchard and C. Allain. Buckling instability induced by polymer solution drying. *Europhysics Letters (EPL)*, 62(6):897–903, 2003.
- [152] F. Giorgiutti-Dauphiné and L. Pauchard. Elapsed time for crack formation during drying. *The European Physical Journal E*, 37(5):39, 2014.
- [153] B. Adhikari, T. Howes, B.R. Bhandari, and V. Truong. In situ characterization of stickiness of sugar-rich foods using a linear actuator driven stickiness testing device. *Journal of Food Engineering*, 58(1):11–22, 2003.
- [154] N.E. Noren, M.G. Scanlon, and S.D. Arntfield. Differentiating between tackiness and stickiness and their induction in foods. *Trends in Food Science & Technology*, 88:290–301, 2019.
- [155] A. Kaci, R. Bouras, M. Chaouche, P.-A. Andréani, and H. Brossas. Adhesive and Rheological Properties of Mortar Joints. *Applied Rheology*, 19(5):51970–9, 2009.
- [156] Y.O. Mohamed Abdelhay, M. Chaouche, J. Chapuis, E. Charlaix, J. Hinch, S. Roux, and H. Van Damme. Tackiness and cohesive failure of granular pastes: Mechanistic aspects. *The European Physical Journal E*, 35(6):45, 2012.
- [157] K.L. Mittal and H.S. Bui. *Surface Science and Adhesion in Cosmetics*. John Wiley & Sons, Ltd, 1 edition, 2021.
- [158] C. Creton and M. Ciccotti. Fracture and adhesion of soft materials: a review. *Reports on Progress in Physics*, 79(4):046601, 2016.
- [159] S. Poivet, F. Nallet, C. Gay, J. Teisseire, and P. Fabre. Force response of a viscous liquid in a probe-tack geometry: Fingering versus cavitation. *The European Physical Journal E*, 15(2):97–116, 2004.
- [160] A. Dupré. *Theorie mecanique de la chaleur*. Gauthier-Villars, 1869.
- [161] J. Crosby, K.R. Shull, H. Lakrout, and C. Creton. Deformation and failure modes of adhesively bonded elastic layers. *Journal of Applied Physics*, 88(5):2956–2966, 2000.
- [162] B.A. Francis and R.G. Horn. Apparatus-specific analysis of fluid adhesion measurements. *Journal of Applied Physics*, 89(7):4167–4174, 2001.
- [163] O. Ben-Zion and A. Nussinovitch. Testing the rolling tack of pressure-sensitive adhesive materials. Part II: Effect of adherend surface roughness. *Journal of Adhesion Science and Technology*, 16(5):599–619, 2002.

- [164] S. Patton, C. Chen, J. Hu, L. Grazulis, A. Schrand, and A. Roy. Characterization of Thermoplastic Polyurethane (TPU) and Ag-Carbon Black TPU Nanocomposite for Potential Application in Additive Manufacturing. *Polymers*, 9(12):6, 2016.
- [165] C. Creton and L. Leibler. How does tack depend on time of contact and contact pressure? *Journal of Polymer Science Part B: Polymer Physics*, 34(3):545–554, 1996.
- [166] H. Lakrout, C. Creton, D. Ahn, and K.R. Shull. Influence of Molecular Features on the Tackiness of Acrylic Polymer Melts. *Macromolecules*, 34(21):7448–7458, 2001.
- [167] J. Nase. *Décollement de matériaux viscoélastiques : du liquide visqueux au solide élastique mou*. phdthesis, Université Pierre et Marie Curie - Paris VI, 2009.
- [168] S. Abbott. *Adhesion science: principles and practice*. DEStech Publications, Inc, 2015.
- [169] B.E. Gdalin, E.V. Bermesheva, G.A. Shandryuk, and M.M. Feldstein. Effect of Temperature on Probe Tack Adhesion: Extension of the Dahlquist Criterion of Tack. *The Journal of Adhesion*, 87(2):111–138, 2011.
- [170] F. Deplace, C. Carelli, S. Mariot, H. Retsos, A. Chateauminois, K. Ouzineb, and C. Creton. Fine Tuning the Adhesive Properties of a Soft Nanostructured Adhesive with Rheological Measurements. *Journal of Adhesion - J ADHES*, 85:18–54, 2009.
- [171] R.E. Webber, K.R. Shull, A. Roos, and C. Creton. Effects of geometric confinement on the adhesive debonding of soft elastic solids. *Physical Review E*, 68(2):021805, 2003.
- [172] D. Maugis and M. Barquins. Fracture Mechanics and Adherence of Viscoelastic Solids. In L.H. Lee, editor, *Adhesion and Adsorption of Polymers*, Polymer Science and Technology, pages 203–277. Springer US, Boston, MA, 1980.
- [173] J. Nase, A. Lindner, and C. Creton. Pattern Formation During Deformation of a Confined Viscoelastic Layer: From a Viscous Liquid to a Soft Elastic Solid. *Physical Review Letters*, 101(7):074503, 2008.
- [174] M. Geerligs. *Skin layer mechanics*. PhD thesis, Technische Universiteit Eindhoven, 2010.
- [175] P. Agache et al. *Physiologie de la peau et explorations fonctionnelles cutanées*. Collection Explorations fonctionnelles humaines. Editions médicales internationales, Cachan, 2000.
- [176] Y-C. Fung. *Biomechanics - Mechanical Properties of Living Tissues*. Springer New York, NY, 1993.
- [177] A. Laplante. *Mécanismes de réépithélialisation des plaies cutanées*. PhD thesis, Université Laval, 2002.
- [178] F.H. Silver, Y.P. Kato, M. Ohno, and A.J. Wasserman. Analysis of mammalian connective tissue: relationship between hierarchical structures and mechanical properties. *Journal of Long-Term Effects of Medical Implants*, 2(2-3):165–198, 1992.
- [179] M-A. Abellan, M. Ayadh, E. Feulvarch, H. Zahouani, and J-M. Bergheau. Caractérisation des paramètres mécaniques de la peau humaine jeune in vivo par essais d’indentation sans contact. In *22ème Congrès Français de Mécanique*, 2015.
- [180] A.K. Dąbrowska, G-M. Rotaru, S. Derler, F. Spano, M. Camenzind, S. Annaheim, R. Stämpfli, M. Schmid, and RM. Rossi. Materials used to simulate physical properties of human skin. *Skin Research and Technology*, 22:3–14, 2016.

- [181] K. Chopra, D. Calva, M. Sosin, KK. Tadisina, and et al. A Comprehensive Examination of Topographic Thickness of Skin in the Human Face. *Aesthetic Surgery Journal*, 35(8):1007–1013, 2015.
- [182] JFM. Manschot, PFF. Wijn, and AJM. Brakkee. The Angular Distribution Function of the Elastic Fibres in the Skin as Estimated from in Vivo Measurements. In *Biomechanics: Principles and Applications*, pages 411–418. Springer, Dordrecht, 1982.
- [183] G.L. Wilkes, I.A. Brown, and R.H. Wildnauer. The biomechanical properties of skin. *CRC critical reviews in bioengineering*, 1:453–95, 1973.
- [184] P.H. Carpentier and H.R. Maricq. Microvasculature in systemic sclerosis. *Rheum Dis Clin N Am*, 16:75–91, 1990.
- [185] K. Langer. On the anatomy and physiology of the skin. *British Journal of Plastic Surgery*, 1978.
- [186] T. Gibson, H. Stark, and JH. Evans. Directional variation in extensibility of human skin in vivo. *Journal of Biomechanics*, 2(2):201–204, 1969.
- [187] C. Brèque. *Développement et mise en oeuvre de méthodes optiques pour la mesure de relief et de champ de déformations en vue de la modélisation d'organes biologiques*. PhD thesis, Université de Poitier, 2002.
- [188] CH. Daly. Biomechanical Properties of Dermis. *Journal of Investigative Dermatology*, 79(1):17–20, 1982.
- [189] JFM. Manschot and JM. Brakkee. The measurment and modeling of the mechanical properties of human skin in vivo - I. The measurment. *Journal of Biomechanics*, 19:511–515, 1986.
- [190] J.C. Barbenel and J.H. Evans. The time dependent mechanical properties of the skin. *The Journal of Investigative Dermatology*, 69:318–320, 1977.
- [191] M.S. Christensen, C.W. Hargens, S. Nacht, and E.H. Gans. Viscoelastic properties of intact human skin: instrumentation, hydratationeffects and the contribution of the stratum corneum. *The Journal of Investigative Dermatology*, 69:282–286, 1977.
- [192] S. Diridollou, M. Berson, V. Vabre, D. Black, B. Karlsson, F. Auriol, J.M. Gregoire, C. Yvon, L. Vaillant, Y. Gall, and F. Patat. An In Vivo Method for Measuring the Mechanical Properties of the Skin Using Ultrasound. *Ultrasound in Medicine & Biology*, 24:215–224, 1998.
- [193] M.G. Dunn and F.H. Silver. Viscoelastic behavior of human connective tissues: relative contribution of viscous and elastic components. *Connective Tissue Research*, 12(1):59–70, 1983.
- [194] P.F.F. Wijn, A.J.M. Brakkee, G.J.M Stienen, and A.J.H Vendrik. Mechanical Properties of The Human Skin in Vivo For Small Deformations; A Comparison of Uniaxial Strain and Torsion Measurements. In *Proceedings of a seminar on Tissue Viability and Clinical Applications*, pages 103–108. Palgrave, London, 1976.
- [195] C. Jacquemoud. *Caractérisation mécanique et modélisation du comportement jusqu'à rupture de membranes biologiques fibreuses : application à la peau humaine*. PhD thesis, INSA Lyon, 2007.
- [196] F.M. Hendriks. *Mechanical behaviour of human epidermal and dermal layers in vivo*. PhD thesis, Technische Universiteit Eindhoven, Eindhoven, 2005.
- [197] S. Nicolle, J. Decorps, B. Fromy, and J-F. Paliérne. New regime in the mechanical behavior of skin: strain-softening occurring before strain-hardening. *Journal of the Mechanical Behavior of Biomedical Materials*, 69:98–106, 2017.

- [198] HV. Tran. *Caractérisation des propriétés mécaniques de la peau humaine in vivo via l'IRM*. PhD thesis, Université de technologie de Compiègne, 2008.
- [199] A. Dai, S. Wang, L. Zhou, H. Wei, Z. Wang, and W. He. In vivo mechanical characterization of human facial skin combining curved surface imaging and indentation techniques. *Skin Research and Technology*, (2):142–149, 2019.
- [200] G.E. Piérard, S.L. Piérard, and T. Hermanns-Lê. Facial Skin Rheology. In MA. Farage, Kenneth W. Miller, and Howard I. Maibach, editors, *Textbook of Aging Skin*, pages 1–13. Springer Berlin Heidelberg, 2015.
- [201] P. Agache, J.P. Boyer, and R. Laurent. Biomechanical properties and microscopic morphology of human stratum corneum incubated on a wet pad in vitro. *Archiv für Dermatologische Forschung*, 246(3):271–283, 1973.
- [202] Y.S. Papir, K-H. Hsu, and R.H. Wildnauer. The mechanical properties of stratum corneum I. The effect of water and ambient temperature on the tensile properties of newborn rat stratum corneum. *Biochimica and Biophysica Acta*, 399:170–180, 1975.
- [203] A.C. Park and C.B. Baddiel. The effect of saturated salt solutions on the elastic properties of stratum corneum. *J Soc Cosmet Chem*, 23:471–479, 1972.
- [204] Y. Afifi, A. Elkhyat, B. Hassam, and et al. Mouillabilité de la peau et peau séborrhéique. In: Uhoda E, Paye M, Pierrad GE, editors, *Actualités en Ingénierie cutanée*, vol.4. Paris; ESKA, 2006.
- [205] A. Mavon, H. Zahouani, D. Redoules, P. Agache, Y. Gall, and P. Humbert. Sebum and stratum corneum lipids increase human skin surface free energy as determined from contact angle measurements: A study on two anatomical sites. *Colloids and Surfaces B: Biointerfaces*, 8:147–155, 1997.
- [206] F. Eudier, G. Savary, M. Grisel, and C. Picard. Skin surface physico-chemistry: Characteristics, methods of measurement, influencing factors and future developments. *Advances in Colloid and Interface Science*, 264:11–27, 2019.
- [207] A. Elkhyat, P. Agache, H. Zahouani, and P. Humbert. A new method to measure in vivo human skin hydrophobia. *International Journal of Cosmetic Science*, 23(6):347–352, 2001.
- [208] A. Chanda. Biomechanical Modeling of Human Skin Tissue Surrogates. *Biomimetics*, 3(3):18, 2018.
- [209] C. Guerra. Development and Investigation of Synthetic Skin Simulant Platform (3SP) in Friction Blister Applications. Master's Thesis, Texas A&M University, 2010. Accepted: 2012-02-14T22:18:57Z.
- [210] O.A. Shergold and N.A. Fleck. Experimental investigation into the deep penetration of soft solids by sharp and blunt punches, with application to the piercing of skin. *Journal of Biomechanical Engineering*, 127(5):838–848, 2005.
- [211] S. Derler, U. Schrade, and L-C. Gerhardt. Tribology of human skin and mechanical skin equivalents in contact with textiles. *Wear*, 263(7-12):1112–1116, 2007.
- [212] M. Teyssier, G. Bailly, C. Pelachaud, E. Lecolinet, A. Conn, and A. Roudaut. Skin-On Interfaces: A Bio-Driven Approach for Artificial Skin Design to Cover Interactive Devices. In *Proceedings of the 32nd Annual ACM Symposium on User Interface Software and Technology - UIST '19*, pages 307–322. ACM Press, 2019.

- [213] F. Shao, THC. Childs, and B. Henson. Developing an artificial fingertip with human friction properties. *Tribology International*, 42(11-12):1575–1581, 2009.
- [214] Z. Wang, AA. Volinsky, and ND. Gallant. Crosslinking effect on polydimethylsiloxane elastic modulus measured by custom-built compression instrument. *Journal of Applied Polymer Science*, 131(22), 2014.
- [215] R. Seghir and S. Arscott. Extended PDMS stiffness range for flexible systems. *Sensors and Actuators A: Physical*, 230:33–39, 2015.
- [216] R.N. Palchesko, L. Zhang, Y. Sun, and A.W. Feinberg. Development of Polydimethylsiloxane Substrates with Tunable Elastic Modulus to Study Cell Mechanobiology in Muscle and Nerve. *PLoS ONE*, 7(12), 2012.
- [217] N. Ahmed, T. Murosaki, A. Katugo, T. Kurokawa, JP. Gong, and Y. Nogata. Long-term in situ observation of barnacle growth on soft substrates with different elasticity and wettability. *Soft Matter*, 7(7281), 2011.
- [218] A. Chanda and W. Upchurch. Biomechanical Modeling of Wounded Skin. *Journal of Composites Science*, 2(4):69, 2018.
- [219] A. Kuo. Poly (Dimethylsiloxane). In *Polymer Data Handbook*, pages 411–435. Oxford University Press, 1999.
- [220] Kenry, M. Leong, M.H. Nai, F.C. Cheong, and C.T. Lim. Viscoelastic Effects of Silicone Gels at the Micro- and Nanoscale. *Procedia IUTAM*, 12:20–30, 2015.
- [221] Y. Zhang, X. Yang, and C. Xiong. Mechanical characterization of soft silicone gels via spherical nanoindentation for applications in mechanobiology. *Acta Mechanica Sinica*, 37(4):554–561, 2021.
- [222] S. Deguchi, J. Hotta, S. Yokoyama, and T.S. Matsui. Viscoelastic and optical properties of four different PDMS polymers. *Journal of Micromechanics and Microengineering*, 25(9):097002, 2015.
- [223] S. Yang, K. Khare, and P-C. Lin. Harnessing Surface Wrinkle Patterns in Soft Matter. *Advanced Functional Materials*, 20(16):2550–2564, 2010.
- [224] J. Genzer and J. Groenewold. Soft matter with hard skin: From skin wrinkles to templating and material characterization. *Soft Matter*, 2(4):310–323, 2006.
- [225] D.F. Moore. *The friction and lubrication of elastomers*,. Pergamon Press, Oxford; New York, 1972. OCLC: 509376.
- [226] O. Pouliquen, M. Nicolas, and P.D. Weidman. Crystallization of non-Brownian Spheres under Horizontal Shaking. *Physical Review Letters*, 79(19):3640–3643, 1997.
- [227] P. Coussot, Q. D. Nguyen, H. T. Huynh, and D. Bonn. Viscosity bifurcation in thixotropic, yielding fluids. *Journal of Rheology*, 46(3):573–589, 2002.
- [228] C.D. Cwalina and N.J. Wagner. Material properties of the shear-thickened state in concentrated near hard-sphere colloidal dispersions. *Journal of Rheology*, 58(4):949–967, 2014.
- [229] C.A. Dahlquist. Pressure-sensitive adhesives. *Treatise on adhesion and adhesives*, 2:219–260, 1969.

- [230] J.J. Guo and J.A. Lewis. Aggregation Effects on the Compressive Flow Properties and Drying Behavior of Colloidal Silica Suspensions. *Journal of the American Ceramic Society*, 82(9):2345–2358, 1999.
- [231] A. Frédéric, A. Pascal, and J-Y. Fouron. Transfer-free make-up or care composition containing a volatile linear silicone, European Patent EP 0 979 646 A1, 2000.
- [232] Glycerine Producers' Association. *Physical properties of glycerine and its solutions*. 1963.
- [233] T.B. Lewis and L.E. Nielsen. Viscosity of Dispersed and Aggregated Suspensions of Spheres. *Transactions of the Society of Rheology*, 12(3):421–443, 1968.
- [234] N.M. James, C-P. Hsu, N.D. Spencer, H.M. Jaeger, and L. Isa. Tuning Interparticle Hydrogen Bonding in Shear-Jamming Suspensions: Kinetic Effects and Consequences for Tribology and Rheology. *arXiv:1901.04904 [cond-mat]*, 2019.
- [235] KC. Basavaraju, J. Jayaraju, SK. Rai, and T. Damappa. Miscibility studies of xanthan gum with gelatin in dilute solution. *Journal of Applied Polymer Science*, 109(4):2491–2495, 2008.
- [236] V. Gupta, P.T. Probst, F.R. Goßler, A.M. Steiner, J. Schubert, Y. Brasse, T.A.F. König, and A. Fery. Mechanotunable Surface Lattice Resonances in the Visible Optical Range by Soft Lithography Templates and Directed Self-Assembly. *ACS Applied Materials & Interfaces*, 11(31), 2019.
- [237] R.D. Birkhoff, L.R. Painter, and J.M. Heller. Optical and dielectric functions of liquid glycerol from gas photoionization measurements. *The Journal of Chemical Physics*, 69(9):4185–4188, 1978.
- [238] G.M. Hale and M.R. Querry. Optical Constants of Water in the 200-nm to 200- μ m Wavelength Region. *Applied Optics*, 12(3):555–563, 1973.

Appendix

A. Impact of the Wetting Length on Flexible Blade Spreading

Marion Krapez, Anaïs Gauthier, Hamid Kellay, Jean-Baptiste Boitte, Odile Aubrun, Jean-François Joanny, and Annie Colin. Impact of the Wetting Length on Flexible Blade Spreading. *Physical Review Letters*, American Physical Society, 2020, 125 (25), 10.1103/PhysRevLett.125.254506. hal-03116506

In this appendix is reproduced the article published about the spreading of Newtonian fluid showing in particular the impact of the wetting length over the deposited thickness. It refers to the Chapter [2](#) of this manuscript.

Impact of the wetting length on flexible blade spreading

Marion Krapez,¹ Anaïs Gauthier,¹ Hamid Kellay,² Jean-Baptiste Boitte,³ Odile Aubrun,³ Jean-François Joanny,^{4,5} and Annie Colin^{6,1}

¹MIE – Chemistry, Biology and Innovation (CBI) UMR8231, ESPCI Paris, CNRS, PSL Research University, 10 rue Vauquelin, Paris, France

²Laboratoire Ondes et Matière d’Aquitaine, UMR 5798, CNRS, Université de Bordeaux, 351 Cours de la Libération, 33405 Talence, France

³Centre de recherche de l’Oréal, 188 Rue Paul Hochart, 94550 Chevilly-Larue

⁴Physico Chimie Curie, Institut Curie, PSL University, 26 rue d’Ulm, 75005 Paris

⁵Collège de France, 11 place Marcelin Berthelot, 75005 Paris, France

⁶Université de Bordeaux, Centre de recherche Paul Pascal, CNRS UMR 5031, 115 avenue Schweitzer,

(Dated: March 2, 2021)

We study the spreading of a Newtonian fluid by a deformable blade, a common industrial problem, characteristic of elasto-hydrodynamic situations. Here, we consider the case of a finite reservoir of liquid, emptying as the liquid is spread. We evidence the role of a central variable: the wetting length l_w , which sets a boundary between the wet and dry parts of the blade. We show that the deposited film thickness e depends quadratically with l_w . We study this problem experimentally and numerically by integration of the elasto-hydrodynamic equations, and finally propose a scaling law model to explain how l_w influences the spreading dynamics.

PACS numbers:

The flapping of flags or the deformation of boat sails are emblematic of the coupling of flexible sheets with a fluid flow. Beyond these large-scale situations, there is a blooming interest for smaller systems, in which the forces responsible for the deformation of the solid are viscous instead of inertial. Such situations are encountered when a fluid is confined by an elastic plate, for example paper sheets gliding on thin air just above the floor after falling from a table [1].

The spreading or the scraping of liquids with a flexible blade (Fig 1) is another paradigmatic example of this class of fluid-structure problems, with a rich non-linear behavior [1–3]. Flexible blade spreading is central in numerous industrial processes such as paper coating, which inspired early studies [4–8]. More recently, this problem has been studied in the light of an elasticity-capillarity analogy [9] and compared with another well-known system, dip coating [10, 11]. Following this approach, the elastic forces induced by the local curvature of the sheet replace surface tension forces [12–14]. An *elastic* Landau-Levich approach [12, 13] can be used to predict the film thickness as a function of the blade properties. This method, which successfully modeled selected experiments [12] is based on two assumptions: *i*) the blade is fully covered with liquid (which amounts to neglecting capillarity) and *ii*) while in motion, it is only deformed over a length l_x close to the tip. This internal length is analogous to the dynamical meniscus length in dip-coating. However, in a large majority of everyday situations, such as the spreading of a paint on a wall, or cream on the skin, the liquid reservoir is finite and the blade partially wet. This introduces a new length scale, l_w (as shown in Fig. 1), and its existence challenges the Landau-Levich approach. In this paper, we evidence the central role of l_w on the

spreading dynamics, and we analyze the similarities and differences with dip-coating.

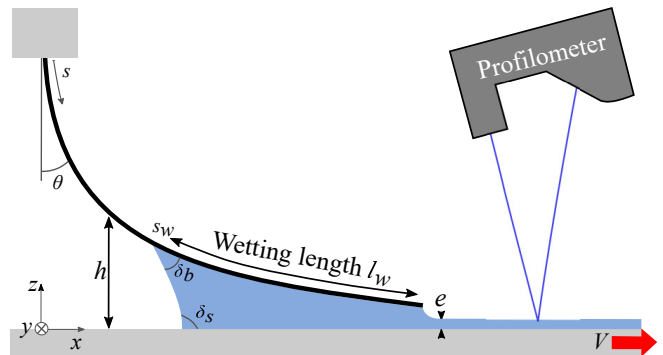


Figure 1: Experimental setup. A finite amount of fluid deposited under an elastic blade is emptied by moving the substrate at a constant speed V . The thickness of the deposited layer e is measured by a profilometer. As the reservoir empties, the wetting length l_w diminishes, which impacts the deposit.

A Newtonian fluid (here silicone oil) with viscosity η ranging from 480 to 960 mPa s is spread on an horizontal smooth PMMA plate by a soft blade made of PET plastic (Mylar) (Fig.1). The dynamic contact angles of oil on both surfaces are denoted by δ_s and δ_b : in a typical experiment, $\delta_s \simeq 100 \pm 10^\circ$, and $\delta_b \simeq 15 \pm 10^\circ$. The blade is cut in a rectangular shape, with a constant width $b = 4$ cm, a length L of typically 6 cm and thickness $u = 125$ or $250 \mu\text{m}$. The upper part of the blade is clamped perpendicularly to the surface, at a height $H = 0.46 L$. This clamping height ensures that the free edge of the blade is exactly tangent to the surface in absence of liquid. It

is also the position for which the film thickness is the largest [12]. The rigidity B of the blade is determined by measuring its deflection under its own weight [15]. B is typically varied by a factor 10 when changing the blade thickness, with $B = 1.0 \pm 0.1$ mN m for $u = 125$ μm and $B = 7.1 \pm 0.5$ mN m for $u = 250$ μm . Using $B = \frac{E^* u^3}{12}$, we obtain a modified Young Modulus E^* of the material, that already includes the Poisson ratio correction. Experimentally, $E^* \simeq 6.2$ GPa, a value in good agreement with what is expected for type A mylar [16].

A known volume of liquid Ω_0 (between 0.1 and 1.5 mL) is deposited under the blade and then spread with a one-way movement, by moving the substrate at a constant speed V ($2.5 < V < 10$ mm/s). The thickness of the scraped liquid film e is measured with an optical profilometer (Keyence LJ-V7060K) positioned above the film, 2 millimeters from the edge of the blade (Fig. 1). A laser sheet of length 16 mm (in the y direction) is projected onto the film, from which the film thickness $e(y, t)$ is measured as a function of time t and position y . The liquid reservoir below the blade slowly empties as oil is scraped over a distance of $\simeq 10$ cm. One important variable here is the length of the blade in contact with the liquid, which we call the *wetting length* l_w (as visible in Fig.1). During an experiment, $l_w(t)$ varies with time and typically diminishes by 2 cm as the reservoir empties. It is measured from the side and from the top using two optical cameras, at 10 frames per second. The camera and the profilometer are synchronized using an in-house Labview program, so that e and l_w are recorded simultaneously during the spreading. The initial time $t = 0$ corresponds to the setting in motion of the horizontal stage.

In Fig. 2a, the thickness e of a silicone oil film (with viscosity $\eta = 960$ mPa s) is mapped as a function of time t and position y ($y = 0$ corresponding to the center of the film). The color code varies from $e \simeq 0$ (dark blue) up to $e = 400$ μm (bright yellow). Despite a small residual noise due to multiple light reflections, the film thickness is relatively uniform in the y -direction along the width of the blade: edge effects are only visible 2 mm from the edges, as shown in Supp. Fig. 1. It represents only 10% of the blade width. However, the film exhibits very large variations with time. This is even more striking when looking at the mean thickness $e(t)$, plotted in white in Fig. 2a. The film profile exhibits a sharp increase in the first 6 seconds, where the thickness grows from 0 to 230 μm . This corresponds to a transient state, associated with the setting in motion of the liquid below the blade, which was previously observed in similar systems [12]. However, the second part of the plot (corresponding to the steady state) strongly differs from previous experiments. We observe here a continuous reduction of the film thickness e with time t - from 230 to 80 μm between 7 s and 20 s. The decrease of e with time is largest with the

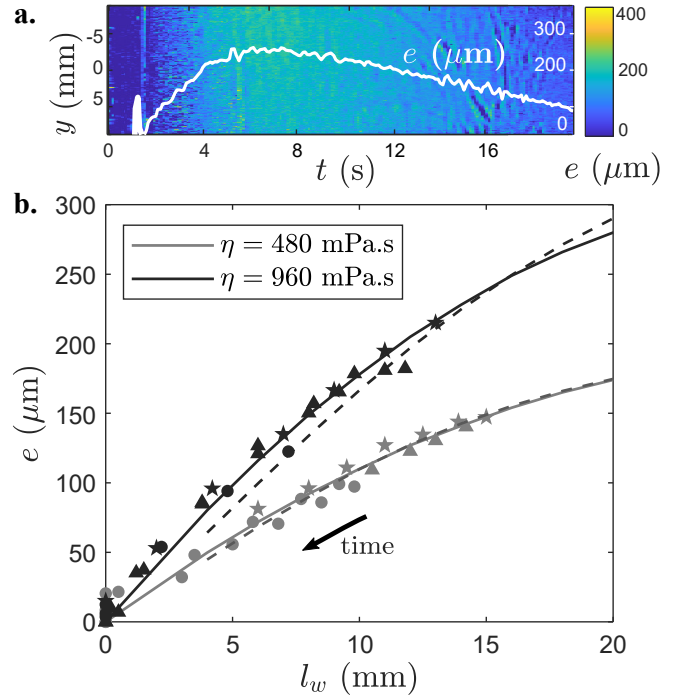


Figure 2: **a.** Map of the central part of the film (with viscosity $\eta = 480$ mPa s) during the spreading, as a function of the width y and time t . The color code varies from $e \simeq 0$ (dark blue) up to $e = 400$ μm (bright yellow). The white line shows the mean thickness $e(t)$ over the film width, as a function of time. **b.** Film thickness $e(t)$ as a function of the wetting length l_w at the same time t , for two different oils with viscosity $\eta = 480$ mPa s (gray) and $\eta = 960$ mPa s (black). The markers correspond to different initial fluid volumes Ω_0 : \bullet : $\Omega_0 = 0.21 \pm 0.01$ cm^3 , \blacktriangle : $\Omega_0 = 0.50 \pm 0.03$ cm^3 and \star : $\Omega_0 = 0.60 \pm 0.02$ cm^3 . The continuous lines show the scaling law (Eq.4) with prefactors 0.15 (for $\eta = 480$ mPa s) and 0.17 (for $\eta = 960$ mPa s) corresponding to the best fits. The dashed lines are the numerical solutions. In both experiments, $V = 5$ mm/s, $B = 1.0$ mN m and $L = 5.7$ cm.

softest blade and the more viscous fluids, and is observed for both silicone oil and glycerine. We interpret this as a consequence of the finite reservoir size. Indeed, as the liquid empties, the length $l_w(t)$ of the blade effectively wet by the liquid diminishes, which in turn impacts the film thickness $e(t)$. This intimate relation between $e(t)$ and $l_w(t)$ is evidenced in Fig. 2b, where $e(l_w)$ is measured for two oils of viscosity $\eta = 480$ mPa s (gray circles) and $\eta = 960$ mPa s (black triangles). Data points are taken at a given time t , so that e and l_w are treated quasi-statically. The markers indicate the initial liquid volume Ω_0 , varied by a factor 3. With η fixed, the data for all Ω_0 overlap, which indicates that the film thickness only depends on the *actual* volume of the reservoir at the time t - a quantity measured by $l_w(t)$. As shown in Fig. 2, the relation between e and l_w is non-linear: e increases more slowly for larger l_w . In addition, a strong dependency of e with the fluid viscosity η is observed: e increases by

roughly 50% from $\eta = 480$ mPa s to $\eta = 960$ mPa s.

To understand how the reservoir size influences the spreading dynamics, we perform a full numerical study of the experiment. Since e and l_w evolve quasi-statically with time, we solve the hydroelastic equations statically, with a constant l_w as an input parameter. The geometry is split in two zones: *i*) the blade itself, which interacts with the fluid below over a length l_w ($< L$) and *ii*) the free liquid film, spread by the blade. In the following, the lubricated blade shape and the free liquid film are modeled by two different sets of equations (Eq. 1 and Eq. 2), coupled by boundary conditions at the tip of the blade. In both cases, the Reynolds number Re in the liquid is small, $Re = \frac{\rho e V}{\eta} < 10^{-3}$, and the oil is highly confined, with $l_w \gg e$, which allow us to use the lubrication approximation to describe the flow.

The blade shape is described as a large deflection problem, using Euler's elastica [17, 18]. In the steady state, the bending torque (expressed as a function of the curvilinear length s along the blade) is equal to the torque Γ produced by the external forces, which arise from the liquid below the beam. The fluid motion generates two forces: a lift, perpendicular to the blade, due to the lubrication pressure p and a viscous drag force f_v , locally tangent to the surface. Both are calculated by solving the Stokes equation in the lubrication approximation (see Supplementary materials). We also include the capillary forces arising from the liquid surface deformation on the left and right parts of the wet area of the blade. They exert a small torque on the blade and, more importantly, impose the fluid pressure at $s = s_w$ and $s = L$ through the curvature of the liquid surface. Finally, the weight of the plate is neglected. With these conditions, the derivative of the torque balance $\Gamma = EI \frac{d\theta}{ds}$ (denoting I the moment of inertia of the blade and θ the local tangent angle of the blade with respect to the vertical) writes:

$$E^* I \frac{d^2\theta}{ds^2} = b \int_s^L f_v \sin(\theta(s) - \theta(s')) - p \cos(\theta(s) - \theta(s')) ds', \quad (1)$$

with b the width of the blade. We neglect the contribution of capillary forces on the torque derivative $\frac{d\Gamma_c}{ds} \sim \gamma b$ (with γ the surface tension of the liquid), which is more than 100 times smaller than the contribution of the lubricating film $\frac{d\Gamma_v}{ds} \sim p b l_w$ (see Supplementary Materials).

In a second part, the free surface of the liquid deposited by the blade is calculated through the canonical Landau Levich equation (following [2]). The variables of the free surface are distinguished here from those of the blade by using an index l):

$$\frac{d^2\theta_l}{ds^2} = -\frac{3\eta}{\gamma} \left(\frac{V h_l - q/b}{h_l^3} \right) \sin \theta_l(s), \quad (2)$$

with h_l the film height, and q the flow rate of the liquid in the reference frame of the blade.

Equations 1 and 2 can both be seen as 1D steady-state non-linear heat equations where θ is equivalent to temperature, with a conductivity equal to 1 and a source distribution $S(s, \theta(s))$ corresponding to the right hand side of the equations. We use this analogy to solve the set of coupled equations 1 and 2 (for the lubricated blade and for the deposited film). To do so, we look for the stationary asymptotic solution to a transient heat equation (Eq. 3) associated to Eqs. 1 and 2, where the derivative of θ versus a virtual time τ is added (the volumetric heat capacity is chosen unitary):

$$\frac{d\theta}{d\tau} = \frac{d^2\theta}{ds^2} + S(s) \quad (3)$$

Starting from an initial guess of the shape ($\theta(s)$ and $\theta_l(s)$) and $p(s=L)$, Eq. 3 is solved numerically by finite differences using a semi-implicit scheme [19]. The non-linear source term $S(s)$ is treated explicitly while the rest is treated implicitly (see Supplementary Materials for the details). This scheme is stable, and thus ensures convergence to the stationary solution $\theta(s)$ (according to Lax equivalence theorem [20]), for a given set of input variables l_w , δ_s and δ_b . Two sets of boundary conditions complete this modeling. For the blade, the fixed mounting imposes $\theta(0) = 0$, and the absence of torque at the tip gives $\frac{d\theta}{ds}|_{s=L} = 0$. For the free surface, the Laplace pressure equation imposes $\frac{d\theta_l}{ds}|_L = -\frac{p(s=L)}{\gamma}$ at the contact of the blade tip, while far from the blade the film is horizontal, so that $\lim_{x \rightarrow +\infty} \theta_l = \pi/2$. Finally, the matching of the two solutions is done iteratively by imposing a continuity of the flow rate q . The liquid height at $s = L$ is continuous [3], but there is an angle discontinuity, similar to what happens at a three phase contact line.

Integration of the blade and deposited film equations thus give the film thickness e for a given l_w , corresponding to the height of the free surface h_l for $x \rightarrow \infty$. In Fig. 2, the calculated film thicknesses (black and grey dashed lines) are compared to the experiments for varying wetting lengths l_w . They match the experimental data for both $\eta = 480$ mPa s and $\eta = 960$ mPa s, without any adjustable parameter. In addition, the numerical solution of the blade shape (Eq. 1) also matches the experiments, as shown in the supplementary materials.

How does the wetting length influence the spreading dynamics? Since the presence of a meniscus below the blade induces a pressure jump at $s = s_w$, a first hypothesis is that the dependency of e with l_w results from an elasto-capillary competition [21, 22]. To check this idea, we compare in Fig. 3 numerical simulations of $e(l_w)$ in two different configurations: in absence of a pressure jump in $s = s_w$ (gray line), and for varying wetting conditions (dotted lines). A major observation from Fig. 3 is that e varies with l_w even when capillary forces are absent. This indicates that the pressure jump at the

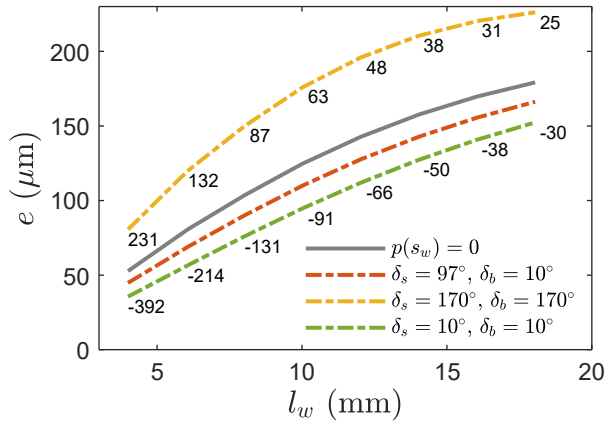


Figure 3: Effect of wetting on $e(l_w)$. The continuous gray line corresponds to the absence of a pressure jump $p(s_w) = 0$. The green, red and yellow dotted lines show three different wetting configurations with varied contact angles δ_s and δ_b on the substrate and on the blade. The numbers indicate the pressure jump $p(s_w)$ due to the meniscus (in Pa).

meniscus does not cause the dependency of e with l_w . Wetting conditions only have a small influence on the film thickness, by shifting the $e(l_w)$ curves: the dotted lines correspond to varying contact angles δ_s and δ_b on the surface and on the blade (as in Fig. 1). While e is potentially increased by a factor two when comparing the almost perfect wetting ($\delta_s = \delta_b = 10^\circ$) to the non-wetting situation ($\delta_s = \delta_b = 170^\circ$), the latter is highly unlikely as the film would be unstable and dewet the substrate. In classical wetting configurations (green and red plots), capillary forces cause a modest variation of e , close to 20%.

A second hypothesis is that the dependency of e with l_w arises from a modified balance between viscous and elastic forces. Indeed, due to the finite size of the reservoir, the pressure within the sheared film applies over a *variable* distance l_w , so that the viscous force lifting the blade diminishes as the reservoir empties. Under this assumption, we propose a scaling law for the film thickness e . The region of the blade wet by oil (of size l_w) is submitted to a lubricating pressure $p \sim \eta \frac{V}{e^2} l_w$. p thus induces a torque Γ_{wet} , pushing up the wet part of the blade (of area bl_w). The lever arm is $\sim L - l_w$, so that Γ_{wet} writes $\Gamma_{\text{wet}} \sim \eta \frac{V}{e^2} bl_w^2 (L - l_w)$. At equilibrium, this torque is compensated by the rigidity of the dry part of the blade, inducing a resisting torque $\Gamma_{\text{dry}} \sim E^* I \frac{d\theta}{ds} \sim \frac{E^* I}{(L - l_w)}$. The torque balance sets the deposition law:

$$e \sim l_w \sqrt{\frac{\eta V L^2 b}{E^* I}} \left(1 - \frac{l_w}{L}\right) \quad (4)$$

This scaling law is plotted in Fig. 2b (with a continuous line). It very convincingly reproduces the dependency of the film thickness e with both l_w and η . The best fits are obtained with similar prefactors: 0.15 for $\eta = 480$ mPa.s

and 0.17 for $\eta = 960$ mPa.s.

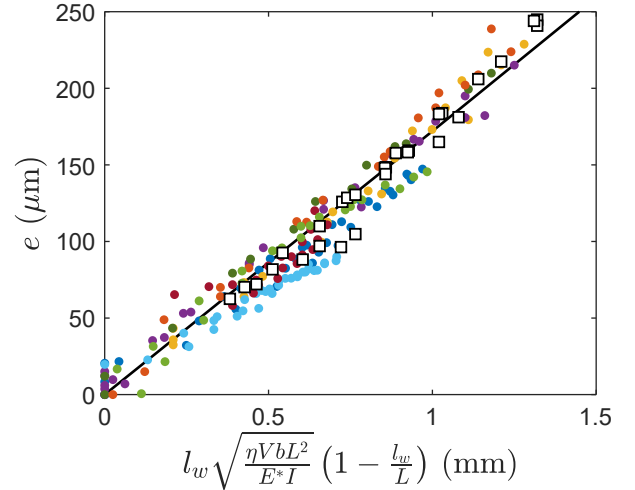


Figure 4: Experimental (colored dots) and numerical (white squares) film thickness, plotted as a function of the theoretical thickness (Eq. 4). All points collapse on a line (in black) with numerical prefactor of 0.17. Data correspond to varying velocities $V = 2.5$ mm/s (light blue), 5 mm/s (blue, yellow, purple), 7.5 mm/s (dark green) and 10 mm/s (red, fuchsia pink, light green), viscosities $\eta = 960$ Pa.s (purple, light green) and 480 Pa.s (all other colors), blade rigidities $B = 7.1 \pm 0.5$ mN m (light green and fuchsia pink) and 1.0 ± 0.1 mN m (all other colors) and lengths $L = 7$ cm (yellow, fuchsia pink, light green) and 5.7 cm (all other colors).

To further validate our approach, we summarize in Fig. 4 the film thickness measurements for different blade rigidities B and length L , varying liquid viscosity η and spreading velocity V (respectively varied by a factor 8, 0.3, 2 and 4). Each color corresponds to a different set of parameters (see legend). When plotted as a function of the theoretical film thickness, all data collapse on a single line with slope 0.17. The numerical solution of the elasto-hydrodynamic equations (Eqs. 1 and 2) is also shown with white squares. Here, the same parameters (V , η , B) as the experiments are used, and capillarity is neglected. The numerical results also collapse on the same master curve, which is a further validation of the scaling law: it shows that the essential physical parameters are taken into account. The residual scattering of the data might be explained by the influence of capillary forces, neglected in Eq. 4, which induce a small variation of the dynamic contact angles with V [23, 24].

The scaling law evidences the fundamental impact of the wetting length l_w , and allows us to put a central point forward. With a finite reservoir, the viscous forces of the lubricated film are exerted over an *externally* imposed distance l_w that varies during the spreading. This is fundamentally different from the capillary-elasticity analogy approach, where the pressure applies over an *internal* dynamical length $l_x \sim (eL^2)^{1/3}$ [9, 12] vary-

ing with the blade and liquid parameters. This in turn impacts the scaling of the film thickness, which writes $e \sim L \left(\frac{\eta V b L^2}{E^* I} \right)^{3/4}$ in the blade-meniscus analogy [12–14]. In addition, the blade is here deformed by the film over its whole length, as visible in Supplementary Figure 3, contrary to the meniscus in dip-coating experiments. For this reason, the blade shape cannot be solved using an asymptotic matching, as usually done for a liquid interface.

This study has an important applicative scope: we indeed demonstrate that it is impossible to obtain a deposit of constant thickness with an elastic blade if the spreading is done at constant speed. In addition, we evidence the role of capillarity, which only plays a role for very hydrophobic substrates. Our work also suggests that the analogy between elastic and capillary interfaces is not valid when the blade is not fully covered with liquid.

-
- [1] AE Hosoi and L Mahadevan. Peeling, healing, and bursting in a lubricated elastic sheet. *Phys. Rev. Lett.*, 93(13):137802, 2004.
- [2] PH Trinh, SK Wilson, and HA Stone. A pinned or free-floating rigid plate on a thin viscous film. *J. Fluid Mech.*, 760:407–430, 2014.
- [3] PH Trinh, SK Wilson, and HA Stone. An elastic plate on a thin viscous film. *arXiv:1410.8558*, 2014.
- [4] F Saita. Simplified models of flexible blade coating. *Chem. Eng. Sci.*, 44(4):817–825, 1989.
- [5] FR Pranckh and LE Scriven. Elastohydrodynamics of blade coating. *AIChE J.*, 36(4):587–597, 1990.
- [6] CM Corvalán and FA Saita. Blade coating on a compressible substrate. *Chem. Eng. Sci.*, 50(11):1769–1783, 1995.
- [7] AJ Giacomini, JD Cook, LM Johnson, and AW Mix. Flexible blade coating. *J. Coat. Technol. Res.*, 9(3):269–277, 2012.
- [8] I Iliopoulos and LE Scriven. A blade-coating study using a finite-element simulation. *Phys. Fluids*, 17(12):127101, 2005.
- [9] JH Snoeijer. Analogies between elastic and capillary interfaces. *Phys. Rev. Fluids*, 1(6):060506, 2016.
- [10] L Landau and B Levich. Dragging of a liquid by a moving plate. In *Dynamics of Curved Fronts*, pages 141–153. Elsevier, 1988.
- [11] B. Derjaguin. Thickness of liquid layer adhering to walls of vessels on their emptying and the theory of photo-and motion-picture film coating. In *CR (Dokl.) Acad. Sci. URSS*, volume 39, pages 13–16, 1943.
- [12] J Seiwert, D Quéré, and C Clanet. Flexible scraping of viscous fluids. *J. Fluid Mech.*, 715:424–435, 2013.
- [13] HN Dixit and GM Homsy. The elastic landau–levich problem. *J. Fluid Mech.*, 732:5–28, 2013.
- [14] K Warburton, DR Hewitt, and JA Neufeld. The elastic landau–levich problem on a slope. *J. Fluid Mech.*, 883, 2020.
- [15] L Mahadevan and JB Keller. Periodic folding of thin sheets. *Siam Rev.*, 41(1):115–131, 1999.
- [16] H Becker. Elastic modulus of mylar sheet. *J. Appl. Polym. Sci.*, 9(3):911–916, 1965.
- [17] SP Timoshenko and JM Gere. *Theory of elastic stability*. Courier Corporation, 2009.
- [18] NB Rao and VG Rao. Large deflections of a cantilever beam subjected to a rotational distributed loading. *Forschung im Ingenieurwesen A*, 55(4):116–120, 1989.
- [19] SJ Ruuth. Implicit-explicit methods for reaction-diffusion problems in pattern formation. *J. Math. Biol.*, 34(2):148–176, 1995.
- [20] PD Lax and RD Richtmyer. Survey of the stability of linear finite difference equations. *Commun. Pure Appl. Math.*, 9(2):267–293, 1956.
- [21] C Py, P Reverdy, L Doppler, J Bico, B Roman, and CN Baroud. Capillary origami: spontaneous wrapping of a droplet with an elastic sheet. *Phys. Rev. Lett.*, 98(15):156103, 2007.
- [22] José Bico, Étienne Reyssat, and Benoît Roman. Elastocapillarity: When surface tension deforms elastic solids. *Annu. Rev. Fluid Mech.*, 50:629–659, 2018.
- [23] OV Voinov. Hydrodynamics of wetting. *Fluid Dyn.*, 11(5):714–721, 1976.
- [24] RG Cox. The dynamics of the spreading of liquids on a solid surface. part 1. viscous flow. *J. Fluid Mech.*, 168:169–194, 1986.

B. Measurement of the thickness of a transparent liquid film with an optical profilometer

To measure the film thickness of the fluid spread by soft blade coating we used an optical profilometer. The detailed calculation of the corrective factor used to access the real thickness from the profilometer data are presented here.

The first hypothesis made is that the measured beams are parallels (case of a telecentric lens). Although this is not the case for the implemented profilometer, it simplifies the calculation of the corrective factor. The error on the thickness value that results from this assumption is discussed at the end of this appendix.

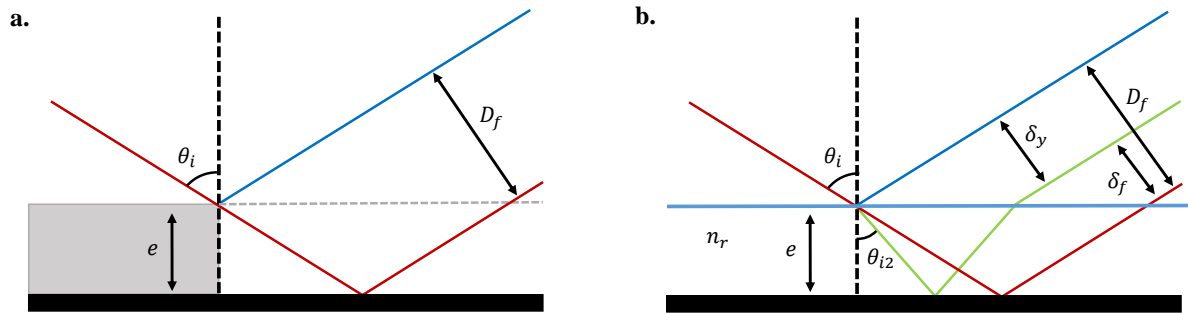


Fig. B.1 – Illustration of the optical path of the rays emitted by the profilometer in a *telecentric* configuration for the measurement of the thickness e . **a.** Case of an opaque solid (grey rectangle). The incident ray undergoes a direct reflection on the support (red line) and on the object (blue line). **b.** Case of a continuous transparent object. The green ray corresponds to the ray refracted by the layer of liquid then reflected by the support. This last one is compared to the red ray (measured in the absence of liquid) to calculate the deposited thickness [3].

Measurement of a step height in the case of an opaque object

To measure the height of a step in the case of an opaque object, the profilometer records the difference in position D_f between the reflected beams at the top (blue ray) and bottom (red ray) of the step (Figure B.1a). The thickness is related to this distance through the equation:

$$e = \frac{D_f}{2 \tan \theta_i \cos \theta_i} \quad (\text{B.1})$$

with D_f the distance between the two beams and θ_i the incident angle. Experimentally, θ_i is fixed at 17.5° .

Measurement of the thickness of a transparent object

First thing to point out is that the profilometer can not give access to the true value of the thickness in the case of a transparent object, as it makes the assumption that the rays are all reflected on a surface (blue and red rays in Fig. B.1a) and not refracted before being reflected as in this situation (green ray in

Figure B.1b). With the profilometer, we first record the reflected rays on the surface in the absence of liquid (red ray), and then the refracted ray in the presence of the liquid film (green ray). The resulting thickness obtained by subtracting these two signals corresponds to $e_r = \frac{\delta_f}{2 \tan \theta_i \cos \theta_i}$.

To find the corrective factor to apply to e_r to access the deposited thickness e we write : $\delta_y = 2e \tan \theta_{i2} \cos \theta_i$, with θ_{i2} is the refracted angle linked to θ_i by Snell-Descartes law: $\sin \theta_i = n_r \sin \theta_{i2}$, where n_r is the refractive index of the transparent medium. The value used for n_r are 1.3455 for xanthane gel [235], 1.4246 for silicone [236], 1.4817 for glycerol [237], and 1.3388 for water [238], at the wavelength of the profilometer laser (404.7 nm). In the case of carbopol gel and HPAM solution the refractive index of water was used. By combining these two equations it leads to $\delta_y = 2e \tan \left(\sin^{-1} \left(\frac{\sin \theta_i}{n_r} \right) \right) \cos \theta_i$. Finally, using $\delta_f = D_f - \delta_y$, and replacing D_f and δ_y by their expressions, this gives the equation linking e and e_r :

$$e = e_r \frac{\tan \theta_i}{\tan \theta_i - \tan \left(\sin^{-1} \left(\frac{\sin \theta_i}{n_r} \right) \right)} \quad (\text{B.2})$$

This last equation highlights the corrective factor to be used in this situation to access the actual deposited thickness e . For silicone, the corrective factor is 3.1735. In general it ranges from 2.91 to 3.60 for the series of considered liquids. The value of the refractive index has a strong impact on the corrective factor and might lead to systematic error in the measurement of the deposited thickness.

Measurement of the thickness of a transparent object lying over a transparent substrate

The use of a transparent PMMA plate, of refractive index n_{rp} and thickness e_p gives rise to a second

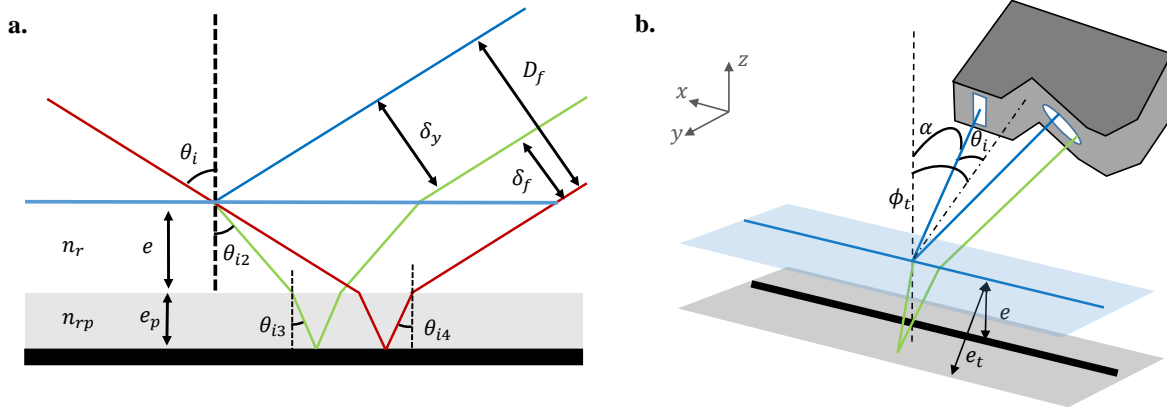


Fig. B.2 – Illustration of the optical path of the rays emitted by the profilometer in a *telecentric* configuration. **a.** Case of a transparent object lying on a transparent substrate whose bottom surface is scattering. Additional refractions are observed at the interface of the object and the substrate for the green and red rays. **b** Schematic view of the rotation of the profilometer around the x -axis. α corresponds to the angle between the incident ray and the z -axis. The rays show our simplified view of the optical paths.

level of reflections and refractions (Figure B.2a). The equations become:

$$\delta_y = 2 \cos \theta_i (e \tan \theta_{i2} + e_p \tan \theta_{i3}) \quad \text{with} \quad \sin \theta_i = n_r \sin \theta_{i2} \quad \text{and} \quad n_r \sin \theta_{i2} = n_{rp} \sin \theta_{i3} \quad (\text{B.3})$$

$$D_f = 2 \cos \theta_i (e \tan \theta_i + e_p \tan \theta_{i4}) \quad \text{with} \quad \sin \theta_i = n_{rp} \sin \theta_{i4} \quad (\text{B.4})$$

Combining together Descartes' relations we get $\theta_{i3} = \theta_{i4}$. Consequently $\delta_f = D_f - \delta_y$ keeps the same expression as before when the liquid was deposited directly on an opaque surface. This transparent PMMA plate will therefore be ignored in the following sections.

Measurement of the thickness of a transparent object with additional tilt ϕ_t

To avoid additional parasitic reflections which disturb the measurement and thus capture only the diffusing rays, a rotation ϕ_t along the x axis is applied, as depicted in Figure B.2b. The angle α between the incident beam and the vertical can be defined as a combination of θ and ϕ_t by using the scalar product between the vector corresponding to the incident beam and the vertical vector. The incident beam vector is obtained by applying a first rotation θ_i around the y -axis, and a second rotation ϕ_t around the x -axis, thus,

$$\mathbf{v} = \begin{bmatrix} 1 & 0 & 0 \\ 0 & \cos \phi_t & -\sin \phi_t \\ 0 & \sin \phi_t & \cos \phi_t \end{bmatrix} \begin{bmatrix} \cos \theta_i & 0 & \sin \theta_i \\ 0 & 1 & 0 \\ -\sin \theta_i & 0 & \cos \theta_i \end{bmatrix} \begin{bmatrix} 0 \\ 0 \\ 1 \end{bmatrix} = \begin{bmatrix} \sin \theta_i \\ -\sin \phi_t \cos \theta_i \\ \cos \theta_i \cos \phi_t \end{bmatrix} \quad (\text{B.5})$$

The scalar product of \mathbf{v} with the vertical vector gives : $\cos \alpha = \cos \theta_i \cos \phi_t$. With a tilt the incident angle corresponds to $\alpha = \arccos(\cos \theta_i \cos \phi_t)$. Note an approximated value of α , obtained by calculating $\tan^2 \alpha$ while considering $\cos^2 \phi_t \approx \cos^2 \theta_i \approx 1$ and neglecting the term $\tan^2 \theta_i \tan^2 \phi_t$ has been used instead : $\alpha = \arctan\left(\sqrt{\tan^2 \theta_i + \tan^2 \phi_t}\right)$. The approximated angle differs by 2% from the exact definition for $\theta_i = 17.5^\circ$ and $\phi_t = 20^\circ$.

The visualisation of the beams become quite complex, as they are no longer in the same plane, and the problem becomes 3D. Indeed, by considering that the rays arriving with an angle α compared to the normal are refracted and reflected only in the same plane, it is not possible to measure them using the sensor of the profilometer. This latter measures rays which return "behind", this is possible in particular thanks to the scattering. A way to simplify the problem is to consider that the equation without tilt is still valid with two differences: the incident ray has an angle α instead of θ_i with respect to the normal, and the thickness of the fluid passed through by the rays, e_t , is larger because of the tilt of the beam: $e_t = \frac{1}{\cos \phi_t} e$. Under this model the equation giving the deposited thickness from the measured one becomes:

$$e = e_r \frac{\tan \alpha \cos \phi_t}{\tan \alpha - \tan\left(\sin^{-1}\left(\frac{\sin \alpha}{n_r}\right)\right)} \quad (\text{B.6})$$

While this model is quite coarse, good agreement with experimental data (error < 5%) were found and validated its use (see below).

As indicated before, the profilometer used is not telecentric, the beams represented are not parallel but pass through the optical center of the lens before being projected onto the sensor. It raises the question of the validity of the previous calculations made under this hypothesis. The calculation of the corrective factor is described below by comparing the expression obtained for the thickness of a step and the thickness of a transparent layer. We restrict ourselves to the calculation without additional tilt.

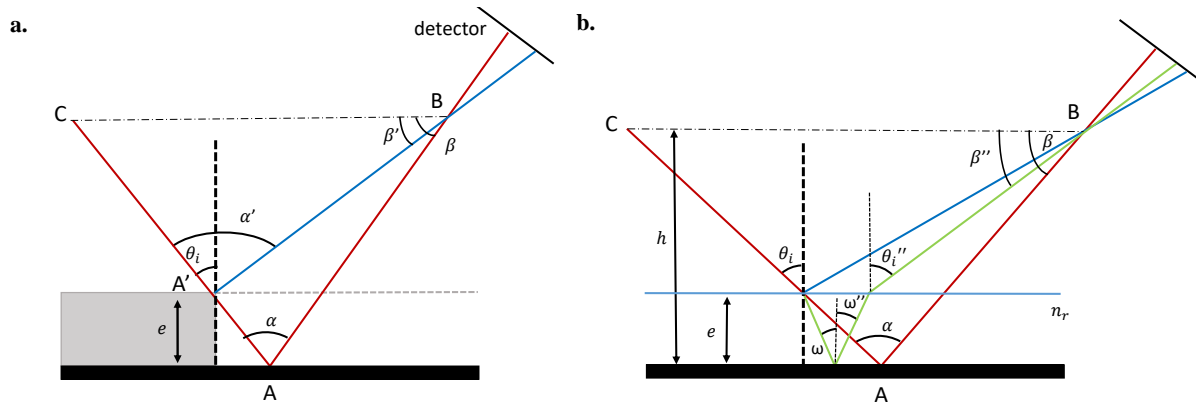


Fig. B.3 – Illustration of the optical path of the rays emitted by the profilometer in a *non-telecentric* configuration for the measurement of the thickness e . **a.** Case of an opaque solid. The incident ray undergoes a direct reflection on the support (red line) and on the object (blue line). The rays measured by the profilometer are no longer parallel but pass through the optical center. The reflection considered is no longer specular (asymmetric angles). **b** Case of a continuous transparent object. The green ray corresponds to the ray refracted by the layer of liquid then reflected by the support.

Non-telecentric lens: Measurement of a step in the case of an opaque object

The system is assumed to be symmetric about the vertical at A (Figure B.3a).

We start by writing: $A'C = AC - \frac{e}{\cos \theta_i}$

The law of sines gives: $\frac{AC}{\sin \beta} = \frac{BC}{\sin \alpha}$, and since we have an isosceles triangle, $\alpha = \pi - 2\beta$.

Finally, $AC = BC \frac{\sin \beta}{\sin 2\beta}$ and likewise we can write $A'C = \frac{BC \sin \beta'}{\sin(\beta + \beta')}$.

So we obtain a relation linking the thickness e to the angle difference $\Delta\beta = \beta - \beta'$, this angle difference then resulting in a position difference on the sensor:

$$e = BC \cos \theta_i \left(\frac{\sin \beta}{\sin 2\beta} - \frac{\sin \beta - \Delta\beta}{\sin 2\beta - \Delta\beta} \right) \quad (\text{B.7})$$

Non-telecentric lens: Measurement of the thickness of a transparent object

Here we can no longer have a reflection with symmetric angles so $\theta_i \neq \theta_i''$ and $\omega \neq \omega''$ (Figure B.3b). The Snell-Descartes relations give $\sin \theta_i = n_r \sin \omega$, and $\sin \theta_i'' = n_r \sin \omega''$. The device being initially

in a symmetric position, the height of the device relative to the support, h , can be expressed as, $h = \frac{BC}{2} \cot \theta_i$. In presence of liquid, this height is reduced to $h - e$, and the side opposite the angle θ_i'' is $\frac{BC}{2} + e(\tan \theta_i - \tan \omega - \tan \omega'')$. Consequently, $\tan \theta_i = \frac{\frac{BC}{2} + e(\tan \theta_i - \tan \omega - \tan \omega'')}{h - e}$, which we can rewrite using $\beta'' = \pi/2 - \theta_i''$, so $\cot \beta'' = \frac{\frac{BC}{2} + e(\tan \theta_i - \tan \omega - \tan \omega'')}{h - e}$. We deduce:

$$e = \frac{BC}{2} \frac{1 - \cot(\beta - \Delta\beta) \cot \theta_i}{\tan\left(\arcsin \frac{\sin \theta_i}{n_r}\right) + \tan\left(\arcsin \frac{\cos(\beta - \Delta\beta)}{n_r}\right) - \tan \theta_i - \cot(\beta - \Delta\beta)} \quad (\text{B.8})$$

In comparison with the opaque surface, one must multiply e by a factor of 3.17 to go from one equation to the other. This average value was obtained using angular variation of β corresponding to thickness values ranging from 0-200 μm (here $\Delta\beta = \beta - \beta''$), $BC = 50$ mm and $n_r = 1.4246$. This value is very close to the value obtained in the case of the parallel beam calculations without additional tilt (difference of order 0.1%). The assumption of parallel beam can be done with confidence. The corrective factor depends on the liquid film thickness. However in our case the thickness is usually limited to 0 to 200 μm which is a sufficiently low range to consider the factor constant at 0.06%.

Note: in the case of converging beams the relations obtained, whether for the opaque surface or the transparent liquid are not linear, meaning there is no relationship of linear proportionality between the thickness and the difference in position on the sensor. However, these phenomena are limited.

Experimental validation of the corrective factor and tilt impact

As described before a certain number of assumption had to be done in order to find a corrective factor that gives access to the value of the deposited thickness. To check that the deviations between the calculated value and the actual value are small, the thickness of a transparent object of known thickness was measured. For this we used a PMMA plate of 3 mm thickness and a glass plate of 150 μm thickness and we varied the angle of inclination ($0 < \phi_t \leq 30^\circ$). The difference between the calliper and profilometer measured values, using the correction factor described in Eq. B.6, is typically between 1 and 5%.

C. Schematic representation of the numerical resolution for Newtonian fluids

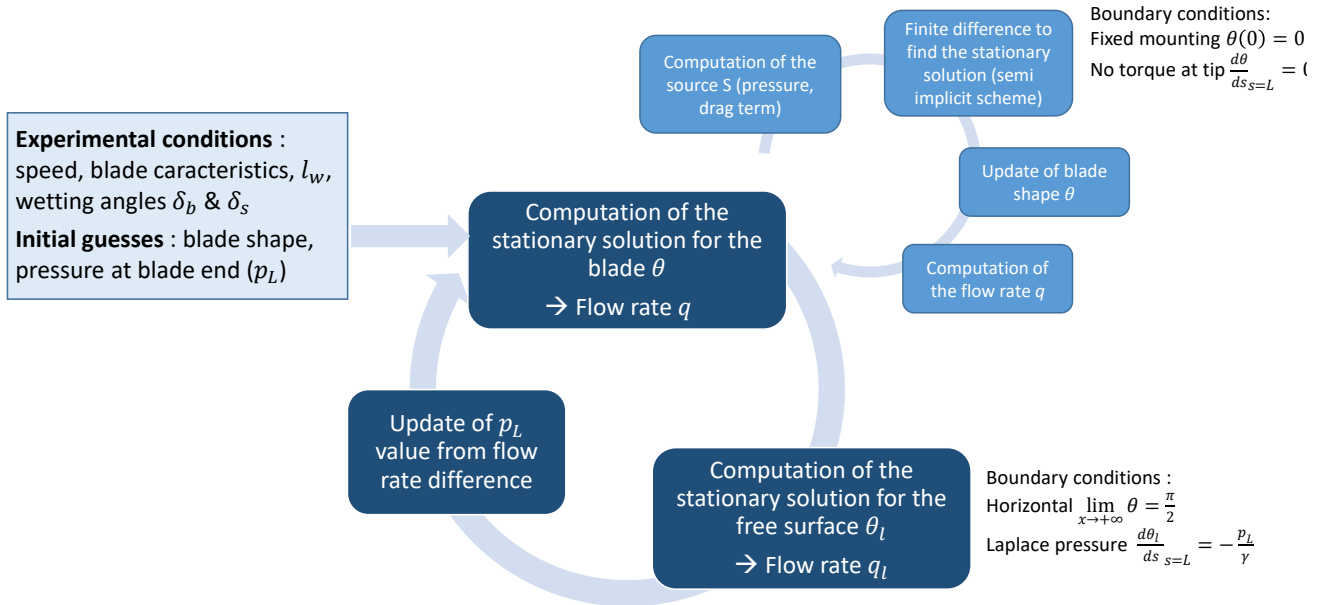


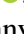


Fig. B.4 – Schematic representation of the steps of the numerical resolution for the simple case of Newtonian fluids. It illustrates the description made in section 2.5.1.

D. Spreading of complex fluids with a soft blade

Marion Krapez, Anaïs Gauthier, Jean-Baptiste Boitte, Odile Aubrun, Jean-François Joanny and Annie Colin Spreading of complex fluids with a soft blade. *Physical Review Fluids*, **7**, 084002, 2022.

In this appendix is reproduced the article published about the spreading of complex fluids, in which the viscous, shear-thinning and normal stress effects are disentangled, showing in particular the negligible effect of the normal stresses in this geometry and the effect of shear-thinning properties on the mechanical work needed for spreading the fluid. It refers to the Chapter [3](#) and [4](#) of this manuscript.

Spreading of complex fluids with a soft blade

Marion Krapez,¹ Anaïs Gauthier ,¹ Jean-Baptiste Boitte,² Odile Aubrun,²
Jean-François Joanny ,^{3,4} and Annie Colin ¹

¹*MIE–Chemistry, Biology and Innovation (CBI) UMR8231, ESPCI Paris, CNRS,
PSL Research University, 75794 Paris, France*

²*Centre de recherche de l'Oréal, 94550 Chevilly-Larue, France*

³*Physico Chimie Curie, Institut Curie, PSL University, 75005 Paris, France*

⁴*Collège de France, 75005 Paris, France*



(Received 15 December 2021; accepted 8 August 2022; published 18 August 2022)

The spreading of complex fluids is not only a part of our everyday life but also a central process in industry to produce functional thin films or protective coatings. Here we consider the spreading of polymer solutions with an elastic blade that deforms during the coating (similarly to a brush or a finger). By using complex fluids with well-chosen rheological properties, we disentangle the effects of shear viscosity, shear thinning, and normal stresses. We reveal two counterintuitive results: First, the mechanical work needed to spread a given volume of a shear-thinning fluid is higher than for the same volume of an equivalent Newtonian fluid at constant spreading velocity. Second, the first normal stress difference, which usually leads to remarkable behaviors such as the swelling of jets or the rise of the fluid on a rotating rod, has strikingly negligible effect here.

DOI: [10.1103/PhysRevFluids.7.084002](https://doi.org/10.1103/PhysRevFluids.7.084002)

I. INTRODUCTION

Many industrial situations require the deposition of a uniform liquid film on a substrate either to produce a functional thin film [1–4] or a protective coating (glass treatment, cosmetics, paint, etc.). The fluid can be deposited directly by drawing the substrate out of a liquid bath (*dip coating*) or with the help of a nondeformable solid [5] or an elastic solid tool, a technique we call here *blade coating*. Interestingly, an analogy is often made between the physics of dip coating and blade coating. In dip-coating experiments, the thickness of the film is set by the deformation of the liquid bath surface close to the substrate. The static meniscus is deformed into a dynamic meniscus, whose shape and curvature is set by a competition between capillary and viscous forces [6,7]. Soft blade coating is currently viewed as an “elastic” dip-coating problem [8–11] where elastic forces due to the bending of the blade resist the viscous force and replace the capillary forces. These studies deal with infinite reservoirs, the blade is always totally covered by the liquid. Recent experiments on Newtonian fluids [12] have shown that this analogy is fragile when the size of the reservoir is finite. The deposited thickness diminishes with time as the fluid reservoir below the blade empties. The film thickness seems to be fixed by the length of the blade wet by the liquid and not by the size of a dynamic “elastic meniscus” due to the deformation of the moving blade. However, these experiments are performed on a restricted range of parameters, which limits the validation of the scaling laws. Here we propose to use complex fluids with well-characterized shear-thinning behavior and first normal stress difference to probe with precision the flows. This allows us to conclude definitively on the possible analogy between dip coating and blade coating. In addition, this approach is also important from an industrial point of view: In most formulations (as in paint and cosmetic creams), at least a small amount of polymer is added to the liquid [13], and its influence on the spreading is not known.

Strikingly, we highlight counterintuitive behaviors. First, it requires a higher mechanical work to spread a shear-thinning fluid than a Newtonian fluid—for an identical initial fluid volume, blade velocity, and spreading duration. Second, normal forces, known to create instabilities and swellings of the deposits during dip coating [14], play little or no role in blade spreading.

The organization of the manuscript is as follows. After presenting the fluids used and our experimental setup (Sec. II), we show experimentally how the fluid rheology impacts the film thickness (Sec. III) and model our results by combining a scaling law analysis and simulations (Sec. IV). We finally discuss how the fluid rheology impacts the spreading process (Sec. V).

II. MATERIALS AND CHARACTERIZATIONS

A. Formulation and rheological properties of the solutions

Three different fluids are used in the experiments: (i) a Newtonian silicone oil (Sigma Aldrich, 500 cSt) with viscosity $\eta = 480$ mPa s; (ii) a shear-thinning solution of xanthan gel (Rhodicare XC, Solvay) (this is made by dissolving 0.9% in mass of polymer in pure water under mechanical agitation), and 0.5% in weight of 2-phenoxyethanol is eventually added as a biocide; and (iii) solutions of partially hydrolyzed polyacrylamid polymer (HPAM, from SNF Floeger) with a high molar mass $M_w = 18 \times 10^6$ g/mol, which are known to generate important normal stress. The polymer is dissolved in water through gentle magnetic agitation to produce solutions with concentrations 0.1%, 0.3%, and 0.5% in weight. Before use, all the polymer solutions are kept at rest for 24 h.

The flow curve of the formulations is obtained using a rheometer (DHR-2, TA) equipped with a cone and plate cell, with radius $R = 20$ mm and angle $\alpha = 2^\circ$. The rheometer imposes a torque T on the rotational axis and measures the angular velocity of the axis ω and the normal force F exerted on the cone by the fluid. As is done classically, the mean shear rate $\dot{\gamma}$ is calculated from ω , with $\dot{\gamma} = \omega / \tan(\alpha)$, the mean shear stress σ is deduced from the torque $\sigma = \frac{3T}{2\pi R^3}$. These definitions ensure that $(\sigma, \dot{\gamma})$ correspond to the mean of the local shear stress $\sigma(r)$ and the mean of the local shear rate $\dot{\gamma}(r)$ in the Newtonian fluid situation. The first normal stress difference N_1 born by the sample is calculated from the vertical force F , with $N_1 = \frac{2F}{\pi R^2}$. It is corrected for inertia, which is not negligible at angular velocities $\dot{\gamma} > 10^2$ s⁻¹, with $N_1^{\text{inertia}} = -\frac{3\rho\omega^2 R^2}{20}$ (denoting ρ the fluid density).

In most experiments, a computer-controlled feedback loop on the torque T is used to keep a constant angular velocity (hence a constant mean shear rate) without any fluctuations ($\frac{\delta\dot{\gamma}}{\dot{\gamma}} < 0.001$). The temperature is set to 298.15 ± 0.1 K using a water circulation around the cell. The flow curves are obtained using a shear-imposed flow-sweep, with five points per decade. The stress value is given when three consecutive 10-s-long measurements have given the same results with 5% tolerance or when the sample has undergone 60 s of constant shear rate. This maximum time is long enough to ensure that the measurements are not sensitive to the inertia of the rheometer.

Figure 1(a) presents the flow curves of the fluids considered here. As expected, silicone oil (shown with red squares) is Newtonian, with a constant viscosity η (independent on $\dot{\gamma}$). The solutions of xanthan gum (blue circles) and HPAM (green triangles), however, are all shear thinning. Their viscosity follow a classical empirical law for polymer solutions:

$$\eta = \begin{cases} \eta_0 & \text{for } \dot{\gamma} < \dot{\gamma}_c \\ k\dot{\gamma}^{n-1} & \text{for } \dot{\gamma} > \dot{\gamma}_c \end{cases} \quad (1)$$

Interestingly, the 0.9% xanthan and the 0.5% HPAM solutions have almost the same viscosity at all the shear rates considered here: The curves $\eta = f(\dot{\gamma})$ overlap. There is, however, a major difference between these two fluids, as shown in Fig. 1(b). In both fluids, the first normal stress difference N_1 follows the law $N_1 = \alpha\dot{\gamma}^m$, but the 0.5% HPAM solution display an important first normal stress difference, contrary to the 0.9% xanthan solution. This is evidenced in the inset of Fig. 1(b): Normal stresses cause the swelling of a 0.5% HPAM jet (green), a phenomenon that is not observed for xanthan (blue). The values of the parameters η_0 , n , k , α , and m for all the suspensions are given in Table I.

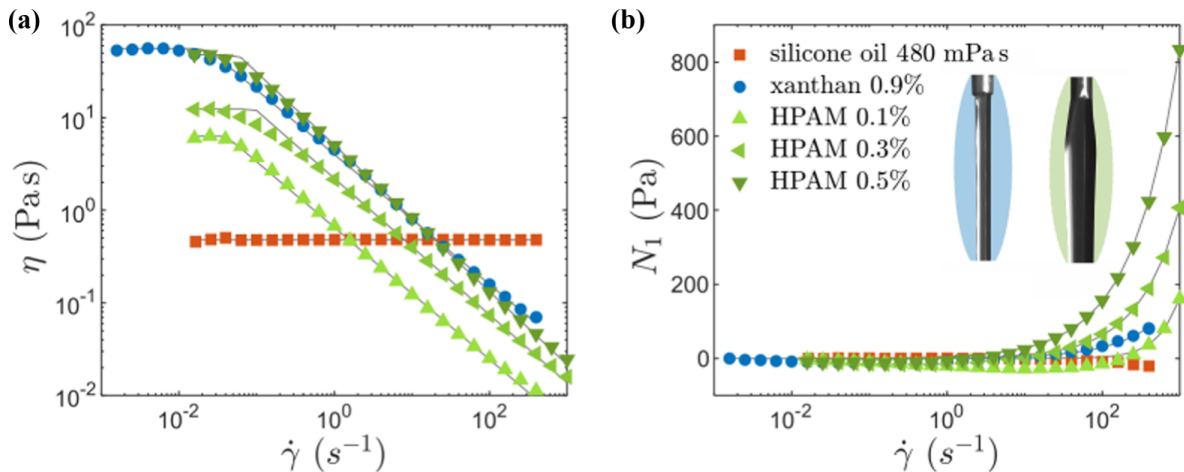


FIG. 1. Rheological curves of silicone oil with viscosity $\eta = 480$ mPa s, xanthan gum at 0.9% and HPAM solutions with concentrations 0.1%, 0.3%, and 0.5%. (a) Viscosity η as a function of the shear rate $\dot{\gamma}$. (b) First normal stress difference N_1 as a function of $\dot{\gamma}$. The pictures show the swelling of a jet of HPAM at 0.5% (green) compared to xanthane at 0.9% (blue) from a capillary tube of outside diameter 0.65 mm and at a flow rate of 0.5 ml s^{-1} .

B. Experimental device

The blade coating experiment is presented in Fig. 2(a). The fluid is spread with a soft blade, made of a rectangular plastic sheet of Mylar, with thickness $u = 125 \mu\text{m}$, width $b = 4 \text{ cm}$ and length $L = 5.7 \text{ cm}$. The modified Young modulus $E^* = \frac{E}{1-\nu^2}$ of the sheet (which includes the Poisson ratio ν) is equal to $6.2 \pm 0.6 \text{ GPa}$. It is determined by measuring the deflection under its own weight, following Refs. [12,15].

The blade is clamped vertically above a PMMA substrate, at a height $y = 0.46L$. This height is chosen so that the tip of the blade is just tangent to the substrate in absence of liquid [8]. Both the blade and the substrate are sanded to avoid a potential dewetting and slippage. The roughness of the blade and the surface is of the order of $5 \mu\text{m}$, which is at least one order of magnitude smaller than the thickness of the deposit. A known volume of liquid Ω_0 (between 0.05 and 1.3 cm^3) is deposited under the blade and spread in a one-way movement by sliding the substrate at a constant velocity $V = 1 \text{ cm/s}$ over 10 cm . The film thickness $e(t)$ is measured 2 mm beyond the tip of the blade using an optical profilometer. Simultaneously, the amount of liquid wetting the blade at a given time t is measured thanks to a camera placed above the translucent mylar sheet. It is quantified by the wetting length l_w , which measures the portion of the blade that is in contact with the liquid [Fig. 2(a)].

TABLE I. Rheological properties of xanthan gum and HPAM solutions.

	Xanthan	HPAM		
	0.9%	0.1%	0.3%	0.5%
η_0 (Pa s)	56	6.3	12.4	48
k	4.0	0.65	2.2	5.1
n	0.30	0.29	0.27	0.21
α	0.99	$2e-3$	1.44	5.24
m	0.74	1.62	0.82	0.73

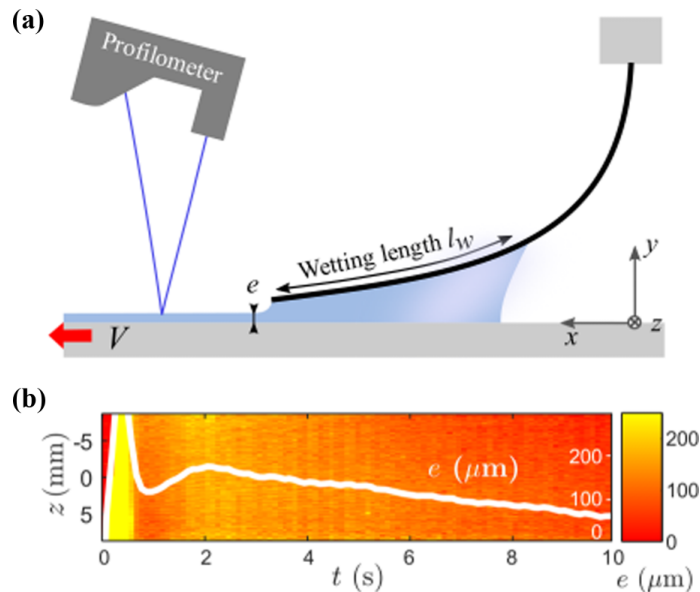


FIG. 2. (a) Schematic representation of the soft blade coating experiment. (b) Map of the central part of the film for xanthane 0.9% during the spreading, as a function of the width z and time t . The color code varies from $e \simeq 0$ (red) up to $e = 250 \mu\text{m}$ (yellow). The first peak is an artifact and is not taken into consideration. The white line shows the mean thickness $e(t)$ over the film width as a function of time.

III. EXPERIMENTAL RESULTS

Figure 2(b) displays the temporal evolution of e along the z axis (with $z = 0$ the center of the blade) as a function of time. The fluid used is xanthan gum, with an initial volume $\Omega_0 = 0.58$ ml. As evidenced by the white line, which plots the mean value of $e(t)$ along the z axis, the film thins out during the course of an experiment. After a transient state (corresponding to the first two seconds), the film thickness $e(t)$ continuously decreases, from 175 to $20 \mu\text{m}$ at the end of the 10-s-long blade movement. This is a consequence of the finite size of the liquid reservoir below the blade. Indeed, and as shown in Fig. 3, $e(t)$ is a function of the wetting length $l_w(t)$, measured at the same time. This observation is valid for all liquids used in the experiment: Figure 3(a) which displays the overlap of more than 30 experiments in total [an experiment corresponds to a set of values $e(t), l_w(t)$]. Interestingly, as highlighted in Fig. 3(b), the measurements obtained with the 0.5% HPAM solution are almost identical to those obtained with the 0.9% xanthan gum solution. Even if these two fluids share the same rheological curve [in Fig. 1(a), the viscosity $\eta(\dot{\gamma})$ of HPAM overlaps the data points of xanthan], the first normal stress difference in HPAM reaches several hundreds of pascals under high shear [Fig. 1(b)] while N_1 is always smaller than 80 Pa in xanthan. Under the conditions of the spreading experiments, one would naively expect the normal stress to play a role: Indeed, the Weissenberg number $\text{Wi} = \frac{N_1}{\tau} \sim \frac{\alpha}{k} \left(\frac{V}{e}\right)^{m-n}$, which compares the first normal stress difference N_1 to the shear stress τ , is around 1 in the case of xanthan gum solutions, whereas it is about 10 in the case of HPAM solutions. This indicates that in our experiments, the normal forces generated by the flow in HPAM are very important compared to the shear stress forces. However, they do not impact the film deposition law.

IV. MODEL

To capture this point and model the relation between e and l_w for the non-Newtonian fluids, we propose a scaling analysis.

In all our experiments, the liquid is highly confined below the blade: The wetting length l_w typically varies between 2 cm and a few millimeters, while e is of the order of $100 \mu\text{m}$, so that $l_w \gg e$. The Reynolds number $\text{Re} = \rho e V / \eta$ is smaller than 10^{-1} (denoting $\rho \simeq 10^3 \text{ kg/m}^3$ the fluid

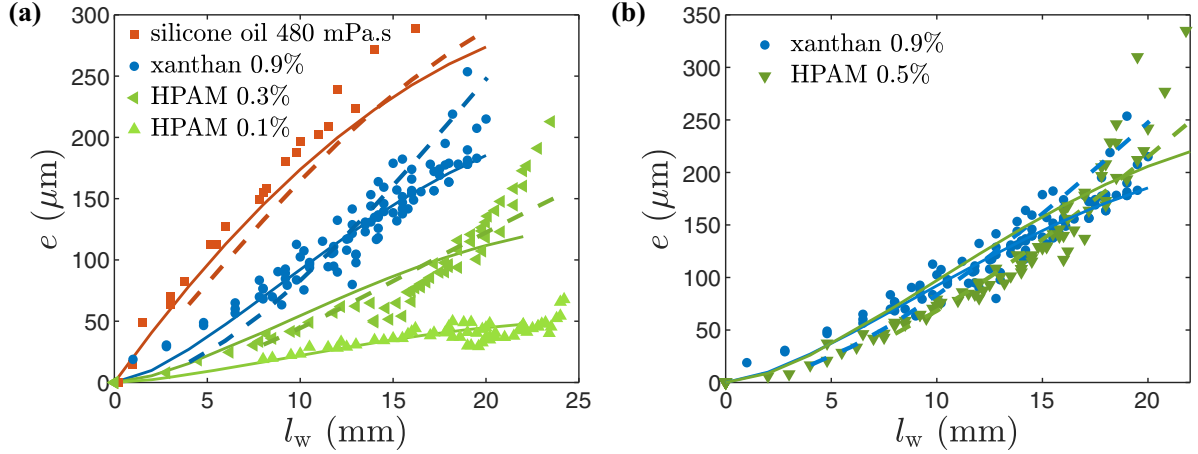


FIG. 3. (a) Evolution of the fluid thickness e with the wetting length l_w for two complex fluids (xanthan 0.9% in blue, HPAM 0.3% in green, and HPAM 0.1% in light green) and a Newtonian fluid (silicone oil, $\eta = 480$ mPa s in red). The markers correspond to the experimental data measured for different initial fluid volumes. The continuous lines show the scaling law [Eq. (1)] with prefactors 0.17 (for silicone oil) and 0.06 (for xanthan and HPAM) corresponding to the best fits. The dashed lines are the numerical solutions. (b) Comparison of xanthan 0.9% and HPAM 0.5% (dark green). The blue symbols correspond to the same experiments in (a) and (b).

density and $\eta > 10^{-2}$ Pa s the fluid viscosity). In addition, the tip of the blade is almost parallel to the substrate, and the mean angle in the wet part of the blade is typically 5° . This implies that the shear gradient is mostly horizontal and the elongational component of the flow is negligible. Thus, the flow below the blade is close to a simple lubrication flow: The fluid velocity \mathbf{v} is oriented along the x axis and varies with y only.

In the general case, and when neglecting gravity, the fundamental relation of dynamics at low Reynolds number is

$$\frac{\partial P}{\partial x} = \frac{\partial \tau_{xx}}{\partial x} + \frac{\partial \tau_{xy}}{\partial y} + \frac{\partial \tau_{xz}}{\partial z}, \quad (2)$$

with P the hydrodynamic pressure within the fluid and τ the deviator of the stress tensor (which has the same symmetry as the velocity field). Equation (2) can be expressed as a function of the first and second normal stress differences N_1 and N_2 . Using $N_1 = \tau_{xx} - \tau_{yy}$ and $N_2 = \tau_{yy} - \tau_{zz}$ and $\tau_{xx} + \tau_{yy} + \tau_{zz} = 0$ (by definition of the pressure), Eq. (2) is written as follows:

$$\frac{\partial P}{\partial x} = \frac{\partial \tau_{xy}}{\partial y} + \frac{\partial \left(\frac{2N_1 + N_2}{3} \right)}{\partial x} + \frac{\partial \tau_{xz}}{\partial z}. \quad (3)$$

In our experiment, symmetry implies that $\tau_{xz} = 0$. In addition, and following Refs. [14] and [16], we consider that $N_2 \ll N_1$, which is classical for polymer solutions. Finally, the steady Stokes equation in the lubrication approximation is

$$\frac{\partial P}{\partial x} = \frac{\partial \tau_{xy}}{\partial y} + \frac{2}{3} \frac{\partial N_1}{\partial x}. \quad (4)$$

The pressure in the liquid film confined below the blade is thus the sum of two terms. The first is the lubrication pressure, which scales as $\tau \frac{l_w}{e}$ (denoting $\tau = \tau_{xy}$) and the second is due to the normal stresses and is proportional to N_1 . During the spreading with a soft blade, the pressure generates a lift force, which is balanced by a restoring elastic force coming from the blade. To evaluate the influence of the normal stresses on the spreading, we define a nondimensional number, $\mathcal{E} = \frac{2N_1 e}{3\tau l_w} \sim \frac{2}{3} \text{Wi} \frac{e}{l_w}$, which compares the contributions of the two terms of the total fluid pressure P . In practice, the condition $\mathcal{E} \ll 1$ is always true for the 0.9% xanthan gum solution, which indicates

that the shear-thinning effects are dominant over the elastic effects. Interestingly, it is also verified for the 0.5% HPAM solution, despite a Weissenberg number $Wi \simeq 10$. Indeed, $\mathcal{E} \ll 1$ as long as $l_w > 0.05$ mm, which is always the case in our experiments.

We now propose a scaling law to model the film thickness e . The blade is subjected to two forces: a lift force F_{lift} created by the flow of the fluid which tends to lift the blade from the plate and an elastic restoring force which tends to stick the blade to the plate F_{blade} . If $\mathcal{E} \ll 1$, then the lift force $F \sim (P - P_0)l_w b$ (with b the width of the blade) created by the fluid on the blade is mainly given by the increase of pressure ($P - P_0$) due to the confined flow. This value is estimated from Eq. (4). When $\mathcal{E} \ll 1$, we get $\frac{P - P_0}{l_w} = \frac{\tau}{e}$ where the tangential stress τ is given by $\tau = k(\frac{V}{e})^n$. The lift force scales thus as $F_{\text{lift}} \sim k(\frac{V}{e})^n \frac{l_w b}{e}$. This force is compensated by the rigidity of the blade, which induces a resisting force $F_{\text{blade}} \sim \frac{E^* I}{(L - l_w)^2}$ (denoting I the second moment of inertia of the blade). This scaling law is found by relying on the equations of elastica [17]. The part of the blade that is not covered by the liquid is in the air. In this situation (i.e., for s between 0 and $L - l_w$), the shape of the blade is given by the following two equations:

$$\frac{d\Gamma}{ds} = (\vec{F} \times \vec{t}) \cdot \vec{u}_z, \quad (5)$$

$$\frac{d\vec{F}}{ds} = 0, \quad (6)$$

where \vec{F} and Γ are respectively the force and the projection of the torque on \vec{u}_z exerted at a point of the blade by the portion of the blade located “on its right,” \vec{t} is the vector tangent to the surface, and \vec{u}_z the vector along the width of the blade. This leads to $E \frac{d^2\theta}{ds^2} = F_{\text{blade}}$ where θ is the angle between the downward vertical and the tangential vector to the blade. If l_w is less than L , then we can estimate $\frac{d^2\theta}{ds^2} = \frac{0 - \frac{\pi}{2}}{(L - l_w)^2}$ as θ goes to $\frac{\pi}{2}$ when s goes to L . If l_w is close to L , then we get $\frac{d^2\theta}{ds^2} = \frac{-\theta}{(L - l_w)^2}$, which differs from the last case as θ goes to 0 when s goes to 0. This point explains why our expression is valid only for l_w less than L and gives $F_{\text{blade}} \sim \frac{E^* I}{(L - l_w)^2}$.

The balance between the two forces sets the film thickness e :

$$e \sim l_w \left\{ \left(1 - \frac{l_w}{L} \right)^2 \left[\frac{k \left(\frac{V}{l_w} \right)^n L^2 b l_w}{E^* I} \right] \right\}^{1/(n+1)}, \quad (7)$$

with the condition $\mathcal{E} \ll 1$, which correspond to $\frac{\alpha}{k} \left(\frac{V}{l_w} \right)^{\frac{m}{n+1}} \left(1 - \frac{l_w}{L} \right)^{\frac{2(1-m+n)}{n+1}} \left(\frac{k L^2 b l_w}{E^* I} \right)^{\frac{1-m+n}{n+1}} \ll 1$.

At first sight this equation is striking since it predicts that e vanishes when l_w goes to zero. We recall that the value of e cannot be deduced from this equation since it is not valid when l_w tends to L , i.e., in the case of an infinite reservoir. This comes from the calculation of the elastic force of the blade which is no longer valid.

For Newtonian fluids, i.e., for $n = 1$, Eq. (7) is similar to the scaling suggested by Krapez *et al.* [12]. In this previous work [12] we have checked the dependence of the scaling law on each of the variables for a Newtonian fluid. We have varied the velocity (four values between 2.5 and 10 mm/s) and the thickness of the blade (between 1 and 7 mN m) and the length of the blade (5.7 and 7 cm) and shown that all the data collapsed. Here we focus on the rheological properties of the fluid and study four non-Newtonian fluids with different rheological laws (the parameters are given in Table I). The effect of speed is analyzed on two different speeds. We anticipate that the wetting conditions and our experimental setup do not allow us to study respectively lower or higher speeds.

In Fig. 3, the scaling law is shown with a continuous line and compared with the experimental data, using the values of n and k extracted from the flow curves (Table I). The experimental data reported correspond to several different films (at least five experiments per concentration). The reported noise is the experimental noise. A prefactor of 0.06 is used for all the shear-thinning fluids and of 0.17 for silicone oil. For $l_w > 15$ mm, the scaling law fits well with the data: It reproduces

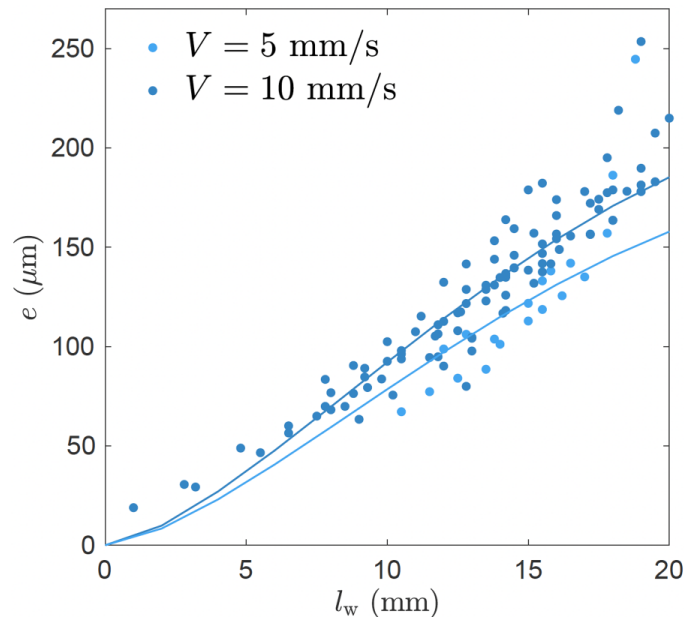


FIG. 4. Evolution of the fluid thickness e with the wetting length l_w for two different velocities and for a solutions of xanthan (and 0.9%). The continuous lines show the scaling law [Eq. (1)] with prefactors of 0.06 corresponding to the best fits.

in particular the dependency of e with l_w and the relative variations of e with the rheology of the fluids. The same agreement is found when the velocity is varied (see Fig. 4).

A sharp increase, however, is observed for large reservoir sizes, typically here for $l_w > 15$ mm that is not predicted by the model. To get a better understanding of this complex situation, we performed a full numerical computation of the experiment. The principle of the computation is detailed in the Appendix. Basically, the spreading dynamics are described using two sets of equations, coupled by boundary conditions at the tip of the blade. The first set of equations models the viscoelastic interaction between the blade and the fluid. It is resolved using Euler's elastica, where the bending torque of the blade is compensated for by the torque arising from the gradient of tangential stress in the lubricated layer of fluid below it. The capillary forces arising from the liquid surface deformation on the left and right parts of the wet area of the blade are included in the boundaries conditions for the pressure p . The second set of equations models the free liquid film at the blade exit. These equations correspond to the canonical Landau-Levich situation: They express the equilibrium between viscosity and surface tension, which sets the behavior of the spread film. The matching between these two sets of equations is done iteratively by imposing the continuity of the flow rate at the tip of the blade. In both sets of equations, the fluid is modelled within the lubrication approximation, taking into account the rheological properties describing the Newtonian or shear-thinning behavior. The values of η_0 , k , and n are taken from Table I. The results of the simulation are shown with dotted lines in Fig. 3. They match well the experimental data for all the fluids considered here and without any adjustable parameter. This confirms our dimensional analysis. Deviations are also observed for high values of l_w . We believe that this is due to a bad description of the shape of the back meniscus of the volume of fluid below the blade when l_w is large.

V. DISCUSSION

The simulations, in which the normal stress is neglected, confirm the very little role played by first normal stress in blade spreading experiments: In Fig. 3(b), the plots $e(l_w)$ are nicely reproduced for both xanthan and HPAM. The difference with other classical situations is striking. In general,

these stresses cause spectacular effects, such as a swelling of the fluid flowing out of a tube in extrusion processes, or the climbing of the fluid along rotating rods [18]. Here, contrary to most flows, the Weissenberg number is not the appropriate characteristic number to characterize the normal stress effects in spreading experiments, and a new number $\mathcal{E} = \frac{2}{3} \text{Wi} \frac{e}{l_w}$ has to be defined. In our experiment, even if the Weissenberg number is close to 10 in the 0.5% HPAM solution—which indicates that the first normal stress difference dominates over the shear stress— \mathcal{E} is of the order of 0.1 due to the geometrical factor $\frac{e}{l_w} \simeq 10^{-2}$. This explains why the effect of normal stresses is negligible in soft blade spreading. This geometrical factor is central to explain the difference with other experiments. For example, de Ryck *et al.* [14] evidence a very strong effect of the normal stresses when dip coating a fiber. They use a 1% PAA solution with properties similar to the 0.5% HPAM solution so that the Weissenberg number is also close to 10. However, in dip coating, the characteristic length scale in the x direction is an internal length $l \sim \sqrt{eb}$ with b the thickness of the fiber. In Ref. [14] the ratio e/l varies between 0.2 and 1 so that \mathcal{E} is always larger than 1. In our experiment, however, the presence of the blade imposes the wetting length l_w as the relevant horizontal length scale. Since $l_w \simeq 100e$, we cannot observe any effect of the normal stresses unless the Weissenberg number is larger than 100, a situation that cannot be obtained with the fluids used here and which will be difficult to achieve.

However, it is important to note that even if the normal stresses play no role here, the shear-thinning rheology of the fluids has a strong influence on blade coating. To evidence this point, we compare the spreading process of shear-thinning and Newtonian fluids, focusing on the work needed to spread the fluid and the film profile

First, it is necessary to carefully select the viscosity of the “equivalent” Newtonian fluid that is compared with a given shear-thinning solution. To do so, we do the following thought experiment: Starting with identical initial conditions (same initial amount of fluid below the blade; i.e., same l_{wi} , same spreading velocity V), it should take the same time t_d to spread a volume Ω_d of the equivalent Newtonian fluid than the shear-thinning fluid of interest. Indeed, if the mechanical properties of the blade are known, then, for a fixed V and l_{wi} , there is a bijective relation between the spreading time and the viscosity of the Newtonian fluid. Figure 5(a) illustrates the choice of the equivalent Newtonian fluid for the 0.9% xanthan solution. Using the simulations, we plot (with a continuous line) the time t_d necessary to spread a given volume Ω_d of xanthan. With dotted lines, we show the spreading time $t_d(\Omega_d)$ for four different Newtonian fluids, with viscosity $\eta = 150, 300, 500,$ and 1000 mPa s. As evidenced in Fig. 5(a), the equivalent Newtonian fluid has a viscosity $\eta = 300$ mPa s: It almost overlaps the xanthan curve and has an identical spreading time $t_d = 6$ s for $l_{wi} = 18$ mm and $\Omega_d = 0.40$ cm³.

To evaluate energy dissipation in blade spreading, we focus on work dissipated by the liquid during the spreading $W = \int_0^{t_d} FV dt$ and compare the 0.9% xanthan solution to its “equivalent” Newtonian solution. We denote here F the force exerted by the fluid on the surface (calculated by integrating the shear stress at the liquid/substrate interface in the x and z directions) and t_d the deposition time. The calculated work is negative. It corresponds to the work dissipated by the fluid. To spread the fluid, the experimenter needs to bring $-W$. Figure 5(b) shows the calculated value of W for the 0.9% xanthan solution, the equivalent Newtonian fluid ($\eta = 300$ mPa s), and four others (with viscosity $\eta = 50, 150, 500,$ and 1000 mPa s). We observe that the energy needed to spread the shear-thinning solution is typically 30% higher than its Newtonian equivalent (e.g., 34% for $\Omega_d = 0.40$ cm³). This result might seem counterintuitive: Indeed, in industrial applications, the addition of polymer to a product is often seen as a way to make the liquid easier to spread. We show here that the opposite happens: Shear-thinning fluids resist more to the spreading than an equivalent Newtonian fluid.

Note that in Fig. 5(b) the xanthan curve is superimposed on the curve of a Newtonian fluid of viscosity 150 mPa s. This means that the same amount of work is needed to spread an equivalent volume of xanthan and a fluid with viscosity 150 mPa s. However, the deposition time is longer for the fluid of viscosity 150 mPa s than with xanthan [Fig. 5(a)]. It is thus not a Newtonian equivalent in our definition, as opposed to 300 mPa s.

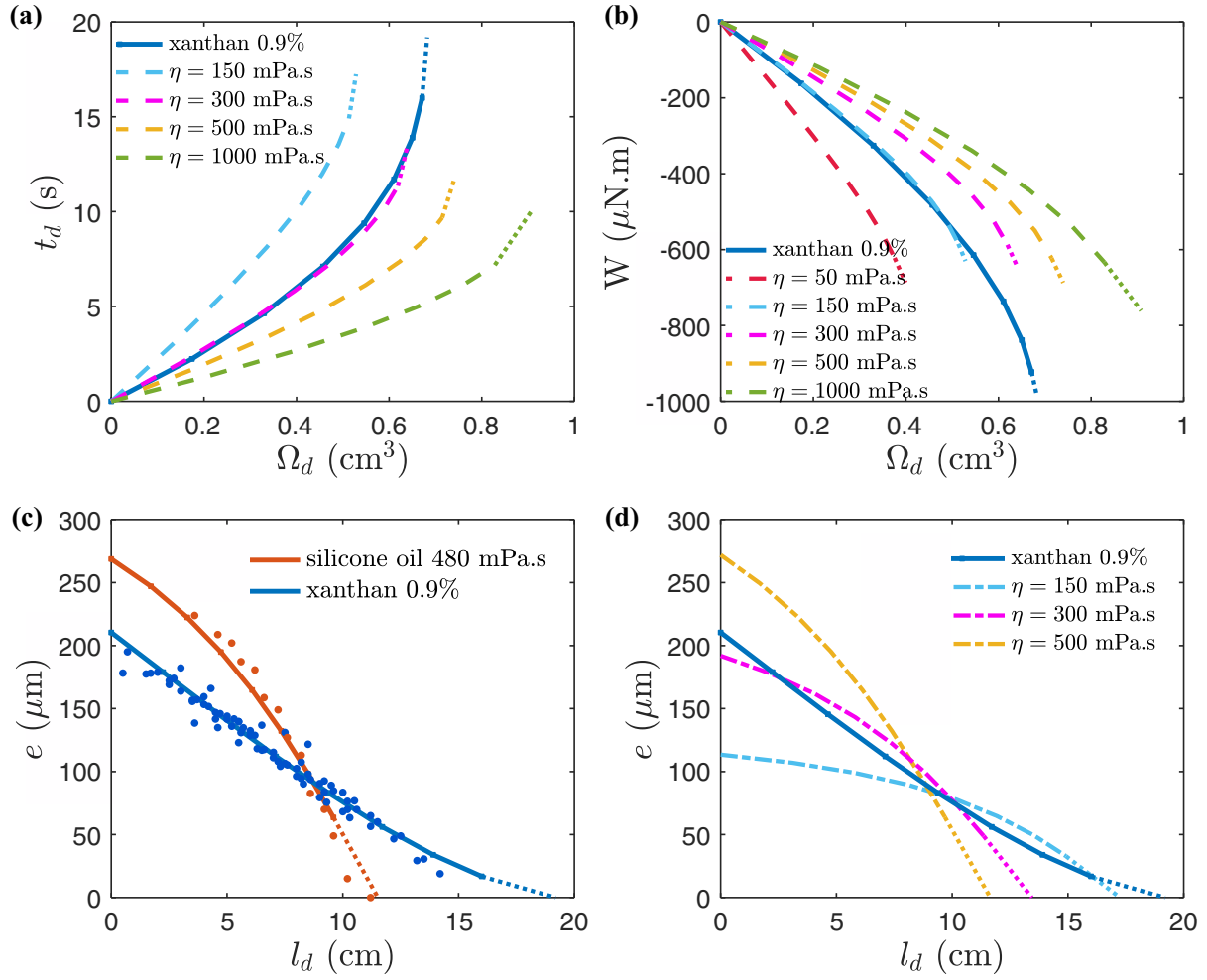


FIG. 5. (a) Deposition time t_d as a function of the deposited volume Ω_d for xanthan at 0.9% (dark blue) and Newtonian fluids with viscosity from top to bottom: 1000 mPa s (green), 500 mPa s (yellow), 300 mPa s (pink), and 150 mPa s (cyan). For $\Omega_0 = 0.40 \text{ cm}^3$, $t_d = 6 \text{ s}$ for the xanthan solution. (b) Work of the viscous forces during the spreading of volume Ω_d for the fluids of Fig. 5(a) and 50 mPa s (red). The xanthan fluid dissipates more energy than the Newtonian fluid at $\eta = 300 \text{ mPa s}$. (c) Evolution of the thickness of the deposit as a function of the deposited length for silicone oil of 480 mPa s (red) and xanthan at 0.9%. Dots are experiments, and lines computations without fitting parameters. The experiments are carried with a velocity equals 1 cm s^{-1} . (d) Shape of deposit for xanthan and Newtonian fluids of viscosity: 500, 300, and 150 mPa s.

Another property of the shear-thinning rheology is to change the profile of the deposited film. This is illustrated in Fig. 5(c), where the film thickness e is plotted as a function of the length l_d of the deposited film for two fluid categories. The dots correspond to the experimental data (in red, a Newtonian fluid, silicone oil with viscosity $\eta = 480 \text{ mPa s}$ and in blue a shear-thinning 0.9% xanthan solution). The lines show the result of the simulations. Note that the length of fluid deposited is only modeled in the steady state. To account for this phenomenon, an offset on l_d must be added to the experimental curves to compare the model and the data. In the Newtonian situation, the film thickness drops sharply to zero at the end of the film (when the reservoir is almost empty), here for $l_d = 7, 5 \text{ cm}$. However, for shear-thinning fluids, the deposited thickness generally decreases more slowly and continuously from the beginning of the process to the end. This experimental observation is confirmed by the simulations shown in Fig. 5(d): The shear-thinning solution (xanthan, in blue) thins out almost linearly, in contrast to its Newtonian equivalent ($\eta = 300 \text{ mPa s}$). Spreading a shear-thinning fluid results in a more regular and longer film.

VI. CONCLUSION

As mentioned in the Introduction, we study in this work the spreading of complex fluids by a flexible blade and we focus on the case where the volume of liquid is finite. This case is found in particular during the spreading of a paint by a pin or of glue with a flexible squeegee or glue with a flexible squeegee. Most of the articles in the literature [8,13,19–26] concern studies where the liquid reservoir is infinite and we are not aware of published data in the situation of a finite reservoir. We have therefore developed an experimental approach to compare numerical simulations, scaling laws, and experiments. By combining experiments with a judicious choice of fluids, and numerical and scaling law models, we give a better understanding of the spreading dynamics of non-Newtonian fluids. In particular, we show that the thickness of the deposit can be predicted as a function of the rheological features of the fluid. Interestingly, we evidence that shear-thinning fluids require more work to be spread than Newtonian fluids but that the deposit thins out more regularly. These results will be valuable in applications, for example to determine whether a polymer needs to be added to a product or to choose the polymer depending on the expected effect: a thicker or a more regular film or a fluid that is more easy to spread.

Interestingly, we also show that normal stresses play only a small role in the spreading process by a soft blade even if the Weissenberg number is of the order of 10. This implies that the analogy that is often made between soft blade coating and dip coating [8–11] is not valid when the reservoir is infinite. Both processes do not involve the same characteristic length scale: an externally imposed length in blade coating (the wetting length l_w) versus an internal length (the meniscus deformation) in dip coating.

APPENDIX: NUMERICAL SOLUTION OF THE ELASTOHYDRODYNAMIC EQUATIONS

We present in this section the equations used to calculate numerically the blade shape and the flow in a soft blade coating experiment. The general principle is the same as in our previous work [12] but here for a shear-thinning fluid. In particular, the shear-rate dependency of the viscosity implies a different set of equations to describe the fluid contribution (the lubrication pressure and the viscous drag force). The shear-thinning fluid is modelled as in Eq. (1) of the main part of the manuscript: Its viscosity is constant at low shear, and it follows a power law at high shear.

The blade and fluid are described using two sets of equations. The first set, called the “blade equations” [Eqs. (A14), (A17), (A19), (A20), and (A24)], describes the interaction between the elastic blade and the hydrodynamic forces arising from the fluid sheared below it. The second set, the “free surface equations” [Eqs. (A29) and (A31)], describes the free film after the tip of the blade. Finally, we detail the numerical resolution method. Its originality is to rely on an analogy between the hydroelastic equations and the stationary heat transfer equation to solve the problem.

1. Blade equations

We consider in this part the interaction between the blade and the liquid. As shown in supplementary Fig. 6(a), we consider an elastic blade submitted to nonuniformly distributed forces, due to the presence of the shear-thinning liquid below. Since the Reynolds number $Re = \rho eV/\eta < 10^{-1}$ in the flow is small and since the mean angle between the tip of the blade and the substrate is of a few degrees, we consider that the fluid flow corresponds to a simple Stokes flow in the lubrication approximation. In particular, any elongational component of the flow is neglected.

When the blade is in motion, the fluid flow induces two forces that are distributed nonuniformly along the part of the blade wet by the liquid. We distinguish here a lift force (perpendicular to the blade), due to the lubrication pressure p , and a viscous force f_v (tangent to the surface) arising from the no-slip boundary condition. In addition, we consider the effect of surface tension forces which are tangent to the meniscus at the positions $s = s_w$ and L . As discussed with Newtonian fluids [12], these local forces have a very small impact on the film deposition (the order of magnitude of torque from local capillary forces is 0.1% of the torque resulting from the lubrication pressure). However,

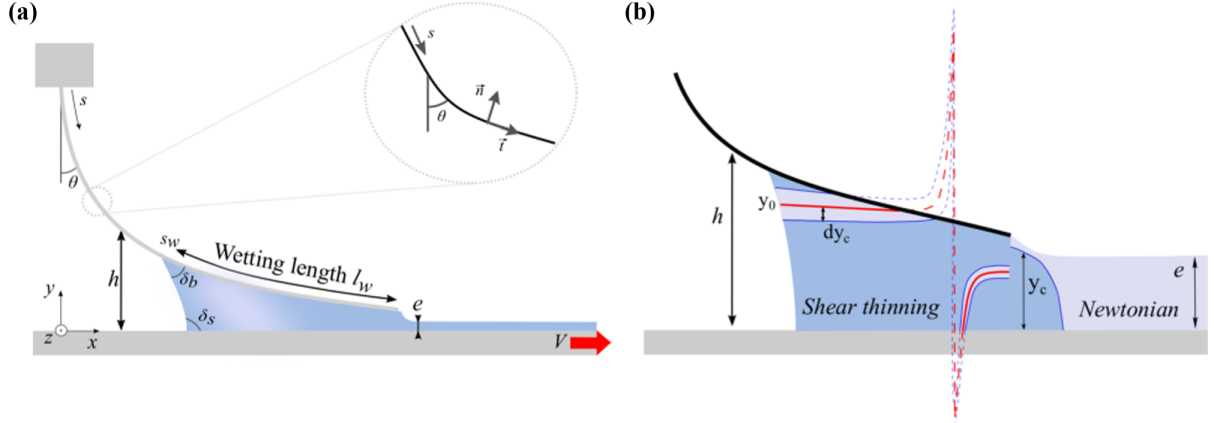


FIG. 6. (a) Soft blade coating experimental setup, notations, and axes convention. (b) Schematic representation of the Newtonian and shear-thinning areas in the liquid.

we still consider the contribution of the Laplace pressure arising from the curvature of the interfaces at $s = s_w$ and $s = L$, which acts as a boundary condition on the lubrication pressure p .

To model the shape of the blade, we use the curvilinear length s along the blade, with $s = 0$ the clamping position and $s = L$ the free edge. The blade is modelled as a large deflection problem, where the normal \vec{n} and tangent \vec{t} vectors [as defined in Fig. 6(a)] both depend on s . We solve the beam equation following a classical method [27]. We consider the variation of the internal torque Γ of the blade with s , which depends on the sum of all the forces exerted on the right of the point of interest s .

By taking into account the lubrication, viscous forces, and capillary forces, the total external force $F(s)$ acting on the right of s on the blade is

$$\vec{F}(s) = \int_s^L [p(s')\vec{n}(s') + f_v(s')\vec{t}(s')]b ds' + \vec{F}_c, \quad (\text{A1})$$

where b is the width of the blade and F_c is the capillary force.

Calculation of the forces

Fluid pressure. We model the flow below the blade as a steady flow in the lubrication approximation. We neglect the effect of a potential recirculation near s_w , as well as the first and second normal stress difference. Within this frame, the fluid pressure does not vary with y , and gravity is neglected. The flow equation reads:

$$\frac{\partial \tau}{\partial y} = \frac{\partial P}{\partial x}. \quad (\text{A2})$$

To model the shear-thinning fluid, we use the following equations:

$$\tau = \begin{cases} \eta_0 \dot{\gamma} & \text{for } \dot{\gamma} < \dot{\gamma}_c \\ k |\dot{\gamma}|^{n-1} \dot{\gamma} & \text{for } \dot{\gamma} > \dot{\gamma}_c \end{cases}. \quad (\text{A3})$$

Depending on the local shear rate in the flow, the liquid behaves as a Newtonian fluid (when $|\dot{\gamma}| < |\dot{\gamma}_c|$) or as a power-law fluid (when $|\dot{\gamma}| > |\dot{\gamma}_c|$), as evidenced in supplementary Fig. 6(b). In addition, we have to take into account that $\dot{\gamma}$ and the pressure gradient can be negative in some parts of the liquid, and that the power-law index n is inferior to 1. Thus, several cases have to be considered at the same time.

To determine the fluid equations, we define y_0 such as $\tau(y_0) = 0$, which marks the separation between positive and negative shear rate. The vertical asymptote observed in y_0 corresponds to the position of the maximum fluid pressure which implies a constant shear stress over y . The integration

of Eq. (A2) over y gives:

$$\tau = \frac{\partial P}{\partial x}(y - y_0). \quad (\text{A4})$$

To calculate the pressure in the reservoir we consider the continuity of the shear rates at the limit between the shear-thinning and Newtonian regions. We define dy_c the half width of the area where the shear rate is below $\dot{\gamma}_c$ and the shear stress is expressed as Newtonian [Fig. 6(b)]. The Newtonian region is symmetrical around the y_0 limit as expected from the Stokes equation. We obtain:

$$\frac{\partial P}{\partial x} \frac{dy_c}{\eta_0} = \left\langle \frac{\partial P}{\partial x} \frac{dy_c}{k} \right\rangle^{1/n}. \quad (\text{A5})$$

Note that the notation $\langle x \rangle^a = \text{sgn}(x)|x|^a$ is used in the equations.

Rewriting this equation gives an expression for the pressure gradient, but the sign still needs to be determined:

$$\frac{\partial P}{\partial x} = \text{sgn}\left(\frac{\partial P}{\partial x}\right) \frac{1}{dy_c} \frac{\eta_0^{\frac{n}{n-1}}}{k^{\frac{1}{n-1}}}. \quad (\text{A6})$$

To calculate dy_c , we use Eq. (A3) (expressed as a function of the velocity, by using $\dot{\gamma} = \frac{dv}{dy}$) and combine it with Eq. (A4). The shear rate is then integrated over y with no-slip boundary conditions at the moving plate [$v(0) = V$] and at the blade [$v(h) = 0$]. At the position $y = y_0 \pm dy_c$ we use the continuity of the velocity. Finally, we obtain a set of equations describing the velocity in the different part of the fluid and the flow rate q is calculated by integrating v over y . A general equation for the linear flow rate is obtained as follows:

$$q = Vy_0 - \frac{1}{3\eta_0} \left\langle \frac{\partial P}{\partial x} \right\rangle (\text{sgn}(y_0) \min(|y_0|, dy_c)^3 + \text{sgn}(h - y_0) \min(|h - y_0|, dy_c)^3) + \left\langle \frac{1}{k} \frac{\partial P}{\partial x} \right\rangle^{1/n} \times \left[\frac{-\langle y_0 \rangle^{1/n+2} - \langle h - y_0 \rangle^{1/n+2} + \text{sgn}(y_0) \min(|y_0|, dy_c)^{1/n+2} + \text{sgn}(h - y_0) \min(|h - y_0|, dy_c)^{1/n+2}}{1/n+2} \right]. \quad (\text{A7})$$

The sign of $\frac{\partial P}{\partial x}$ is the same as $Vy_0 - q$ [result obtained from Eq. (A7)] which gives:

$$\frac{\partial P}{\partial x} = \text{sgn}(Vy_0 - q) \frac{1}{dy_c} \frac{\eta_0^{\frac{n}{n-1}}}{k^{\frac{1}{n-1}}}. \quad (\text{A8})$$

By writing the condition of velocity continuity at y_0 we obtain another equation:

$$0 = V - \frac{1}{2\eta_0} \left\langle \frac{\partial P}{\partial x} \right\rangle [\min(|y_0|, dy_c)^2 - \min(|h - y_0|, dy_c)^2] - \left\langle \frac{1}{k} \frac{\partial P}{\partial x} \right\rangle^{1/n} \left[\frac{\max(|y_0|, dy_c)^{1/n+1} - \max(|h - y_0|, dy_c)^{1/n+1}}{1/n + 1} \right]. \quad (\text{A9})$$

By injecting Eq. (A8) into Eqs. (A7) and (A9) we obtain two equations that are used to calculate y_0 and dy_c for a given flow rate, q , and blade shape, h . The derivative along the curvilinear abscissa, obtained using the relation $\frac{dp}{ds} = \frac{dP}{dx} \sin \theta$, and integrated between s_w and s gives the fluid pressure p , defined as the pressure relative to the atmospheric pressure, $p = P - P_{\text{atm}}$:

$$p(s) = \int_{s_w}^s \frac{\partial p}{\partial x} \sin \theta ds = \int_{s_w}^s \text{sgn}(Vy_0 - q) \frac{1}{dy_c} \frac{\eta_0^{\frac{n}{n-1}}}{k^{\frac{1}{n-1}}} \sin \theta(s') ds' + p_{\text{sw}}, \quad (\text{A10})$$

with p_{sw} the Laplace pressure arising from the presence of a meniscus at $s = s_w$. To obtain an expression of p_{sw} , we model the meniscus by a circular arc which radius of curvature R is determined

from the wetting angles δ_s and δ_b :

$$p_{sw} = \frac{\gamma}{R} = -\frac{\cos[\delta_b + \pi/2 - \theta(sc)] + \cos\delta_s}{h} \gamma. \quad (\text{A11})$$

Contrary to what can be done for Newtonian fluids, it is not possible to use the value of the pressure at the position $s = L$ to obtain an explicit equation of the flow rate $q = f(h, \theta, p_L, p_{sc}, V, b, s_w)$. Here the problem is highly nonlinear, so we use solvers to find a value of q , y_0 , and dy_c . Once injected in Eq. (A10) at the position $s = L$, they give a pressure at the blade tip approximately equal to its guess p_L .

Finally, the pressure at $s = L$ is determined by considering the pressure at $x = +\infty$ fixed to $P_{atm} = 0$ and using this condition to solve the shape of the liquid surface after the blade (see Sec. 4 of the Appendix).

Viscous stress. The viscous stress f_v , exerted by the fluid on the blade, is defined as:

$$f_v = -\tau(h) = -\frac{\partial P}{\partial x}(h - yo), \quad (\text{A12})$$

which we now write, using Eq. (A8), as f_v :

$$f_v = -\text{sgn}(Vy_0 - q) \frac{1}{dy_c} \frac{\eta_0^{\frac{n}{n-1}}}{k^{\frac{1}{n-1}}}(h - yo). \quad (\text{A13})$$

Capillary forces. The capillary forces are expressed as:

$$\vec{F}_c = \gamma b \vec{e}_\gamma, \quad (\text{A14})$$

with \vec{e}_γ the vector tangent to the free liquid surface at the triple line position.

2. Simplification: Pure shear-thinning fluid under the blade

We observed numerically that taking into account the Newtonian area under the blade has a very limited impact on the results: The pressure profile only differs by less than $10^{-3}\%$ between a simple power-law fluid and the fluid described by Eq. (A3) (with a Newtonian viscosity plateau at low shear). Thus, we used the hypothesis of pure shear-thinning behavior under the blade to speed up the computation. With this simplification, Eq. (A7) becomes

$$q = Vy_0 - \left\langle \frac{1}{k} \frac{\partial P}{\partial x} \right\rangle^{1/n} \left[\frac{\langle yo \rangle^{1/n+2} + \langle h - yo \rangle^{1/n+2}}{1/n + 2} \right]. \quad (\text{A15})$$

The velocity continuity at y_0 gives:

$$V(1/n + 1) = \left\langle \frac{1}{k} \frac{\partial P}{\partial x} \right\rangle^{1/n} (|yo|^{1/n+1} - |h - yo|^{1/n+1}). \quad (\text{A16})$$

By combining Eqs. (A16) and (A15) we obtain a new equation of the flow rate that depends only on y_0 and h :

$$q = V \left[yo - \frac{1/n + 1}{1/n + 2} \left(\frac{\langle yo \rangle^{1/n+2} + \langle h - yo \rangle^{1/n+2}}{|yo|^{1/n+1} - |h - yo|^{1/n+1}} \right) \right]. \quad (\text{A17})$$

We can express the pressure derivative from Eq. (A15):

$$\frac{\partial P}{\partial x} = k \left\langle \frac{(Vy_0 - q)(1/n + 2)}{\langle yo \rangle^{1/n+2} + \langle h - yo \rangle^{1/n+2}} \right\rangle^n, \quad (\text{A18})$$

$$p(s) = \int_{sc}^L k \left\langle \frac{(Vy_0 - q)(1/n + 2)}{\langle yo \rangle^{1/n+2} + \langle h - yo \rangle^{1/n+2}} \right\rangle^n \sin \theta ds + p_{sw}. \quad (\text{A19})$$

The viscous stress f_v becomes

$$f_v = -k \left\langle \frac{(Vyo - q)(1/n + 2)}{\langle yo \rangle^{1/n+2} + \langle h - yo \rangle^{1/n+2}} \right\rangle^n (h - yo). \quad (\text{A20})$$

3. Torque balance

To solve the blade shape in the large deflection problem, a first step is the calculation of the total external torque $\Gamma(s)$ applied by the fluid on the blade. It corresponds to the sum of all elementary torques applied by the fluid (due to the lubrication force, viscous stress and capillarity) between the working position s and the tip of the blade L . To do so, we need to project the blade angle θ (as defined in Fig. 6) on the x and y axis:

$$\Gamma(s) = b \int_s^L S\vec{S}' \wedge [p\vec{s}' + f_v\vec{s}'] ds' \cdot \vec{u}_z + S\vec{L} \wedge \vec{F}_c \cdot \vec{u}_z \quad (+S\vec{S}_w \wedge \vec{F}_c \cdot \vec{u}_z \text{ if } s < s_w), \quad (\text{A21})$$

$$\begin{aligned} &= b \int_s^L [p[(x(s') - x(s)) \sin \theta(s') - (y(s') - y(s)) \cos \theta(s')] - f_v[(x(s') - x(s)) \cos \theta(s') \\ &\quad + (y(s') - y(s)) \sin \theta(s')]] ds' - F_c[(x_L - x(s)) \cos \theta_{mL} + (y_L - y(s)) \sin \theta_{mL} \\ &\quad + (x_{sw} - x(s)) \cos \theta_{msw} + (y_{sw} - y(s)) \sin \theta_{msw}]. \end{aligned} \quad (\text{A22})$$

θ_{msw} and θ_{mL} are the angles of the tangent of the meniscus with respect to the y axis at the positions $s = s_w$ and $s = L$ respectively.

Since the blade is in an equilibrium position, Euler's elastica implies that the torque produced by the internal stress $E^*I \frac{d\theta}{ds}$ is equal to the total torque $\Gamma(s)$ produced by external forces. Now we write:

$$\Gamma(s) = -E^*I \frac{d\theta}{ds}. \quad (\text{A23})$$

Combining Eqs. (A22) and (A23) gives:

$$\begin{aligned} \frac{d^2\theta}{ds^2} &= \frac{b}{E^*I} \int_s^L [-p \cos(\theta(s) - \theta(s')) + f_v \sin(\theta(s) - \theta(s'))] ds' \\ &\quad + F_c [\sin(\theta(s) - \theta_{mL}) + \sin(\theta(s) - \theta_{msw})]. \end{aligned} \quad (\text{A24})$$

We finally obtain the equation describing the shape of the blade $\theta(s)$ by replacing p , f_v , and F_c by their expressions [Eq. (A19), (A20), and (A14) respectively].

4. Free surface equations

In a second part, we define a second set of equations to calculate the thickness, shape, and flow in the free liquid film in the 0.8 cm after the tip of the blade. This interval is chosen to be sufficiently large so that the atmospheric pressure is eventually reached into the fluid $p(x = \infty) = 0$. The equations that govern the shape of the free surface are given below and follow an approach discussed by Trinh *et al.* [28]. To distinguish the variables of the free surface from those of the blade we use an index l .

The lubrication equation [Eq. (A2)] is integrated with the boundary condition $\tau(0) = 0$ (no tangential stress on the free surface), which give:

$$\tau = \frac{\partial p}{\partial x}(y - h_l). \quad (\text{A25})$$

Again, we have to consider separately two regions, in which the fluid behaves either as a Newtonian fluid (at low shear rate) or as a power-law liquid (at high shear rate). We define, as before, the boundary between these two regions y_c . Since most of the liquid in the free film is at

rest (with $\dot{\gamma} = 0$), it is particularly important to take into account the Newtonian plateau in the rheological law, contrary to what is done below the blade.

The shear rate equality at y_c gives an expression for the derivative of p :

$$\frac{\partial p}{\partial x} = \operatorname{sgn}\left(\frac{\partial p}{\partial x}\right) \frac{1}{h_l - y_c} \frac{\eta_0^{\frac{n}{n-1}}}{k^{\frac{1}{n-1}}}. \quad (\text{A26})$$

To determine y_c , the no-slip boundary condition on the substrate [$v(0) = V$] and the velocity continuity at y_c are used to obtain the expressions of the velocity in both regions. The integration gives the flow rate:

$$q_l = V h_l - \frac{1}{3\eta_0} \frac{\partial p}{\partial x} (h_l - y_c)^3 + \left\langle \frac{1}{k} \frac{\partial p}{\partial x} \right\rangle^{1/n} \frac{(h_l - y_c)^{1/n+2} - h_l^{1/n+2}}{(1/n + 2)}. \quad (\text{A27})$$

From this equation it can be shown that the sign of $\frac{\partial p}{\partial x}$ is equivalent to the sign of $V h_l - q_l$. This results leads to a new expression for the pressure derivative:

$$\frac{\partial p}{\partial x} = \operatorname{sgn}(V h_l - q_l) \frac{1}{h_l - y_c} \frac{\eta_0^{\frac{n}{n-1}}}{k^{\frac{1}{n-1}}}. \quad (\text{A28})$$

The equation describing the flow rate [Eq. (A27)] can be rewritten only as a function of the variables h_l and y_c by using Eq. (A28):

$$q_l = V h_l - \operatorname{sgn}(V h_l - q_l) \left(\frac{\eta_0}{k}\right)^{\frac{1}{n-1}} \left[\frac{1}{3} (h_l - y_c)^2 + \frac{1}{(h_l - y_c)^{1/n}} \frac{(h_l - y_c)^{1/n+2} - h_l^{1/n+2}}{(1/n + 2)} \right]. \quad (\text{A29})$$

Since the liquid is incompressible, the flow rate q_l is equal to the flow rate q below the blade. Thus, we use in the numerical resolution of the equations that at $x = \infty$, $q = V h_l(\infty) = V e$.

The pressure p in the liquid at the end of the blade is set by the Laplace pressure within the meniscus, which gives a second expression for p :

$$p = -\gamma \frac{d\theta}{ds}. \quad (\text{A30})$$

By combining Eqs. (A30) and (A28), and using the relation between the derivatives with respect to s and x , we finally obtain:

$$\frac{d^2\theta}{ds^2} + \operatorname{sgn}(V h_l - q_l) \frac{1}{h_l - y_c} \frac{\eta_0^{\frac{n}{n-1}}}{\gamma k^{\frac{1}{n-1}}} \sin(\theta) = 0. \quad (\text{A31})$$

This equation governs the shape of the free surface of the deposited layer of fluid behind the blade. To accelerate of the convergence, the equivalent equation for pure Newtonian fluid is used at s where $y_c = 0$:

$$\frac{d^2\theta}{ds^2} + \frac{3\eta_0}{\gamma} \left(\frac{V h_l - q_l}{h_l^3} \right) \sin \theta_l(s) = 0. \quad (\text{A32})$$

5. Numerical method

The numerical method used to solve the two sets of equations governing the blade shape and fluid flow is the same as in Ref. [12]. We summarize here what was done.

It is important to notice first that the equations governing the shape of the blade [Eq. (A24)] and the free surface [Eq. (A31)] have the same structure. They can both be written as:

$$\frac{d^2\theta}{ds^2} = -S(s, \theta(s)). \quad (\text{A33})$$

where $-S$ is the right member of Eqs. (A24) and (A31). Interestingly, Eq. (A33) can be seen as a one-dimensional steady-state nonlinear heat equation, where θ is equivalent to temperature and S is a heat source distribution, depending on both s and θ . The heat conductivity is here equal to 1. Following this analogy, we thus solve Eqs. (A24) and (A31) by referring to the transient heat equation [Eq. (A34)], where we add the derivative of θ versus a virtual time t_v , $\frac{\partial\theta}{\partial t_v}$ and a volumetric heat capacity equal to 1,

$$\frac{\partial\theta}{\partial t_v} = \frac{\partial^2\theta}{\partial s^2} + S(s). \quad (\text{A34})$$

The boundary conditions depend on the solved set of equations:

(i) for the hydroelastic equations (the blade and the fluid below) the fixed mounting imposes $\theta(0) = 0$. In addition, since there is no torque at the end of the blade, we also have $\frac{\partial\theta}{\partial s}|_L = 0$.

(ii) for the free surface equations, since the fluid deposited is horizontal far from the tip of the blade (at $x = \infty$), we have $\theta_l(\infty) = \pi/2$. In addition, the Laplace pressure equation written at L imposes: $\frac{\partial\theta_l}{\partial s}|_L = -\frac{p_L}{\gamma}$.

Finally, the matching of the two solutions of Eqs. (A24) (for the blade) and (A31) (for the free film) is done by imposing a continuity of the flow rate q at $x = L$, as well as of the liquid height: $h(x = L) = h_l(x = L)$.

6. Resolution method

The transient heat equation [Eq. (A34)] is solved numerically by finite differences, which gives the asymptotic stationary solution. We start from an initial guess of the shape $\theta(s)$ of the blade. This initial shape is obtained through a rough calculation for a Newtonian fluid (that satisfies the initial guess of the pressure p_L), using the equations of our previous work [12]. The viscosity of this fluid is $\eta = 478$ mPa s and, to facilitate the following calculations, it has the same wetting properties (surface tension, contact angles, and pressure p_{sw}) as the shear-thinning fluid that is studied afterwards.

We chose an implicit-explicit scheme [29,30] as a compromise between stability and computing time. Thus, the source term S is defined explicitly, while θ is not,

$$\frac{\theta_i^{n+1} - \theta_i^n}{\Delta t_v} = \frac{\theta_{i-1}^{n+1} - 2\theta_i^{n+1} + \theta_{i+1}^{n+1}}{\Delta s^2} + S(s, \theta^n), \quad (\text{A35})$$

where $\theta_i^n \approx \theta(i\Delta s, n\Delta t_v)$.

According to the Lax equivalence theorem [31], this scheme is stable and converges to the stationary solution, when it exists. Usually, the timestep Δt_v follows the condition $\Delta t_v < \Delta t_v^{\text{lim}}/2$, where $\Delta t_v^{\text{lim}} = \frac{\Delta s^2}{E^*I}$ and Δs is the size of a cell. However, in most simulations, the model converges nicely so that we can accelerate the calculation, and use instead $\Delta t_v = 20 \Delta t_v^{\text{lim}}$. For the spatial discretization of the blade equations, we chose to set $\Delta s \in [0.1, 0.5]$ mm. The spacing is nonuniform for the free surface calculation: We increase exponentially the size of the cell from the meniscus area to the “end” of the free film, with Δs increasing from 10^{-5} to 10^{-1} mm.

7. Convergence criteria

For shear-thinning fluids the equation of the flow rate under the blade [Eq. (A17)] requires an additional convergence criteria compared to what is necessary for a Newtonian fluid. Thus, the convergence of the numerical simulation is achieved when three conditions are simultaneously met:

(1) The steady state is reached for the transient heat equation [Eq. (A34)] which provides the solution for the governing equations of the shape of the blade [Eq. (A24)] or the free surface [Eq. (A31)].

(2) The two flow rates, calculated from the blade equations [Eq. (A17)] and from the free film equation [where $q = Vbh_l(\infty)$] equalize (because of flow conservation).

(3) The pressure at L calculated through Eq. (A19) matches the guess value of p_L .

8. Coupling of the blade and free surface calculation

In the resolution process, a given input is the wetting length l_w , which implies that e and l_w both vary quasistatically with time. A new simulation is thus necessary to determine e for each value of l_w . The other inputs are the wetting angles at the position s_w , δ_s , and δ_b (see Fig. 6), whose values are measured experimentally. It is also necessary to make an initial guess of the shape of the blade $\theta(s)$ and of the free surface $\theta_l(s)$ and provide a first estimate of the value of the pressure at the tip of the blade, p_L , as well as the meniscus angle at this position, θ_{mL} . As stated before, the initial guess of $\theta(s)$ is obtained from a rough calculation of the blade shape with a Newtonian fluid, without taking into account the free surface. The shape of free surface is initially modelled as an hyperbolic tangent (to reproduce the meniscus shape). These guesses are used in the computation of the transient heat equations [Eq. (A24)] and [Eq. (A31)], where each step gives an updated $\theta(s)$, $\theta_l(s)$, and $\theta_{mL} = \theta_l(L)$. The arbitrary value of p_L is adjusted through a corrective factor extracted from the difference between the two values of flow rates, q and q_l . This process is iterated until the flow rates can be considered equal, usually within 10^{-4} , leading to the “correct” value of p_L . The fluid thickness e is finally extracted from the height of the deposited fluid for $x \rightarrow \infty$.

-
- [1] Y. Lu, R. Ganguli, C. Drewien *et al.*, Continuous formation of supported cubic and hexagonal mesoporous films by sol–gel dip-coating, *Nature* **389**, 364 (1997).
 - [2] Y. Diao, B. K. Tee, G. Giri *et al.*, Solution coating of large-area organic semiconductor thin films with aligned single-crystalline domains, *Nat. Mater.* **12**, 665 (2013).
 - [3] A. Lee, P. T. Brun, J. Marthelot *et al.*, Fabrication of slender elastic shells by the coating of curved surfaces, *Nat. Commun.* **7**, 11155 (2016).
 - [4] S. Chu, W. Chen, Z. Fang *et al.*, Large-area and efficient perovskite light-emitting diodes via low-temperature blade-coating, *Nat. Commun.* **12**, 147 (2021).
 - [5] S. J. Weinstein and K. J. Ruschak, Coating flows, *Annu. Rev. Fluid Mech.* **36**, 29 (2004).
 - [6] B. Derjaguin, Thickness of liquid layer adhering to walls of vessels on their emptying and the theory of photo-and motion-picture film coating, *Dokl. Acad. Sci. USSR* **39**, 13 (1943).
 - [7] L. Landau and B. Levich, Dragging of a liquid by a moving plate, in *Dynamics of Curved Fronts* (Elsevier, Amsterdam, 1988), pp. 141–153.
 - [8] J. Seiwert, D. Quéré, and C. Clanet, Flexible scraping of viscous fluids, *J. Fluid Mech.* **715**, 424 (2013).
 - [9] J. H. Snoeijer, Analogies between elastic and capillary interfaces, *Phys. Rev. Fluids* **1**, 060506 (2016).
 - [10] K. Warburton, D. R. Hewitt, and J. A. Neufeld, The elastic landau–levich problem on a slope, *J. Fluid Mech.* **883**, A40 (2020).
 - [11] H. N. Dixit and G. M. Homsy, The elastic landau–levich problem, *J. Fluid Mech.* **732**, 5 (2013).
 - [12] M. Krapez, A. Gauthier, H. Kellay, J. B. Boitte, O. Aubrun, J. F. Joanny, and A. Colin, Impact of the Wetting Length on Flexible Blade Spreading, *Phys. Rev. Lett.* **125**, 254506 (2020).
 - [13] A. Deblais, R. Harich, A. Colin, and H. Kellay, Taming contact line instability for pattern formation, *Nat. Commun.* **7**, 12458 (2016).
 - [14] A. de Ryck and D. Quéré, Fluid coating from a polymer solution, *Langmuir* **14**, 1911 (1998).
 - [15] L. Mahadevan and J. B. Keller, Periodic folding of thin sheets, *SIAM Rev.* **41**, 115 (1999).
 - [16] J. Ashmore, A. Q. Shen, H. P. Kavehpour, H. A. Stone, and G. H. McKinley, Coating flows of non-newtonian fluids: weakly and strongly elastic limits, *J. Eng. Math.* **60**, 17 (2008).
 - [17] R. P. Feynman, R. B. Leighton, and M. Sands, The feynman lectures on physics; vol. i, *Am. J. Phys.* **33**, 750 (1965).
 - [18] R. B. Bird, R. C. Armstrong, and O. Hassager, *Dynamics of Polymeric Liquids, Vol. 1: Fluid Mechanics* (John Wiley and Sons Inc., New York, NY, 1987).
 - [19] T. Sullivan, S. Middleman, and R. Keunings, Use of a finite-element method to interpret rheological effects in blade coating, *AIChE J.* **33**, 2047 (1987).

- [20] A. B. Ross, S. K. Wilson, and B. R. Duffy, Blade coating of a power-law fluid, *Phys. Fluids* **11**, 958 (1999).
- [21] S. Bhatti, M. Zahid, R. Ali, A. Sarwar, and H. A. Wahab, Blade coating analysis of a viscoelastic carreau fluid using adomian decomposition method, *Math. Comput. Simul.* **190**, 659 (2021).
- [22] F. R. Pranckh and L. E. Scriven, Elastohydrodynamics of blade coating, *AIChE J.* **36**, 587 (1990).
- [23] A. E. Hosoi and L. Mahadevan, Peeling, Healing, and Bursting in a Lubricated Elastic Sheet, *Phys. Rev. Lett.* **93**, 137802 (2004).
- [24] P. H. Trinh, S. K. Wilson, and H. A. Stone, An elastic plate on a thin viscous film, [arXiv:1410.8558](https://arxiv.org/abs/1410.8558).
- [25] A. J. Giacomini, J. D. Cook, L. M. Johnson, and A. W. Mix, Flexible blade coating, *J. Coat. Technol. Res.* **9**, 269 (2012).
- [26] C. M. Corvalán and F. A. Saita, Blade coating on a compressible substrate, *Chem. Eng. Sci.* **50**, 1769 (1995).
- [27] S. P. Timoshenko and J. M. Gere, *Theory of Elastic Stability* (Courier Corporation, North Chelmsford, MA, 2009).
- [28] P. H. Trinh, S. K. Wilson, and H. A. Stone, An elastic plate on a thin viscous film, [arXiv:1410.8558](https://arxiv.org/abs/1410.8558).
- [29] G. D. Smith, *Numerical Solution of Partial Differential Equations: Finite Difference Methods* (Oxford University Press, Oxford, 1985).
- [30] S. J. Ruuth, Implicit-explicit methods for reaction-diffusion problems in pattern formation, *J. Math. Biol.* **34**, 148 (1995).
- [31] P. D. Lax and R. D. Richtmyer, Survey of the stability of linear finite difference equations, *Commun. Pure Appl. Math.* **9**, 267 (1956).

E. Expression of the velocity for soft blade coating of shear-thinning fluid

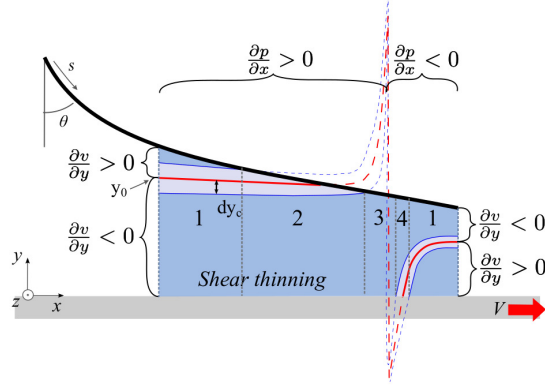


Fig. E.1 – Illustration of the different zones under the blade. Zone 1 corresponds to a Newtonian region between two shear thinning regions. In zone 3, the liquid can be described over its entire height with shear thinning equations. Zone 2 and 4 describe the presence of a Newtonian region above (zone 2) or below (zone 4) the shear thinning region. The sign of $\frac{\partial p}{\partial x}$ and $\frac{\partial v}{\partial y}$ changes depending on the position under the blade. The limit between the positive and negative region correspond to $y_0(x)$ for $\frac{\partial v}{\partial y}$ and the vertical asymptote in y_0 for $\frac{\partial p}{\partial x}$.

We distinguish four areas depending on the presence and the position of the Newtonian region (Fig. E.1). We note dy_c the difference between y_0 defined as $\tau(y_0) = 0$ and y_c defined as the boundary between the Newtonian and shear-thinning regime. Additionally the shear rate and pressure derivative change signs inside some of those zone which has to be taken into account when writing the corresponding equations.

Here is given an example of the set of equation describing the velocity field obtained from the integration of Equation 3.10 in the zone 1 (Newtonian region comprised between two shear-thinning regions). Using the no-slip boundary conditions at the moving plate $v(0) = V$, and at the blade $v(h) = 0$, and the velocity continuity at $y = y_0 - dy_c$ and $y = y_0 + dy_c$ we can write a set of equations describing the velocity at the different height y :

$$v(y) = \begin{cases} \left\langle \frac{1}{k} \frac{\partial p}{\partial x} \right\rangle^{1/n} \frac{(y_0 - y)^{1/n+1} - y_0^{1/n+1}}{1/n+1} + V & \text{for } y \in [0, y_0 - dy_c] \\ \frac{1}{2\eta_0} \frac{\partial p}{\partial x} ((y - y_0)^2 - dy_c^2) + \left\langle \frac{1}{k} \frac{\partial p}{\partial x} \right\rangle^{1/n} \frac{dy_c^{1/n+1} - y_0^{1/n+1}}{1/n+1} + V & \text{for } y \in [y_0 - dy_c, y_0] \\ \frac{1}{2\eta_0} \frac{\partial p}{\partial x} ((y - y_0)^2 - dy_c^2) + \left\langle \frac{1}{k} \frac{\partial p}{\partial x} \right\rangle^{1/n} \frac{dy_c^{1/n+1} - (h - y_0)^{1/n+1}}{1/n+1} & \text{for } y \in [y_0, y_0 + dy_c] \\ \left\langle \frac{1}{k} \frac{\partial p}{\partial x} \right\rangle^{1/n} \frac{(y - y_0)^{1/n+1} - (h - y_0)^{1/n+1}}{1/n+1} & \text{for } y \in [y_0 + dy_c, h] \end{cases} \quad (\text{E.1})$$

Writing the velocity continuity at $y = y_0$ gives Equation 3.15 in the main text, recalled here:

$$0 = V - \frac{1}{2\eta_0} \left\langle \frac{\partial P}{\partial x} \right\rangle \left(\min(|y_0|, dy_c)^2 - \min(|h - y_0|, dy_c)^2 \right) - \left\langle \frac{1}{k} \frac{\partial P}{\partial x} \right\rangle^{1/n} \left(\frac{\max(|y_0|, dy_c)^{1/n+1} - \max(|h - y_0|, dy_c)^{1/n+1}}{1/n + 1} \right)$$

The flow rate can be calculated in this domain by integrating the velocity equations from $y = 0$ to $y = h$. It can be written under a generalized equation that takes into account the sign change between the different regions:

$$q = Vy_0 - \frac{1}{3\eta_0} \left\langle \frac{\partial p}{\partial x} \right\rangle \left(\operatorname{sgn}(y_0) \min(|y_0|, dy_c)^3 + \operatorname{sgn}(h - y_0) \min(|h - y_0|, dy_c)^3 \right) + \left\langle \frac{1}{k} \frac{\partial p}{\partial x} \right\rangle^{1/n} \left(\frac{-\langle y_0 \rangle^{1/n+2} - \langle h - y_0 \rangle^{1/n+2} + \operatorname{sgn}(y_0) \min(|y_0|, dy_c)^{1/n+2} + \operatorname{sgn}(h - y_0) \min(|h - y_0|, dy_c)^{1/n+2}}{1/n + 2} \right)$$

This equation correspond to the Equation 3.14 presented in Chapter 3.

F. Determination of the position of the solid region under the blade for yield stress fluids coating

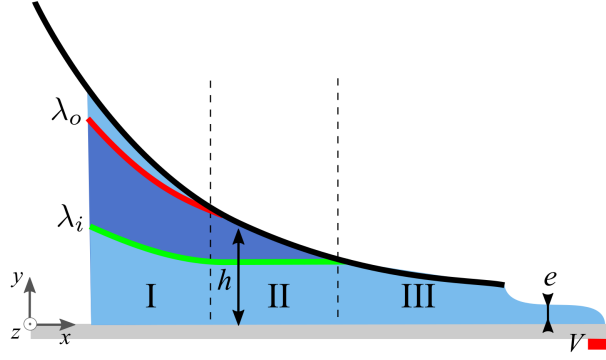


Fig. F.1 – Illustration of the different zones under the blade encountered when spreading a yield stress fluid. Zone I corresponds to a solid-like region ($|\tau| < \tau_y$) between two liquid regions. In zone III, the yield stress fluid can be described over its entire height as a liquid. Zone II describes the presence of a solid-like region above the liquid-like region. λ_i and λ_o are represented by green and red lines respectively.

In this appendix is presented the detailed calculation of λ_i and λ_o , the positions delimiting the solid-like and liquid-like regions of yield stress fluid in a soft blade coating experiment. This calculation was proposed by Kusina and coworkers [3]. The Stokes equation 3.8 is integrated under the same assumptions as for shear-thinning fluids (lubrication approximation and gravity neglected). Using λ_i and λ_o , defined by $\tau(\lambda_i) = -\tau_y$ and $\tau(\lambda_o) = \tau_y$, as the integration constant, it gives the stress field:

$$\tau = \frac{2\tau_y}{\lambda_o - \lambda_i} \left(z - \frac{\lambda_o + \lambda_i}{2} \right) \quad (\text{F.1})$$

where $\frac{\partial p}{\partial x} = \frac{-2\tau_y}{\lambda_i - \lambda_o}$. The shear rate can be expressed using the Herschel-Bulkley model:

$$\dot{\gamma} = \begin{cases} - \left(\frac{2\tau_y}{k} \right)^{1/n} \left(\frac{\lambda_i - y}{\lambda_o - \lambda_i} \right)^{1/n} & \text{for } y < \lambda_i \\ 0 & \text{for } y \in [\lambda_i, \lambda_o] \\ \left(\frac{2\tau_y}{k} \right)^{1/n} \left(\frac{y - \lambda_o}{\lambda_o - \lambda_i} \right)^{1/n} & \text{for } y > \lambda_o \end{cases} \quad (\text{F.2})$$

This expression of the shear rate is used to write the velocity at $y = 0$, using the boundary conditions $v(0) = V$ and $v(h) = 0$:

$$V = - \int_0^h \frac{\partial v}{\partial y} dy = - \int_0^h \dot{\gamma} dy \quad (\text{F.3})$$

The conservation of the flow rate under the blade, and in the deposited film, is expressed as a function of $\dot{\gamma}$ by performing an integration by part and using the fact that $[y\nu(y)]_0^h = 0$, which gives:

$$eV = \int_0^h \nu(y) dy = - \int_0^h y\dot{\gamma}(y) dy \quad (\text{F.4})$$

Equations F.3 and F.4 are solved by injecting Equation F.2 while distinguishing the three regions.

Region I: $h > \lambda_i$ and $h > \lambda_o$

In the region I the following equations are obtained:

$$\frac{1+n}{n} \left[\frac{k(\lambda_o - \lambda_i)}{2\tau_y} \right]^{\frac{1}{n}} V = \lambda_i^{1+\frac{1}{n}} - (h - \lambda_o)^{1+\frac{1}{n}} \quad (\text{F.5})$$

$$\frac{(1+n)(1+2n)}{n} \left[\frac{k(\lambda_o - \lambda_i)}{2\tau_y} \right]^{\frac{1}{n}} eV = n\lambda_i^{2+\frac{1}{n}} - (h + nh + n\lambda_o)(h - \lambda_o)^{1+\frac{1}{n}} \quad (\text{F.6})$$

Region II: $h > \lambda_i$ and $h < \lambda_o$

In region II, the velocity and flow rate conservation equation gives respectively:

$$\frac{1+n}{n} \left[\frac{k(\lambda_o - \lambda_i)}{2\tau_y} \right]^{\frac{1}{n}} V = \lambda_i^{1+\frac{1}{n}} \quad (\text{F.7})$$

$$\frac{(1+n)(1+2n)}{n} \left[\frac{k(\lambda_o - \lambda_i)}{2\tau_y} \right]^{\frac{1}{n}} eV = n\lambda_i^{2+\frac{1}{n}} \quad (\text{F.8})$$

By combining these two equations it is possible to express λ_i by:

$$\lambda_i = \frac{1+2n}{n} e \quad (\text{F.9})$$

λ_i is independent of x in this region.

For a given blade shape $h(x)$ and the corresponding deposited thickness e , both of which are measured experimentally, it is therefore possible to compute $\lambda_i(x)$ and $\lambda_o(x)$ and thus evaluate whether a solid-like region is present in the fluid and where it is precisely located under the blade.

RÉSUMÉ

L'étalement de fluides complexes est un processus clé dans l'industrie. Les exemples classiques sont la pose d'enduit ou de peinture, l'application de crème et de maquillage, et la fabrication de papier. Dans toutes ces situations, les fluides sont non-newtoniens en raison de la présence de polymères et/ou de particules, ce qui induit un comportement rhéologique complexe. En nous concentrant sur les applications cosmétiques, nous avons cherché à comprendre comment les propriétés du fluide impactent le film déposé.

Dans une première partie, nous avons considéré l'étalement de solutions de polymères avec une lame flexible qui se déforme pendant l'étalement. Ces expériences ont été combinées avec des modèles numériques et des lois d'échelles. Nous montrons que l'épaisseur du film déposé diminue lorsque le réservoir de fluide se vide menant à des dépôts inhomogènes en épaisseur. En utilisant des fluides newtoniens et complexes aux propriétés rhéologiques bien choisies, nous avons caractérisé les effets de la viscosité, du caractère rhéofluidifiant, et des contraintes normales sur les caractéristiques du film déposé et du processus d'étalement. Ainsi en jouant sur les propriétés rhéologiques du fluide les dépôts peuvent être plus ou moins homogènes. Nous révélons également deux résultats contre-intuitifs : il faut plus d'énergie pour étaler un même volume en un même temps avec un fluide rhéofluidifiant qu'avec un fluide Newtonien. Deuxièmement, les contraintes normales, qui conduisent habituellement à des comportements remarquables, ont ici un effet négligeable en raison de la géométrie d'étalement. Avec les fluides à seuil, des phénomènes parasites associés au seuil rendent les dépôts moins prédictibles.

Dans une deuxième partie, nous avons étudié les défauts d'étalement en se concentrant sur la formation d'agrégats apparaissant parfois lors de l'étalement d'une formulation après séchage sur la peau. Nous avons identifié les paramètres de formulation et d'étalement qui impactent l'apparition de ces défauts, et nous proposons un modèle basé sur la cohésion et l'adhésion. Enfin, nous proposons un critère à respecter pour limiter leur occurrence.

MOTS CLÉS

Fluide complexe, Étalement, Rhéologie, Enduction, Agrégats

ABSTRACT

The spreading of complex fluids is a key process in the industry. Classic examples are the coating of paint or protective layer, cream and make-up application on the skin, and the fabrication of paper. In all these situations, the fluids are non-Newtonian due to the presence of polymers or/and particles, resulting in more complex rheological behavior under shear. Focusing on cosmetic applications, we sought to understand how the fluid properties impact the deposited film.

In the first part, we considered the spreading of polymer solutions with a flexible blade that deforms during spreading. We combined these experiments with numerical models and scaling laws. We show that the thickness of the deposited film decreases as the fluid reservoir empties leading to inhomogeneous deposits in thickness. Using Newtonian and complex fluids with well-chosen rheological properties we disentangled the effects of shear viscosity, shear-thinning, and normal stresses over the characteristics of the deposited film and the coating process. Thus, by playing on the rheological properties of the fluid, the deposits can be more or less homogeneous. We reveal two counterintuitive results: it takes more energy to spread a volume of shear-thinning fluid than a volume of a Newtonian fluid in a given time. Second, the normal stresses, which usually lead to remarkable behaviors have a strikingly negligible effect here due to the coating geometry. With yield stress fluids, specific phenomena associated with the yield make the deposits less predictable.

In the second part, we studied spreading defects by focusing on the formation of aggregates, which sometimes appear during the spreading of a formulation after drying on the skin. We identified the formulation and spreading parameters that influence the development of these defects, and proposed a model based on cohesion and adhesion. Finally, we suggest a criterion to limit their occurrence.

KEYWORDS

Complex fluid, Spreading, Rheology, Coating, Aggregates